# ACADEMIE DE MONTPELLIER

# Université Montpellier II

---

**SPECIALITE PHYSIQUE**

**ECOLE DOCTORALE : SCIENCES PHYSIQUES ET CHIMIQUES**

**FORMATION DOCTORALE : PHYSIQUE DE LA MATIERE CONDENSEE**

## HABILITATION A DIRIGER DES RECHERCHES
## DOCUMENT DE SYNTHESE

Présenté par

**MATTEO CICCOTTI**

Sujet

# ETUDE DE LA PROPAGATION DE FRACTURES DES ECHELLES TRES GRANDES (TECTONIQUE) AUX ECHELLES TRES PETITES (NANOMETRIQUE)

Soutenue le 14 Décembre 2006 devant le jury composé de :

| | |
|---|---|
| Elisabeth BOUCHUD | *Rapporteur* |
| Elisabeth CHARLAIX | *Rapporteur* |
| Christian FRETIGNY | *Rapporteur* |
| Walter KOB | *Examinateur* |
| Christian MARLIERE | *Examinateur* |
| Stéphane ROUX | *Examinateur* |

# Sommaire

**Curriculum Vitae** ..... **1**

**Remerciements** ..... **13**

**Introduction générale** ..... **15**

**Chapitre 1** ..... **17**

**La dynamique de stick-slip dans la propagation d'un front de fissure sur une interface adhésive** ..... **17**

1.1 Introduction ..... 17
1.2 Expériences de déroulement et modélisation ..... 18
1.3 Travail en cours et perspectives ..... 19

**Chapitre 2** ..... **23**

**Etude des tremblements de terre en laboratoire** ..... **23**

2.1 Introduction ..... 23
2.1 Etude de la propagation sous-critique de fractures dans les roches ..... 24
2.1.1 Mesure des paramètres de fracture lente dans les roches ..... 24
2.1.2 Correction de la technique de Torsion Double ..... 25
2.2 Etude du processus de fracturation des roches sous l'action d'un taux de déformation très faible ..... 27
2.3 Etude de la différence entre les modules élastiques dynamiques et statiques des roches ..... 29
2.4 Invariance d'échelle et biais dans l'analyse fractale des images naturelles ..... 31
2.5 Collaboration en tant qu'éditeur associé à l'écriture d'un livre résumant l'état d'avancement des connaissances dans la physique des tremblements de terre ..... 33
2.6 Développement d'un nouveau modèle pour expliquer la physique des tremblements de terre ..... 33

**Chapitre 3** ..... **37**

**Etude par AFM des mécanismes de propagation des fissures dans les matériaux vitreux** ..... **37**

3.1 Introduction ..... 37
3.2 Etude du vieillissement dans les verres colloïdaux ..... 38
3.3 La fracture des verres et l'équipe 'Nanomécanique' ..... 40
3.4 Le rôle de l'eau dans la propagation des fissures dans les verres ..... 43
3.4.1 Etude de la formation d'un condensat capillaire à la pointe de fissure ..... 43
3.4.2 Interprétation du phénomène de diffusion ionique ..... 45
3.5 Développements instrumentaux ..... 47
3.5.1 Mesure de la phase AFM par détection synchrone ..... 47
3.5.2 Estimations des effets de l'humidité relative sur l'équipement de mesure ..... 47
3.5.3 Modélisation des dérives de l'interféromètre ..... 48
3.6 Projets et perspectives ..... 49

**Bibliographie** ..... **53**

# CURRICULUM VITAE DU DR. MATTEO CICCOTTI

## Données Personnelles:

Matteo Ciccotti, né à Macerata (MC), Italie, le 24 Juillet 1972.

Adresse personnelle : 59 rue des Perdigals – 34000 Montpellier.

Tel: 06-71813929.

Nationalité: Italienne.

Web page: http://www.lcvn.univ-montp2.fr/ciccotti

E-mail: ciccotti@lcvn.univ-montp2.fr

## Cursus:

**Depuis Octobre 2005 :** Chargé de Recherche (CR1) au CNRS (section 5) UMR 5587, Laboratoire des Colloïdes, Verres et Nanomatériaux, Université de Montpellier II. Opération de recherche "Nanomécanique".

**Septembre 2004 – Août 2005 :** ATER (service entier) à l'Université de Montpellier II, Laboratoire des Colloïdes, Verres et Nanomatériaux. Expériences: étude par AFM des nanocavitations qui accompagnent la fissuration lente du verre.

**Septembre 2003 - Août 2004**: Chercheur contractuel au Laboratoire de Physique de l'Ecole Normale Supérieure de Lyon. Titre du projet de recherche: "Dynamics and statics of glasses and spin glasses". Expériences: analyse des instabilités liées au vieillissement d'un gel (Laponite) par mesures diélectriques et de diffusion dynamique de lumière.

**Septembre 2000 - Août 2003**: PostDoc de trois ans (Assegno di Ricerca) auprès du Département de Physique de l'Université de Bologne, Italie. Titre du projet de recherche: "Studio dei terremoti in laboratorio" (Etude des tremblements de terre en laboratoire).

**Avril 2000 - Août 2000**: Contrat de recherche avec le Département de Physique de l'Université de Bologne, Italie pour la réalisation d'un système d'acquisition des émissions ultrasoniques produites par des microfissures dans des roches.

**Janvier 1999 - Mai 1999**: Hôte au Laboratoire de Physique et Mécanique des Milieux Hétérogènes à l'Ecole Supérieure de Physique et Chimie Industrielles de la Ville de Paris pour réaliser une expérience sur la dynamique des fractures dans les milieux viscoélastiques.

**Depuis 1997**, membre associé du INFN (Institut National de Physique Nucléaire), groupe théorique, Bologne, Italie.

**Novembre 1996 - 9 Mars 2000:** Doctorat de Physique à l'Université de Bologne, Italie. Titre de la thèse: "An exhaustive analysis of the Double Torsion method for sub-critical fracture propagation in lava rocks and its implications for the understanding of earthquake physics".

**Septembre 1994 - Juin 1995:** étudiant ERASMUS à l'Université Paris VII, maîtrise de physique fondamentale.

**Septembre 1991 - 22 Mars 1996**: Diploma di Laurea in Fisica (équivalent de DEUG + licence + maîtrise + DEA) à l'Université de Bologne, Italie. Note: 110/110 avec félicitation. Titre de la thèse: "Analisi di modelli per la dinamica della linea di frattura del nastro adesivo" (Etude d'une modèle de la dynamique de la ligne de fissure dans un ruban adhésif).

**Juillet 1991**: Classé dans les 10 premiers aux Olympiades de Physique, Senigallia, Italie.

**Septembre 1986 - Juillet 1991**: Diplôme de Maturità Scientifica (équivalent du Baccalauréat) au Lycée Scientifique Enrico Fermi de Bologne, Italie, avec 5 ans de spécialisation en Physique et Chimie expérimentale. Note: 60/60.

# Langues étrangères:

**Anglais et Français :** bon, écrit et parlé. I**Italien :** langue mère.

# Connaissances Informatiques:

**Systèmes d'exploitation**: DOS, Windows 3.11/95/NT/98/ME/2000/XP, Linux, Unix.

**Logiciels**: MSC Marc, Office, Origin, Frontpage, Corel Draw, Adobe Illustrator

**Langages de programmation**: Fortran, C, C++, Basic, Pascal, Matlab, HTML, LaTeX.

# Collaborations avec des journaux scientifiques:

**“Referee” pour les articles soumis à**: Applied Physics Letters, International Journal of Fracture, Materials Science, Rock Mechanics and Rock Engineering, Geophysical Research Letters, Geophysical Journal International, Annals of Geophysics.

**“Associate Editor” pour les articles soumis à**: Medical Physics.

# Affiliations scientifiques:

**American Ceramic Society** depuis Janvier 2006.

**American Geophysical Union** depuis Janvier 2003.

**European Geophysical Union** depuis Janvier 2003.

## Publications dans livres scientifiques à diffusion internationale

1. **Ciccotti M.** and Giorgini B. The emergence of complexity in a common scotch roller. Dans: Symétries, brisures de symétries et complexité. Edité par L. Boi. Peter Lang, Bern, 2006. pp. 187-216.
2. Editeur associé du livre: Earthquake Science and Seismic Risk Reduction. NATO SCIENCE SERIES: IV: Earth and Environmental Sciences Volume 32. Edité par F. Mulargia et R. Geller. Kluwer, 2003. Auteur des contributions suivantes:
    1. **Ciccotti M.** Section 2.1: Seismology and Geodesy. pp. 43-49.
    2. Mulargia F., Castellaro S. and **Ciccotti M.**. Section 2.8: Earthquake Energy Balance. pp. 80-89.
    3. Mulargia F., Main I., **Ciccotti M.**, Castellaro S. and Kertesz J. Chapter 3: Physics of Complex Systems and Earthquakes. pp. 107-152.

## Articles soumis :

1. George M., **Ciccotti M.**, Wondraczek L., Dittmar A., Oelgardt C., Célarié F. and Marlière C. Formation and evolution of a confined liquid condensate at the crack tip in glasses. Proceedings de la conférence Fractography of Glasses and Ceramics V. 9-12 juillet 2006. Rochester, NY (USA). A paraître.
2. Célarié F., **Ciccotti M.**, George M. and Marlière C. Effect of stress gradient at the vicinity of a crack tip on ionic diffusion in silicate glasses: an AFM study. Proceedings de la conférence Fractography of Glasses and Ceramics V. 9-12 juillet 2006. Rochester, NY (USA). A paraître.
3. Kumar J., De R., **Ciccotti M.** and Ananthakrishna G. Unfolding the hidden order in acoustic emission data in the peeling of an adhesive tape. Proceedings de la conférence : Multiscale Material Modeling, 18-22 septembre, 2006. Freiburg, Allemagne. Soumis en juillet 2006.
4. Cortet P.-P., **Ciccotti M.** and Vanel L. Imaging the stick-slip peeling of an adhesive tape. *Int. J. Adhes. Adhes.* En préparation.
5. Mulargia F., Castellaro S. and **Ciccotti M.**. Ignition threshold and self-similarity allow earthquakes to be triggered by tiny stresses. *Geophys. Res. Lett.* Soumis en janvier 2006.

## Publications dans des journaux internationaux:

1. Célarié F., **Ciccotti M.** and Marlière C. Stress-enhanced ion diffusion at the vicinity of a crack tip as evidenced by atomic force microscopy in silicate glasses. *J. Non-Crist. Solids.* A paraître.
2. Wondraczek L., **Ciccotti M.**, Dittmar A., Oelgardt C., Célarié F. and Marlière C., 2006. Real-time observation of non-equilibrium liquid condensate confined at tensile crack tips in oxide glasses. *J. Am. Cer. Soc.* 89[2], pp. 746-749.
3. **Ciccotti M.**, Giorgini B., Vallet D. and Barquins M., 2004. Complex dynamics in the peeling of an adhesive tape. *Int. J. Adhes. Adhes.* 24/2, pp. 143-151.
4. Mulargia F., Castellaro S. and **Ciccotti M.**, 2004. Earthquakes as three stage processes. *Geophys. J. Int*. 158[1], pp. 98-108.

5. **Ciccotti M.** and Mulargia F., 2004. Experimental differences between static and dynamic measurements of the elastic moduli in a typical seismogenic rock. *Geophys. J. Int.* 157[1], pp. 474-477.
6. **Ciccotti M.**, Almagro R. and Mulargia F., 2004. Static and dynamic moduli of the seismogenic layer in Italy. *Rock Mech. and Rock Eng.* 37[3], pp. 229-238.
7. **Ciccotti M.** and Mulargia F., 2002. Pernicious effect of physical cutoffs in fractal analysis. *Physical Review E.* 65, pp. 37201-04.
8. **Ciccotti M.**, Negri N., Gonzato G., Mulargia F., 2001. Practical application of an improved methodology for the Double Torsion load relaxation method. *Int. J. of Rocks Mech. and Mining Sciences*, 38, pp. 569-576.
9. **Ciccotti M.**, Gonzato G., and Mulargia F., 2000. The double torsion loading configuration for fracture propagation: an improved methodology for the load-relaxation at constant displacement. *Int. J. of Rock Mech. and Mining Sciences.* 37/7, pp. 1103-1113.
10. Gonzato G., Mulargia F. and **Ciccotti M.,** 2000. Measuring the fractal dimension of ideal and actual objects: implications for application in geology and geophysics. *Geophys. J. Int.* 142, pp. 108-116.
11. **Ciccotti M.**, 2000. A realistic finite element study of the Double Torsion loading configuration. *Journal of the American Ceramic Society.* 83 [11], pp. 2737-44.
12. **Ciccotti M.**, Negri N., Sassi L., Gonzato G. and Mulargia F., 2000. Elastic and fracture parameters of Etna, Stromboli and Vulcano lava rocks. *Journal of Volcanology and Geothermal Research.* 98/1-4, pp. 209-217.
13. **Ciccotti M.**, Giorgini B., Barquins M., 1998. Stick-slip in the peeling of an adhesive tape : evolution of theoretical model. *Int. J. Adhes. Adhes.* 18, pp. 35-40.
14. Barquins M., **Ciccotti M.**, 1997. On the kinetics of peeling of an adhesive tape under a constant imposed load. *Int. J. Adhesion and Adhesives*. 17, 65-68.
15. Barquins M., Boilot A., **Ciccotti M.**, Varotto A., 1995. Sur la cinétique de décollement d'un ruban adhésif sous l'action d'un poids mort. *C. R. Académie des Sciences Paris*., t. 321, Série II b, p. 393-399.

# Publications dans des actes de congrès avec comité de lecture :

1. Bellon L., Buisson L., **Ciccotti M.**, Ciliberto S. et Douarche F., Thermal noise properties of two ageing materials. Dans : Jamming, Yielding, and Irreversible Deformation in Condensed Matter. Série: Lecture notes in physics, vol 688. Proceedings of the XIX Sitges Conference (June 2004). Edité par M. Rubí et C. Miguel (Springer Verlag, Berlin, 2006). cond-mat/0501324.
2. Buisson L., **Ciccotti M**., Bellon L. and Ciliberto S.. Electrical noise properties in aging materials. In: Fluctuations and Noise in Materials, edité par D. Popovic, M.B. Weissman et Z.A. Racz. Proceedings of SPIE Vol. 5469 (SPIE, Bellingham, WA, 2004). Invited paper. pp. 150-163. cond-mat/0403294.

# Conférences et congrès internationaux:

1. Kumar J., De R., **Ciccotti M.** and Ananthakrishna G. Unfolding the hidden order in acoustic emission data in the peeling of an adhesive tape. Présentation orale à la conférence : Multiscale Material Modeling, 18-22 septembre, 2006. Freiburg, Allemagne.
2. **Ciccotti M.**, George M., Wondraczek L., Célarié F. and Marlière C. Nanomechanics of slow crack propagation in oxide glasses. **Présentation orale** à la 16th European Conference on Fracture. 3-7 juillet 2006. Alexandroupolis, Grece.
3. George M., **Ciccotti M.**, Wondraczek L., Dittmar A., Oelgardt C., Célarié F. and Marlière C. Formation and evolution of a confined liquid condensate at the crack tip in glasses. **Presentation orale** à la conference Fractography of Glasses and Ceramics V. 9-12 juillet 2006. Rochester, NY (USA).
4. Célarié F., **Ciccotti M.**, George M. and Marlière C. Effect of stress gradient at the vicinity of a crack tip on ionic diffusion in silicate glasses: an AFM study. **Présentation orale** à la conférence Fractography of Glasses and Ceramics V. 9-12 juillet 2006. Rochester, NY (USA).
5. Wondraczek L., Célarié F., Dittmar A., Oelgardt C., **Ciccotti M.** and Marlière C., 2005. Real-time observation of liquid condensate confined at tensile crack tips in silca glasses. **Présentation orale** au 2005 MRS Fall Meeting, Boston, MA, USA, 28 Novembre – 2 Décembre 2005.
6. **Ciccotti M.**, George M., Marlière C., 2005. Nanomechanics of slow crack propagation in glasses. **Poster** au 3rd International Workshop on Flow and Fracture of Advances Glasses, State College, PA, USA, 2-5 octobre 2005.
7. Célarié F., **Ciccotti M.**, Marlière C., 2005. A Study of the vicinity of a crack tip at nanometer scale enhanced nano migration-of ions in silicate glasses. **Présentation orale** à la 5th international conference and 7th annual general meeting of the EUropean Society for Precision Engineering and Nanotechnology. Le Corum, Montpellier, France, 8-11 May 2005.
8. **Ciccotti M.**, 2004. Earthquake: the geophysicist's point of view. **Présentation orale invitée** au Workshop: Geological evidence of earthquake source dynamics. INOA, Florence, Italie, 30 Août 2004.
9. **Ciccotti M.** and Mulargia F., 2003. Static and dynamic measurements of the elastic properties of a lava rock from Mount Etna volcano and of a typical seismogenic rock of Italy. **Presentation orale invitée** au Workshop: New Technologies in Geophysics, Geomechanics and Volcanology. Napoli, Italy, 18-20 Septembre 2003.
10. **Ciccotti M.**, Castellaro S. and Mulargia F., 2003. Very low strain rate damage evolution monitored by acoustic emissions. **Présentation orale et poster** à la EURO-Conference on Rock Physics and Geomechanics. Kijkduin, The Nederlands, 7-11 Septembre 2003.
11. **Ciccotti M.**, Mulargia F. and Almagro R., 2003. Static and dynamic measurements of the elastic moduli in a typical seismogenic rock of Italy and in a lava rock from Mount Etna volcano. **Poster** à la EGS-AGU-EUG Joint Assembly 2003. Nice, France, 6-11 Avril 2003.

12. Vallet D., **Ciccotti M.**, Giorgini B. and Barquins M., 2002. The stick-slip dynamics in the peeling of an adhesive tape. **Présentation orale**. EUROCOAT 2002 Congress, International Exhibition & Congress for the paint, Pigment, Varnish, Printing Ink, Glue & Adhesive Industries. Barcelona, Palau Sant Jordi (Espagne), 4-6 Juin 2002.
13. Vallet D., **Ciccotti M.**, Giorgini B. and Barquins M., 2002. The stick-slip dynamics in the peeling of an adhesive tape. **Présentation orale**. Swiss Bonding 2002 - 16th International Symposium Bonding and Sealing Technology, ITR Rapperswill (Swisse), 27-29 Mai 2002.
14. Barquins M., **Ciccotti M.**, Giorgini B., Vallet D., 2001. A complex dynamics in the peeling of an adhesive tape. **Présentation orale** au congrès international: Determinism, holism and complexity, tenu au Castello Aldobrandesco di Arcidosso, Italie, 3-8 Septembre 2001.
15. **Ciccotti M.**, 2000. Critical rupture in the laboratory. **Présentation orale** à l'ARW2000: State of scientific knowledge regarding earthquake occurrence and implications for public policy. Arbus, Sardinia, Italie. 15-19 Octobre 2000.
16. Mulargia F., **Ciccotti M.**, Castellaro S.and Gonzato G, 2000. A very low strain rate rupture experiment. **Présentation orale** à l'EGS2000: European Geophisical Society. XXV General Assembly. Nice, France, 25-29 Avril 2000.
17. Gonzato G., **Ciccotti M.** and Mulargia F., 2000. Fractal dimension of river patterns: a geological context-recognition technique. **Présentation orale** à l'EGS2000: European Geophisical Society. XXV General Assembly. Nice, France, 25-29 Avril 2000.
18. **Ciccotti M.**, Gonzato G., Mulargia F., 2000. An improved methodology for the double torsion load-relaxation method. **Présentation orale** à l'EGS2000: European Geophisical Society. XXV General Assembly. Nice, France, 25-29 Avril 2000.
19. Gonzato G., Mulargia F. and **Ciccotti M.,** 1999. Other potential sources of bias measuring fractal dimension through box counting. **Présentation orale** à l'EGS99: European Geophisical Society. XXIV General Assembly. The Hague, The Netherlands, 19-23 Avril 1999.
20. **Ciccotti M.,** Negri N., Gonzato G. and Mulargia F., 1999. The double torsion loading configuration: a detailed numerical study. **Présentation orale** à l'EGS99: European Geophisical Society. XXIV General Assembly. The Hague, The Netherlands, 19-23 Avril 1999.
21. **Ciccotti M.,** 1998. A Wavelet application in the analysis of fracture mechanics data. **Présentation orale et contribution écrite** à la International Wavelet Conference - Tangier 98, Maroc.
22. **Ciccotti M.**, 1996. On the kinetics of peeling of an adhesive tape under a constant imposed load. **Présentation orale** au Workshop: Complexity and Chaos, Institute for Scientific Interchange, 1-12 Juillet 1996, Torino, Italie.
23. Barquins M., **Ciccotti M.,** 1996. On the kinetics of peeling of an adhesive tape under a constant imposed load. **Présentation orale invitée + proceedings** du congres EUROCOAT 1996. International Congress of Paintings and Adhesives. 18-20 Septembre 1996, Genova, Italie.

# Conférences nationales:

1. **Ciccotti M.,** George M., Célarié F. and Marlière C. Étude par AFM des mécanismes de corrosion sous contrainte du verre. **Présentation orale** à la réunion conjointe de l'Union pour la Science et la Technologie Verrières et du GDR Matériaux Vitreux. Montpellier, France, 8-9 Juin 2006.
2. **Ciccotti M.**, George M., Célarié F. and Marlière C. Nanomechanics of slow crack propagation in glasses. **Poster** au Forum des microscopies à sonde locale 2006, Autrans, France, 27-31 Mars 2006.
3. Célarié F., **Ciccotti M.**, George M. et Marlière C. Diffusion ionique sous contrainte en tête de fissure : étude par AFM de verres sodo-silicatés. **Présentation orale** au Forum des microscopies à sonde locale 2006, Autrans, France, 27-31 Mars 2006.

1. **Ciccotti M.**, George M., Marlière C.. Nanomécanique de la propagation lente de fractures dans les verres. **Poster et présentation orale invitée** à la reunion conjonte de l'Union pour la Science et la Technologie Verrières et du GDR Matériaux Vitreux. Bourg la Reine, France, 20-21 Octobre 2005.
2. **Ciccotti M.**, Célarié F., Dittmar A., Oelgardt C., Wondraczek L., and Marlière C. Quid de l'observation en volume des cavités d'endommagement crées lors de la propagation lente d'une fissure dans un matériau vitreux ? **Présentation orale** au Forum des microscopies à sonde locale 2005, Anglet, France, 29-31 Mars 2005.
3. **Ciccotti M.**, Giorgini B., Barquins M., Vallet D., 2004. La dynamique de stick-slip dans la propagation d'un front de fracture sur une interface adhésive. **Présentation orale** à la 9ème réunion du Club Fissures : Mécanismes de Fissuration. CEA Saclay. 13 Octobre 2004
4. Vallet D., **Ciccotti M.**, Giorgini B., Barquins M., 2001. La dynamique de Stick-Slip dans le pelage d'un ruban adhésif. **Présentation orale et contribution écrite** au 4ème Rencontre du Non-Linéaire. Institut Henry Poincaré, Paris, 15-16 Mars 2001.
5. Mulargia F., **Ciccotti M.** and Castellaro S., 2001. Static and dynamic elastic constants. **Présentation orale**. Réunion annuelle GNV. Roma, Italia, 9-11 Septembre 2001.
6. **Ciccotti M.,** Castellaro S. and Mulargia F., 2001. Costanti elastiche statiche e dinamiche. **Présentation orale**. Workshop sur le projet GNV-POSEIDON. Catania, Italie, 19-20 Juillet 2001.
7. Gonzato G., **Ciccotti M.** and Mulargia F., 1999. Si fa presto a dire invarianza di scala. **Présentation orale**. 18ème réunion annuelle du GNGTS
8. **Ciccotti M.**, Gonzato G. and Mulargia F., 1999. La propagazione stabile e controllata di fratture in laboratorio. **Présentation orale**. 18ème réunion annuelle du GNGTS.
9. **Ciccotti M.**, 1999. Le Déroulement du Scotch. **Présentation orale et contribution écrite** à la Journée du Laboratoire de Physique et Mécanique des Milieux Hétérogènes. 16 Février 1999. Ecole Supérieure de Physique et Chimie Industrielles, Paris. Journée présentée par le prix Nobel P.G. de Gennes.

## Autres Workshops et Ecoles thématiques:

1. 8th ESG Conference : « Glass, The art of Science » avec rencontre annuel de l'ICG et de la SGT, 10-14 septembre 2006. Sunderland, UK.
2. 12ème Colloque sur les cristaux liquides, 13-16 Septembre 2005, Montpellier.
3. Ecole thématique CNRS : Nanosciences et sondes locales. 1-5 Avril 2005, Anglet.
4. 3ème rencontre du PPF : « Dynamique des Systèmes Complexes » de l'Université Grenoble I, 6-7 décembre 2004, Pinsot, Massif de Belledonne.
5. ERMES - Earthquake mechanics, Earth structure and related problems. 22nd Course of the International School of Geophysics. Erice, Sicily, 1-8 Août 2002.
6. EAGE2002 Symposium. New Technologies for Land Monitoring: from Digital Elevation Models to Subsidence Estimation. 27 Mai 2002. Florence, Italie.
7. Natural and Anthropogenically Induced Hazards. Euresco Conference. 24-29 Juin 2000. Acquafredda di Maratea, Italy.
8. International Wavelet School. Juillet 1998. Orsay, Paris, France.
9. Workshop sur ``Complexity and Chaos'' à l'Institute for Scientific Interchange, Torino (Italy), 1-12 Juillet, 1996.

## Séminaires :

1. Nanomeccanica della propagazione lenta di fratture nei vetri di silice. Département de Physique, Université de Bologne, Italie.
2. Real-time observation on non-equilibrium liquid condensate confined at tensile crack tips in oxide glasses. 07/10/2005. NIST. Gaithersburg, MD, Etats-Unis.
3. Nuove osservazioni sulla fisica della fratturazione lenta della silice amorfa. 26/10/2005. INGV. Roma, Italie.
4. La dynamique de stick-slip dans la propagation d'un front de fracture sur une interface adhésive. 13/01/2005. LPPMD-ESPCI ,Paris.
5. Dynamique complexe dans le pelage d'un ruban adhésif. 01/10/2004. Université Lyon I, Lyon.
6. La dynamique de stick-slip dans la propagation d'un front de fracture sur une interface adhésive. 11/05/2004. LPS, ENS, Paris.
7. La dynamique de stick-slip dans la propagation d'un front de fracture sur une interface adhésive. 04/05/2004. IUSTI, Université de Aix-Marseille.
8. La dynamique de stick-slip dans la propagation d'un front de fracture sur une interface adhésive. 30/04/2004. GPS, Université Paris 6, Paris.
9. La dynamique de stick-slip dans la propagation d'un front de fracture sur une interface adhésive. 30/03/2004. LCVN, Université de Montpellier 2.
10. La dynamique de stick-slip dans la propagation d'un front de fracture sur une interface adhésive. 11/11/2001. Laboratoire de Physique. ENS-Lyon.
11. La dynamique de stick-slip dans la propagation d'un front de fracture sur une interface adhésive. 31/10/2001. Département de Physique, Université de Bologne, Italie.
12. Analisi approfondita del metodo di Double Torsion per lo studio della propagazione subcritica di fratture in rocce laviche, 13/12/2000. Département de Physique, Université de Bologne, Italie.

## Stages de Formation Professionnelle:

Stage "Découverte des métiers" auprès de l'Association de Formation Professionnelle de l'Industrie rhodanienne. Lyon. Le stage comporte une activité de **21 heures** de formation à l'utilisation des machines d'atelier (tour, fraise, perceuse) pour la réalisation de pièces en métal et en plastique. 4-6 Février 2004.

## Activités d'Animation Scientifique:

1. Séminaires au Lycee La Merci (Montpellier) sur la 'Physique de la Fracture' dans le cadre de la Fête de la Science 2006, Octobre 2006.
2. Participation à l'animation de l'exposition "Jeux de grains" dans le cadre de l'Année Mondiale de la Physique 2005 en Languedoc-Roussillon, Mars 2005.
3. Participation à l'animation du stand du Laboratoire de Physique de l'ENS-Lyon dans le cadre de la Fête de la Science 2003, Octobre 2003.

## Activités en matière de responsabilités collectives:

1. Membre nommé du Technical Committee 6 : Mechanical Properties of Glasses dans le cadre de l'International Commitee on Glass (ICG) qui a pour but de promouvoir des échanges et des coopérations internationales sur la science et la technologie verrières. Depuis juin 2006.
2. Chef de l'équipe Nanomécanique au Laboratoire de Colloïdes, Verres et Nanomatériaux à partir de octobre 2005.
3. Coresponsable de la structuration de l'Axe Verres du LCVN qui comporte la coopération transversale de plusieurs équipes.
4. Membre nommé du Conseil du Laboratoire des Colloïdes, Verres et Nanomatériaux à partir de février 2005.

## Implication dans des projets :

1. Participation à la mise en place d'un PPF Verres regroupant les activités du pole verrier Montpelliérain et dans l'organisation d'une rencontre du GDR Matériaux Vitreux à Montpellier.
2. Appel Projet Jeunes Chercheurs 2005 de l'Université de Montpellier 2. Financement obtenu sur le projet : 'Etude par Microscopie à Force Atomique (AFM) de la propagation lente de fissures dans les verres. Vers une mesure quantitative des propriétés nanomécaniques locales'.
3. Porteur d'un projet pour l'appel blanc ANR 2006 (CORCOSIL) qui comporte une collaboration avec le CEA-Saclay.
4. Participation à la mise en place d'un projet européen sur la Mécanique des Fractures dans le cadre du 7ème PCRD.
5. Participation à la rédaction d'un projet sur les verres et la nanoscience pour le CPER 2007-2013.

# Activités d'enseignement:

1. 2006 : participation à la préparation des fiches projets pour le cours de Physique Experimentale (L1) à l'Université de Montpellier II, Département de Physique.
2. 2004-2005 : ATER (entier) à l'Université de Montpellier II, Département de Physique. Activité d'enseignement effectuée : **197 heures** de ETD :
    1. Physique Expérimentale, L1 (**66 heures cours/TD + 54 heures TP**) ;
    2. Passeport Minimale Informatique, L1 (**30 heures TP**) ;
    3. Thermodynamique, DEUG 2ème année (**30 heures TP**) ;
    4. Thermodynamique et Mécanique des Fluides, Licence (**65 heures TP**).
3. **32 heures de cours + 58 heures TD** de Physique Générale, L1. Département d'Ingénierie de Gestion de l'Université de Bologne, Italie, de Janvier à Juin 2003.
4. **8 heures de cours** sur l'analyse des données scientifiques avec le logiciel Matlab. Formation des doctorants de l'Université de Sienne, Italie (année 2003).
5. **48 heures de TD/TP** sur l'utilisation du logiciel Microsoft Office XP pour la création de documents formatés et feuilles de calcul. Institut de formation professionnelle ECIPAR. Mars-Juillet 2002.
6. **2 x 10 heures de TD** sur l'utilisation du logiciel "Octave" pour l'analyse et la représentation des données. Dans le cours de "Géodynamique" (3ème année) tenu par Pr. F. Mulargia à l'Université de Bologne, Italie. Mai 2002 et Mai 2003.
7. Agrégation de Physique et de Mathématique (en Italie) depuis Mai 2001.
8. **5 x 20 heures de TD** de Mécanique des Milieux Continus. Dans l'enseignement "Physique de la Terre" (4ème année) tenu par Pr. F. Mulargia à l'Université de Bologne, Italie (1998-2003).
9. **10 heures de cours** de Sciences Naturelles au Lycée Statale Copernico de Bologne, Italie, 2000: "Introduction à la phénoménologie des systèmes complexes".
10. **3 x 50 heures de TD** de Thermodynamique. Dans l'enseignement "Physique Technique" tenu par B. Giorgini (1996-1999). Ecole Polytechnique de Milan, Italie.

# Encadrement d'Etudiants:

Encadrement en cotutelle de thésards:

a. Thèse doctorale en Physique du Dr. A. Grimaldi à l'Université Montpellier 2 à partir de Octobre 2006. Ecole Doctorale de Chimie et Physique. Titre : "Etude par AFM des mécanismes de corrosion sous contraintes du verre". Dirécteur : Ahmed Zahab..
b. Thèse doctorale en Sciences Géologiques du Dr. S. Castellaro à l'Université de Bologne, Italie, 1998-2001. Titre : "Studio del Meccanismo Sismico in Laboratorio e al Calcolatore" (Etude du mécanisme sismique en laboratoire et à l'ordinateur). Dirécteur Francesco Mulargia.

Encadrement en cotutelle d'étudiants de Tesi di Laurea (équivalent d'un stage de DEA):

c. Tesi di Laurea en Sciences Géologiques du Dr. F. Menapace à l'Université de Bologne, Italie, dans l'année 2003-2004. Titre de la thèse: "Studio di propagazione sottocritica delle fratture su roccia in configurazione di carico double-torsion" (Etude de la propagation sous-critique de fissures dans les roches en configuration de charge de torsion-double).
d. Tesi di Laurea en Sciences Géologiques du Dr. R. Almagro à l'Université de Bologne, Italie, dans l'année 2001-2002. Titre de la thèse: "Caratterizzazione meccanica di un litotipo sismico italiano: il Calcare Massiccio" (Caractérisation mécanique d'un lytotype sismique italien: Calcare Massiccio).
e. Tesi di Laurea en Physique du Dr. E. Lunedei à l'Université de Bologne, Italie, dans l'année 2001-2002. Titre de la thèse: "Modellizzazione ed analisi dei dati in un esperimento di dinamica delle fratture" (Modèles et analyse des données d'une expérience de dynamique de fractures).
f. Tesi di Laurea en Sciences Géologiques du Dr. M. Morrone à l'Université de Bologne, Italie, dans l'année 1998-99. Titre de la thèse: "Un modello a stick-slip e sue applicazioni in sismotettonica" (Une modèle de stick-slip et ses applications en sismotectonique).
g. Tesi di Laurea en Sciences Geologiques du Dr. N. Negri à l'Université de Bologne, Italie, dans l'année 1997-98. Titre de la thèse: "Caratterizzazione dei parametri morfologici, chimici, elastici e di frattura di lave eoliane" (Caractérisation des paramètres morphologiques, chimiques, élastiques et de fracture des laves Aeoliennes).

Encadrement en cotutelle d'étudiants de stage à l'Université de Montpellier 2 :

h. Vincent Ranieri. Stage de M2 Matériaux, durée 7 mois à partir de janvier 2006. 'Mesure par AFM de la propagation lente de fissures dans des verres de silice'
i. Félix Barre. Stage de M1 Physique, durée 2 mois à partir de avril 2006. 'Modélisation des effets environnementaux sur le fonctionnement d'un interféromètre hétérodyne de précision'.
j. Camille Echampard. Stage de M1 PhyMaTech, durée 3 mois à partir de février 2006. Titre : 'Mesure par DLS de la dynamique lente dans un verre colloïdale'.

## Remerciements

Le travail présenté dans ce mémoire doit énormément à mes encadrants de recherche : F. Mulargia, B. Giorgini et G. Turchetti à l'Université de Bologne, M. Barquins à l'ESPCI de Paris, S. Ciliberto et L. Vanel à l'ENS-Lyon, et enfin C. Marlière à l'Université de Montpellier II qui m'à accueilli dans son équipe en septembre 2004 et qui m'a ensuite confié son brillant montage expérimental. Leur passion de la recherche, leur disponibilité, et leur enthousiasme ont été un moteur très important pour mes activités de recherche.

Je dois aussi beaucoup à tous les étudiants que j'ai pu encadrer, de près ou de loin : R. Almagro, L. Sassi, M. Morrone, E. Lunedei, F. Menapace pendant leur stage annuel pour la Tesi di Laurea en Italie, S. Castellaro pendant sa thèse et son postdoc, C. Simonnet, V. Ranieri, F. Barre et C. Echampard pendant des stages de courte durée.

Par ailleurs je voudrais aussi remercier tous mes collaborateurs proches ou lointains, parmi lesquels je nommerais particulièrement Matthieu George avec qui je forme une jeune équipe très dynamique.

Beaucoup de choses n'auraient jamais abouti sans le soutien du personnel technique (pour me limiter à ma période montpelliéraine je citerai P. Solignac, R. Vialla, J.-M. Fromental, G. Prevot, E. Alibert, S. Clément et B. Colaiocco) et le support administratif sans failles de Doris, Sylvie, Geneviève, Tina et Sahondra qui doivent souvent composer avec d'imprévisibles chercheurs.

Je voudrais aussi remercier tous les chercheurs et enseignants-chercheurs du LCVN pour leur contribution à une ambiance de labo chaleureuse et ouverte à tous les sujets de discussion.

Je remercie enfin Lalla, ma douce compagne, pour m'avoir à la fois stimulé et supporté dans mon travail souvent déréglé et dans mes déplacements, ainsi que ma famille et mes amis.

# Introduction générale

Mon parcours de recherche pourrait paraître très hétérogène : il commence par l'étude de la dynamique de stick-slip dans le déroulement des rubans adhésifs, pour continuer avec une étude de mécanique de fracture des roches visant à la compréhension de la physique des tremblements de terre et des éruptions volcaniques, et s'achemine ensuite (moyennant une courte parenthèse sur le vieillissement des matériaux amorphes) vers l'étude de la propagation lente de fissures dans les verres, étudiée à l'échelle nanométrique.

Le thème de cette habilitation à diriger des recherches, que j'ai titré : « Etude de la propagation de fractures des échelles très grandes (tectonique) aux échelles très petites (nanométrique) » est de montrer l'unité de ce parcours, guidé par la passion pour le sujet de la fracture (l'un des plus complexes phénomènes physiques, encore non complètement maîtrisé) et pour l'interdisciplinarité, qui permet d'observer le même phénomène depuis des points de vue très différents dans l'espoir d'acquérir le recul nécessaire à une vraie innovation.

Le sujet du ruban adhésif se rapproche d'une part à la physique des systèmes dynamiques complexes, de l'autre du monde des applications industrielles, tout en restant un objet de la vie de tous les jours.

La mécanique des roches dans un contexte de géophysique nous confronte à la difficulté d'expliquer des mécanismes fondamentaux à partir d'échantillons tellement hétérogènes qu'ils paraissent avoir été conçus pour n'avoir rien en commun avec ce qu'un physicien choisirait pour ses expériences. Pourquoi s'acharner ? Pour le rêve (probablement irréalisable) d'arriver un jour à la prévision des tremblements de terre.

Mais il vient un jour ou le physicien retrouve la fascination pour un matériau modèle (ou du moins ce qu'il pensait en être un) : le verre, et la possibilité d'étudier ce qui fait avancer les fissures à un niveau vraiment fondamental : l'échelle nanométrique, soit ce niveau supramoléculaire où se situent les hétérogénéités de ce matériau sinon complètement amorphe.

Ces trois mondes sont aussi trois communautés scientifiques très différentes, chacune avec ses plus et ses moins, ce qui est un stimuli de plus pour développer ce fameux recul. A présent, je peux dire que je suis encore impliqué dans chacune, grâce aussi aux bonnes relations que j'ai eu la chance de développer. Je dédierai donc un chapitre autonome à chaque discipline, comportant son introduction plus détaillée, ainsi que quelques exemplaires de mes travaux et l'état des perspectives.

# Chapitre 1

## La dynamique de stick-slip dans la propagation d'un front de fissure sur une interface adhésive

### 1.1 Introduction

Ce sujet représente pour moi quelque chose de ‘sentimental’ ayant marqué mes premières activités de recherche lors d’un stage ERASMUS dans un module de Physique Expérimentale pendant ma maîtrise à Paris7. Pendant ce court stage de six mois, j’ai eu l’occasion de rencontrer Michel Barquins de l’ESPCI de Paris et les discussions très stimulantes qu’on a eues, m’ont permis d’obtenir les premiers résultats originaux. C’était le début d’une longue amitié et d’une collaboration informelle qui a abouti à mon mémoire de ‘Laurea’ à Bologne et qui a accompagné mes travaux dans des autres domaines tout en amenant, de temps en temps, de nouvelles idées et des résultats encourageants. Alors que Michel prend sa bien méritée retraite cette année, le ruban adhésif est encore présent dans mes travaux à travers une nouvelle expérience d’imagerie rapide réalisée en collaboration avec l’ENS-Lyon, et une collaboration avec une équipe en Inde sur l’analyse statistique des séries temporelles. Pour témoigner de cette bonne expérience, j’ai récemment reproposé ce sujet comme projet du module de Physique Expérimentale aux étudiants de l’Université Montpellier II dans l’attente que d’autres esprits curieux apportent leur point de vue.

Le décollement (ou ‘pelage’) d’un ruban adhésif constitue un prototype très simple de propagation bidimensionnelle d’une fissure entre deux milieux dissemblables, la colle étant un système viscoélastique fortement dissipatif (Maugis et Barquins, 1988). Dans l’expérience de tous les jours, on observe que le déroulement d’un rouleau de scotch peut se faire de façon régulière ou bien saccadée, accompagnée par un son caractéristique (le ‘zip’ du scotch). Cette dynamique saccadée, que l’on appelle ‘stick-slip’, est tout à fait analogue au mouvement saccadé d’un bloc tiré sur une surface rugueuse ; par ailleurs elle est aussi responsable du grincement d’une porte, du son émis lors du glissement d’un archer de violon ou des tremblements de terre sur les failles tectoniques. C’est en général une dynamique typique des systèmes où l’on a une traction (ou déformation) stationnaire, et un mécanisme de glissement (ou fracture) caractérisé par une chute de la force résistante au delà d’un seuil. Le nom de ‘stick-slip’ vient du fait qu’il s’agit d’une alternance de phases de grippage ‘stick’ durant lesquelles se produit une accumulation d’énergie et de phases d’avancement rapide ‘slip’ durant lesquelles l’énergie est libérée soudainement avec émission acoustique. Si dans certaines conditions on peut avoir une dynamique de stick-slip bien périodique, dans d’autres elle peut devenir fortement irrégulière et imprévisible, en analogie à ce qui arrive avec les tremblements de terre. Le ruban adhésif a l’avantage d’être un système suffisamment simple et économique pour essayer de comprendre les clés de ce phénomène qui échappe encore à une modélisation satisfaisante.

## 1.2 Expériences de déroulement et modélisation

Les deux montages de base pour l'étude de la dynamique de la ligne de fissure d'un ruban adhésif sont les suivants :

1) Déroulement sous l'action d'une force constante : réalisé en appliquant une masse à l'extrémité libre du ruban. Dans ces conditions le déroulement est censé être toujours régulier, mais il présente une région de forces dans laquelle on a deux vitesses de déroulement possible, les transitions se réalisant par des sauts de vitesses accompagnés par un phénomène d'hystérésis.

2) Déroulement sous l'action d'une vitesse de traction constante : réalisé avec l'aide d'un moteur qui rembobine le ruban sur un autre cylindre. En fonction d'un paramètre de contrôle (la vitesse de traction) la dynamique de propagation est stable dans une première branche de la courbe caractéristique (force-vitesse), instable dans une deuxième branche avec propagation saccadée (stick-slip), et enfin à nouveau stable, mais très rapide, dans une troisième branche. Dans le domaine de stick-slip, la dynamique devient de plus en plus irrégulière avec l'augmentation du paramètre de contrôle, avec des transitions entre des régimes périodiques, apériodiques et désordonnés.

Dans le cadre de ma 'Tesi di Laurea' (1996, titre : « Etude d'un modèle de la dynamique de la ligne de fissure dans un ruban adhésif ») j'ai développé des techniques de mesure des intervalles temporels de stick-slip basées sur l'analyse des émissions acoustiques et lumineuses associées aux événements de slip. J'ai mis en évidence une nouvelle instabilité de stick-slip dans le déroulement sous l'action d'un poids constant, avec la propriété de maintenir la vitesse de chute constante pour des valeurs très différentes de la masse accrochée (Barquins and Ciccotti, 1997). J'ai ensuite analysé et développé des modèles dynamiques pour expliquer la dynamique complexe observée (Ciccotti *et al.*, 1998).

En parallèle à ma thèse de doctorat et à mon postdoc à Bologne, j'ai développé des nouvelles techniques pour mesurer les variables dynamiques dans le régime de stick-slip à vitesse de traction imposée pour les comparer avec des simulations numériques (Ciccotti et Giorgini, 2006). Une nouvelle méthode d'analyse automatisée des émissions acoustiques m'a permis de mettre en évidence l'émergence de structures hiérarchiques sur plusieurs échelles temporelles dans une région spécifique du régime de stick-slip. Les différents modèles dynamiques que l'on peut proposer permettent difficilement de rendre compte de ces observations (Ciccotti, Giorgini *et al.*, 2004).

L'ensemble de ces études est résumé dans un chapitre que j'ai écrit pour un ouvrage édité par Luciano Boi avec le titre : « Symétries, brisures de symétries et complexité » (Peter Lang, Bern, 2006) que je reporte intégralement ici.

# THE EMERGENCE OF COMPLEXITY IN A COMMON SCOTCH ROLLER

M. Ciccotti and B. Giorgini
Physics Department and INFN, Bologna, Italy
April 2002

## Abstract

The fracture is a very complicated phenomenon and its dynamics is not well described, until today, by a consistent physical and/or mathematical model. In this paper we synthetically present the main experimental and theoretical results for the peeling of an adhesive tape, i.e. a viscoelastic dissipative system, viewed as a two dimensional fracture propagation. Varying the control parameter the crack dynamics appears stable in a first branch of the state curve, unstable in a second branch with stick-slip propagation, and finally again stable, but very rapid, in a third region. The unstable stick-slip dynamics becomes more and more irregular increasing the control parameter and exhibits different behaviors with transitions between periodic, aperiodic and disordered regimes. In an experiment recently performed at ESPCI-PMMH (Paris, France), the emergence of hierarchical structures in a broad range of time scales was observed in a definite region of the stick-slip regime, and this is one the indicators commonly used speaking of complex systems. At last, we underline that we do not still have a complete mathematical description of empirical data and that we lack a physical model able to explain the observed complex dynamics.

## Introduction

Our physical world is no longer symbolized only by the stable and periodic orbits, with the harmonic oscillator and modes paradigm, that are at the heart of classical Newtonian mechanics. A new world of instabilities and fluctuations, which are ultimately responsible for the amazing variety and richness of the forms and structures that we see in nature, is included in the horizon of natural philosophy from about thirty years (Gallagher and Appenzeller, 1999). Surely, if we want to understand for example the nature of earthquakes, the weather variations, the growing of threes, the origin and the evolution of life, the reductionist paradigm, i.e. the explanation in terms of elementary components, is powerless. In a first qualitative sense, we can call this world "complex" and define "science of complexity" the set of experiments, models, theories, paradigms that contribute to study these phenomena. More precisely, three disciplines have modified our outlook on the physical world: statistical mechanics (in particular the non-equilibrium physics with phase transitions), the modern theory of dynamical systems, and the information theory, along with an exponential growth of the computer performance (Parisi, 1992; Livi et al., 1986). One of the more significant properties that characterize the complex physics is nonlinearity. Essentially, nonlinearity means that some effect (reaction) is not proportional to its cause (action) and therefore we cannot apply the superposition principle. This implies that the behavior of a considered system cannot be described in terms of elementary components, i.e. it cannot be studied as a "simple" system. Moreover, nonlinearity generally implies a great difficulty in solving the equations that represent the system. Even if we think that it would be possible to exactly know the initial conditions (and this is not the case, because the position for example is a real number, described by an infinite numeral succession, that means either an infinite time or an infinite quantity of information), usually nonlinear equations don't have analytic solutions. Furthermore, the initial condition sensitivity which is proper to many systems, even with few degrees of freedom, produces very quickly a completely unpredictable time evolution of the system, despite its deterministic nature, and the orbits become chaotic. On the other hand, we have systems with a very large number of components that can be understood in a simple manner (for example a perfect gas) if we choose the right level of description (statistical and/or thermodynamical for the gas). Nonlinear processes are ubiquitous in nature and most phenomena can be studied in this "complex" optics, not only in

physics, but also in chemistry, biology, neuroscience and in fields outside natural science such as economy, sociology, psychology, and cognitive science (Nicolis and Prigogine, 1989). But what does it mean, in natural philosophy, complexity? In the literature one can find many different definitions, qualitative, philosophical, quantitative (for example the Kolmogorov algorithmic complexity), but, as befits its name, the science of complexity lacks a simple and univocal definition. In a generic sense, you can refer to systems that operate at the edge of chaos and/or that are in an intermediate state between perfect order and complete disorder (Livi et al, 1988). Notwithstanding these difficulties over formal definition, we have some properties and characteristics generally assumed as indicators of complexity: power laws, degree of mixing, entropy, thermodynamic functions, cellular automaton representations, etc (Peliti and Vulpiani, 1987). But one of the most meaningful signatures of complexity is the presence of a hierarchical organization, i.e. the emergence of hierarchical structures over a range of scales. Furthermore, we will speak of self-organization (Yates, 1987) whenever the iteration of few basic rules produce the emergence of structures having features not shared by the rules themselves. It should be clear at this point that until today a "theory of complexity" does not exists. We do not have general principles or laws or equations underlying the whole complex world from which we can derive the behavior of the single specific complex system. Each complex system must be investigated in its proper way even if some features, equations and models as for example the strange attractors with fractal geometry, the logistic map with bifurcations, the cellular automata, the neural networks, can be applied to study different phenomena, physical, but also biological or human. At this step of our scientific understanding of the complex world, we could consider the "theory of complexity" a sort of theory of modeling, so defining heuristically a complex system as a system which is intrinsically hard to model, no matter which is its nature, physical or biological or another one, and no matter which mathematical or experimental tools are used (Badii and Politi, 1997). We underline that this heuristic approach does not give an answer to the fundamental question: why, if the basic physical laws are relatively simple, the world is full of so complicated phenomena? For example the fracture process, which is the object of our investigation in this work, is one of the most complicated phenomena of the physical world (Sethna et al., 2001). Fracture results of the interplay between the creation of new interfaces and the elastic deformation of the bulk material. While the creation of new interfaces is dominated by the properties of elasticity of the surrounding medium and the amount of accumulated strain energy, the constitutive properties of the medium are strongly affected by the fracture propagation. In the full three dimensional fracture of a brittle material (which is commonly referred to as "rupture"), the medium generally undergoes a progressive process of diffused damaging which then spontaneously concentrates into some region that is gradually crushed into fragments that slide and roll on each other, involving a great deal of different physical phenomena such as friction, adhesion, and plastic deformation (Atkinson, 1987; Scholz 1990). Modeling such a complicated mixture of phenomena is almost hopeless even with the spreading power of modern computers (Main, 1996). Some simpler context must be chosen where a smaller number of phenomena are considered along with a simplified geometry. The peeling of an adhesive tape provides an excellent example since the phenomenon is reduced to the propagation of a single coherent fracture front along a predetermined bidimensional interface (Aubrey and Sheriff, 1980). Moreover, the dissipative nature of the viscoelastic systems has the significant effect of stabilizing the fracture dynamics. Even with these simplifications, the phenomenon remains highly nonlinear and the dynamics shows a variety of instabilities and structures that suggest a possible underlying complexity. Furthermore, the peeling of an adhesive tape can be easily set up in experiments that provide very long data series from which it is possible to extract useful information on the nonlinear features of the system. A last remark is that the physics of complex systems is very young and some research programs that today seem fruitful might eventually in the future prove to be cul-de-sacs.

## 1) The fracture dynamics and the peeling of an adhesive tape

Many phenomena like materials failure, granular dynamics, earthquakes, convection in granular flow induced by vibrations, fracture dynamics and the peeling of an adhesive tape have generic nonlinear features. In particular, one of the essential characteristics common to all these

systems is that they require a threshold to initiate the dynamical process and this introduces a very strong nonlinearity. In this section we will focus on the crack propagation in elastic solids and viscoelastic systems, giving some general concepts and formulae to study the fracture dynamics, the peeling and the stick-slip regime (Barquins, 1994).

The crack propagation in elastic solids is dissipative, usually irregular and accompanied by the emission of energy with characteristic noise (Maugis and Barquins, 1978). If we have two solids in contact and we want to describe the adhesion or separation between them (Figure 1), we can use the equation

$$w = \gamma_1 + \gamma_2 - \gamma_{12} \tag{1}$$

where $\gamma_1$ and $\gamma_2$ represents the free surface energies, $\gamma_{12}$ the bound surface energy, and $w$ is the Dupré adhesion energy; obviously if $w > 0$ we have adhesion, i.e. some energy is needed for creating a free surface. The second relevant observable is the released energy; more precisely, the strain energy release rate $G = \frac{\partial U_M}{\partial A}$, i.e. the amount of mechanical energy $\Delta U_M$ released by the system when the fracture surface advances of $\Delta A$, for $\Delta A \to 0$ (we observe here that we have reduced the fracture problem to a bidimensional one).

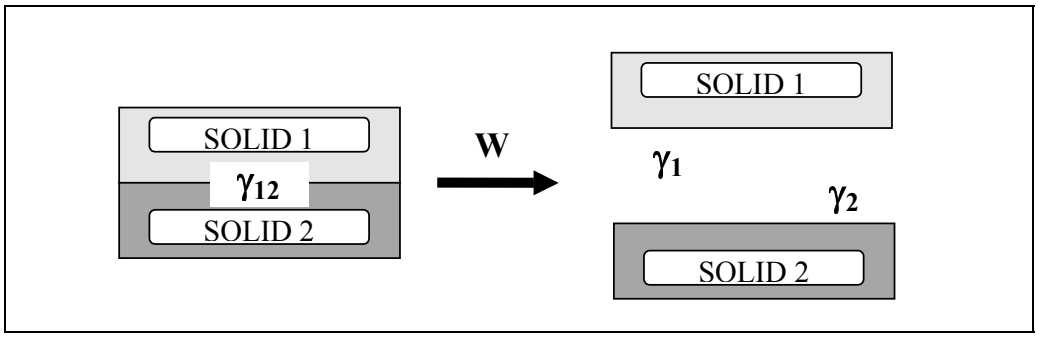


Figure 1 – Energy balance for the adhesion of two solids

For

$$G = w \tag{2}$$

the crack is in an equilibrium state that can be stable or unstable if $G$ rises or drops following an hypothetical advancement of the fracture. When $G > w$ the crack propagates spontaneously giving rise to highly dissipative phenomena due to the elevated stress near the crack tip. As a result, a constant crack velocity is attained which is a function of the difference between $G$ and $w$. Equation (2) can thus be extended to the dynamic case by adding a dissipative term such as

$$G = w + w\varphi(a_T \mathrm{v}) = \Phi(\mathrm{v}) \tag{3}$$

where $\mathrm{v}$ is the crack velocity, $\varphi$ is a phenomenological relation that depends on the scaled velocity $a_T \mathrm{v}$, with $a_T$ depending from temperature (following the WLF equation for viscoelasticity (Ferry, 1980)). We underline that the dissipative term is proportional to the adhesion energy and that $\varphi$ depends only on the temperature T and the crack velocity $\mathrm{v}$. In this context we can trace a curve $G = \Phi(\mathrm{v})$, that is represented in logarithmic scale in Figure 2.

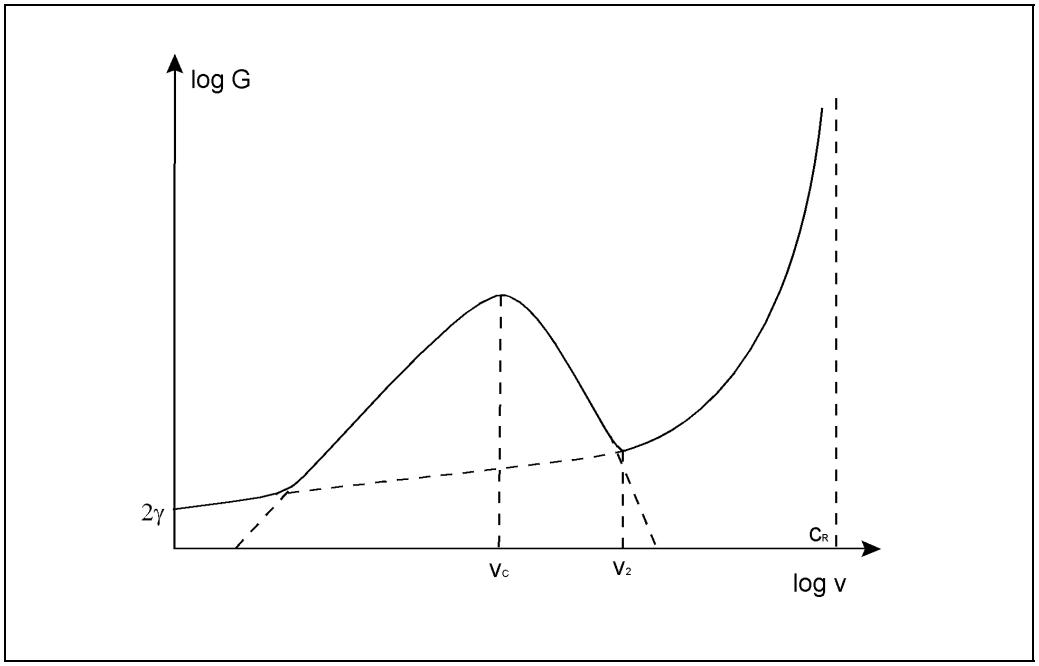


Figure 2 – Characteristic curve $G = \Phi(\mathrm{v})$

This curve can be viewed as the superposition of a term representing surface and kinetic energy with $G$ monotonically increasing with v and diverging at the limit Rayleigh wave velocity, and a broad peak due to viscoelastic losses.

We refer to peeling when a thin adhesive film is separated from a rigid substrate. Peeling exhibits a rich and interesting dynamics with stable or unstable regimes, depending on the value of the control parameters. Two different types of peel tests are generally used to investigate the dynamics:

a) the film is peeled apart from flat rigid substrate (Figure 3);
b) the film is wound to a reel and the peeling is accompanied by rotation of the reel (Figure 4);

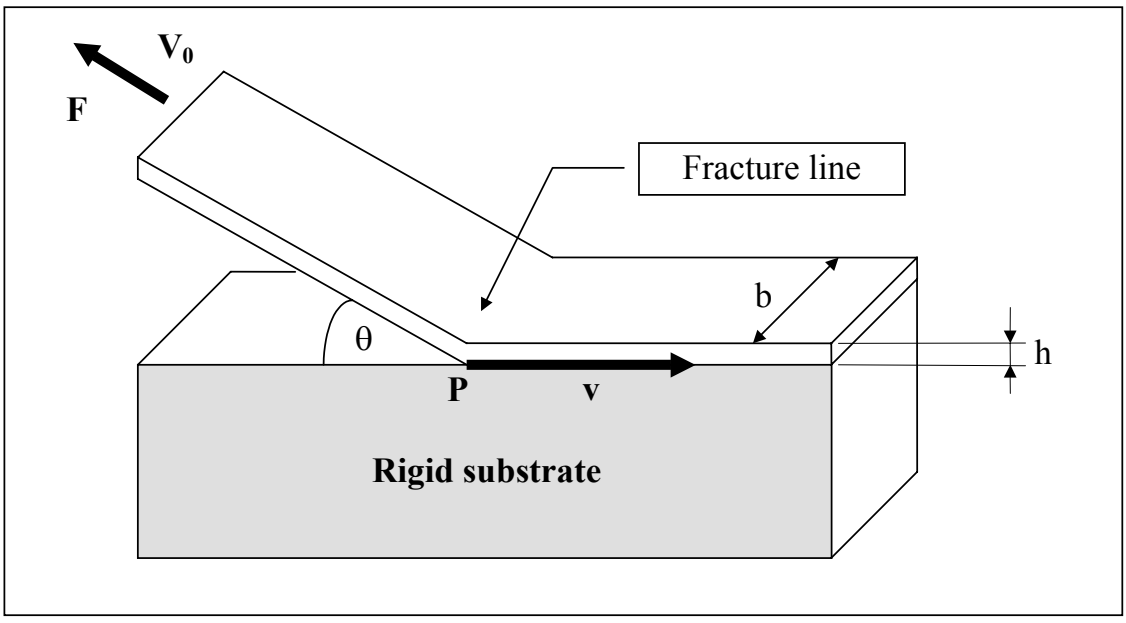


Figure 3 – A film of width b and thickness h is peeled apart from a flat rigid substrate. The force F makes an angle θ (peeling angle) with the rigid substrate.

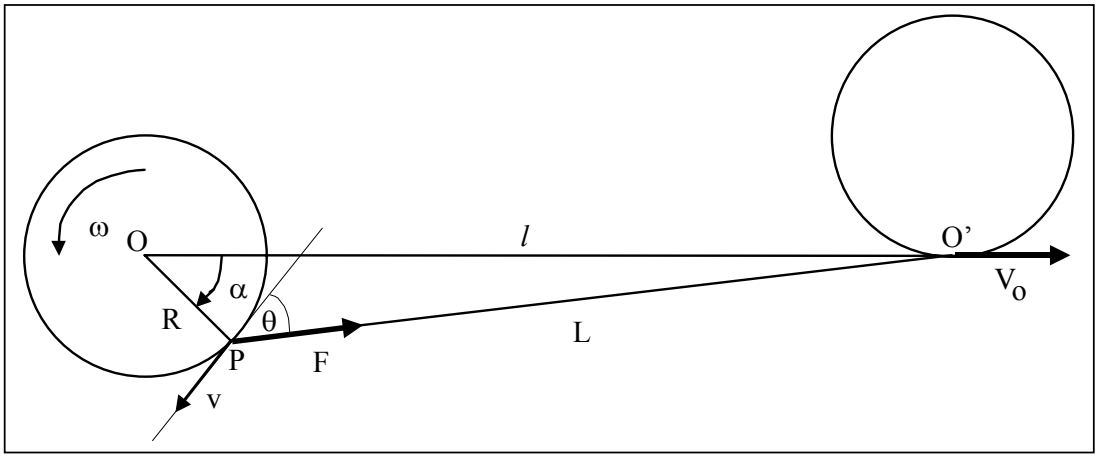


Figure 4 - The film is wound to a reel of radius R rotating with an angular velocity ω . The apparent position of the fracture is indicated by the angle α. $V_0$ is the traction velocity at point O' at a distance L from the fracture front. θ is the peel angle.

In this paper we will discuss above all the second experimental fracture model.

The relation between the fracture dynamics and peeling was established by Kendall (1975), which linked the pull force $F$ applied to the free end of the film to the strain energy release rate $G$ obtaining the equation:

$$G = \frac{F}{b}\left(1-\cos\vartheta\right)+\left(\frac{F}{b}\right)^2\frac{1}{2Eh} \tag{4}$$

(for the meaning of symbols see Figures 3 and 4, $E$ being the Young modulus). The first linear term is related to the geometric configuration, and the quadratic one derives from the strain energy of the new peeled film. The Kendall equation is well established since it derives from the conservation of energy and is furthermore confirmed by experiments.

If we define $F_0(\mathrm{v}) = \frac{\partial U_M}{\partial x}$ as the adherence force, we can write

$$G = \Phi(\mathrm{v}) = \frac{\partial U_M}{\partial A} = \frac{1}{b}\frac{\partial U_M}{\partial x} = \frac{F_0(\mathrm{v})}{b} \quad \Rightarrow \quad F_0(\mathrm{v}) = b\Phi(\mathrm{v}) \tag{5}$$

For the peeling angle $\theta > 30^\circ$ (which is common in stick-slip dynamics) the equation (5) reduces to

$$G = \frac{F}{b}\left(1-\cos\vartheta\right) \quad \text{or} \quad F_0(\mathrm{v}) = F\left(1-\cos\vartheta\right) \tag{6}$$

that relates univocally the adhesion force $F_0(\mathrm{v})$ to the pull force $F$ . This is very important because we lack a direct knowledge of $F_0(\mathrm{v})$ and moreover we don't have a microscopical model for it. The equation (6) is a sort of state equation, i.e. it was derived in equilibrium conditions. However, it is expected to work also if the evolution of the variables is not too rapid in relation to some characteristic time which is still not estimated. So its applications in highly dynamical conditions and in presence of strong nonlinearity is very delicate and probably not completely correct in order to describe the instability propagation.

At last, the stick-slip (or run-arrest). We show a simple stick-slip model in Figure 5. The spring extremity A is pulled with constant velocity $V$ with $\mu_d$ and $\mu_s$ being respectively the dynamical and static friction coefficients. At t = 0, the mass $m$ is at rest (stick-state) and the spring is extended

proportionally with $V$. The static force is equal to $kx$ ($k$ is the elastic constant, $x$ the elongation of the spring) and increases with $x$ up to $mg\mu_s$. At this point the slip begins obeying to the following equation:

$$m\ddot{x} + kx = mg\mu_d, \quad \text{with} \quad x(0) = mg\mu_s / k \ , \quad \dot{x}(0) = V \tag{7}$$

the solution of which is

$$x(t) = \frac{mg}{k}\left[(\mu_s - \mu_d)\cos\omega t\right] + \frac{V}{\omega}\operatorname{sen}\omega t + \frac{mg\mu_d}{k}, \quad \text{with} \quad \omega^2 = \frac{k}{m}$$

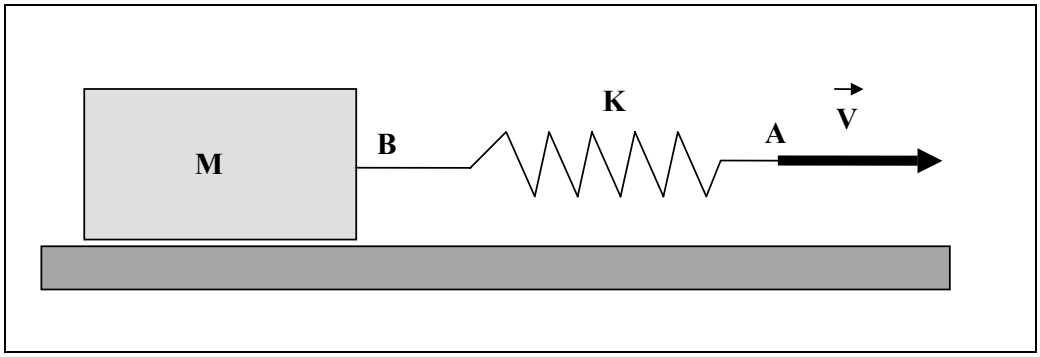


Figure 5 – Spring block slider on a flat surface

The mass arrests again for $\omega t = \pi$ (considering $V$ very small with respect to the slip speed) with $x = mg(2\mu_d - \mu_s)/k$ and we have a new stick phase. We can also calculate the characteristic times of slip $T_{SLIP}$ and of stick $T_{STICK}$:

$$T_{SLIP} = \pi\sqrt{\frac{m}{k}} \ , \quad T_{STICK} = 2mg(\mu_s - \mu_d)/kV, \quad \text{where } T_{STICK} >> T_{SLIP} \tag{8}$$

The stick-slip is observed in a variety of phenomena like rock friction and earthquakes, or tearing of rubber and crack propagation in epoxy resins, etc. And also in the peeling of an adhesive tape. This intermittent motion (or self-sustained oscillations) is created by a mechanism that generates cycles of crack growth (or sliding) instability followed by subsequent arrest. The stability and instability alternation in peeling is produced by the competition between the change in the driving force (or energy release rate) and the change in the crack-growth resistance. In the next section we will describe some experiments performed in order to understand the peeling dynamics and we will give the main obtained results.

## 2) The previous main experiments and the empirical results

In general, the experiments on the peeling of an adhesive tape were performed utilizing two possible different set-ups. In the first the peeling was studied when a constant traction velocity $V_0$ is imposed onto the free end by the action of an electric motor (Figure 4). In this case, with a fixed geometry, $V_0$ is the only dynamical control parameter, and the limit between the adhesive tape ribbon and the free tape may be seen as a crack tip propagating with speed v. In a second type of experiment the peeling is studied when a constant applied load is clamped to its extremity (Figure 7) and the control parameter is the imposed force.

Barquins et al. (1986), Maugis and Barquins (1988), performed a series of experiments in the first above described setup. In these experiments an adhesive roller tape of radius $R$ was unwound

at a given linear velocity $V_0$ (up to 20 m/s) by a couplemeter motor allowing the peel force to be measured. In a modified version the winding roller was mounted on an elastic plate, the deflection of which was used to measure the peel force. The observed peeling dynamics exhibits the following behavior: at slow traction velocity the tape is peeled regularly and the dynamics is stationary; at high velocity the dynamics is also regular, but very rapid; in the intermediate range of $V_0$ a stick-slip phenomenon appears, the peeling of the tape being jerky with emission of a characteristic noise. Moreover, an empirical $G(\mathrm{v})$ curve was traced (Figure 6) showing that the strain-energy release rate varied as a power law of the crack velocity v:

$$\Phi(\mathrm{v}) = w + wa(T)\mathrm{v}^{n_1} \qquad n_1 = 0.35 \qquad \text{for the first stable branch}$$

$$\Phi(\mathrm{v}) = G_C\left(\frac{\mathrm{v}}{\mathrm{v}_1}\right)^{n_2} \qquad n_2 = 5.5 \qquad \text{for the second (rapid) stable branch.}$$

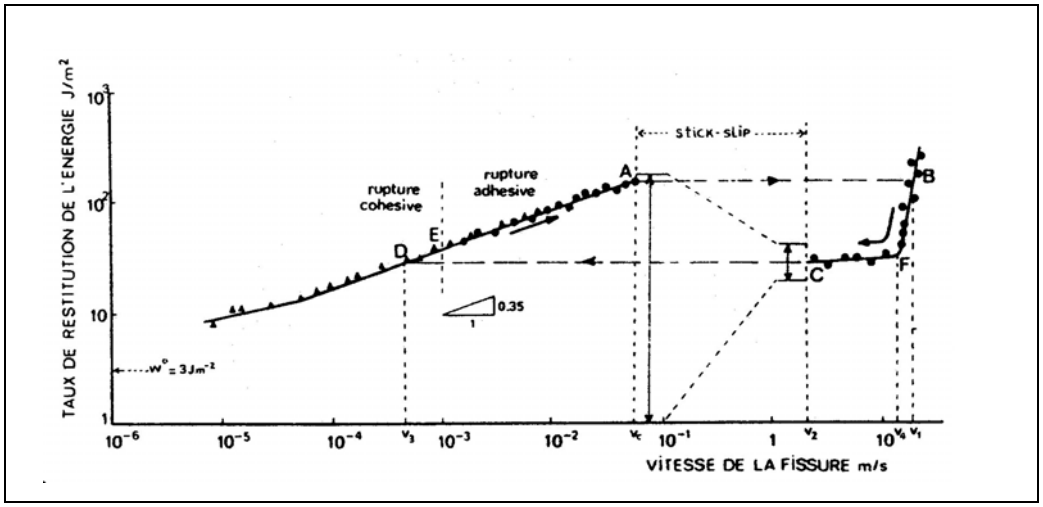


Figure 6 – Empirical $G(\mathrm{v})$ curve from Barquins et al. 1986.

In an experiment where the peeling was produced by a constant applied load (Barquins et al., 1995 and figure 7) the first stable region was found to be actually metastable, an unexpected stick-slip regime appears which was related to the inertia of the falling load, and the rapid stable branch was confirmed. The most relevant result was that the average value $\langle V \rangle$ of the measured peeling velocity remains approximately constant increasing the value of the load of one order of magnitude (Figure 8).

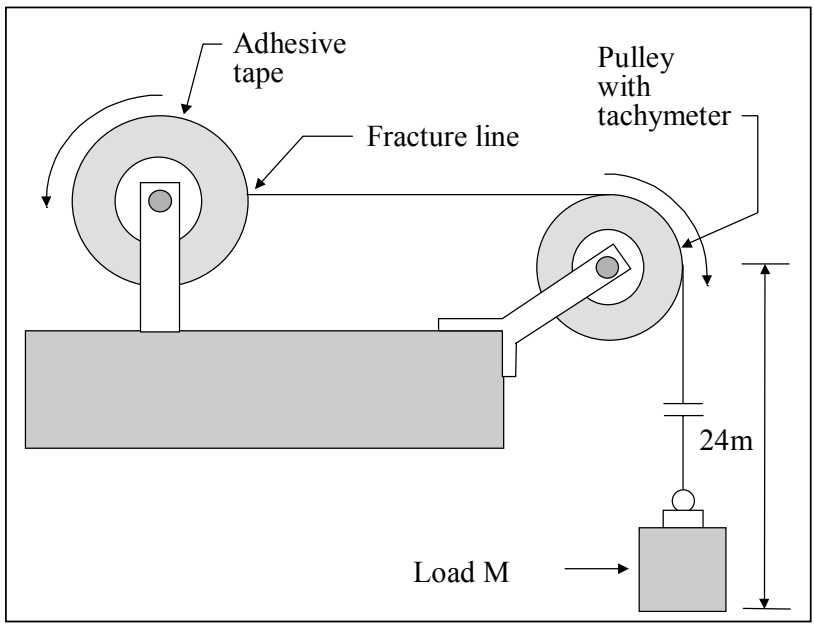


Figure 7 – Experimental set up for the peeling at constant load.

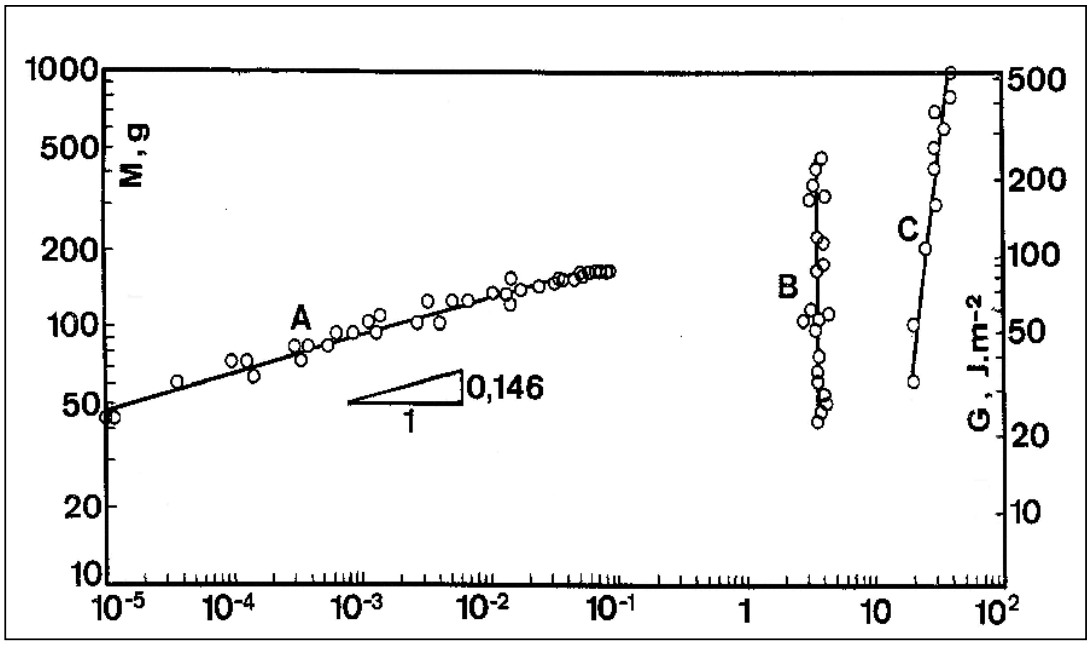


Figure 8 - Empirical $G(\mathrm{v})$ curve from Barquins et al., 1995 with vertical stick-slip branch at constant average velocity.

Obviously, in all these experiments, we must consider some influences due to temperature and humidity. Our adhesive tape is substantially composed by polymer melts, made of long flexible molecules that naturally provide the properties of sticky materials: under stress, at long time scales, they have the properties of viscous liquids, and at short time scales they deform as elastic solids. As it is well known, they depend strongly on temperature, especially near the glass transition temperature (Ferry, 1980) when the polymer transforms progressively from a viscous material to a solid. But we want to study the fracture propagation and not the phase transition of the system; if

temperature and humidity don't change too drastically, they don't affect the dynamics in a significant way. More precisely, since the stick-slip dynamics is very fast (the slowest cycles have a period of 1 s), it is not affected by long term environment variations, and even the long series of events are taken in substantially unchanged conditions. However, an effort must be spent in order to provide similar conditions between different series of experiments.

## 3) The modelling

As a matter of fact, if one observes finely the macroscopic fracture line, he discovers that it is composed by a huge number of microfractures and microfilaments, but at present a microscopic model for the adhesion force and the crack in a viscoelastic system does not exist. This is the main difficulty in order to give a deep physical interpretation of the investigated phenomenon, i.e. to understand, describe and explain the fracture evolution. So we are constrained at the macroscopic level and generally the authors model the system by means of dynamical equations.

The first model (Barquins et al, 1986) only takes into account the elastic degree of freedom, writing the equation:

$$\dot{G} = -\frac{k}{b}\left(\mathrm{v} - \mathrm{V}_0\right) \qquad \text{with } \theta = \frac{\pi}{2}\ , \quad G = \Phi(\mathrm{v}) = \frac{F}{b} = \frac{Eh\delta}{L} = k\frac{\delta}{b} \tag{9}$$

where δ is the elongation of the free portion of the adhesive tape. The equation (9) explains the stable branches of the curve G(v), where the fixed points are $\mathrm{v} = V_0$ , $G = \Phi(V_0)$, but it is not able to describe the stick-slip domain, unless speed jumps are artificially introduced. A common method to model the dynamical systems which have an unstable and/or irregular behavior is increasing the number of degrees of freedom. Following this, a second step was to add the roller inertia (Maugis, 1987; Maugis and Barquins, 1988). If we assume $G = \Phi(\mathrm{v}) - \frac{\partial U_k}{\partial A}$, $U_k = \frac{1}{2} I\omega^2$ , with I momentum of inertia, we can write the equations:

$$\begin{cases} \dot{G} = -\dfrac{k}{b}\left(\mathrm{v} - \mathrm{V}_0\right) \\ \dot{\mathrm{v}} = \dfrac{\mathrm{b}}{\mathrm{m}}\left[G - \Phi(\mathrm{v})\right] \end{cases} \qquad \text{with } \theta = \frac{\pi}{2} \text{ and } m = \frac{I}{R^2} \tag{10}$$

which represents a two variable model. Choosing $\left[V_0, \Phi(V_0)\right]$ as the origin and letting $x = \mathrm{v} - \mathrm{V}_0$ we can write $F(x) = \Phi(\mathrm{v}) - \Phi(V_0)$ , $f(x) = \frac{\partial F}{\partial x}$ and so the equation (10) becomes the well known Lienard equation:

$$\ddot{x} + \mu\omega f(x)\dot{x} + \omega^2 x = 0 \tag{11}$$

which typically has limit cycles in the branch with negative slope. By linearization one obtains Hopf bifurcation at points A and C (see fig 9(a)) where stable stationary equilibrium gives way to limit cycles (see Figure 9(b)). In figure 10 we can see that increasing the value of the control parameter $V_0$ the orbits go out of the quadrant, i.e. the solutions are not physical (Lunedei, 2001). More precisely, the two variable model produces results fitting the experimental data only when applied to the initial part of the stick-slip region where the phenomenon is periodic. But when increasing the traction velocity the self-sustained oscillations become more and more irregular, our equations (10,11) are unable to describe and to predict the observed behavior.

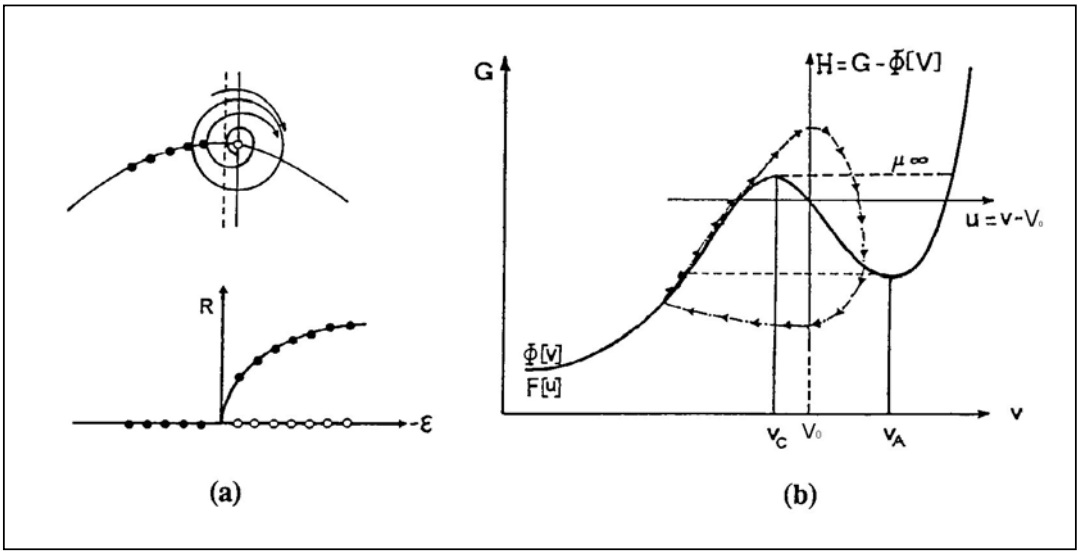


Figure 9 (a) – supercritical Hopf bifurcation (b) limit cycle over the G(v) curve.

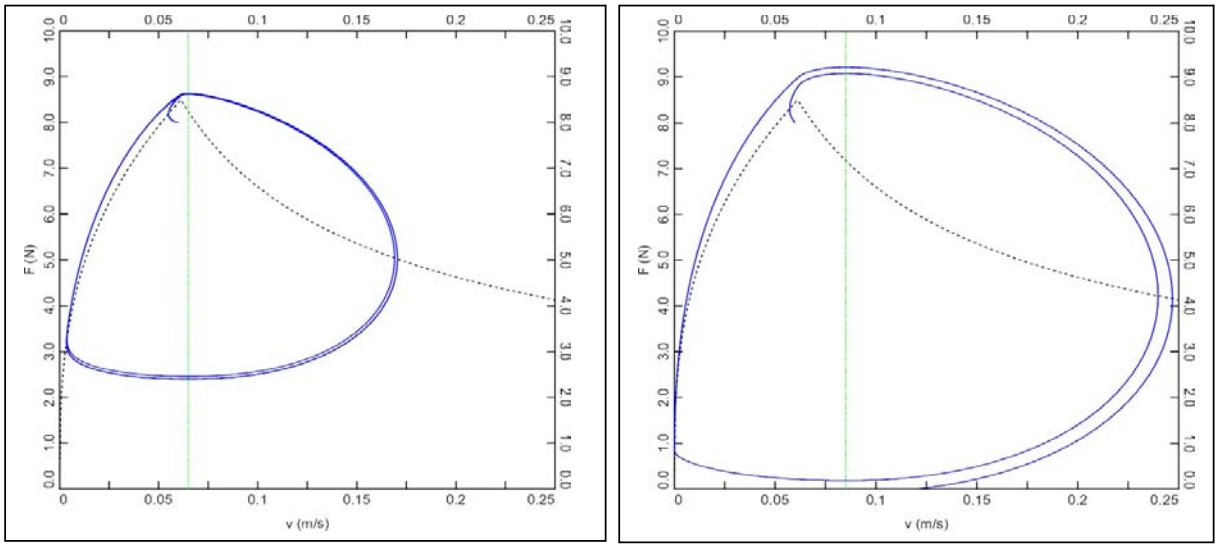


Figure 10 – Simulation of the limit cycles on the empirical G(v) curve. For incresing $V_0$ the cycle becomes larger and eventually it reaches the border of the positive quadrant (Lunedei, 2001).

Maugis and Barquins are quite conscious of this: "the model is more complicated when the variation of the peel angle is taken into account, which gives a third degree of freedom (…) allowing a road to chaos when limit cycles are changed into strange attractors". Following this suggestion Hong and Yue (1995) add a third variable (the peeling angle θ or the position α of the crack tip) obtaining the system:

$$\begin{cases} R\cdot\dot{\alpha}=\omega\cdot R-\mathrm{v} \\ \dot{F}=-k\cdot\left[\left(\mathrm{v}-V_0\right)+\left(\omega R-\mathrm{v}\right)\cos\theta\right] \\ I\cdot\dot{\omega}=F\left(\mathrm{v}\right)R\cos\theta \\ \mathrm{F}\left(1+\alpha\right)=F_0\left(\mathrm{v}\right) \end{cases} \tag{12}$$

In our analysis we used the slightly different system (Ciccotti et al., 1998):

$$\begin{cases} F\cdot\left(1-sin\alpha\right)=F_0\left(v\right) \\ I\cdot\dot{\omega}=F\cdot R\cdot sin\alpha \\ \dot{F}=k\cdot\left[R\cdot sin\alpha\cdot\dot{\alpha}-\left(v-V_0\right)\right] \\ R\cdot\dot{\alpha}=v-\omega\cdot R \end{cases} \tag{13}$$

Namely, we used a different convention for the sign of some variable, we eliminated the variable θ and we did not approximate sinα with α.

Solving the equations numerically the authors affirm that chaotic orbits are present (they found three positive Lyapunov exponents). So the stick slip would be a deterministic chaotic phenomenon and the problem seems to be closed. But firstly a well defined route to chaos does not exist and furthermore we can notice that the equation $\mathrm{F}\left(1+\alpha\right)=F_0\left(\mathrm{v}\right)$ is a constraint derived in stationary conditions. Therefore it is not so natural and obvious to impose it in a highly dynamical regime. Moreover, if we study the equations (13) in a more fine way (Lunedei 2001) we discover that the proposed solutions were obtained imposing jumps of the crack velocity v. Using the constraint to eliminate α we can rewrite (Ciccotti et al., 1998) in terms of a set of three equations in three variables (F,v,ω):

$$\begin{cases} \dot{F}=-k\cdot\left[\dfrac{F-F_0\left(\mathrm{v}\right)}{F}\cdot\left(\mathrm{v}-\omega\cdot R\right)-\left(\mathrm{v}-V_0\right)\right] \\ \dot{\mathrm{v}}=\dfrac{1}{\dfrac{dF_0}{d\mathrm{v}}\left(\mathrm{v}\right)}\cdot\left[\dot{F}\cdot\dfrac{F_0\left(\mathrm{v}\right)}{F}-F\cdot\sqrt{1-\left(1-\dfrac{F_0\left(\mathrm{v}\right)}{F}\right)^2}\cdot\dfrac{\mathrm{v}-\omega\cdot R}{R}\right] \\ \dot{\omega}=\dfrac{R}{I}\cdot\left(F-F_0\left(\mathrm{v}\right)\right) \end{cases} \tag{14}$$

which are valid for $\dfrac{dF_0}{d\mathrm{v}}\neq 0$, $F\neq 0$ with two singular points at $\mathrm{v}=\mathrm{v_C}$ , $\mathrm{v}=\mathrm{v_A}$. The numerical solutions of (14) admit a cycle only if they are forced by hand to avoid the singularities. More precisely, the solutions must be obliged to jump from one branch to the other when the critical velocities are encountered. Without that the system has no physical solution. So we argue that the deterministic chaos in the stick-slip seems to be rather artificial and not completely proved as intrinsic to the phenomenon. At this point, we can guess that the philosophy based on increasing the dynamical variables number in order to have a model able to describe the irregular stick-slip regime, is not the more suitable one. Moreover, the phenomenon of instability propagation in a viscoelastic medium could be more complicated than a "simple" dynamical system and could have some characteristics proper to a complex system (De Gennes, 1979; Kinloch and Young, 1983). This criticism has stimulated further theoretical and experimental research. The aim was to have a more accurate knowledge of the stick-slip propagation, firstly empirical. The highly nonlinear phenomena as the fracture dynamics produce really unpredictable evolutions. In order to extract useful information on the motion from experiments, we must record sufficiently long time series,

i.e. sequences of data representing the time evolution of one or more observable. After that, we can use the statistical analysis, or the geometrical reconstruction of the attactors in a suitable phase space, or some other technique to investigate the dynamics. The general philosophy of this approach is to draw out a physical meaning from an empirical signal, bypassing the knowledge of the underlying dynamics and/or the corresponding equations (Eckmann and Ruelle, 1985; Ruelle, 1987). In this optics, we can search the significant points (bifurcations and so on) and eventually we can detect the emergence of hierarchical structures, one of the most significant complexity indicators (D'Alessandro and Politi, 1990). The problem will be to choose the good observable, i.e. the more proper observable to be measured with a sufficient precision and over a convenient long time. For this, Barquins, Ciccotti, Giorgini and Vallet have set up a new experiment and the first provisional results show a stick-slip behavior more complex than we could expect basing strictly on the theory of dynamical systems (Vallet et al., 2001).

## 4) The new experiment

The new experiment that has been set up at the PMMH – ESPCI (Paris, France) aims at a complete description of the phase space of the stick-slip dynamics and its evolution as a function of the control parameter $V_0$.

The experimental assembly is the classic one with constant traction velocity. This condition is enforced with the aid of a very stiff motor that enrolls the tape on a new ribbon (Fig. 4). Stable peeling is observed for traction velocities lower that a first critical velocity $v_C$ and larger than a second velocity $v_A$. In the intermediate range the peeling is jerky and with rising velocity the stick-slip dynamics becomes more and more complicated.

### *Measuring the phase variables*

We proceed now to a synthetic description of the techniques developed in order to measure and record the evolution of the fundamental dynamical observables of the experiment, namely the traction force, the rotation velocity of the reel, the apparent position of the fracture front on the reel (which determines the peeling angle), and the acoustic emissions. A picture of the assembly is shown in figure 11.

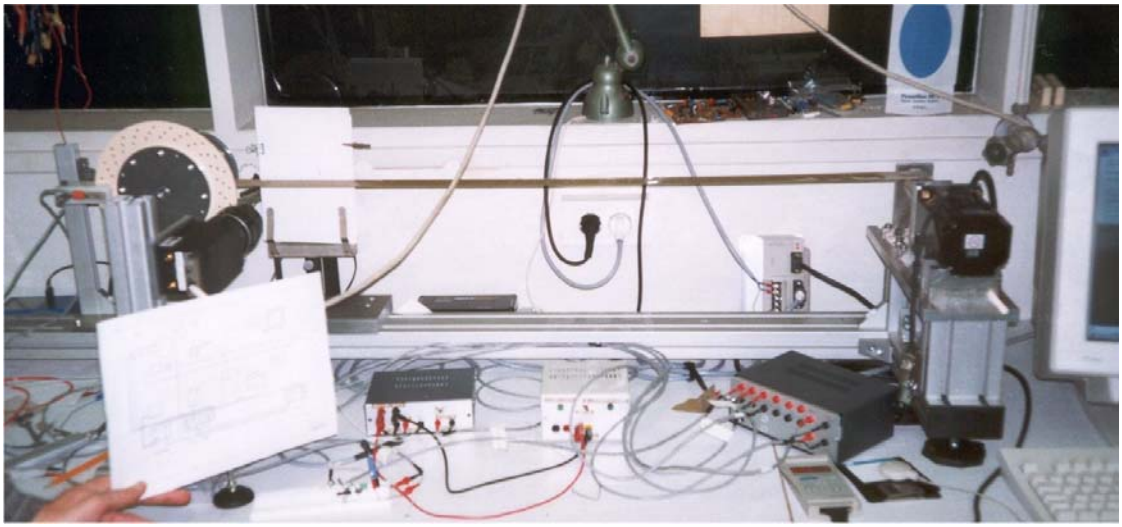

Fig 11 – General overview of the experimental set up

The rotation velocity of the reel is measured by a tachymetric wheel (Fig 12). Three shells of holes induce an ordered sequence of commutation of the three photocells. The signals are electronically combined into one three-level analogic signal that is recorded by a computer, then converted into the ordered sequence of activated photocells that allows one to calculate the rotation velocity along with its sign. Since 24 timings are available for one tour, the average velocity can be monitored with valuable resolution in time. When elevated values of the rotation velocity have to be measured, the wheel is changed with another one which has an inferior number of larger holes.

The reel of the adhesive tape is installed over a vertical steel beam that is sufficiently stiff in order not to affect the peeling dynamics, but whose small deflections in the stick-slip regime are large enough to be measured by laser ranging. The deflection is calibrated to measure the force $F$ applied to the adhesive tape.

To evaluate the apparent position of the fracture front (denoted by the angle $\alpha$), we set up a high frequency digital camera (Fig. 13) that acquires a vertical line every millisecond. The sequence is analyzed on a computer to extract the vertical position of the adhesive tape at the given cross

section. This measure is then related to the apparent position of the fracture front by simple geometric relations.

At last, a high precision microphone is placed near the position of the crack front to record the characteristic noise produced by the stick-slip dynamics. The identification of the acoustic bursts associated with the slip events are the most precise method for determining the long series of inter-event times that are the main observable of the present study. The significance of the acoustic method for the recognition of events was previously tested (Barquins et al., 1995) by a correlation with the light emissions (sparks) associated with the strong ionization produced by the rapid slip and measured by a photomultiplier.

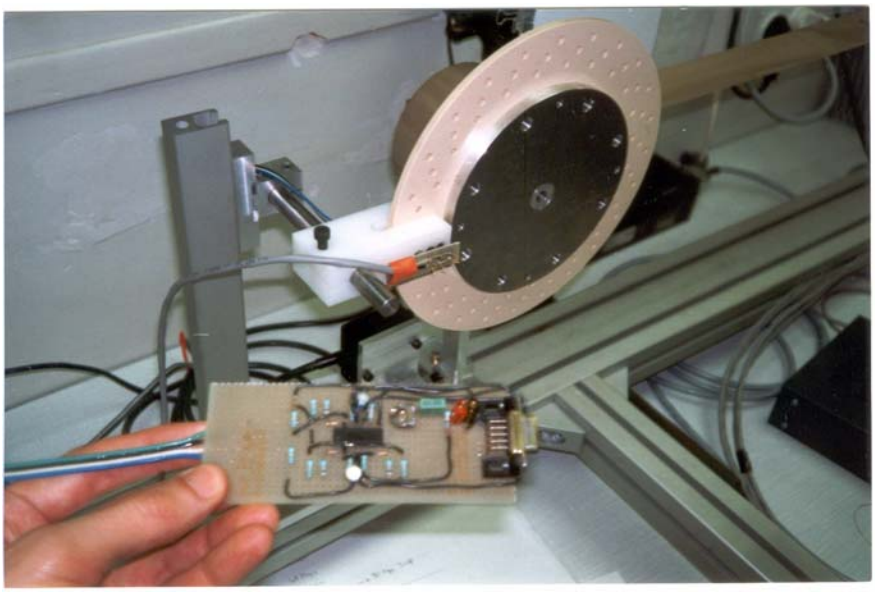

Fig 12 – A tachymetric wheel measures the evolution of the rotation velocity ω of the support. The electronic device produces a code related to the active photocells that are situated inside the white support.

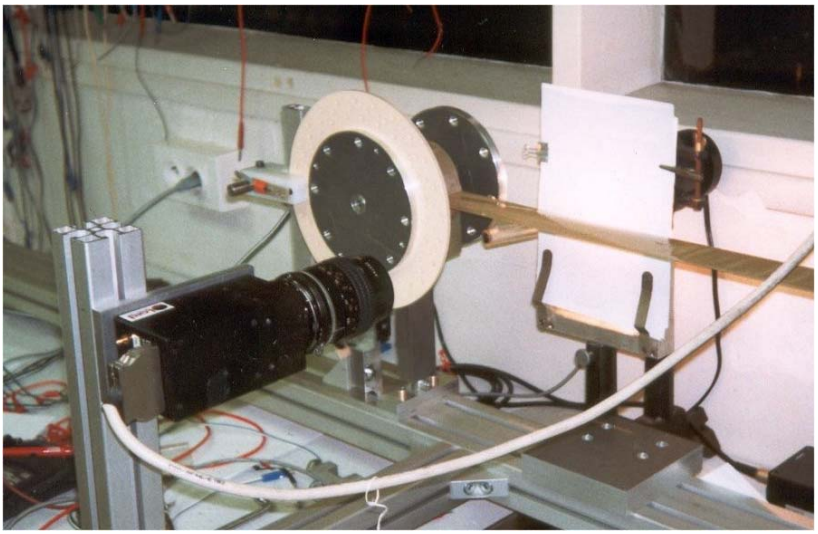

Figure 13 – The high frequency digital camera measures the vertical position of the tight tape, providing the evolution in time of the apparent position of the fracture front.

## 5) The results

As a first experimental step, we choose to measure the time interval between two subsequent events, i.e. our observable is the period $\Delta t$. Usually, in physics, and especially in dynamics, the time is not a variable, but rather a parameter. However, in our situation the dynamical equations proposed to describe and explain the stick-slip at least partially failed. The time interval $\Delta t$ is the indicator that we can measure more precisely in order to evaluate the irregularity of the dynamics. Exactly as we do studying the behavior of a pendulum, for which we can define periodic, quasi-periodic, aperiodic regimes, only measuring the periods, even if we do not know the equations governing the phenomenon. Obviously, the knowledge of the time interval series is not sufficient to model completely the dynamics. For example, we can not discover if we are in presence of space-time chaos only by numerical time series of periods, even if these series were chaotic. But at least our philosophy can put in evidence the time structures underlying the phenomenon and give a criterion to discriminate different dynamical regimes, as a function of the control parameter.

### *Analysis of data*

The acoustic emission of the adhesive tape in the stick-slip regime is recorded by a high quality microphone and digitized at the standard audio sampling frequency of 44100 Hz with a 16 bit signal that is stored in raw binary .wav files.

Long records of events have been acquired for many values of the control parameter, i.e. the traction velocity $V_0$, spanning the unstable stick-slip regime. Since the sequences may involve thousands of events, some automatic recognition process is necessary for the analysis.

For low values of the traction velocity, the stick-slip events are clearly separated and regular. They appear as abrupt acoustic bursts, followed by a gradual oscillating decay. A very simple threshold-window method is appropriate in this case: an event is detected any time the signal crosses a given threshold (evaluated as three times the root mean square of the signal), then a time window is skipped in order to let the signal decay below the threshold. Since the events are similar in intensity and well separated in time, the time window is easily chosen below the least observed interval and above the estimated decay time.

When the traction velocity grows to higher values, the events become more and more frequent and irregular both in timing and intensity, making their separation problematic. The above simple algorithm is no longer sufficient and some more elaborate criterion was developed. Since the oscillations become more persistent, the focus is shifted to the identifications of rapid changes in the signal. Due to the band filtering of the microphone, the burst is characterized by an irregular oscillation with a characteristic frequency given by the upper limit of the band (e.g. 6 kHz for the first microphone that was used). The acoustic power spectrum of the signal will be observed to rapidly fall above such a frequency. On the other hand, the abrupt initiation of the burst, is characterized by a local enhancement of the high frequency content. For that reason we performed a moving window Fast Fourier Transform on the signal and built a new index based on the integration of the high frequency acoustic power. Such an index is plotted in red in figure 14 and is evidently well correlated to the events.

A special attention has been taken in order to evaluate the misfits of the recognition method. These may be of two kinds: (1) a “missed event” results in the substitution of two proper time intervals with a false longer time interval, (2) a “false event” results in the loss of one proper time interval in favor of two false small ones. In order to ascertain that the observed structures are not due to the effects of these misfits, several set of data have been analyzed manually and presented a good agreement with the results of the above algorithm.

This method allowed us to identify the events up to a traction velocity $V_0$ = 10 cm/s with an efficiency better than 90%. After that, the oscillations in the signal appear to be almost continuous. A possible interpretation is that chaos and/or turbulence is completely installed (Becker, 2000). But at present we can not exclude that we have reached the limit of resolution of our apparatus, and that we are not able of distinguishing the events.

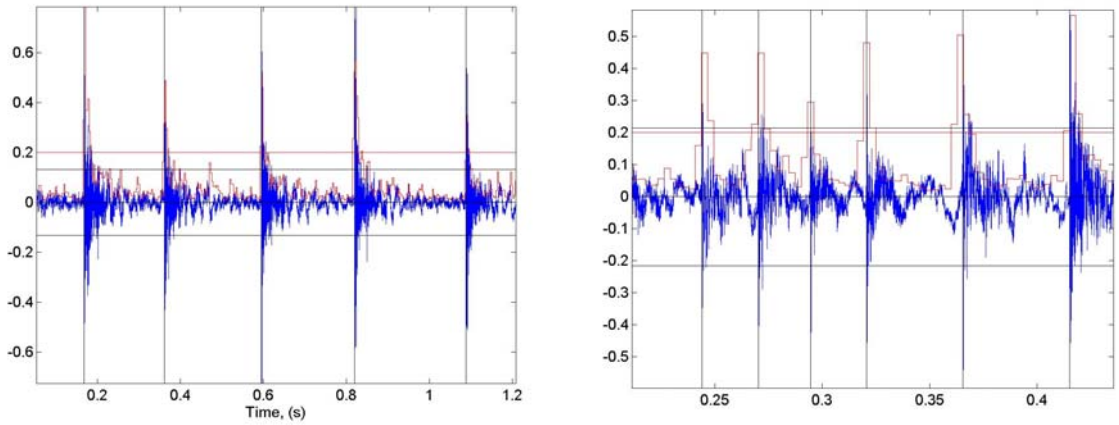


Figure 14 – Automatic recognition of the slip events in the acoustic signal. Black horizontal lines indicate standard thresholds, the red signal is the FFT based index along with its threshold.

### *The emergence of hierarchical structures*

Although the stick-slip cycles are generally not periodic, it is interesting to plot the average period as a function of the traction velocity (see Figure 15). In first approximation the average frequency is proportional to the traction velocity and a linear fit provides the relation:

$$\nu_m = \frac{1}{\langle T \rangle} = 0.53Hz\left(\frac{V_0}{2.1mm/s}\right)$$

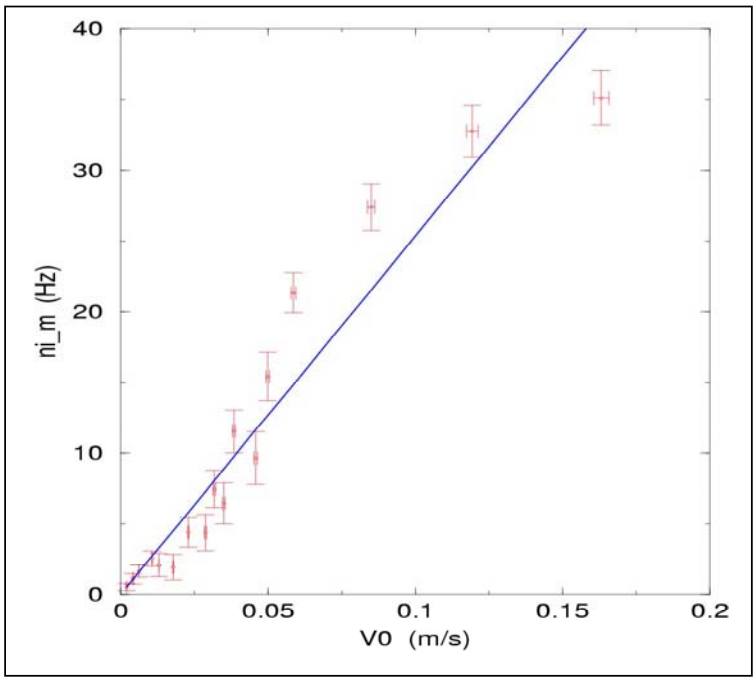


Figure 15 – Average period of stick-slip cycles as a function of the traction velocity.

Actually, the cycles are only quasi periodic for low traction velocities, while they become irregular increasing speed. The analysis of the time intervals has put into evidence that the dynamics goes through a series of progressive complications when the traction velocity $V_0$ passes some subsequent critical values. In particular, there is a first low velocity domain in which the cycles are approximately periodic and for which the period diminishes as the traction velocity is increased (Figure 16). This domain is followed by the appearance of sparse rapid events which have a period

(here simply meaning the time interval between two subsequent events) that is a multiple of the fixed time interval 0.02s (Figure 17). The events of double or triple period become progressively more frequent leading to the establishment of an ordered structure with three possible periods, then they decrease again in frequency until a new regular regime is observed with substantially periodic events at the short time interval of 0.02s. This time interval does not change with traction velocity, until at higher speed, the cycles undergo a second bifurcation with the appearance of sparse events with a duration multiple of a new shorter fixed time interval which is about ten times shorter than the previous one. These measures are still in analysis, due to the increased difficulties of separating such a frequent series, but we can anticipate that a new structure is again developed. At higher velocities the acoustic signal is mixed to such an extent that we can not distinguish any event at the present state. However, at a traction velocity of 3 m/s the peeling becomes again stable without the crackling noise and it remains stable until the reach of the limit velocity given by the Rayleigh wave velocity in the crack surface.

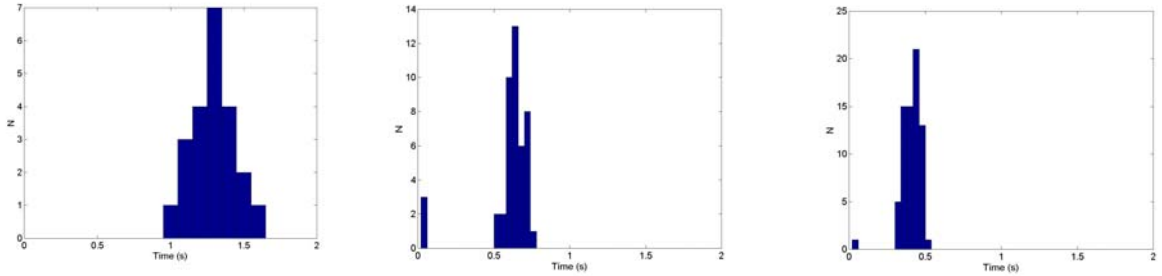


Figure 16 – Distribution of the time intervals for $V_0$ = 2, 4, 6 mm/s.

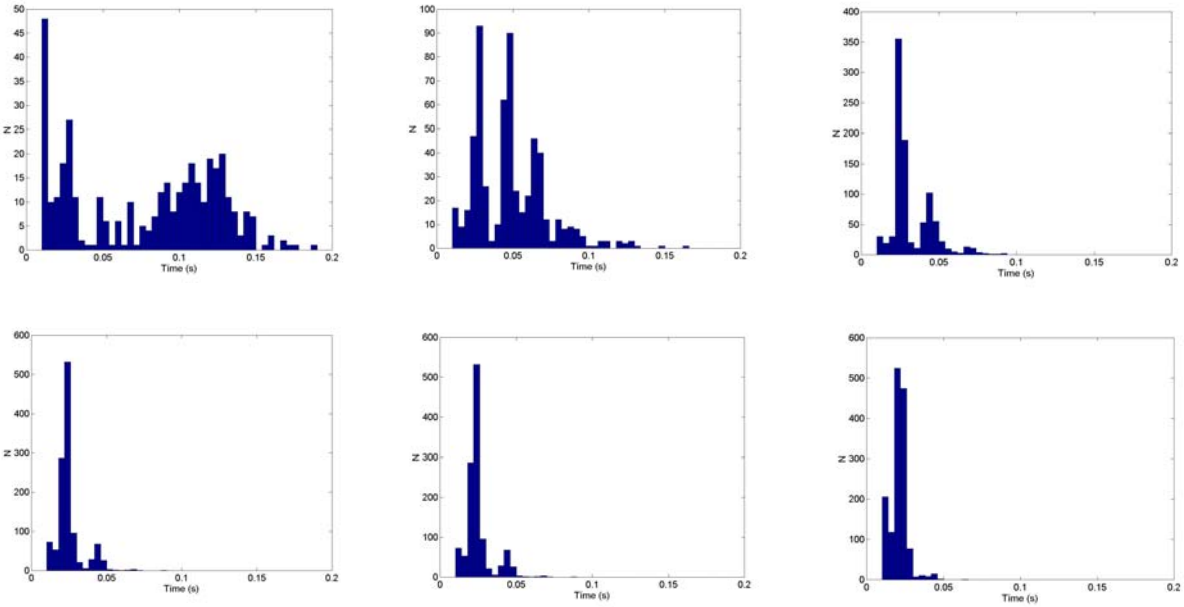


Figure 17 – Distribution of the time intervals for $V_0$ = 2, 3, 4, 5, 6, 7 cm/s.

We can resume complication cascade like follows:

- Up to 0.7 mm/s: stable peeling
- At 0.7 mm/s beginning of regular stick-slip. Time periods fall with growing traction velocity
- At 1 cm/s apparition of first multiplets with $\Delta t \approx 0.02, 0.04, 0.06$ s. The structure develops up to 3 cm/s, then it concentrates on the shortest interval
- At 6 cm/s apparition of sub-multiplets with $\Delta t \approx 0.001, 0.002, 0.003$ s. The structure develops, but the signal is lost at 10 cm/s
- At 3 m/s the peeling becomes again stable and humming up to the maximum traction velocity of the engine 6 m/s

### *Developments*

Some numerical simulations of the stick-slip dynamics have been set up taking into special care the large variations of the peeling velocity during the cycles. Preliminary tests show that the simulations can accurately describe the low velocity regime and they also predict a series of bifurcations which correspond to a progressively complicating dynamics. Although the simulated dynamics appears qualitatively different than the observed one, we are performing a new set of simulations which include the effective mechanical parameters of the experiment in order to verify if at least the location of the critical values of the bifurcations are reproduced.

The data are also being analyzed with a different approach, that is by a statistical analysis of the series of time intervals (figure 18), with the aim of investigating the correlation between subsequent cycles and extracting the predictive information hidden in the data (Packard et al., 1980).

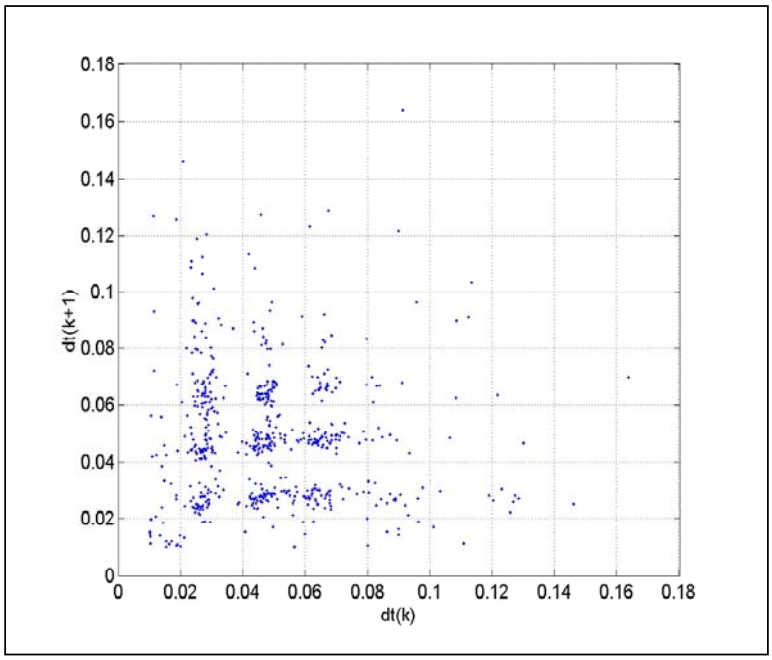


Figure 18 – Correlation between adjacent events of the three level structure ($V_0$ = 3 cm/s) in a phase space ($t_n$ , $t_{n+1}$).

In particular, we analyzed the series of time intervals of the data with $V_0$ = 3 cm/s, for which the intervals only have the three multiple lengths, denoted with letters A, B, C. A simple statistical analysis shows that the subsequent intervals are not independent, but they are neither well described by a first order Markov process. We are presently evaluating the predictive power of the series and the presence of nonlinear correlations by an evaluation of the embedding dimension.

## Conclusions

As we have seen, the main dynamical models constructed to explain the peeling evolution of an adhesive tape can predict correctly only the stationary behaviors and the approximately periodic stick-slip cycles. But when the stick-slip becomes very irregular the proposed models are insufficient also if we increase the number of degrees of freedom.

On the other hand, the results of new experiments show that the stick-slip dynamics is more rich and complicated than a simple bifurcation's route to chaos.

We observe hierarchical structures in a definite traction velocity range that can suggest the emergence of complexity, at least in qualitative sense, when a fracture is produced and evolves in a viscoelastic system.

Strong efforts are being spent in the direction of resolving the series of more rapid events associated to the higher traction velocities, to understand the complex dynamics which is progressively installing. The dynamical models predict a cascade of bifurcations leading to deterministic chaos. We do not have the classic cascade with Feigenbaum universality (Cvitanovic 1989), but it could be possible that the observed complex dynamics leads to time chaos. Another point of view could be statistical: for high traction velocities the peeling in the stick-slip regime could not any longer be described by dynamical equations, but would rather be the result of a large number of degrees of freedom cooperating to constitute a self-organized system in a critical state far from equilibrium. But, before venturing an interpretation, we must measure the other observables $F$, $\omega$ and, above all, the crack speed v. Furthermore, we must investigate the possible mathematical correlations of our time series of data. Finally, the goal would be to find a physical interpretation of the phenomenon or, more precisely, discovering the physical laws and equations that originate the observed fracture complex dynamics.

However, the peeling apparatus set up in the PMMH-ESPCI laboratory provides a good experimental model to study nonlinear phenomena in a fine way, following step by step the increasing instability and furnishing the suitable long time series of data.

At last, we want underline how a common scotch roller can be so enigmatic and full of mystery to justify the ancient saying “I know that I don't know”. Perhaps this sentence could be the deep meaning of “complexity”.

## Acknowledgements

The authors thank a lot Michel Barquins and Denis Vallet for the kind hospitality at Laboratoire de Physique et Mécanique des Milieux Hétérogènes (PMMH) at the Ecole Supérieure de Physique et Chimie Industrielle de la Ville de Paris (ESPCI), and obviously for the intensive collaboration that produced the results related in this paper. We also had many useful discussions with Giorgio Turchetti of the Physics department of Bologna, Italy. A financial contribution was furnished by INFN – theoretical group - section of Bologna.

## References


Atkinson B.K., 1987. Fracture mechanics of rock. Academic Press.

Aubrey D.W., and Sheriff M., 1980. Peel adhesion and viscoelasticity of rubber-resin blends, *J.Polymer Sci.*, **18**, p. 2597.

Badii R. and Politi A., 1997. Complexity, hierarchical structures and scaling in physics. Cambridge University Press.

Barquins M., 1994. Le collage. Une alternative "moderne" aux trois techniques classiques d'assemblage: rivetage, vissage et soudage. *Bullettin de l'Union des Physiciens*, 88 ° annèe, **762.**

Barquins M., Khandani B. and Maugis D., 1986. Propagation saccadèe de fissure dans le pelage d'un solide viscoelastique. *C.R.Acad. Sci. Paris*, **303**, p. 1517.

Barquins M., Boilot A., Ciccotti M. et Varotto A., 1995. Sur la cinetique de decollement d'un ruban adhèsif sous l'action d'un poids mort, *C. R. Acad. Sci. Paris*, **321**, p. 393.

Becker T.W., 2000. Deterministic chaos in two State-variables Friction Sliders and the Effect of Elastic Interactions. In "GeoComplexity and the Physics of Earthquakes". Geophysical Monograph 120. *Am. Geophys. Un.*

Ciccotti M., Giorgini B., Barquins M., 1998. Stick-slip in the peeling of an adhesive tape: evolution of theoretical model. *Int. J. Adhesion and Adhesives*. **18**, p. 35.

Cvitanovic P., 1989. Universality in Chaos. Adam Hilger.

D'Alessandro G. and Politi A., 1990. Hierarchical approach to complexity with applications to dynamical systems. *Phys. Rev. Lett.*, **64**, p. 1609.

De Gennes P.G., 1979. Scaling concepts in polymer physics. Cornell University Press.

Eckmann J.P. and Ruelle D., 1985. Ergodic theory of chaos and strange attractors. *Rev. Mod. Phys.,* **57**, p. 617.

Ferry J.D., 1980. Viscoelastic properties of polymers. John Wiley & Sons.

Gallagher R. and Appenzeller T., 1999. Beyond reductionism. *Science*. **284**, p. 79.

Hong D.C. and Yue S., 1995. Deterministic chaos in failure dynamics: dynamics of peeling of adhesive tape, *Physical Review Letters*, **74**, p. 254.

Kendall K., 1975. Thin film peeling, the elastic term. *J. Phys. D: Appl. Phys.*, **8,** p. 1449.

Kinloch A.J. and Young R.J., 1983. Fracture Behaviour of Polymers. Applied Science Publishers.

Livi R., Ruffo S., Ciliberto S. and Buiatti M., 1988. Chaos and complexity. World scientific.

Livi R., Parisi G., Ruffo S. and Vulpiani A., 1986. Il computer da abaco veloce a strumento concettuale in Il Ponte, luglio/ottobre.

Lunedei E., 2001. Modellizzazione ed analisi dei dati in un esperimento di dinamica delle fratture. Tesi di Laurea. Dipartimento di Fisica. Bologna, Italy.

Main I., 1996. Statistical physics, seismogenesis and seismic hazard. *Revs. of Geophys.* **34**, p. 433.

Maugis D. and Barquins M., 1978. Fracture mechanics and the adherence of viscoelastic bodies. *J. Phys. D: Appl. Phys.*, **11**, p. 1989.

Maugis D. and Barquins M., 1988. Stick-slip and peeling of adhesive tapes. In *Adhesion 12*, K.W. Allen Ed., Elsevier Applied Science, London, p. 205.

Maugis D., 1987. Propagation saccadèe de fissure en pelage, role de l'inertie*, C. R. Acad. Sci. Paris*, **304**, p. 775.

Nicolis G. and Prigogine I., 1989. Exploring complexity. W. H. Freeman and C.

Packard N.H., Crutchfield J.P., Farmer J.D. and Shaw R.S., 1980. Geometry from a time series. *Phys. Rev. Lett.*, **45**, no. 9, p. 712.

Parisi G., 1992. Order, disorder and simulations. World Scientific.

Peliti L. and Vulpiani A., 1987. Measures of complexity. Lectures Notes in Physics. Springer-Verlag.

Ruelle D., 1987. Chaotic evolution and strange attractors. Cambridge University Press.

Sethna J.P., Dahmen K.A. and Myers C.R., 2001. Crackling noise. *Nature*. **410**, no. 6825, p. 242.

Scholz C.H., 1990. The mechanics of earthquakes and faulting. Cambridge University Press.

Vallet D., Ciccotti M., Giorgini B., Barquins M., 2001. La dynamique de Stick-Slip dans le pelage d'un ruban adhesif. In Comptes rendus de la quatrième Rencontre du Non-Linéaire, Éditeurs Y. Pomeau et R. Ribotta, Non Linéaire Publications, Paris (2001) 249-254.

Yates F.E., 1987. Self-organizing systems: the emergence of order. Plenum. New York.

## 1.3 Travail en cours et perspectives

Le développement technologique de caméras rapides de plus en plus performantes permet à présent d'essayer une investigation directe et très riche des mécanismes dynamiques effectivement présents autour de la ligne de fissure. Dans le cadre d'une collaboration avec Loïc Vanel de l'ENS-Lyon et grâce au travail du thésard Pierre-Philippe Cortet nous avons réalisé un montage pour pousser à l'extrême les capacités d'une caméra rapide (Photron Ultima) sur l'étude du mouvement de stick-slip de la ligne de fissure pour un ruban entraîné par un poids mort. En combinant sagement différents compromis entre la résolution des images, la taille du champ visuel et la rapidité d'acquisition, on a pu se focaliser séparément sur les différents aspects de cette dynamique et notamment aller vérifier le bien fondé des assomptions et approximations qui séparent l'expérience de la modélisation du phénomène.

En figure 1.3.1 a) je reporte un exemple de suivi de la ligne de fissure pour un rouleau monté sur un roulement à billes accroché au plafond et déroulé à l'aide d'une masse appliquée, suffisamment lourde pour induire une dynamique de stick-slip. L'acquisition est faite à 8000 images par seconde (une image sur 10 est reportée). On peut reconnaître la silhouette noire du rouleau en haut et le ruban pelé vers le bas. Pour plus de précision un rapporteur est monté sur le rouleau. Après traitement d'image on peut calculer le mouvement du rouleau et le mouvement relatif de le ligne de fissure qui est reporté en fig. 1.3.1 b. Une première observation montre que les phases de slip (pente plus élevée) ont une durée comparable à celles de stick (pente faible), contrairement à l'assomption typique qu'elles aient une durée négligeable. Par ailleurs, en appliquant la résolution de 1/8000 s près, on constate que la vitesse de propagation montre de vrais sauts entre les phases de stick et de slip en accord avec ce que j'avais soutenu dans mes premiers articles (Ciccotti *et al.*, 1998).

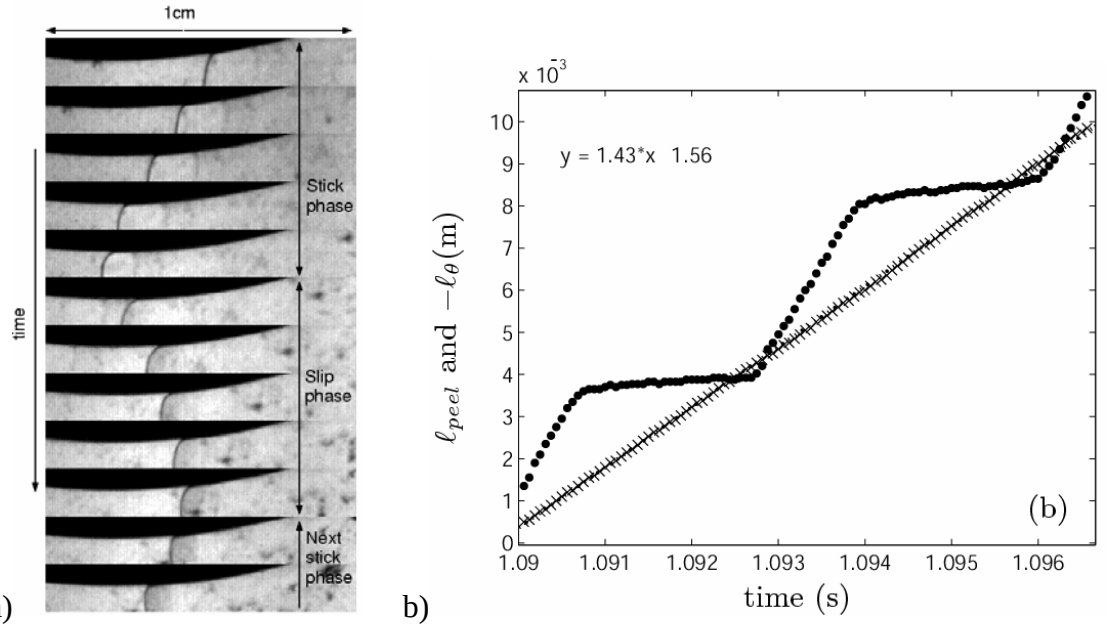


Figure 1.3.1 a) Chronographe du mouvement de la ligne de fissure en régime de stick-slip (8000 im/sec). b) Diagramme du mouvement de la ligne de fissure (cercles = longueur pelée ; croix = longueur d'arc équivalent de la rotation du support).

Ce point est très important dans la modélisation dynamique et en particulier dans les techniques de solution numériques parce qu'il peut modifier la nature chaotique des solutions. En outre il est important pour des raisons fondamentales qui regardent la nature de la transition de branches comme discuté in Ciccotti *et al.*, 1998.

En utilisant une reprise différente (voir fig. 1.3.2) on a en outre été en mesure de mettre en évidence la propagation d'ondes le long du ruban adhésif détaché. Cet aspect est très important car c'est cette portion du ruban qui transmet la force au point de pelage et ces ondes peuvent entraîner une modulation de la force qui peut interférer avec la dynamique de la ligne de fissure.

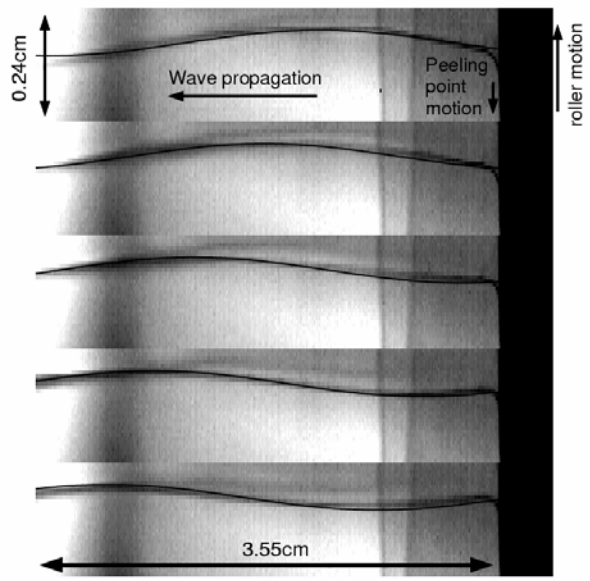


Figure 1.3.2. Chronographe de la propagation d'ondes élastiques le long du ruban (16000 im/sec). NB : Les images sont pivotées de 90° et la gamme verticale est dilatée pour la visualisation. La silhouette noire sur la droite représente toujours le rouleau débiteur.

L'analyse des caractéristiques de propagation de ces ondes nous a permis de vérifier l'hypothèse que le ruban reste tendu après les slip et que les modulations de force restent faibles vis-à-vis de la tension du ruban, mais le fait que leur fréquence est proche de celle de stick slip est problématique et renvoie à la nécessité d'une analyse plus fine de ce couplage dynamique. Ces résultats sont en cours de soumission à Int. J. Adhes. Adhes (Cortet *et al.*, 2006).

En parallèle, à travers une collaboration avec le professeur G. Ananthakrishna de l'Indian Institute of Science (Bangalore, India), nous avons récemment conduit une nouvelle analyse des émissions acoustiques émises pendant le stick-slip, qui a mis en évidence la présence de lois de puissance dans la statistique de l'énergie émise (Kumar, Ciccotti *et al.*, 2006).

# Chapitre 2

## Etude des tremblements de terre en laboratoire

### 2.1 Introduction

Les études sur l'irrégularité du stick-slip dans les rubans adhésifs m'ont porté à m'intéresser progressivement à la plus déconcertante imprédictibilité des tremblements de terre. Depuis deux siècles on sait que l'activation de failles dans la croûte terrestre est le phénomène à l'origine des tremblements de terre. La sismologie a ensuite produit des solutions asymptotiques pour le mécanisme de génération d'un évènement sismique, satisfaisant dans la limite des basses fréquences. Pourtant la physique du comment, du pourquoi et du quand se produira-t-il un tremblement de terre, reste inconnue. Une multitude de modèles de prévision ont été proposés, et pourtant chaque événement sismique majeur nous prend encore par surprise avec son énorme potentiel de destruction de vies humaines.

Le développement récent de modèles fondés sur la mécanique statistique et sur des simulations numériques a alimenté de grands espoirs pour modéliser la physique des tremblements de terre. Ces modèles considèrent la croûte terrestre comme un ensemble thermodynamique proche d'une transition de phase (Self Organized Criticality) et ils permettent de reproduire (sans les assumer à priori !) quelques caractéristiques dynamiques de la sismicité, tels que la présence de lois d'échelle dans la distribution des tremblements de terre et la tendance à se vérifier en clusters de fore-, after- et main-shock. Malheureusement la solution n'est pas unique et la contribution générale à la 'compréhension' du phénomène a été faible. D'autres approches espèrent réduire le problème à quelques équations déterministes simples et avec un faible nombre de variables (le 'chaos'), mais cette éventualité parait peu crédible face à l'énorme nombre de degrés de libertés du système. Le problème parait avoir sa racine dans l'absence d'une phénoménologie clairement interprétable. La masse de données expérimentales, contre laquelle les modèles devraient être validés, est énorme et inhomogène. En outre elle se base sur des évidences indirectes qui mènent vers des thèses essentiellement contradictoires.

D'ailleurs, le problème de la rupture des matériaux hétérogènes est certainement l'un des plus compliqués de la Physique entière, et les variables relatives à la croûte sont difficilement mesurables. En tant que physicien, mon approche à cette problématique a été de transporter le problème en laboratoire pour pouvoir bien définir ses termes.

Cette opération ambitieuse ne pouvant pas aller sans une étude approfondie des différences entre la condition terrestre et la condition en laboratoire, j'ai consacré une partie de mon temps à étudier les fondements d'un changement d'échelles spatiale et temporelle si importants (invariance d'échelle), ensuite la différence entre les propriétés mécaniques des roches au sein de la croûte terrestre et du laboratoire, enfin l'effet de la différence de conditions physiques : pression, température, présence de liquides. L'ensemble de ces études m'a mené à proposer un modèle pour la physique de la source des évènements sismiques et pour l'organisation de la distribution des tremblements de terre.

## 2.1 Etude de la propagation sous-critique de fractures dans les roches

### 2.1.1 Mesure des paramètres de fracture lente dans les roches

Le but de ma thèse de doctorat a été d'étudier la propagation de fissures de façon contrôlée dans des matériaux aussi hétérogènes que les roches. Ces mécanismes sont fondamentaux dans les lentes phases préparatoires d'un tremblement de terre ou d'une éruption volcanique. Il est en fait connu que même pour des valeurs du facteur d'intensité des contraintes (« stress intensity factor », K) qui sont inférieures à la valeur critique (correspondante à une propagation instable d'une fracture à haute vitesse) on peut observer une croissance lente (dite 'sous-critique') des fissures préexistantes dans un matériau fragile. Ceci est dû à un mécanisme coopératif entre la concentration des contraintes mécaniques sur les fissures et l'affaiblissement des liaisons cohésives à leur pointe en raison de l'interaction chimique avec l'humidité ambiante (« corrosion sous contraintes »).

La méthode de Torsion Double est très utilisée pour la mesure des paramètres de fracture lente dans les matériaux très fragiles grâce à sa stabilité mécanique. Nous avons construit une machine très rigide (Fig. 2.1.1.1) et développé les techniques pour mesurer ces paramètres de fracture dans des matériaux hétérogènes tels que des roches volcaniques.

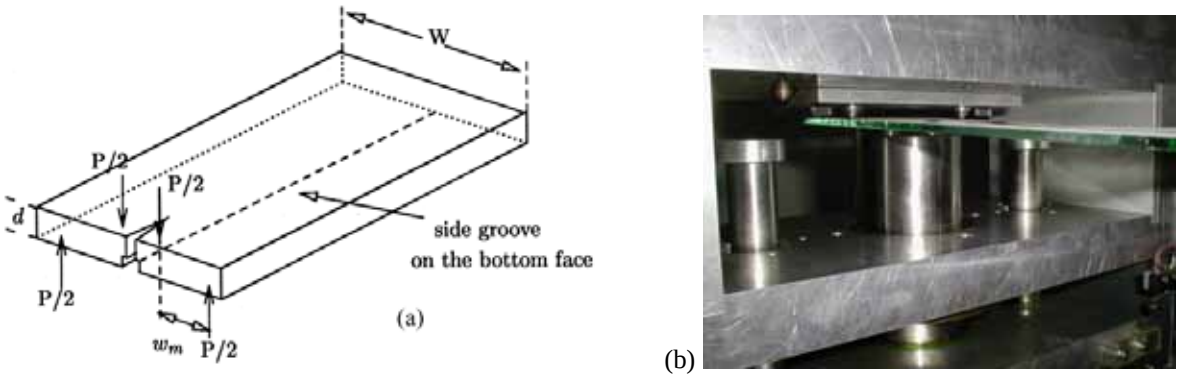


Fig 2.1.1.1 (a) Echantillon de Torsion Double et schéma d'application des contraintes à quatre points. (b) Aperçu de la machine de chargement avec un échantillon de verre.

L'article qui suit contient la description du montage, de la technique de mesure et des résultats pour une série de roches volcaniques provenant des volcans italiens : Etna, Stromboli et Vulcano (Ciccotti, Negri *et al.*, 2000). Ces paramètres sont d'importance fondamentale dans l'application de modèles de fonctionnement des volcans, en particulier, concernant la possibilité que des montées de magma par avancement de fractures (« dykes ») puissent briser les couches de roches volcaniques externes en donnant lieu à des éruptions avec coulées laviques.

ELSEVIER

Journal of Volcanology and Geothermal Research 98 (2000) 209–217

Journal of volcanology and geothermal research

www.elsevier.nl/locate/jvolgeores

# Elastic and fracture parameters of Etna, Stromboli, and Vulcano lava rocks

M. Ciccotti*, N. Negri, L. Sassi, G. Gonzato, F. Mulargia

*Dipartimento di Fisica, Settore di Geofisica, Università di Bologna, Viale Berti Pichat 8, 40100 Bologna, Italy*

Received 15 October 1998; received in revised form 5 November 1999; accepted 5 November 1999

**Abstract**

The results of a series of experiments aimed at characterizing the elastic and failure parameters of lava specimens from Mount Etna, Vulcano and Stromboli volcanos is presented. The double torsion—constant configuration—load relaxation method has been employed to obtain the behavior of the stress intensity factor versus mode I subcritical crack velocity. The experimental technique has been optimized in several respects. First, a very stiff machine, expressly designed and built, has been used. Second, all samples have been carefully machined to low tolerance. Third, the experimental conditions have been carefully controlled, with temperature variations within 1°C and humidity within 10%. Fourth, high resolution electronic measuring systems have been used together with a pulse stacking procedure. Fifth, the length of the prefracture has been optically checked. This optimization allowed us to measure the slope of the subcritical fracture propagation curve in the III region, which extends from velocities of $10^{-7}$ m/s to catastrophic, with a standard deviation around 20%, suggesting that the results can be effectively used for modeling purposes. As a by-product, we could measure the elastic parameters with an accuracy of a few percent. 

*Keywords*: Mount Etna; Vulcano; Stromboli; elastic and fracture parameters; double torsion

## 1. Introduction

It has been widely acknowledged that fracture is the physical process ruling many geophysical phenomena such as earthquake generation and the onset of volcanic eruptions. Unfortunately, fracture physics is so complex that it has proved so far impossible to develop widely applicable theoretical models. Some models have indeed been developed, but their practical application is tied to the knowledge of fracture parameters, such as the mode I critical stress intensity factor $K_{IC}$ and the subcritical crack growth index $n$, which is lacking due to the traditional impossibility of acquiring coherent data. We have focused our interest on this specific problem, attempting to improve the existing experimental techniques. Thus, we started from the most reliable experimental procedure for measuring fracture parameters, double torsion at constant configuration, and attempted to improve it. We have apparently been successful.

## 2. The double torsion testing method

The double torsion—load relaxation—constant configuration method was developed by Evans (1972) to obtain the velocity of crack propagation versus the mode I stress intensity factor. A constant displacement is applied to the specimens through a

* Corresponding author. Fax: +39-51-630-5058.
*E-mail address:* matteo@ibogeo.df.unibo.it (M. Ciccotti).

0377-0273/00/$ - see front matter 
PII: S0377-0273(99)00154-7

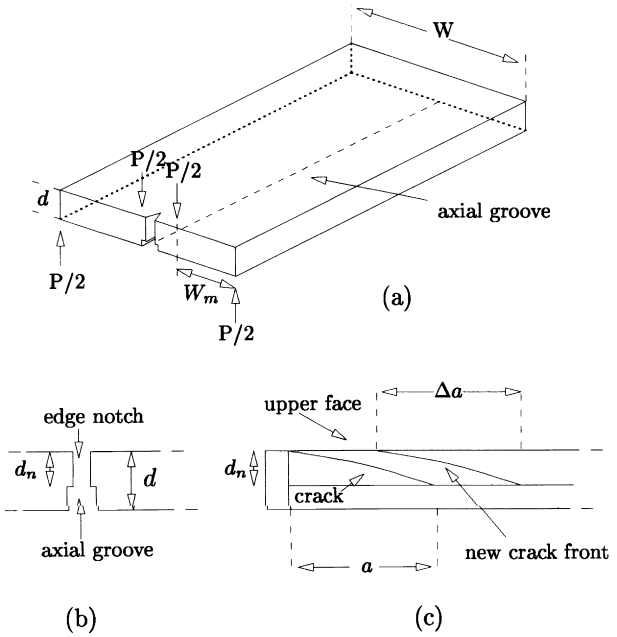


Fig. 1. Sketch of a double torsion specimen configuration: (a) general view; (b) axial cross section; (c) longitudinal cross-section (modified after Atkinson, 1979). The moment arm $W_m$ for our loading machine is fixed at 20 mm.

four point bending scheme as in Fig. 1a. The fracture front proceeds along a straight line starting from a machined initial notch and guided by a side groove thus producing a relaxation of the load.

The method has various advantages, the main of which is its capability to produce stable crack propagation, which makes it very convenient for studying fracture in brittle materials like rocks (Atkinson, 1987). Another advantage of the method is that it only requires one to monitor the decrease of the load with time to measure both the stress intensity factor and the crack velocity, without any need to measure the crack length during the experiment. The mode I stress intensity factor is given by (Williams and Evans 1973):

$$K_I = \sqrt{EG} = PW_m\sqrt{\frac{3(1+\nu)}{Wd^3d_n}} \quad (1)$$

where $E$ is the Young modulus, $G$ the strain energy release rate, $P$ the applied load, $W_m$ the moment arm of the torsion, $\nu$ the Poisson's ratio, $W$ the specimen width, $d$ the specimen thickness, and $d_n$ the thickness of the specimen minus the groove depth.

By differentiating the equation of the specimen compliance:

$$C = \frac{y}{P} = \frac{3W_m^2 a}{Wd^3\mu} \quad (2)$$

with a constant displacement assumption we obtain the crack velocity $v$ using the load relaxation data and a single measure of initial (or final) crack length, provided that this is a relatively large fraction of the specimen dimensions (Williams and Evans, 1973):

$$v = -\phi a_{i,f} P_{i,f} \frac{1}{P^2}\frac{dP}{dt} \quad (3)$$

where $t$ is time, $a$ is the crack length and the suffixes i and f denote reference measurements taken either at the beginning or at the end of a test (we used the initial reference in our tests). The factor $\phi = d_n/\sqrt{\Delta a^2 + d_n^2}$ is necessary to balance the effect of the difference $\Delta a$ in the crack length between the upper and lower face of the specimen (Atkinson, 1987): the crack front is actually diagonal (Fig. 1c), so that its effective normal velocity $v$ equals $da/dt$ reduced

by a factor $\phi$. The difference $\Delta a$ in crack advancement between the upper and lower faces of the specimen has been empirically found to be fixed and equal to five times the thickness $d_n$ in the crack plane.

This approach has been followed by various authors, but the precision achieved so far has been poor, with $v$ vs. $K_I$ curves taken even on the same specimen yielding considerable scatter (Atkinson, 1984; Swanson, 1984).

## 3. Test material

Our specimens were cut from samples of volcanic rocks extracted from the Mount Etna, Sicily, 1981 flank eruption, from the Punta dello Scoglitto lava flow, from the Fossa latitic eruption, from the Lentia rhyolitic dome, all at Vulcano, Aeolian Islands, and from the shoshonitic basaltic eruption at the Filo del Fuoco in Stromboli, Aeolian Islands. The rocks from Vulcano and Stromboli are all dated between 113 000 years b.p. and the historical epoch (Calanchi et al., 1996). Petrographic analysis shows a homogeneous vesicular porphyritic structure in most of the samples, allowing us to assume isotropic mechanical properties. The porosity is determined by sub-spherical pores of variable dimensions ranging from fractions of a mm to a few mm. The chemical composition of each type of rock is determined by XRF analysis; the percentages of the main oxides are reported in Table 1. The lithotypes are displayed on a TAS diagram (Total-Alkali–Silica) in Fig. 2.

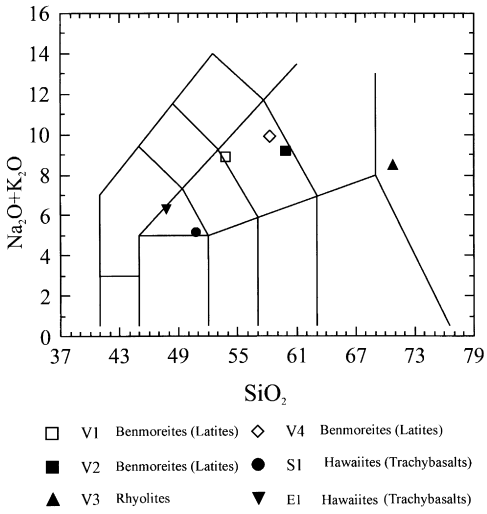


Fig. 2. TAS diagram (Total-Alkali-Silica) for all the lithotypes analyzed. The symbols show the various lithotypes analyzed.

## 4. Optimizing the experimental technique

We attempted to achieve a better accuracy in measuring the fracture parameters by optimizing several experimental aspects. These were:

- A very sturdy machine, run at a small fraction of its load capability.
- Careful specimen preparation, which included low tolerance machining.
- Tight control of the experimental conditions (temperature and humidity).
- High resolution digital electronics and data processing, which also allowed an improved accuracy in the measured elastic parameters.
- An optical check of the prefracture length.

Table 1
Percentage of major oxides in the specimens (from XRF analysis) normalized to 100 and LOI percentage (Lost Oxides Index). The content of FeO was zero for all rocks except E1, for which it was 6.83%. The different lithotypes analyzed are relative to the Mount Etna, Sicily, 1981 flank eruption (E1), to the Punta dello Scoglitto lava flow (V1), to the Fossa latitic eruption (V2 and V4), to the Lentia rhyolitic dome (V3), all at Vulcano, Aeolian Islands, and to the shoshonitic basaltic rocks at the Filo del Fuoco in Stromboli (S1), Aeolian Islands. The rocks from Vulcano and Stromboli are all dated between 113 000 years b.p. and the historical epoch

| Specimen | $SiO_2$ (%) | $TiO_2$ (%) | $Al_2O_3$ (%) | $Fe_2O_3$ (%) | MnO (%) | MgO (%) | CaO (%) | $Na_2O$ (%) | $K_2O$ (%) | $P_2O_5$ (%) | LOI (%) |
|---|---|---|---|---|---|---|---|---|---|---|---|
| V1 | 54.13 | 0.60 | 17.22 | 8.12 | 0.16 | 3.20 | 7.20 | 5.14 | 3.73 | 0.49 | 0.79 |
| V2 | 59.71 | 0.47 | 17.42 | 6.13 | 0.13 | 1.87 | 4.54 | 4.17 | 5.03 | 0.33 | 5.29 |
| V3 | 70.74 | 0.22 | 14.21 | 3.32 | 0.08 | 0.66 | 2.15 | 3.87 | 4.62 | 0.11 | 0.53 |
| V4 | 58.19 | 0.60 | 18.72 | 7.06 | 0.11 | 1.37 | 3.70 | 4.05 | 5.74 | 0.46 | 1.59 |
| S1 | 51.11 | 0.86 | 18.49 | 8.64 | 0.17 | 4.81 | 10.51 | 2.82 | 2.17 | 0.42 | 0.1 |
| E1 | 47.88 | 1.58 | 17.74 | 3.29 | 0.19 | 4.73 | 10.36 | 4.69 | 1.53 | 0.42 | 0.75 |

Table 2
The scatter in the P and S wave velocities in each specimen for all directions of propagation is given by the I and III quartile values (in units of $10^3$ m/s). The median value of the Poisson's ratio $\nu$ is given in the third column. The last column shows the corresponding fracture toughness $K_{IC}$ value. The different lithotypes are given in the caption of Table 1

| Specimen | $V_p$ (km/s) $I_q$–$III_q$ | $V_s$ (km/s) $I_q$–$III_q$ | $\nu$ | $K_{IC}$ (M Nm$^{-3/2}$) |
|---|---|---|---|---|
| V1 | 1.44–1.78 | 0.88–1.04 | 0.24 | 0.445 |
| V2 | 3.05–3.16 | 1.80–2.13 | 0.17 | 1.006 |
| V3 | 3.48–3.62 | 1.92–2.26 | 0.24 | 1.248 |
| V4 | 2.30–2.53 | 1.26–1.69 | 0.26 | 0.165 |
| S1 | 1.86–2.06 | 1.21–1.39 | 0.11 | 0.227 |
| E1 | 3.31–3.43 | 1.89–2.15 | 0.21 | 1.763 |

### 4.1. The loading machine

The machine we used to apply the load is functionally similar to the widely used Instron testing machine and consists essentially of a servo-controlled electric motor which, through a cascade of worm gears, can apply a given displacement to a specimen, while measuring the applied load by a load cell mounted in series with the specimen. Our machine is custom designed and built to maximize stiffness, with a solid stainless steel frame 25.4 mm thick. It was designed for a nominal working load of 20 000 N and, to further guard against frame deformation, it was always used at loads less than 1500 N. Specimens may be up to 20 mm thick and up to 200 mm wide.

### 4.2. Specimen preparation

Specimens for double torsion testing were machined using a precision diamond head into slabs 200 mm long, 70 mm wide, and with a set of different thickness values ranging between 4.7 and 9.4 mm. A groove with a depth equal to 1/3 the specimen thickness was also machined along one of the faces along with a 10-mm-long, 1-mm-wide edge notch to guarantee a rectilinear propagation of the fractures. The tolerance was always kept within 0.4 mm. We used width to thickness ratios between 8:1 and 15:1, at which Eq. (1) can be shown to be well applicable (Ciccotti, 1999).

### 4.3. Control of the experimental conditions

Since tiny deformations in the frame of a stiff loading machine can greatly affect the applied load, it is essential that temperature be kept as constant as possible. We used a heat pump and an electronic differential thermostat to keep temperature variations within 1°C in a dedicated room. The variations of humidity, which do not affect the loading machine, but which can affect the fracture properties of the rock, were kept within 10%.

### 4.4. High resolution electronics

The high resolution achievable through up-to-date electronic devices was beneficial to two different experimental steps. First, the output of the load cell was fed into an analog–digital converter, digitally amplified, and sent via a serial port to a computer workstation where it was recorded, to guarantee the acquisition of massive data sets. Second, since Eq. (1) requires the knowledge of the Poisson's ratio $\nu$, we developed a procedure that used isotropic elastic wave velocities to measure $\nu$:

$$\nu = \frac{\left[\left(\frac{V_p}{V_s}\right)^2 - 2\right]}{2\left[\left(\frac{V_p}{V_s}\right)^2 - 1\right]} \tag{4}$$

Essentially, we used the standard time-of-flight measurement for pulse trains of P and S waves between a sensor and an emitter placed at given positions on the specimen. Step functions with exponential fall were generated by a function generator, pulsed at frequencies varying from 10 Hz to 1 kHz, and injected into the specimen as elastic waves by means of a custom-built piezoelectric transducer, checking in all cases that the frequency value was far from the resonance of the specimen. Time stacking of the recorded signal was then used together with an averaging over 1000 pulses. This allowed an

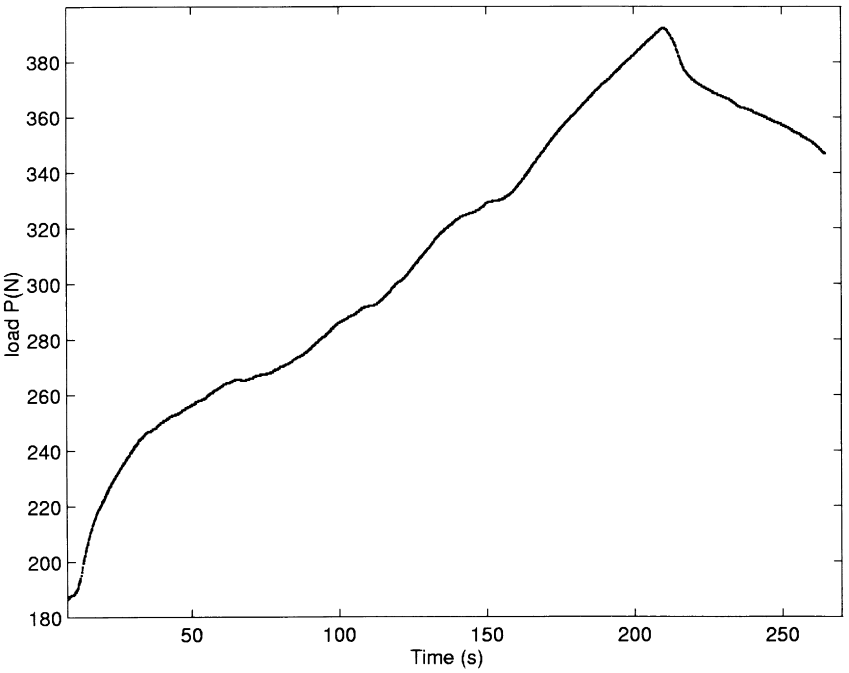


Fig. 3. The load curve in a typical pre-fracture run. The fracture is initiated at ≈ 220 s when a load drop occurs.

improvement in the signal to noise ratio of approximately 20 db.

For each specimen the wave velocities were calculated twice for seven different configurations of the transmitter and receiver, which were glued to the specimen by using cyanoacrilate compounds to ensure good mechanical coupling. The internal scatter of each P and S wave velocity measurement was within a few percent, and also the variation for the different travel paths was limited to about 10% for P waves and 20% for S waves. This indicated a fairly modest anisotropy, which made it possible to apply the isotropic approximation, implemented by taking the median value for each sample. The scatter on the measurements is given by the I and III quartile values of the velocities measured in all directions, which are shown in Table 2 along with the median Poisson's ratio.

### *4.5. Optical check of the prefracture length*

In order to employ Eqs. (1) and (3) it is necessary to create an initial fracture of known length in the specimen. The traditional approach consists, first of all, of cutting a notch of given length along its major axis (see Fig. 1a and b). Since this cut will have a blunt end, while it is necessary to have a sharp fracture, the specimen is loaded at the lowest possible constant strain rate and the load is closely monitored. As soon as a decrease in load is observed, loading is immediately stopped. A typical prefracture load vs. time curve is shown in Fig. 3. It clearly shows the loading at constant rate, followed by a knee. The drop in load is interpreted as the initiation of a fracture, which is nevertheless classically assumed to have propagated for such a short length that it can be disregarded. In light of this, the length of the initial fracture is classically taken to be that of the notch. We checked this by observing the presence of a fracture in the groove (opening side) with an optical stereo microscope. We have in most cases found that a fracture can be quite easily observed and that its length (generally a few centimeters) can never be disregarded. In general, we were also able to observe the final length of the fracture after a relaxation run and this value was cross-checked by integrating the measured velocities of fracture propagation.

The apparatus proved very stable so that several

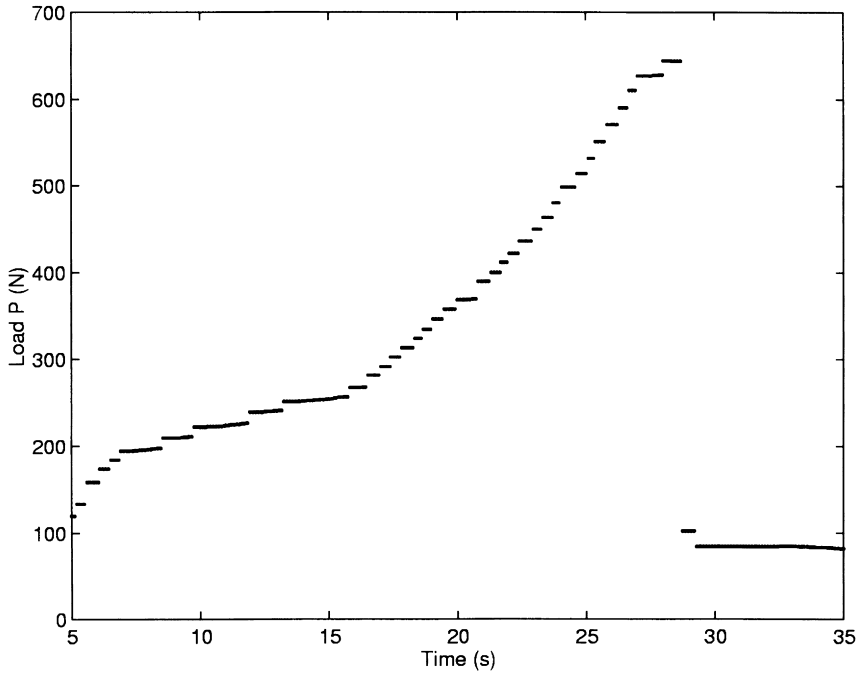


Fig. 4. The general aspect of a critical loading curve consists of a sharp rise of the load followed by an instant drop consequent to the specimen failure.

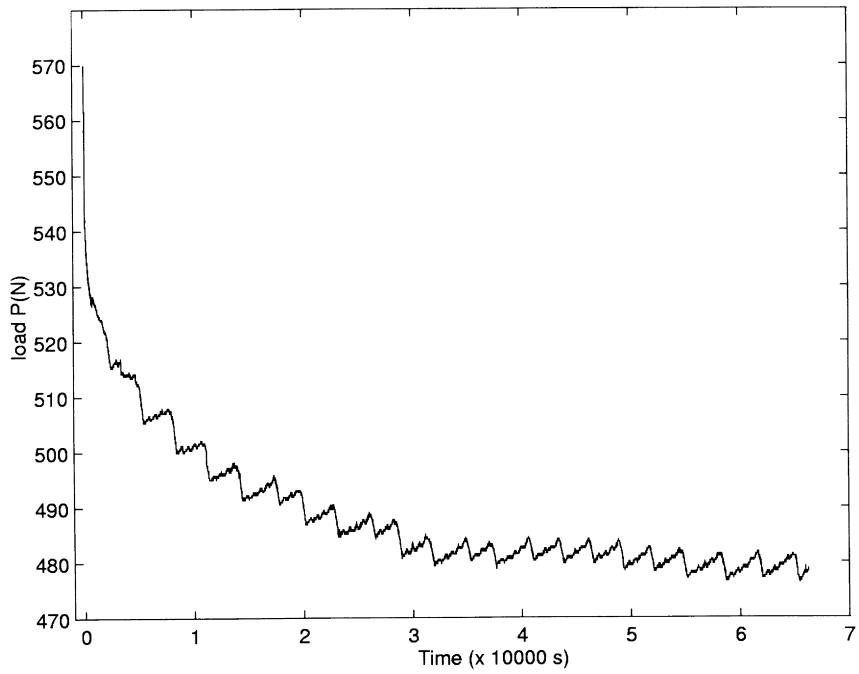


Fig. 5. A typical load relaxation curve. The load fluctuations induced by periodic temperature variations are clearly apparent.

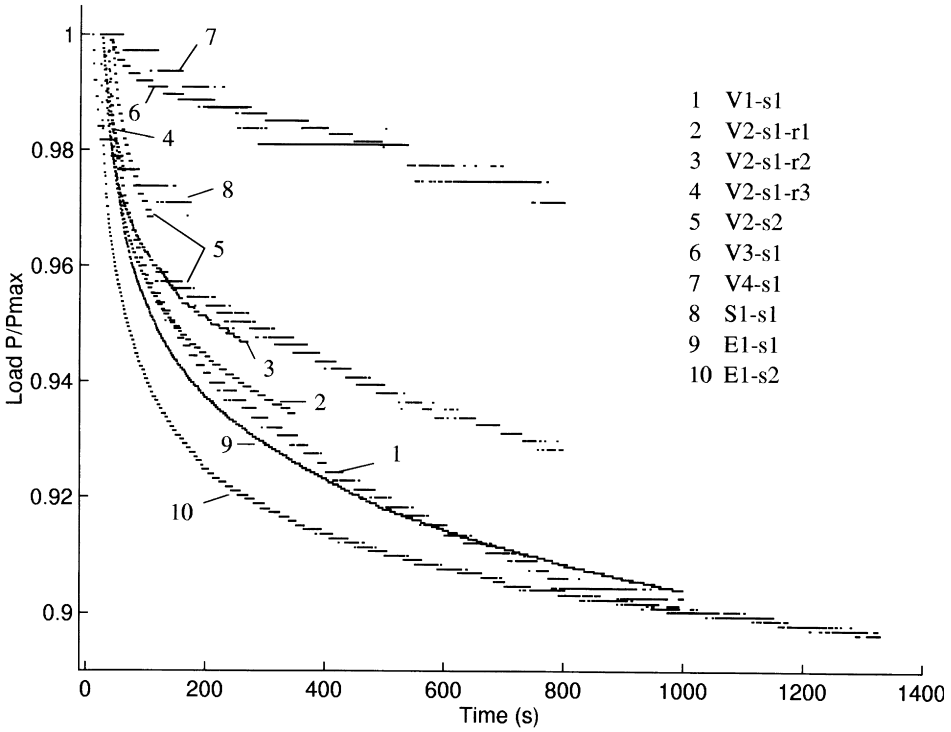


Fig. 6. The initial part of the load relaxation curves, which were used in the analysis, each one normalized to the maximum load $P_{max}$ reached in the run. The label numbers are the same as in Table 3.

relaxation runs could sometimes be performed on the same specimen.

### 4.6. Determination of fracture toughness $K_{IC}$

All the measurements of the critical load $P_C$ were performed on pre-fractured specimens. One or more specimens for each lithotype were loaded at the highest possible rate until they broke and the relative $K_{IC}$ was then calculated through Eq. (1) (the median value for each lithotype is reported in Table 2). The loading curves have a general aspect as in Fig. 4, showing that no significant relaxation takes place before the failure. At this point the load relaxation procedure was ready to start.

### 4.7. Load relaxation

A specimen was loaded at the highest possible rate up to 90–95% of the load relative to $K_{IC}$, the machine was stopped and the load relaxation with time was recorded.

Table 3
The experimental log exponents of the velocity of fracture propagation versus stress intensity factors in the III regime of the mode I subcritical fracture propagation, for the lithotypes we considered. The different lithotypes are given in the caption of Table 1. Letter 's' denotes different specimens of the same lithotype. Letter 'r' denotes different relaxation tests on the same specimen

| | Specimen | *n* |
|---|---|---|
| 1 | V1-s1 | 25.4 |
| 2 | V2-s1-r1 | 49.3 |
| 3 | V2-s1-r2 | 61.5 |
| 4 | V2-s1-r3 | 47.2 |
| 5 | V2-s2 | 36.5 |
| 6 | V3-s1 | 125 |
| 7 | V4-s1 | 22.6 |
| 8 | S1-s1 | 92.1 |
| 9 | E1-s1 | 43.1 |
| 10 | E1-s2 | 45.9 |

Load was sampled at 10 Hz for the whole run, which typically lasted 10 h. Only the initial part of load relaxation was actually used (≃1000 s), though, due to the load fluctuations induced by temperature in spite of its tight control, which are apparent when the relaxation rate becomes slow (see Fig. 5 and the discussion below).

## 5. Results

Sixty-five specimens were cut from a total of 70 kg of lava rocks. A fraction of them had to be discarded because they contained void inclusions large enough to prevent effective measurements. Another fraction accidentally broke during the machining. A further fraction had to be discarded for an insufficient number of samples of identical lithotype.

We measured six different lithotypes, respectively, one coming from Mount Etna volcano, four from Vulcano and one from Stromboli. In spite of the tight control of the environment conditions, the load fluctuation induced by the near periodical temperature variation due to the thermoregulation cycle was generally large (see Fig. 5). We could thus only measure the initial part of the relaxation curve, in which the relaxation rates are high and the load fluctuations induced by temperature variations are comparatively small. Each relaxation curve was therefore analyzed only in the interval preceding the first evident effect of temperature fluctuations (Fig. 6). As a consequence, we could not measure the whole subcritical $v$ vs. $K_I$ curve of mode I fracture propagation, but only its region III, which regards the highest velocities of propagation. This one is actually the most important one for modeling purposes, since it immediately precedes catastrophic propagation. The dependence of $v$ on $K_I$ in region III is a power law:

$$v = AK_I^n \tag{5}$$

where $A$ is a constant and $n$ is the subcritical crack growth index. The experimental results are reported in Fig. 7.

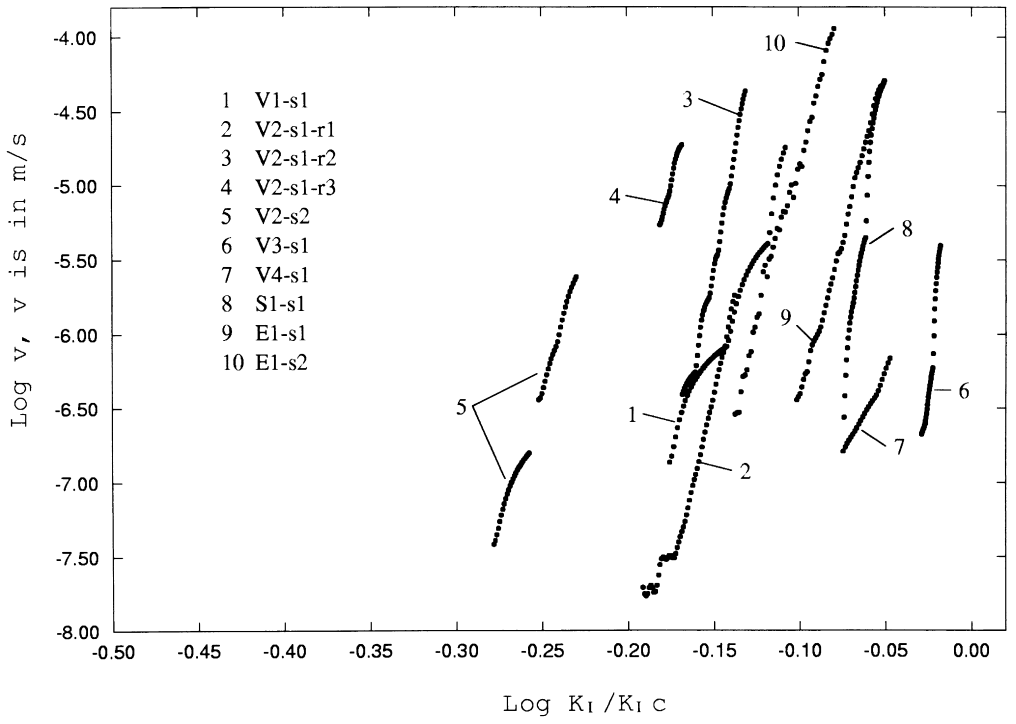


Fig. 7. Region III of the subcritical crack growth curves ($v - K_I$). The stress intensity factor is normalized to the critical value of each lithotype. Notice the coherence and linearity in the slope. The horizontal separation is due to the different values of $K_I$ and is related to the different lithotypes.

The measured velocities of propagation were in the range $10^{-7}$–$10^{-4}$ m/s, in which a log-linear relation was found to provide a very good fit to the data ($r^2 \geq 0.90$ in all cases). Since theoretical considerations yield that these slopes remain constant up to the critical value of the stress intensity factor (e.g. Atkinson, 1987), it is possible to calculate the evolution of fracture propagation from velocities of $10^{-7}$ m/s to catastrophic propagation. The values of the subcritical fracture propagation index $n$ for each lithotype are given in Table 3. Particularly important is the case of the Etna (E1) and Vulcano (V2) lithotypes, for which several independent relaxation runs could be performed, respectively, two for E1 and four for V2. A good coherence was found, with repeatability of the measurement of the region III fracture slope within 20%.

## 6. Conclusions

While fracture is the physical process ruling many geophysical phenomena, it is so complex that developing theoretical models which can be effectively applied in practice has proved so far to be an impossible task. Furthermore, even the applicability of the models which have been developed has been hampered by the lack of a sufficiently accurate knowledge of fracture parameters. We have focused our interest on this problem, attempting to improve the existing experimental techniques for the measurement of fracture parameters. We started from the most reliable experimental procedure, double torsion at constant configuration, and optimized several experimental aspects. These ranged from mere mechanical features like the stiffness of the loading machine, to the tight control of the environment, to data acquisition and inversion procedures. This optimization has been apparently successful and allowed us to measure the subcritical fracture propagation index $n$ with good coherence and repeatability. The standard deviations of order 20% obtained for this index suggest that it can be effectively used for modeling purposes.

Quite obviously, the reliability of each model will be tied to its assumptions and the incorporation of the present results into a model will have also to satisfy this compatibility.

## Acknowledgements

This study was performed with contributions of EEC grant EV-5V-CT 92-0190 and CNR, Gruppo Nazionale per la Vulcanologia. We wish to thank B. Evans and G. Ito for their constructive critiques and M. Bacchetti, who skillfully and patiently machined the specimens.

## References

Atkinson, B.K., 1979. Technical note. Int. J. Rock Mech. Min. Sci., Geomech. Abstr. 16, 49–53.

Atkinson, B.K., 1984. Subcritical crack growth in geological materials. J. Geophys. Res. 89, 4077–4114.

Atkinson, B.K., 1987. Fracture Mechanics of Rock. Academic Press, New York.

Calanchi, N., Rossi, P.L., Sanmarchi, F., Tranne, C.A., 1996. Guida escursionistico vulcanologica delle isole Eolie. Centro Studi e Ricerche di Storia e Problemi Eoliani.

Ciccotti, M., in prep. A realistic finite element study for the Double Torsion loading configuration. Submitted for publication.

Evans, A.G., 1972. A method for evaluating the time-dependent failure characteristics of brittle materials—and its applications to polycrystalline alumina. J. Mater. Sci. 7, 1137–1146.

Swanson, P.L., 1984. Subcritical crack growth and other time—and environment—dependent behavior in crustal rocks. Journ. Geoph. Res. B 89 (6), 4137–4152.

Williams, D.P., Evans, A.G., 1973. A simple method for studying slow crack growth. J. Test. Eval. 1, 264–270.

### 2.1.2 Correction de la technique de Torsion Double

Dans le but de réduire la grande variabilité qui subsiste entre les résultats des laboratoires différents (Swanson, 1984 ; Atkinson, 1984) je me suis ensuite dédié à une révision de la méthode classique de Torsion Double. Toutes les hypothèses et assomptions ont été examinées et discutées dans ma thèse. La formule analytique de Evans (Evans, 1972) couramment utilisée pour traiter les données, est construite sur un modèle simplifié d'échantillon mince, dans lequel la partie fissurée de l'échantillon est idéalisé comme deux plaques parallèles libres de subir deux torsions indépendantes. Pour mieux connaître le comportement d'un échantillon de forme réelle, j'ai effectué une fine simulation par éléments finis de l'éprouvette qui prend en considération : son épaisseur finie, le contact entre les deux parties en torsion, la présence de la gravure latérale, de l'entaille initiale et l'effet de l'inclinaison du front de fissure. En combinant plusieurs valeurs pour chaque paramètre, j'ai calculé le taux de restitution de l'énergie pour 600 combinaisons géométriques différentes. Ceux-ci sont exprimés en termes de facteurs correctifs à appliquer à la formule de Evans (Ciccotti, 2000).

Une analyse plus approfondie m'a amené ensuite à conclure qu'en conséquence de ces corrections, toute la procédure d'analyse doit être revisitée pour éviter des distorsions importantes dans la forme de la courbe K-v. On est ainsi en mesure de réduire considérablement les effets de bord et de contrôler l'influence de la géométrie (Ciccotti, Gonzato and Mulargia, 2000).

Les deux articles qui suivent contiennent respectivement les détails de la simulation numérique et la nouvelle méthode d'analyse.

journal

*J. Am. Ceram. Soc.*, **83** [11] 2737–44 (2000)

# Realistic Finite-Element Model for the Double-Torsion Loading Configuration

Matteo Ciccotti

Dipartimento di Fisica, Settore di Geofisica, Università di Bologna, Bologna, Italy

**The analytical approach to the double-torsion, constant-displacement-configuration technique has forced a strong oversimplification of the specimen model, and, therefore, of the strain field in classical applications. For the present study, accurate three-dimensional finite-element analysis was performed on a realistic specimen; that is, one with finite thickness, a groove, and an initial notch. The influence on the strain-energy release rate of the specimen width and length, the fracture length, the presence and shape of the side groove, the presence of an initial notch, and the curved shape of the fracture front was estimated from this analysis. Significant deviations from the classical analytical solution were found. The present results should reduce the discrepancies found among measurements made in various laboratories and that traditionally have prevented the development of effectively applicable fracture models.**

## I. Introduction

THE double-torsion, load-relaxation, constant-displacement-configuration method was developed by Evans[1] to determine the velocity of crack propagation, $v$, versus the strain-energy release rate, $G$ ($G$–$v$ curve). A typical double-torsion specimen is shown in Fig. 1(a). According to Williams and Evans,[2] $G$ is given by

$$G = -\left(\frac{dU}{dA}\right)_y = \frac{P^2}{2d_n}\frac{dC}{da} = \frac{w_m^2 P^2}{2\eta W d^3 d_n \mu} \quad (1)$$

where $U$ is the total strain energy, $A$ the crack area, $P$ the measured load, $y$ the constant displacement imposed on the loading points, $C$ the compliance of the specimen, $w_m$ the moment arm of the torsion, $W$ the specimen width, $d$ the specimen thickness, $d_n$ the reduced thickness of the specimen in the region of the groove (see Fig. 1(b)), $\mu$ the shear modulus, and $\eta$ a tabled function of $W/d$.[4]

Equation (1) is based on the following model. The double-torsion (DT) specimen is a symmetrical system of two independent plates with lengths equal to the crack length, each plate subject to simple torsion. The part of the specimen beyond the fracture tip is considered undeformed. The compression induced by the torsion at the contact zone of the two plates on the upper face is ignored. The presence of the side groove, the effect of its shape, and the presence of the initial notch are ignored. Finally, the model does not account for the fact that the crack has a different extension, $\Delta a$, on each of the two faces and a curved profile at its tip (see Fig. 1(c)).

The practical importance of these approximations, made necessary by the analytical approach, is unknown. For this reason, the present study consisted of an accurate, three-dimensional, finite-element analysis of a realistic specimen, that is, one with finite thickness, a groove, and an initial notch. The purpose of the present study was to estimate the influence on $G$ of the specimen width and length, the fracture length, the presence and shape of the side-groove, the presence of the initial notch, and the curved shape of the fracture front.

This approach was explored earlier by Trantina.[5] His results were interesting but not very useful in practice, because his study of 176 linear elements produced only five values of $G$ for a specific specimen with no side groove and no initial notch. Furthermore, his use of linear elements prevented him from obtaining a crack front with a realistic inclination.

## II. Finite-Element Model

### *(1) Choice of the Physical Quantity G*

Evans's equation[1] is based on the computation of the strain-energy release rate (SERR) by derivation of the compliance of the DT specimen. He uses the plane-stress relationship to obtain the Mode I stress-intensity factor, $K_I$. Because the plane-stress assumption and the exact fracture modality are, to date, not well understood in the DT loading configuration, direct measurement of the SERR in the finite-element simulation seems best for studying Evans's equation. The idea is to measure the difference, $\delta U$, in

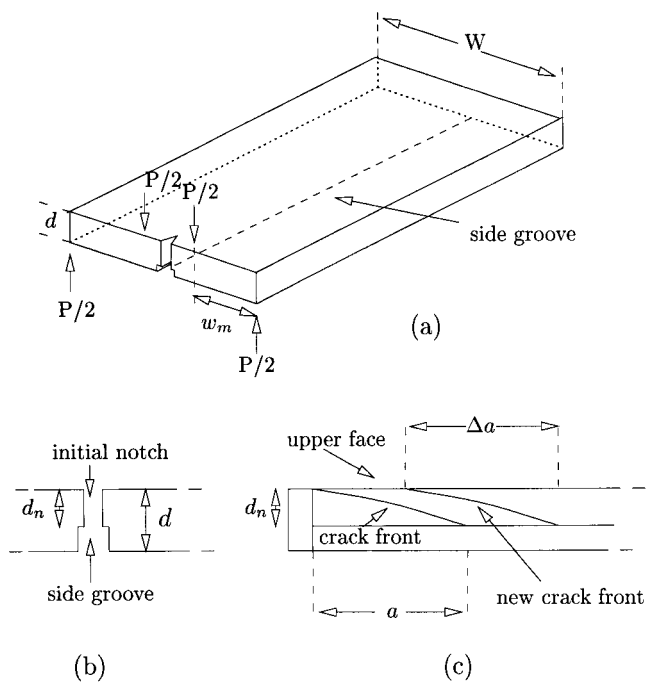


**Fig. 1.** Sketch of a double-torsion specimen: (a) general view, (b) axial cross section, and (c) longitudinal cross section. (After Atkinson.[3])

A. Jagota—contributing editor

Manuscript No. 189276. Received November 1, 1999; approved May 23, 2000.

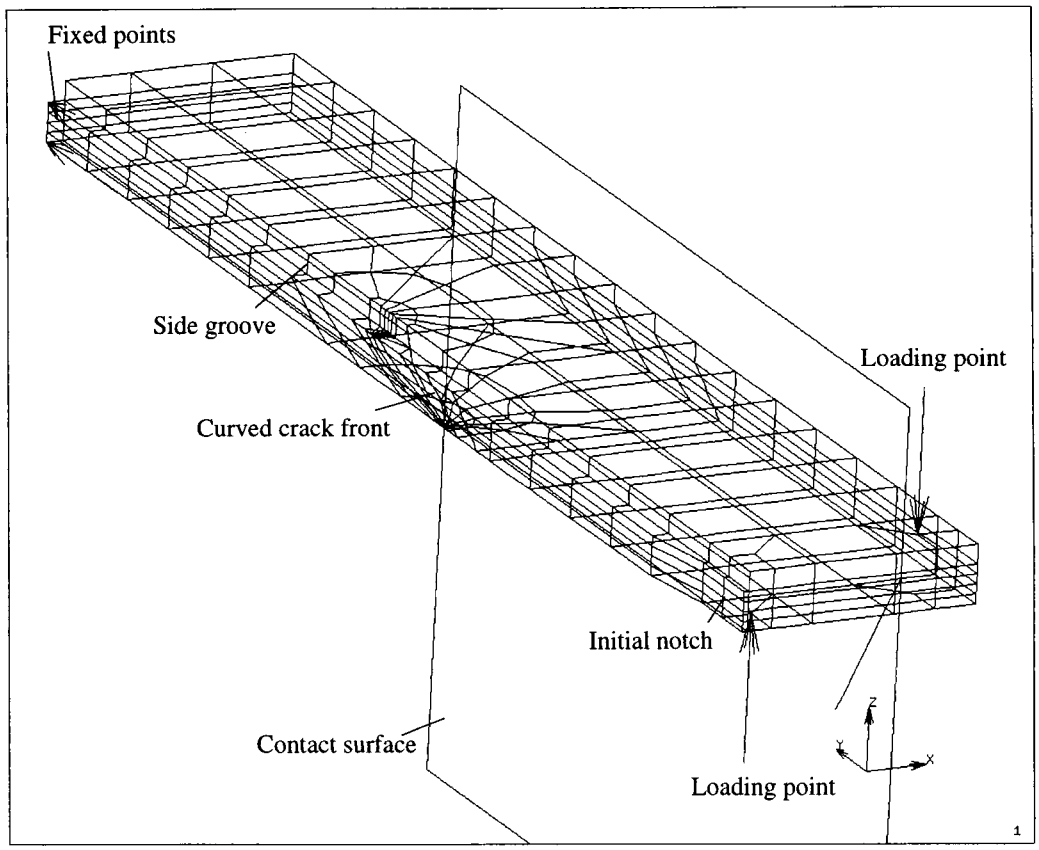


**Fig. 2.** Finite-element mesh. Model represents one-half of the DT specimen. Remaining part is replaced by symmetrical conditions and by a contact surface along the failed interface. Side groove and initial notch are reproduced. Crack front is designed by hand to represent the experimental shape.

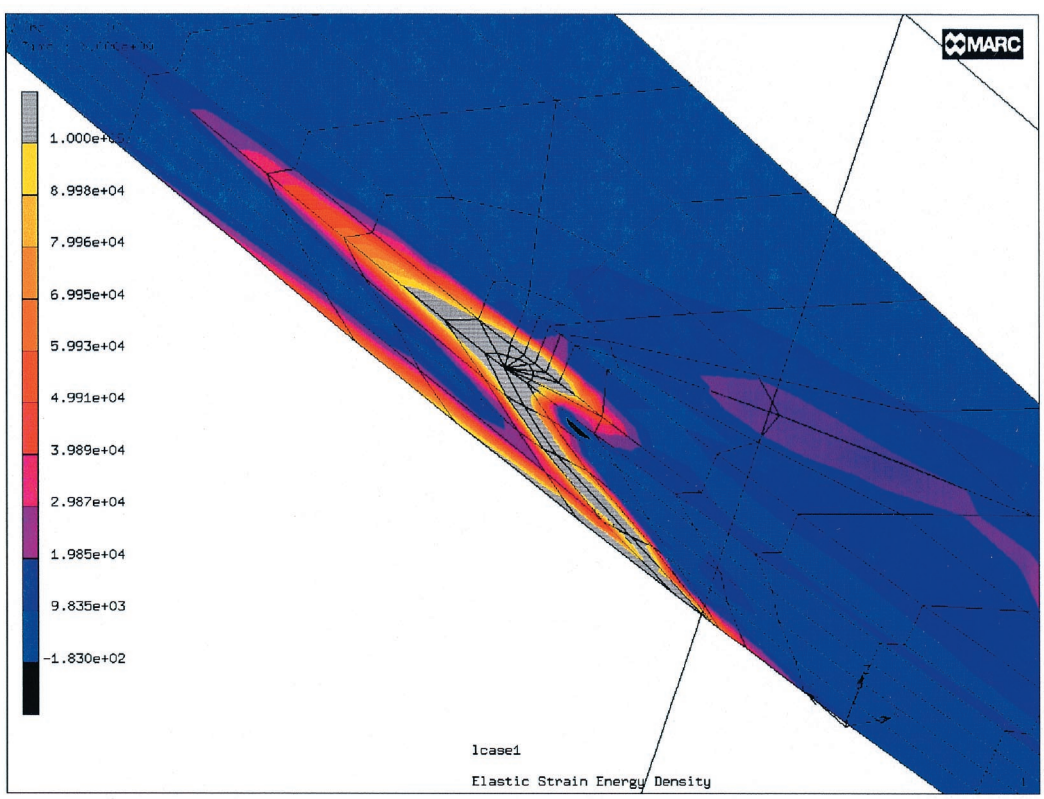


**Fig. 3.** Plot of the strain-energy density field near the fracture front. Energy is concentrated along the curved front and inside the groove.

**Table I. Corrective Factors for Specimens of Length, $L = 17$ cm, and Width, $W = 6$ cm**

| Grove depth, $d_n/d$[‡] | Grove width, $g_w$ (mm) | Notch length, nl (cm) | Inclination, $c$[§] | Corrective factor, $\psi$ | | | | |
|---|---|---|---|---|---|---|---|---|
| | | | | $a = 4.5$ cm | $a = 6.5$ cm | $a = 8.5$ cm | $a = 10.5$ cm | $a = 12.5$ cm |
| 1 | 0 | 0 | 0 | 0.936 | 0.962 | 0.966 | 0.971 | 1.039 |
| 1 | 0 | 0 | 2 | 0.861 | 0.950 | 0.959 | 0.963 | 1.038 |
| 1 | 0 | 0 | 4 | 0.774 | 0.934 | 0.949 | 0.956 | 1.013 |
| 2/3 | 2 | 0 | 0 | 0.944 | 0.965 | 0.971 | 0.987 | 1.119 |
| 2/3 | 2 | 0 | 2 | 0.938 | 0.965 | 0.971 | 0.987 | 1.091 |
| 2/3 | 2 | 0 | 4 | 0.925 | 0.961 | 0.968 | 0.981 | 1.068 |
| 2/3 | 4 | 0 | 0 | 0.968 | 0.991 | 0.997 | 1.021 | 1.186 |
| 2/3 | 4 | 0 | 2 | 0.962 | 0.988 | 0.995 | 1.015 | 1.149 |
| 2/3 | 4 | 0 | 4 | 0.948 | 0.985 | 0.992 | 1.010 | 1.115 |
| 1/2 | 2 | 0 | 0 | 0.964 | 0.991 | 0.999 | 1.048 | 1.281 |
| 1/2 | 2 | 0 | 2 | 0.961 | 0.988 | 1.000 | 1.040 | 1.252 |
| 1/2 | 2 | 0 | 4 | 0.952 | 0.984 | 0.997 | 1.034 | 1.219 |
| 1/2 | 4 | 0 | 0 | 0.977 | 1.025 | 1.047 | 1.118 | 1.440 |
| 1/2 | 4 | 0 | 2 | 0.973 | 1.022 | 1.044 | 1.111 | 1.398 |
| 1/2 | 4 | 0 | 4 | 0.964 | 1.021 | 1.040 | 1.099 | 1.354 |
| 1 | 0 | 2 | 0 | 0.909 | 0.961 | 0.965 | 0.971 | 1.039 |
| 1 | 0 | 2 | 2 | | 0.948 | 0.961 | 0.963 | 1.037 |
| 1 | 0 | 2 | 4 | | 0.931 | 0.948 | 0.954 | 1.012 |
| 2/3 | 2 | 2 | 0 | 0.929 | 0.966 | 0.969 | 0.989 | 1.120 |
| 2/3 | 2 | 2 | 2 | 0.921 | 0.964 | 0.972 | 0.988 | 1.093 |
| 2/3 | 2 | 2 | 4 | 0.897 | 0.961 | 0.968 | 0.978 | 1.067 |
| 2/3 | 4 | 2 | 0 | 0.952 | 0.989 | 0.996 | 1.017 | 1.186 |
| 2/3 | 4 | 2 | 2 | 0.941 | 0.987 | 0.994 | 1.018 | 1.149 |
| 2/3 | 4 | 2 | 4 | 0.911 | 0.981 | 0.992 | 1.009 | 1.115 |
| 1/2 | 2 | 2 | 0 | 0.961 | 0.990 | 0.998 | 1.046 | 1.282 |
| 1/2 | 2 | 2 | 2 | 0.955 | 0.987 | 0.998 | 1.041 | 1.253 |
| 1/2 | 2 | 2 | 4 | 0.944 | 0.985 | 0.995 | 1.035 | 1.220 |
| 1/2 | 4 | 2 | 0 | 0.976 | 1.026 | 1.045 | 1.119 | 1.438 |
| 1/2 | 4 | 2 | 2 | 0.970 | 1.021 | 1.044 | 1.113 | 1.400 |
| 1/2 | 4 | 2 | 4 | 0.958 | 1.018 | 1.040 | 1.098 | 1.347 |

[†]Some data are missing because the curved crack front would cross the initial notch. [‡]Where $d_n$ is the reduced thickness and $d$ the specimen thickness. [§]Of the crack front, expressed as the ratio between the difference, $\Delta a$, in the crack length on the two faces and the reduced thickness, $d_n$.

total strain energy for two meshes with a small difference, $\delta a$, in crack length and to normalize $\delta U$ to the difference in crack area. Thus,

$$G = -\frac{1}{d_n}\left(\frac{\delta U}{\delta a}\right)_y \tag{2}$$

Consequently, the mesh does not have to be very fine, because an extremely accurate representation of the deformation field around the crack tip is necessary only if the crack-surface displacement approach is used.

### *(2) Finite-Element Code and Computing Resources*

The present meshes were designed using a graphic editor (MENTAT 3.2, MARC Corporate, Palo Alto, CA) and analyzed using a parallel code (MARC K7.3, MARC Corporate). The solution process was very laborious, but it was made feasible by access to the powerful resources of the CINECA computing center (Consorzio Interuniversitario Nord-Est Calcolo Automatico, Bologna, Italy) and, in particular, a supercomputer (Model Origin™ 2000, SGI™, Mountain View, CA) with 16 parallel CPUs (MIPS R10 K, 195 MHz), 8 gigabytes of RAM, and a peak performance of 6.24 gigaflops. The operating system used was CELLULAR IRIX 6.5.3 (SGI). Because this supercomputer used ~5 CPU min to solve a model, the present study analyzed 1800 models in 150 CPU h, obtaining 600 values of $G$ that explored combinations of various parameters.

### *(3) Mesh Design*

The finite-element model is designed to represent a DT specimen under a constant-displacement configuration. Because the model is symmetrical, the mesh describes only one-half of the specimen (see Fig. 2). The model consists of ~500 brick elements divided into five slices, one of which is partially removed to simulate the presence of the side groove. Some elements at the beginning of the groove are shrunk to produce an empty space that simulates the initial notch. The refined subdivision of the elements in the first row allows the positioning of the loading points (four-point bending).

The most sophisticated part of the design is the region surrounding the crack. The most common solution for representing cracks is to design a spider-web mesh around the crack front, with quarter-point nodes on the first shell of elements. This solution allows for better adaptation to the physical behavior of the strain field near the crack tip and has been validated against the predictions of the analytical solution for the double cantilever beam.[5]

Trantina[5] also used this spider-web mesh for the DT loading configuration, introducing a weak inclination of the fracture front. Because the strain field near the curved crack tip of the DT specimen was not known in detail, Trantina removed the inner shell of elements near the crack tip. In contrast, the present study involved first testing the elements with quarter-point nodes and then the normal elements; an attempt also was made to remove the inner shell. Because all the variations in $G$ generally were <1%

**Table II. Corrective Factors for Specimens of Length, $L = 17$ cm, and Width, $W = 10$ cm**

| Grove depth, $d_n/d$[‡] | Grove width, $g_w$ (mm) | Notch length, nl (cm) | Inclination, $c$[§] | Corrective factor, $\psi$ | | | | |
|---|---|---|---|---|---|---|---|---|
| | | | | $a = 4.5$ cm | $a = 6.5$ cm | $a = 8.5$ cm | $a = 10.5$ cm | $a = 12.5$ cm |
| 1 | 0 | 0 | 0 | 0.892 | 0.946 | 0.976 | 1.038 | 1.251 |
| 1 | 0 | 0 | 2 | 0.695 | 0.898 | 0.932 | 0.992 | 1.205 |
| 1 | 0 | 0 | 4 | 0.562 | 0.859 | 0.892 | 0.944 | 1.113 |
| 2/3 | 2 | 0 | 0 | 0.904 | 0.958 | 0.997 | 1.095 | 1.430 |
| 2/3 | 2 | 0 | 2 | 0.876 | 0.938 | 0.979 | 1.066 | 1.361 |
| 2/3 | 2 | 0 | 4 | 0.845 | 0.917 | 0.958 | 1.039 | 1.297 |
| 2/3 | 4 | 0 | 0 | 0.921 | 0.975 | 1.023 | 1.138 | 1.529 |
| 2/3 | 4 | 0 | 2 | 0.891 | 0.954 | 1.002 | 1.112 | 1.457 |
| 2/3 | 4 | 0 | 4 | 0.856 | 0.931 | 0.979 | 1.079 | 1.384 |
| 1/2 | 2 | 0 | 0 | 0.937 | 0.999 | 1.060 | 1.221 | 1.721 |
| 1/2 | 2 | 0 | 2 | 0.918 | 0.984 | 1.044 | 1.195 | 1.646 |
| 1/2 | 2 | 0 | 4 | 0.894 | 0.969 | 1.026 | 1.166 | 1.586 |
| 1/2 | 4 | 0 | 0 | 0.960 | 1.037 | 1.119 | 1.338 | 1.987 |
| 1/2 | 4 | 0 | 2 | 0.935 | 1.020 | 1.103 | 1.303 | 1.902 |
| 1/2 | 4 | 0 | 4 | 0.912 | 1.004 | 1.081 | 1.269 | 1.804 |
| 1 | 0 | 2 | 0 | 0.835 | 0.935 | 0.973 | 1.038 | 1.255 |
| 1 | 0 | 2 | 2 | | 0.899 | 0.928 | 0.986 | 1.201 |
| 1 | 0 | 2 | 4 | | 0.861 | 0.885 | 0.940 | 1.114 |
| 2/3 | 2 | 2 | 0 | 0.856 | 0.951 | 0.995 | 1.096 | 1.424 |
| 2/3 | 2 | 2 | 2 | 0.836 | 0.931 | 0.975 | 1.067 | 1.362 |
| 2/3 | 2 | 2 | 4 | 0.799 | 0.908 | 0.953 | 1.037 | 1.298 |
| 2/3 | 4 | 2 | 0 | 0.874 | 0.967 | 1.019 | 1.140 | 1.524 |
| 2/3 | 4 | 2 | 2 | 0.847 | 0.943 | 1.000 | 1.110 | 1.459 |
| 2/3 | 4 | 2 | 4 | 0.805 | 0.920 | 0.977 | 1.078 | 1.387 |
| 1/2 | 2 | 2 | 0 | 0.908 | 0.991 | 1.061 | 1.221 | 1.714 |
| 1/2 | 2 | 2 | 2 | 0.883 | 0.977 | 1.045 | 1.190 | 1.647 |
| 1/2 | 2 | 2 | 4 | 0.856 | 0.960 | 1.027 | 1.167 | 1.579 |
| 1/2 | 4 | 2 | 0 | 0.924 | 1.030 | 1.120 | 1.339 | 1.988 |
| 1/2 | 4 | 2 | 2 | 0.897 | 1.012 | 1.100 | 1.304 | 1.903 |
| 1/2 | 4 | 2 | 4 | 0.865 | 0.992 | 1.083 | 1.270 | 1.806 |

[†]Some data are missing because the curved crack front would cross the initial notch. [‡]Where $d_n$ is the reduced thickness and $d$ the specimen thickness. [§]Of the crack front, expressed as the ratio between the difference, $\Delta a$, in the crack length on the two faces and the reduced thickness, $d_n$.

(with better consistency between quarter-point and normal elements), the simpler normal elements were used here. The radius of the inner shell of nodes was $R = 1.6$ mm ($R/d = 0.23$).

The geometry of the inclined spider web was matched carefully with the presence of the groove, and the internal position of each node was optimized, with the purpose of reaching the maximum curved-front inclination allowed by the deformation limits of the elements. (The graphic mesh editor MENTAT has an internal element-check function that highlights elements whose distortion is above a threshold value.)

For the low strain used in the present model, and assuming the use of second-order elements, the code indicated a threshold value of 0.95. In regard to distortion, this value indicated that the internal angles of each element could not decrease below 10°. In regard to the aspect ratio (the ratio between the surface and the volume of an element), the 0.95 threshold value meant that the ratio between the lengths of the different sides of an element could not be $>12$.

These restrictions limited the extent of curvature of the crack profile. Experimental results have shown that the ratio of inclination, $c$, between $\Delta a$ and $d_n$ typically is $\sim 5$.[1] In the present case, optimization allowed a maximum inclination at $c = 4$, a substantial improvement over the value of $c = 1.7$ obtained by Trantina[5] with lower-order elements. To simulate the curvature, a different inclination was used for each quarter of $d_n$. For the specimens with $c = 4$, the four inclinations were 30°, 20°, 10°, and 10°. A series of specimens with a straight front ($c = 0$) and a series with an intermediate inclination, $c = 2$ (angles of 49°, 34°, 19°, and 19°) also were designed to clarify the influence of the front inclination. Figure 3 provides a close-up view of the crack tip for $c = 4$, and a plot of the strain-energy density field.

For the specimen represented by the basic mesh, shown in Fig. 2, $L = 17$ cm, $W = 6$ cm, and $d = 7$ mm. The moment arm of the torsion was $w_m = 2$ cm. Longer specimens, with $L = 25$ cm, were generated by adding rows of elements. Wider specimens, with $W = 10$ cm, were generated by expanding the external row of elements, so that only the moment arm was changed, to $w_m = 3.5$ cm, leaving all of the internal region containing the groove unaltered.

For each combination, five crack lengths were obtained by moving the central part with the crack and resubdividing the elements of the remaining parts. The crack-length values, $a$, were measured from the position of the loading points—in the present case, 0.5 cm from the beginning of the specimen to the end of the crack on the lower opening side. For the shorter specimens, the crack-length ($a$) values were 4.5, 6.5, 8.5, 10.5, and 12.5 cm; for the longer specimens, the crack-length ($a$) values were 5.5, 8.5, 12.5, 16.5, and 20.5 cm.

The width of the groove was changed by incrementally decreasing the width of the corresponding row of elements from 4 to 2 mm. The change in depth of the groove, from one-third to one-half of the specimen thickness ($d/3$ to $d/2$), needed more attention: The entire slice under the groove was contracted in the $z$ direction, but the central block surrounding the crack front also had to be contracted by the same amount along the direction of the groove, to preserve the same aspect ratio for the crack-front profile relative

**Table III. Corrective Factors for Specimens of Length, $L = 25$ cm, and Width, $W = 6$ cm**

| Grove depth, $d_n/d$[‡] | Grove width, $g_w$ (mm) | Notch length, nl (cm) | Inclination, $c$[§] | Corrective factor, $\psi$ | | | | |
|---|---|---|---|---|---|---|---|---|
| | | | | $a = 4.5$ cm | $a = 6.5$ cm | $a = 8.5$ cm | $a = 10.5$ cm | $a = 12.5$ cm |
| 1 | 0 | 0 | 0 | 0.956 | 0.966 | 0.965 | 0.967 | 1.046 |
| 1 | 0 | 0 | 2 | 0.922 | 0.960 | 0.964 | 0.965 | 1.040 |
| 1 | 0 | 0 | 4 | 0.892 | 0.951 | 0.956 | 0.956 | 1.022 |
| 2/3 | 2 | 0 | 0 | 0.960 | 0.967 | 0.968 | 0.974 | 1.127 |
| 2/3 | 2 | 0 | 2 | 0.960 | 0.969 | 0.966 | 0.975 | 1.092 |
| 2/3 | 2 | 0 | 4 | 0.953 | 0.965 | 0.967 | 0.970 | 1.068 |
| 2/3 | 4 | 0 | 0 | 0.984 | 0.991 | 0.992 | 0.992 | 1.185 |
| 2/3 | 4 | 0 | 2 | 0.983 | 0.991 | 0.992 | 1.000 | 1.146 |
| 2/3 | 4 | 0 | 4 | 0.977 | 0.987 | 0.992 | 0.993 | 1.127 |
| 1/2 | 2 | 0 | 0 | 0.983 | 0.985 | 0.991 | 1.001 | 1.275 |
| 1/2 | 2 | 0 | 2 | 0.982 | 0.985 | 0.989 | 1.003 | 1.242 |
| 1/2 | 2 | 0 | 4 | 0.976 | 0.982 | 0.986 | 0.999 | 1.219 |
| 1/2 | 4 | 0 | 0 | 1.018 | 1.016 | 1.022 | 1.048 | 1.448 |
| 1/2 | 4 | 0 | 2 | 1.014 | 1.019 | 1.022 | 1.044 | 1.389 |
| 1/2 | 4 | 0 | 4 | 1.009 | 1.016 | 1.018 | 1.038 | 1.348 |
| 1 | 0 | 2 | 0 | 0.951 | 0.965 | 0.965 | 0.966 | 1.041 |
| 1 | 0 | 2 | 2 | | 0.960 | 0.962 | 0.960 | 1.043 |
| 1 | 0 | 2 | 4 | | 0.946 | 0.955 | 0.956 | 1.020 |
| 2/3 | 2 | 2 | 0 | 0.961 | 0.967 | 0.966 | 0.975 | 1.128 |
| 2/3 | 2 | 2 | 2 | 0.956 | 0.968 | 0.968 | 0.976 | 1.093 |
| 2/3 | 2 | 2 | 4 | 0.949 | 0.967 | 0.965 | 0.971 | 1.069 |
| 2/3 | 4 | 2 | 0 | 0.983 | 0.991 | 0.991 | 1.000 | 1.187 |
| 2/3 | 4 | 2 | 2 | 0.980 | 0.990 | 0.991 | 0.997 | 1.148 |
| 2/3 | 4 | 2 | 4 | 0.968 | 0.987 | 0.988 | 0.996 | 1.121 |
| 1/2 | 2 | 2 | 0 | 0.984 | 0.990 | 0.989 | 1.008 | 1.276 |
| 1/2 | 2 | 2 | 2 | 0.982 | 0.986 | 0.986 | 1.004 | 1.242 |
| 1/2 | 2 | 2 | 4 | 0.976 | 0.983 | 0.987 | 0.994 | 1.220 |
| 1/2 | 4 | 2 | 0 | 1.016 | 1.023 | 1.024 | 1.049 | 1.439 |
| 1/2 | 4 | 2 | 2 | 1.014 | 1.016 | 1.020 | 1.045 | 1.390 |
| 1/2 | 4 | 2 | 4 | 1.007 | 1.014 | 1.020 | 1.039 | 1.349 |

[†]Some data are missing because the curved crack front would cross the initial notch. [‡]Where $d_n$ is the reduced thickness and $d$ the specimen thickness. [§]Of the crack front, expressed as the ratio between the difference, $\Delta a$, in the crack length on the two faces and the reduced thickness, $d_n$.

to $d_n$. Specimens without grooves were produced by eliminating the first slice, expanding the remaining part in the $z$ direction, and again expanding the central block along the direction of the groove.

All the present specimens also were doubled in number, to create a version with an initial notch 2 cm long and another without a notch. The parameter values can be summarized as follows.

(1) Five crack lengths of $a = 4.5$, 6.5, 8.5, 10.5, and 12.5 cm for $L = 17$ cm, and five crack lengths $a = 5.5$, 8.5, 12.5, 16.5, and 20.5 cm for $L = 25$ cm.
(2) Three front inclinations of $c = \Delta a/d_n = 0$, 2, and 4.
(3) Three groove depths of $g_d = 1 - d_n = 0$, $d/3$, and $d/2$.
(4) Three groove widths of $g_w = 0$, 2, and 4 mm.
(5) Two specimen lengths of $L = 17$ and 25 cm.
(6) Two specimen widths of $W = 6$ and 10 cm.
(7) Two notch lengths of nl = 0 and 2 cm.

Combining these parameters by Cartesian product resulted in 600 different models (not all combinations are possible). For the computation of $G$, three meshes were produced for each model, moving forward the region around the crack front in two steps of 0.2 mm each. The two strain-energy increases were verified to be consistent, and the strain-energy release rate on the global increment was calculated.

The total number of meshes analyzed was 1800. To accelerate the design process, only 60 basic meshes were worked out individually with the graphic editor. All the other meshes were generated automatically by moving some sets of nodes using external C programs and Unix shell scripts expressly written for that purpose.

### *(4) Boundary Conditions*

The load was applied using a four-point bending scheme, by imposing a fixed vertical displacement onto the loading points, as shown in Fig. 2. The inner loading point on the bottom face was moved up 0.15 mm, and the outer loading point on the top face was moved down by the same amount, so that the global deformation, $y$, was 0.3 mm. Because the deformation was not symmetrical with respect to the $z$ direction, all other points had to be free to move vertically for the whole specimen to find its equilibrium position. To prevent other global translations or rotations of the model, two points at the end of the specimen were fixed in the $x$ and $y$ directions (see Fig. 2).

The symmetrical boundary conditions at the interface between the two halves of the specimen were implemented in two steps.

(1) The nodes on the intact portion of the interface were bound to move on a vertical plane.

(2) The nodes of the cracked portion were free to move away from the vertical plane, but they were bound by a rigid contact surface that simulated the compressive effect against the other half of the specimen (see Fig. 2).

The contact surface started before the first node on the top of the cracked surface. In the specimens with a curved crack front, this positioning left out some nodes along the crack surface, but the

**Table IV. Corrective Factors for Specimens of Length, $L = 25$ cm, and Width, $W = 10$ cm**

| Grove depth, $d_n/d$[‡] | Grove width, $g_w$ (mm) | Notch length, nl (cm) | Inclination, $c$[§] | Corrective factor, ψ | | | | |
|---|---|---|---|---|---|---|---|---|
| | | | | $a = 4.5$ cm | $a = 6.5$ cm | $a = 8.5$ cm | $a = 10.5$ cm | $a = 12.5$ cm |
| 1 | 0 | 0 | 0 | 0.929 | 0.962 | 0.966 | 0.983 | 1.251 |
| 1 | 0 | 0 | 2 | 0.841 | 0.913 | 0.937 | 0.946 | 1.203 |
| 1 | 0 | 0 | 4 | 0.775 | 0.883 | 0.898 | 0.914 | 1.118 |
| 2/3 | 2 | 0 | 0 | 0.937 | 0.964 | 0.972 | 1.005 | 1.430 |
| 2/3 | 2 | 0 | 2 | 0.915 | 0.950 | 0.958 | 0.983 | 1.343 |
| 2/3 | 2 | 0 | 4 | 0.891 | 0.932 | 0.939 | 0.972 | 1.304 |
| 2/3 | 4 | 0 | 0 | 0.951 | 0.978 | 0.982 | 1.019 | 1.537 |
| 2/3 | 4 | 0 | 2 | 0.927 | 0.959 | 0.966 | 1.008 | 1.427 |
| 2/3 | 4 | 0 | 4 | 0.901 | 0.942 | 0.953 | 0.987 | 1.382 |
| 1/2 | 2 | 0 | 0 | 0.965 | 0.981 | 0.987 | 1.056 | 1.711 |
| 1/2 | 2 | 0 | 2 | 0.948 | 0.973 | 0.985 | 1.047 | 1.631 |
| 1/2 | 2 | 0 | 4 | 0.932 | 0.959 | 0.970 | 1.029 | 1.586 |
| 1/2 | 4 | 0 | 0 | 0.981 | 1.004 | 1.014 | 1.118 | 1.974 |
| 1/2 | 4 | 0 | 2 | 0.965 | 0.990 | 1.002 | 1.098 | 1.862 |
| 1/2 | 4 | 0 | 4 | 0.949 | 0.978 | 0.987 | 1.089 | 1.801 |
| 1 | 0 | 2 | 0 | 0.905 | 0.959 | 0.963 | 0.976 | 1.254 |
| 1 | 0 | 2 | 2 | | 0.908 | 0.936 | 0.949 | 1.205 |
| 1 | 0 | 2 | 4 | | 0.876 | 0.895 | 0.917 | 1.109 |
| 2/3 | 2 | 2 | 0 | 0.922 | 0.963 | 0.967 | 0.995 | 1.431 |
| 2/3 | 2 | 2 | 2 | 0.901 | 0.946 | 0.959 | 0.984 | 1.344 |
| 2/3 | 2 | 2 | 4 | 0.872 | 0.927 | 0.940 | 0.973 | 1.305 |
| 2/3 | 4 | 2 | 0 | 0.932 | 0.974 | 0.983 | 1.020 | 1.522 |
| 2/3 | 4 | 2 | 2 | 0.911 | 0.959 | 0.967 | 1.010 | 1.444 |
| 2/3 | 4 | 2 | 4 | 0.881 | 0.940 | 0.954 | 0.989 | 1.383 |
| 1/2 | 2 | 2 | 0 | 0.950 | 0.985 | 0.988 | 1.056 | 1.712 |
| 1/2 | 2 | 2 | 2 | 0.930 | 0.974 | 0.979 | 1.047 | 1.631 |
| 1/2 | 2 | 2 | 4 | 0.912 | 0.960 | 0.971 | 1.029 | 1.587 |
| 1/2 | 4 | 2 | 0 | 0.967 | 1.001 | 1.015 | 1.118 | 1.975 |
| 1/2 | 4 | 2 | 2 | 0.947 | 0.987 | 1.003 | 1.099 | 1.883 |
| 1/2 | 4 | 2 | 4 | 0.927 | 0.972 | 0.995 | 1.078 | 1.802 |

[†]Some data are missing because the curved crack front would cross the initial notch. [‡]Where $d_n$ is the reduced thickness and $d$ the specimen thickness. [§]Of the crack front, expressed as the ratio between the difference, $\Delta a$, in the crack length on the two faces and the reduced thickness, $d_n$.

omission was not a cause for concern, because loading clearly would move the nodes away from the contact surface.

### *(5) Element Properties*

For the present model, 20-node elements belonging to the serendipity family were used. These second-order elements, characterized by the presence of additional nodes in the middle of each edge, provided a good balance between rapidity of convergence and computational cost. Full integration, based on five points, made the solution more accurate. The analysis was based on linear elasticity, with the physical properties of the material given by the values of Young's modulus, $E = 10^4$ MPa; Poisson's ratio, $\nu = 0.2$; and density, $\rho = 2.2$ kg/dm$^3$—these values are typical for lava rocks, but the results can be easily scaled to more-suitable values for engineering ceramic materials.

## III. Testing Stability

For better control of the solution process, the load application was divided into 10 steps, a method that assured optimal linearity with load. The compliance $C = y/P$ was constant within $10^{-5}$ up to values of the displacement that were 1 order of magnitude larger than the displacements effectively used.

The convergence control was based on the displacement check. The code calculated the convergence ratio using the equation $CR = \max(\delta u_i)/\max(du_j)$, where CR is the convergence ratio, $\delta u_i$ the node-displacement increments in the last iteration, and $du_j$ the final displacements. The values of CR were always between $2 \times 10^{-12}$ and $4 \times 10^{-8}$, indicating excellent convergence, because the threshold proposed by the code supporters is 0.05. In this type of analysis, the displacement check is more significant than the residual-force check, which is based on the ratio between the maximum residual force and the maximum reaction force. Because the load is applied only on two nodes, the maximum reaction force is always very high, resulting in very low convergence ratios.

Another important test index is the singularity ratio, SR, which is related to the conditioning number, CN, of the system of linear equations to be solved by the Crout elimination process. CN is defined as the ratio between the highest and the lowest eigenvalues of the system. The SR is an upper boundary for the inverse of the matrix conditioning number ($1/SR \leq CN$).

The number of digits lost in the elimination process is $n_{lost} \approx -\log_{10} SR$. SR values obtained in the present solution were always between $8 \times 10^{-7}$ and $1.8 \times 10^{-2}$; this result indicates a maximum loss of about six digits. Because the code works in double precision—that is, with an internal accuracy of $10^{-12}$—the first six digits are not affected by numerical approximations. The numerical precision of the strain energy, $U$, then, is $<10^{-6}$, but the strain-energy release rate is obtained from differences between two values of $U$ with different crack lengths. The crack-length increment chosen for the present study assured that such differences were never $<0.1\%$ of the strain-energy values. Thus, the numerical precision of the differences was always $<10^{-3}$, a good result, because the global accuracy of the present results was $\sim 1\%$.

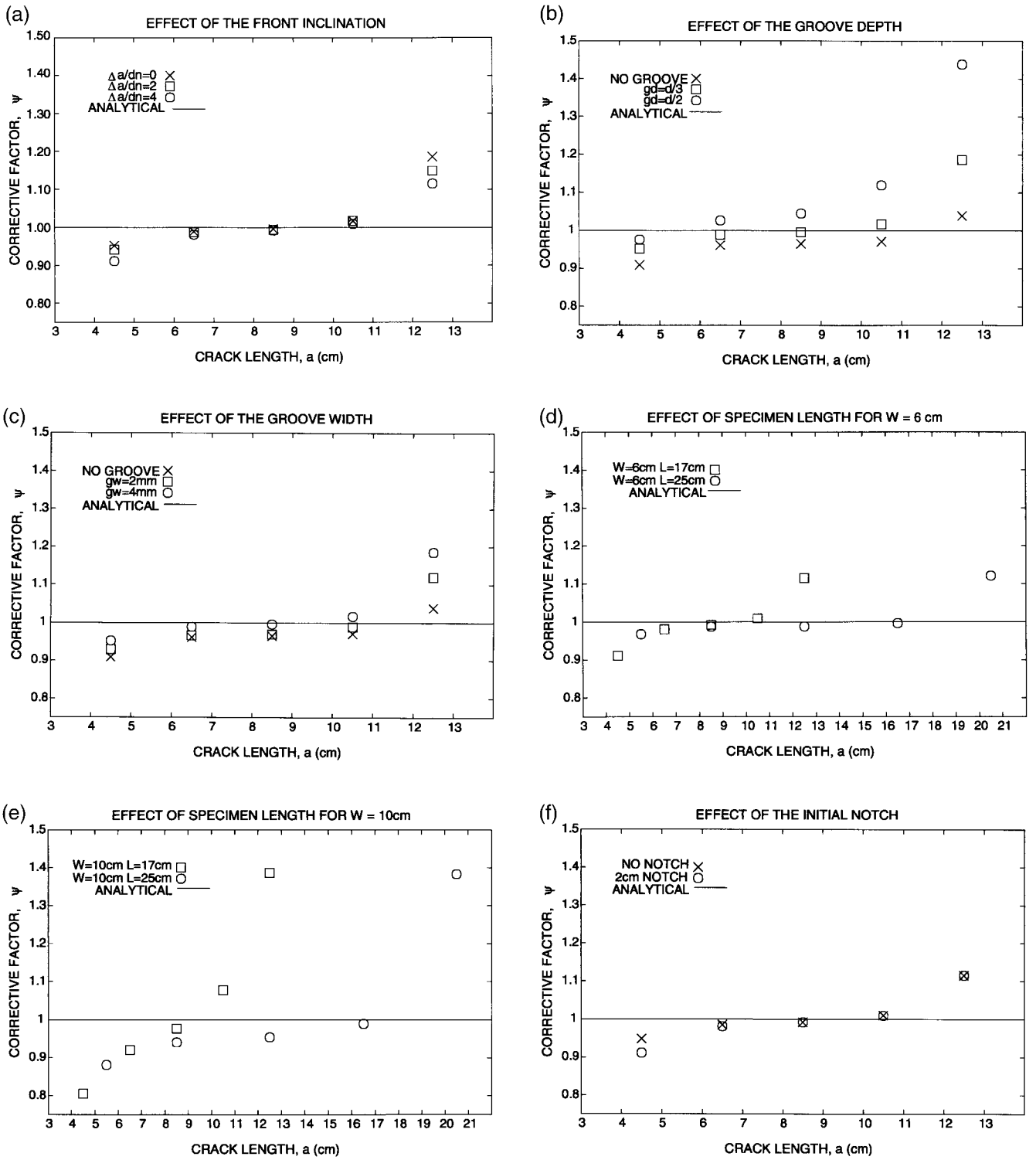


**Fig. 4.** Effect of the variation of each parameter. For each plot the corrective coefficients, ψ, for the five crack lengths are reported and one parameter is changed: (a) variation of the front inclination, *c*; (b) variation of the groove depth, $g_d = (1 - d_n)$; (c) variation of the groove width, $g_w$; (d) variation of the specimen length for $W = 6$ cm; (e) variation of the specimen length for $W = 10$ cm; and (f) variations of the notch length, nl.

The full Newton–Raphson iterative procedure was used to solve the meshes. To test the reliability of the procedure for the present case, some solutions were derived using a large-displacement procedure, as well as an updated Lagrange procedure. The obtained results were consistent within 1%. The values for total strain energy were obtained by integrating the strain-energy density over the entire mesh. The high degree of linearity observed suggested the recalculation of the total strain energy using the relationship $U = y(P/2)$, where $P$ is the reaction force at the loading points. The two values were consistent within $10^{-5}$, a proof of physical reliability. The consistency between the local trend of strain energy caused by small displacements of the nodes during the calculation of $G$ and the general trend of the strain energy among the five different crack lengths, also was checked.

To test the stability of the model, many different meshes, corresponding to the same geometric model, were designed. The number and position of the rows and the slices were changed, as was the extension of the set of nodes that was moved along with

the crack front. The variations obtained were always <1%, giving the present results a precision of 1%.

## IV. Results

The present results, consisting of 600 $G$ values, for all combinations of the various parameters, are reported in Tables I–IV as corrective factors, $\psi$, with respect to Evans's equation. Thus,

$$G = \psi \frac{w_m^2 P^2}{2\eta W d^3 d_n \mu} \tag{3}$$

More precisely, the finite-element value of $G$, $G_{FE}$, was evaluated using Eq. (2), where $U$ is twice the total strain energy obtained by the finite-element analysis of the halved specimen. The load, $P$, was evaluated using the well-verified equation $U = y(P/2)$, where $y$ is the value of the constant displacement. Finally, the values for $G_{FE}$ were divided by the analytical value, $G_{AN}$, obtained from Eq. (1) for the same load, $P$. The values of $\eta$ for $W = 6$ and $W = 10$ cm were 0.285 and 0.304, respectively.[4]

Some of the present results are plotted in Figs. 4(a)–(f) to show the influence on $G$ of each parameter. The correction value is important. Variations from 10% to 50% are apparent for the five different crack lengths, with a increasing trend, in agreement with other experimental observations.[6,7]

The use of three different front inclinations ($c = \Delta a/d_n = 0$, 2, and 4) produced very consistent results in the center of the specimen (Fig. 4(a)). However, away from the center, the SERR varied by ~8% near the borders, and $G$ increased with inclination. The value of $c = 5$, observed in earlier experiments,[1] was not obtained here, because the distortion of the elements around the crack tip was too high, but such a value could be reasonably expected to produce a slightly higher value of $\psi$.

Changes in the groove depth produced a general shift in the coefficients, accentuated for long cracks (Fig. 4(b)). The SERR increased by ~5% when the groove depth increased from zero to one-half of the specimen thickness. This major effect resulted from the weakening of the specimen. A similar effect influenced the dependence of $G$ on groove width ($G$ increased by ~4% when the groove width increased from 0 to 4 mm, as shown in Fig. 4(c)).

The dependence of $G$ on specimen dimensions was important and complex. For all the specimen widths considered, short crack lengths exhibited consistent results, but the shorter specimens had an earlier deviation of $\psi$ for large values of $a$ (Figs. 4(d) and (e)). This deviation showed that the increase in $\psi$ for long cracks was some type of an end effect. Furthermore, a comparison of Figs. 4(d) and (e) showed a higher deviation for the larger specimen. These results were in agreement with earlier experimental observations[6,7] and also with Fuller's[8] conclusion that such effects should be evaluated in terms of distance of the fracture from the ends of the specimen (expressed in units of width) rather than in terms of the ratio between crack and specimen length.

The difference caused in the SERR by the presence of the initial notch was generally very weak, except for short crack lengths, in which it produced variations of ~5% (Fig. 4(f)).

## V. Conclusions

The present finite-element analysis showed that the classical equation for describing DT fracture experiments generally was inadequate. The presence and shape of the side groove, along with the presence of the initial notch, the crack-front shape, and the end effects, were important in affecting the strain-energy release rate. The effect on $G$ of all these parameters was examined exhaustively in the present study in terms of corrective coefficients of the classical equation. The importance of the corrections proved to be considerable (up to 40%) and likely a major cause of the large scatter among the $G$–$v$ curves measured in various laboratories. Further developments may be found in a companion paper.[9]

## Acknowledgments

I thank F. Mulargia for the helpful criticism about the double-torsion model; G. Gonzato for the help in the workout of the scripts for automatic mesh generation; F. Mariani from Espri-MARC (Genova, Italy) for the careful examination of the good fitness of my finite-element models; and the CINECA computing center in Bologna, which provided powerful computing resources and technical support.

## References

[1]A. G. Evans, "A Method for Evaluating the Time-Dependent Failure Characteristics of Brittle Materials—And Its Applications to Polycrystalline Alumina," *J. Mater. Sci.*, **7** [10] 1137–46 (1972).

[2]D. P. Williams and A. G. Evans, "A Simple Method for Studying Slow Crack Growth," *J. Test. Eval.*, **1** [4] 264–70 (1973).

[3]B. K. Atkinson, "Technical Note," *Int. J. Rock Mech. Miner. Sci. Geomech. Abstr.*, **16**, 49–53 (1979).

[4]S. Timoshenko and J. N. Goodier, *Theory of Elasticity*, 2d ed.; p. 277. McGraw-Hill, New York, 1951.

[5]G. G. Trantina, "Stress Analysis of the Double-Torsion Specimen," *J. Am. Ceram. Soc.*, **60** [7–8] 338–41 (1977).

[6]B. J. Pletka, E. R. Fuller Jr., and B. G. Koepke, "An Evaluation of Double-Torsion Testing—Experimental"; pp. 19–37 in *Fracture Mechanics Applied to Brittle Materials*, ASTM STP 678. American Society for Testing and Materials, Philadelphia, PA, 1979.

[7]D. K. Shetty and A. V. Virkar, "Determination of the Useful Range of Crack Length in Double-Torsion Specimens," *J. Am. Ceram. Soc.*, **61** [1–2] 93–94 (1978).

[8]E. R. Fuller Jr., "An Evaluation of Double-Torsion Testing—Analysis"; see Ref. 6, pp. 3–18.

[9]M. Ciccotti, G. Gonzato, and F. Mulargia, "The Double-Torsion Loading Configuration for Fracture Propagation: Improvement of the Methodology for the Load-Relaxation at Constant Displacement," *Int. J. Rock Mech. Min. Sci.*, in press. □

PERGAMON

International Journal of Rock Mechanics & Mining Sciences 37 (2000) 1103–1113

International Journal of
Rock Mechanics
and Mining Sciences

www.elsevier.com/locate/ijrmms

# The double torsion loading configuration for fracture propagation: an improved methodology for the load-relaxation at constant displacement

M. Ciccotti*, G. Gonzato, F. Mulargia

*Dipartimento di Fisica, Settore di Geofisica, Università di Bologna, Viale Berti Pichat 8, 40127, Bologna, Italy*

Accepted 27 June 2000

**Abstract**

For most materials the dynamics of subcritical crack propagation during stress-corrosion can be described uniquely by a relationship between the mode-I stress intensity factor $K_I$ and the crack velocity $v$ that generally has the form of a power law. In last 30 years, the double-torsion load-relaxation test has shown to be the most reliable method for measuring such a relation. The standard analysis, developed by Evans (J Mater Sci 1972;7:1137–46), is based on an analytical approxatimation that fails to accurately describe the specimen compliance outside a narrow region in the center of the specimen. This paper deals with the implications on data inversion of the exhaustive three-dimensional finite-element analysis recently performed by Ciccotti (J Am Ceram Soc 2000, in press) on double-torsion specimens. The results are presented in terms of corrective coefficients to the classical analytical approximation. A full methodology is developed for the numerical implementation of such corrections. By numerically simulating some relaxation tests, the classical analysis based on the analytical approximation is shown to generally underestimate the stress-corrosion index up to 30% even if the most conservative operational constraints are satisfied. On the contrary, the operational constraints can be comfortably relaxed as a consequence of the capability of correcting the finite size effects in relation to the different experimental parameters. 

## 1. Introduction

For most materials the dynamics of subcritical crack propagation during stress-corrosion can be described uniquely by a relationship between the mode-I stress intensity factor $K_I$ and the crack velocity $v$ that generally has the form of a power law [1]:

$$v = AK_I^n \tag{1}$$

with parameters $A$ and $n$ (the latter called the stress-corrosion index) depending on the materials properties and on environmental conditions.

In last 30 years, the double-torsion load-relaxation method has been widely used as the most reliable method for measuring subcrtitical crack growth curves ($v-K_I$) owing to the great stability of the four-point bending loading configuration and since it does not require the difficult monitoring of the crack length during the test.

A typical double-torsion (hereafter referred to as $DT$) specimen is shown in Fig. 1(a). According to Williams and Evans [4], $K_I$ is evaluated by

$$K_I = \sqrt{EG} = Pw_m\sqrt{\frac{(1+v)}{\eta W d^3 d_n}}, \tag{2}$$

where $E$ is the Young modulus, $G$ the strain-energy release rate, $P$ the applied load, $w_m$ the moment arm of the torsion, $v$ the Poisson's ratio, $W$ the specimen width, $d$ the specimen thickness, $d_n$ the thickness of the specimen along the groove (see Fig. 1(b)), and $\eta$ a corrective factor depending on the ratio $W/d$ [5] (Evans [1] assumes $\eta = 1/3$ for thin specimens).

The crack velocity $v$ is obtained using the load relaxation data together with a single measure of the initial or final crack length, provided that this is "far" from the ends of the specimen [4]:

$$v = -\phi a_{i,f} P_{i,f} \frac{1}{P^2}\frac{dP}{dt}, \tag{3}$$

*Corresponding author. Tel.: +390-51-20-95001; fax: +390-51-20-95058.

*E-mail address:* matteo@ibogfs.df.unibo.it (M. Ciccotti).

1365-1609/00/$ - see front matter 
PII: S1365-1609(00)00045-9

where $t$ is time, $a$ the crack length (measured on the opening side of the specimen, starting from the loading points), and the subfixes i and f denote reference measurements taken at the beginning or at the end of the run. The factor $\phi = d_n/\sqrt{\Delta a^2 + d_n^2}$ was introduced by Evans [1] to take the inclination of the crack front into account (Fig. 1(c)). An improved calculation of $\phi$ can be found in [6].

This approach has been followed by several authors, but the measurements of the $v-K_I$ curves, even if measured in the same laboratory, are unavoidably marred by considerable scatter [7,8]. The reason for this variability is the heterogeneity of the rock samples combined with the sensitivity to environmental conditions and with the difficulty and cost of preparing specimens with low geometrical tolerances. In the present work, we will show that a substantial part of the scatter among different measurements is due to Evans' model not describing the effective deformation of a realistic $DT$ specimen with sufficient accuracy.

The analytical approximation proposed by Evans was based on the following assumptions: the $DT$ specimen is a symmetrical system of two independent plates, each of which subjected to simple torsion, with length equal to the crack length. The part of the specimen beyond the fracture tip is considered undeformed. The compression induced by torsion at the contact zone of the two plates on the upper face is ignored. Moreover, the presence of the side-groove, the effect of its shape, and the presence of the initial notch are ignored as well. Finally, the effect of the inclination of the crack front is only taken into account for what concerns the crack velocity, but not for $G$.

Some aspects of the problem have already been discussed in the literature [9–12]. Experiments carried out by Shetty and Virkar [13] showed that Eq. (2) overestimates $K_I$ for short crack lengths, and underestimates it for long crack lengths. The same authors proposed the definition of an operational range for crack length, as the range in which the deviations of $K_I$ from the value calculated through Eq. (2) were within 5%. Another inference on the acceptable operational range was obtained through a finite-element analysis of a $DT$ specimen with an inclined crack front by Trantina [14], who nevertheless left unexplored the influence of the side groove, of its geometry and of the initial notch.

Ciccotti [2] investigated the importance of all these factors in an exhaustive three-dimensional finite-element analysis of the problem, and calculated the corrective coefficients to be applied to Evans' equation for $G$, as a function of the combination of each parameter with crack length and specimen dimensions. The finite-element mesh was made of about 500 quadratic brick elements, and represented a realistic specimen with side-groove, initial notch, and curved crack-front (see Fig. 2).

The aim of the present study is to define a new methodology for the analysis of the double-torsion load-relaxation constant-displacement tests, based on the use of the corrective coefficients obtained by the finite-element analysis. For a given specimen geometry, the corrective coefficients are dependent on the crack length, and therefore they are not constant during the relaxation test. As a consequence, the estimation of $K_I$ must be corrected during the test and, since the inversion of the crack velocity $v$ is affected in a non-linear way, the $v-K_I$

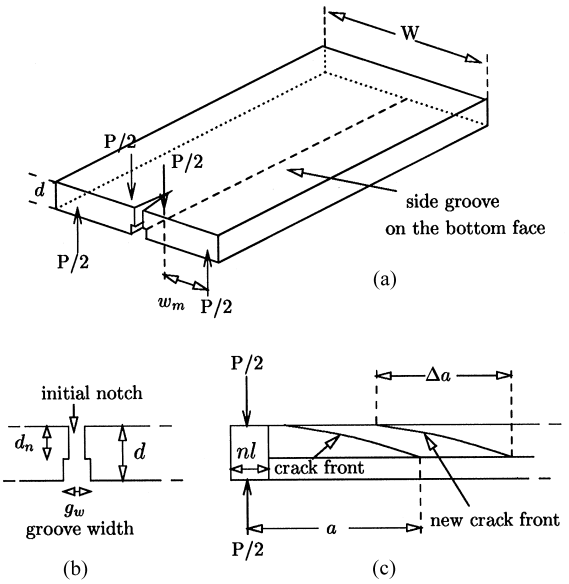


Fig. 1. The sketch of a double-torsion specimen: (a) general view, (b) axial cross-section, (c) longitudinal cross-section (modified after Atkinson [3]).

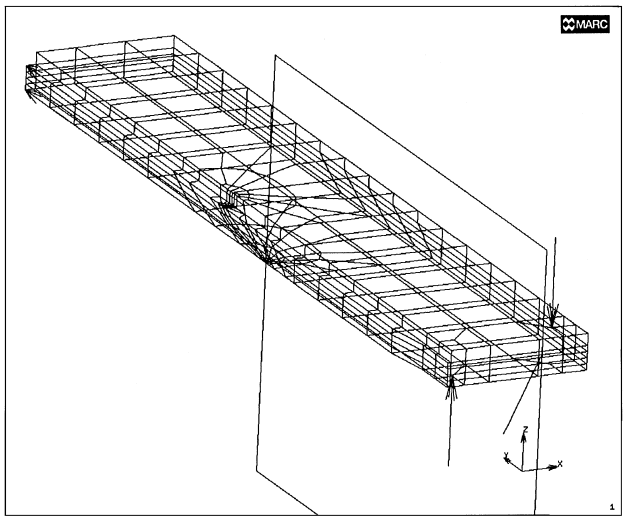


Fig. 2. The finite-element mesh. The model represents one half of a $DT$ specimen. The remaining part is replaced by symmetry conditions and by a contact surface in the ruptured interface. The side-groove and initial notch are reproduced. The crack front is curved as observed in the experiments.

curve and the stress-corrosion index result to be significantly altered.

## 2. Corrective factors $\xi$ and $\psi$

Evans' model leads to a linear dependence of the compliance on the crack length $a$:

$$C = \frac{y}{P} = \frac{w_m^2 a}{\eta W d^3 \mu} = Ba, \tag{4}$$

where $y$ is the constant displacement imposed at the loading points. Experimental compliance-calibrations [1] lead to a more general affine relation $C = Ba + D$. Since $G$ is related to the first derivative of the compliance,

$$G = -\left(\frac{\mathrm{d}U}{\mathrm{d}A}\right)_y = \frac{P^2}{2d_n}\frac{\mathrm{d}C}{\mathrm{d}a} \tag{5}$$

it appears to be independent of the crack length.

The finite-element analyses of Trantina [7] and Ciccotti [2] showed that the dependence of $C$ on the crack length contains some weak nonlinear terms, hardly appreciable through experimental compliance-calibrations, which nevertheless produce significant variations in the first derivative, making $G$ dependent on the crack length.

In order to account for such non-linear terms, a corrective factor $\xi$ dependent on the crack length $a$ has been introduced in Evans' equation for the compliance

$$C(a) = \frac{y}{P} = \xi(a)Ba = \xi(a)C^{\mathrm{E}}(a), \tag{6}$$

where the superscript E stands for "Evans' model" and $B$ is the proportionality constant of Eq. (4). Taking the first derivative of Eq. (6), another corrective coefficient $\psi$ is obtained that has to be applied to Evans' equation for the constant-displacement $G$,

$$G_y(a,P) = (\xi(a) + a\frac{\mathrm{d}\xi(a)}{\mathrm{d}a})G_y^{\mathrm{E}}(P) = \psi(a)G_y^{\mathrm{E}}(P). \tag{7}$$

The finite-element analysis produced the values of $\xi$ and $\psi$ calculated for five different crack lengths for each set of geometric parameters of the specimens. The values of the $\xi$ coefficients are reported here in Tables 1–4. The values of $\psi$ were already reported in [2], where the discussion was focused on the corrections to $G$.

The corrective coefficients for specimens with length $L = 17$ cm and width $W = 6$ cm were reported in Figs. 3 and 4 as an example. The shape of the function $\psi(a)$ is characterized by a positive trend with a flatter region in the center of the specimen, and strong deviations moving towards the ends. The scatter introduced by the dependence on the geometric parameters is considerable.

The overall behavior of the corrective functions can be understood as follows. Using the two independent torsion bars model, the compliance falls linearly to zero together with the length $a$ of the bars. In real specimens with short cracks, the deformation also affects the region beyond the crack, so that the compliance is larger and its slope is lower. As a consequence, when the crack length approaches zero, $\xi$ increases and diverges to infinity and $\psi$ decreases towards zero. When the crack approaches the end of the specimen, the unfractured portion becomes very weak, so that the compliance increases faster than predicted by Evans' equation, and diverges when the crack reaches the end (i.e., when the specimen fails). As a consequence, both $\xi$ and $\psi$ diverge to infinity for $a \to L$.

## 3. New equations for $K_I$ and $v$

We will now discuss how the introduction of crack-length dependent corrective factors affects the estimates of $K_I$ and $v$. As far as $K_I$ is concerned, the square root of the corrective coefficients $\psi$ should be used (see Eq. (2)):

$$K_I(a,P) = \sqrt{\psi(a)}K_I^{\mathrm{E}}(P). \tag{8}$$

The calculation of the crack velocity is based on the derivation of the crack length $a(t)$, which is inverted from the load relaxation curve $P(t)$, through the constant displacement condition. Differentiation of Eq. (6) for constant displacement leads to

$$\left(\frac{\mathrm{d}a}{\mathrm{d}t}\right)_y = -\frac{\xi(a)}{\psi(a)}\frac{a}{P}\frac{\mathrm{d}P}{\mathrm{d}t}, \tag{9}$$

where $P(t)$ is the measured relaxation load, and $a(t)$ has to be inverted from $P(t)$ using the relation

$$y = C(a(t))P(t) = C(a_{\mathrm{i,f}})P_{\mathrm{i,f}}, \tag{10}$$

where $y$ is the constant displacement, and the subfixes i or f again denote a reference measurement taken at the beginning or at the end of the test. Thus,

$$a(t) = C^{-1}\left(\frac{C(a_{\mathrm{i,f}})P_{\mathrm{i,f}}}{P(t)}\right). \tag{11}$$

Substituting Eq. (11) into Eq. (9) and multiplying by the appropriate factor $\phi$ we obtain

$$v = \phi\left(\frac{\mathrm{d}a}{\mathrm{d}t}\right)_y = -\phi\,\frac{\xi(a_{\mathrm{i,f}})}{\psi\left(C^{-1}\left(\frac{C(a_{\mathrm{i,f}})\cdot P_{\mathrm{i,f}}}{P}\right)\right)}\frac{a_{\mathrm{i,f}}P_{\mathrm{i,f}}}{P^2}\frac{\mathrm{d}P}{\mathrm{d}t}. \tag{12}$$

Eq. (11) also has to be substituted into Eq. (8) to calculate $K_I$ as a function of time, and thus produce the subcritical crack-growth curve $v-K_I$.

The above corrections affect both $K_I$ and $v$ in a non-linear way which changes the overall shape of the logarithmic $v-K_I$ curve, both in its location and slope. The corrections reduce $K_I$ in the first part of the test, when it is larger, and increase it when it is lower, thus resulting in a rise in the slope, i.e., the stress-corrosion index $n$, in agreement with [13]. Note that the correction

Table 1
The corrective factors $\xi$ for specimens of length $L = 17$ cm and width $W = 6$ cm; $d$ the specimen thickness, $d_n$ is the thickness along the groove, $g_w$ is the groove width in mm, $nl$ is the notch length in cm, $c = \Delta a/d_n$ is the inclination of the crack front. Some data missing because the curved crack front would cross the initial notch

| $d_n/d$ | $g_w$ | $nl$ | $c$ | $a = 4.5$cm | $a = 6.5$ cm | $a = 8.5$ cm | $a = 10.5$ cm | $a = 12.5$ cm |
|---|---|---|---|---|---|---|---|---|
| 1 | 0 | 0 | 0 | 1.101 | 1.057 | 1.036 | 1.023 | 1.018 |
| 1 | 0 | 0 | 2 | 0.892 | 0.902 | 0.916 | 0.925 | 0.936 |
| 1 | 0 | 0 | 4 | 0.752 | 0.787 | 0.827 | 0.853 | 0.875 |
| 2/3 | 2 | 0 | 0 | 1.221 | 1.141 | 1.100 | 1.077 | 1.069 |
| 2/3 | 2 | 0 | 2 | 1.156 | 1.095 | 1.065 | 1.047 | 1.042 |
| 2/3 | 2 | 0 | 4 | 1.081 | 1.042 | 1.024 | 1.014 | 1.013 |
| 2/3 | 4 | 0 | 0 | 1.285 | 1.192 | 1.145 | 1.118 | 1.110 |
| 2/3 | 4 | 0 | 2 | 1.215 | 1.143 | 1.107 | 1.087 | 1.082 |
| 2/3 | 4 | 0 | 4 | 1.134 | 1.085 | 1.062 | 1.050 | 1.049 |
| 1/2 | 2 | 0 | 0 | 1.395 | 1.267 | 1.198 | 1.159 | 1.150 |
| 1/2 | 2 | 0 | 2 | 1.354 | 1.238 | 1.175 | 1.141 | 1.132 |
| 1/2 | 2 | 0 | 4 | 1.304 | 1.202 | 1.148 | 1.118 | 1.111 |
| 1/2 | 4 | 0 | 0 | 1.513 | 1.365 | 1.282 | 1.238 | 1.233 |
| 1/2 | 4 | 0 | 2 | 1.471 | 1.334 | 1.258 | 1.218 | 1.213 |
| 1/2 | 4 | 0 | 4 | 1.412 | 1.292 | 1.226 | 1.191 | 1.186 |
| 1 | 0 | 2 | 0 | 1.111 | 1.063 | 1.040 | 1.026 | 1.021 |
| 1 | 0 | 2 | 2 | — | 0.907 | 0.920 | 0.929 | 0.939 |
| 1 | 0 | 2 | 4 | — | 0.793 | 0.831 | 0.856 | 0.877 |
| 2/3 | 2 | 2 | 0 | 1.224 | 1.143 | 1.101 | 1.077 | 1.070 |
| 2/3 | 2 | 2 | 2 | 1.159 | 1.096 | 1.066 | 1.048 | 1.043 |
| 2/3 | 2 | 2 | 4 | 1.086 | 1.043 | 1.025 | 1.015 | 1.013 |
| 2/3 | 4 | 2 | 0 | 1.290 | 1.195 | 1.147 | 1.119 | 1.112 |
| 2/3 | 4 | 2 | 2 | 1.221 | 1.146 | 1.109 | 1.088 | 1.083 |
| 2/3 | 4 | 2 | 4 | 1.142 | 1.088 | 1.065 | 1.052 | 1.050 |
| 1/2 | 2 | 2 | 0 | 1.397 | 1.268 | 1.199 | 1.160 | 1.151 |
| 1/2 | 2 | 2 | 2 | 1.356 | 1.239 | 1.176 | 1.141 | 1.133 |
| 1/2 | 2 | 2 | 4 | 1.306 | 1.203 | 1.148 | 1.118 | 1.111 |
| 1/2 | 4 | 2 | 0 | 1.516 | 1.366 | 1.283 | 1.239 | 1.233 |
| 1/2 | 4 | 2 | 2 | 1.474 | 1.335 | 1.259 | 1.219 | 1.213 |
| 1/2 | 4 | 2 | 4 | 1.416 | 1.293 | 1.227 | 1.191 | 1.187 |

on the crack velocity $v$ also affects the slope through the $\psi$ coefficient in Eq. (12), which increases with $a$ during the test. As a result, initial large velocities are increased and final low velocities are decreased, so that the slope $n$ is further increased. The practical importance of the corrections to be applied to the stress-corrosion index $n$ will be discussed in the following.

## 4. Numerical implementation

For each set of geometrical parameters, the finite-element analysis produced a set of five corrective coefficients $\xi$ for the compliance and five coefficients $\psi$ for its derivative, relative to different crack lengths.

The first operation is to determine a set of coefficients for the geometry of the specific specimen used in the test. In other words, the specimen geometry has to be interpolated from the set of tabulated geometries. Linear interpolation is generally adequate, except for the effect of specimen length which requires a scaling of the crack length.

The scaling of the crack lengths corresponding to the five corrective coefficients can only be effected for specimens with the same ratio $d : W : L$ explored here. Extrapolations far from such ratios would require further numerical analysis. Note that the scaling also affects the length of the notch and the position of the loading points, which has to be taken as a new reference for the measurement of the crack length.

Table 2
The corrective factors $\xi$ for specimens of length $L = 17$ cm and width $W = 10$ cm

| $d_n/d$ | $g_w$ | $nl$ | $c$ | $a = 4.5$ cm | $a = 6.5$ cm | $a = 8.5$ cm | $a = 10.5$ cm | $a = 12.5$ cm |
|---|---|---|---|---|---|---|---|---|
| 1 | 0 | 0 | 0 | 1.085 | 1.037 | 1.020 | 1.016 | 1.034 |
| 1 | 0 | 0 | 2 | 0.764 | 0.783 | 0.819 | 0.850 | 0.891 |
| 1 | 0 | 0 | 4 | 0.615 | 0.659 | 0.719 | 0.767 | 0.815 |
| 2/3 | 2 | 0 | 0 | 1.223 | 1.135 | 1.098 | 1.086 | 1.108 |
| 2/3 | 2 | 0 | 2 | 1.103 | 1.048 | 1.029 | 1.029 | 1.054 |
| 2/3 | 2 | 0 | 4 | 1.010 | 0.979 | 0.975 | 0.983 | 1.012 |
| 2/3 | 4 | 0 | 0 | 1.289 | 1.186 | 1.142 | 1.128 | 1.154 |
| 2/3 | 4 | 0 | 2 | 1.166 | 1.096 | 1.071 | 1.068 | 1.098 |
| 2/3 | 4 | 0 | 4 | 1.067 | 1.023 | 1.013 | 1.020 | 1.052 |
| 1/2 | 2 | 0 | 0 | 1.456 | 1.305 | 1.235 | 1.210 | 1.238 |
| 1/2 | 2 | 0 | 2 | 1.381 | 1.251 | 1.192 | 1.173 | 1.202 |
| 1/2 | 2 | 0 | 4 | 1.313 | 1.201 | 1.153 | 1.140 | 1.169 |
| 1/2 | 4 | 0 | 0 | 1.595 | 1.414 | 1.330 | 1.303 | 1.343 |
| 1/2 | 4 | 0 | 2 | 1.518 | 1.358 | 1.285 | 1.265 | 1.305 |
| 1/2 | 4 | 0 | 4 | 1.442 | 1.301 | 1.240 | 1.225 | 1.265 |
| 1 | 0 | 2 | 0 | 1.101 | 1.042 | 1.022 | 1.018 | 1.035 |
| 1 | 0 | 2 | 2 | — | 0.788 | 0.822 | 0.853 | 0.892 |
| 1 | 0 | 2 | 4 | — | 0.665 | 0.723 | 0.769 | 0.817 |
| 2/3 | 2 | 2 | 0 | 1.232 | 1.137 | 1.099 | 1.087 | 1.108 |
| 2/3 | 2 | 2 | 2 | 1.113 | 1.051 | 1.030 | 1.029 | 1.055 |
| 2/3 | 2 | 2 | 4 | 1.021 | 0.982 | 0.976 | 0.983 | 1.012 |
| 2/3 | 4 | 2 | 0 | 1.301 | 1.189 | 1.143 | 1.129 | 1.154 |
| 2/3 | 4 | 2 | 2 | 1.178 | 1.100 | 1.072 | 1.069 | 1.099 |
| 2/3 | 4 | 2 | 4 | 1.082 | 1.027 | 1.015 | 1.021 | 1.053 |
| 1/2 | 2 | 2 | 0 | 1.461 | 1.306 | 1.235 | 1.210 | 1.239 |
| 1/2 | 2 | 2 | 2 | 1.387 | 1.252 | 1.192 | 1.174 | 1.203 |
| 1/2 | 2 | 2 | 4 | 1.320 | 1.203 | 1.153 | 1.140 | 1.170 |
| 1/2 | 4 | 2 | 0 | 1.602 | 1.415 | 1.330 | 1.303 | 1.344 |
| 1/2 | 4 | 2 | 2 | 1.526 | 1.359 | 1.286 | 1.265 | 1.305 |
| 1/2 | 4 | 2 | 4 | 1.451 | 1.304 | 1.241 | 1.226 | 1.265 |

Provided that the notch extends towards the center of the specimen past the loading points, the external part of the specimen does not affect the strain energy. As a consequence, the part of the notch that should be compared among different specimens is the one exceeding the position of the loading points. For example, if the notch is 2 cm long and the loading points are 0.5 cm from the end of the specimen, the effective length is 1.5 cm.

In Tables 1–4 some coefficients are missing. These correspond to the shortest crack length of notched specimens without groove, for which the meshes could not be drown since the large horizontal extension of the curved crack front would make it intrude in the initial notch. But these missing coefficients are necessary for the interpolation process, and their values were estimated by combining the coefficients relative to the corresponding unnotched specimens together with the weak effect of the presence of the notch observed on specimens with deeper grooves. The results are reported in Table 5.

The maximum crack front inclination in our numerical analysis was $c = \Delta a/d_n = 4$ due to the limitations in the skewness of the elements, necessary to perform an accurate numerical analysis. Even though the typical front inclination is $c = 5$ [1], the use of the finite-element analysis with $c = 4$ is recommended in order to guarantee reliable solutions.

Through interpolation among the lines of coefficients reported in the tables, we have now determined the set of five $\psi$ and $\xi$ values for the appropriate specimen geometry along with the five corresponding values of the crack length. Since the crack propagates during the experiment, both coefficients should be fitted with smooth functions of the crack length.

Table 3
The corrective factors $\xi$ for specimens of length $L = 25\,\text{cm}$ and width $W = 6\,\text{cm}$

| $d_n/d$ | $g_w$ | $nl$ | $c$ | $a = 5.5\,\text{cm}$ | $a = 8.5\,\text{cm}$ | $a = 12.5\,\text{cm}$ | $a = 16.5\,\text{cm}$ | 20.5cm |
|---|---|---|---|---|---|---|---|---|
| 1 | 0 | 0 | 0 | 1.075 | 1.036 | 1.014 | 1.003 | 0.998 |
| 1 | 0 | 0 | 2 | 0.894 | 0.915 | 0.932 | 0.940 | 0.948 |
| 1 | 0 | 0 | 4 | 0.763 | 0.827 | 0.871 | 0.894 | 0.911 |
| 2/3 | 2 | 0 | 0 | 1.173 | 1.100 | 1.057 | 1.036 | 1.029 |
| 2/3 | 2 | 0 | 2 | 1.119 | 1.064 | 1.033 | 1.017 | 1.013 |
| 2/3 | 2 | 0 | 4 | 1.056 | 1.024 | 1.005 | 0.996 | 0.995 |
| 2/3 | 4 | 0 | 0 | 1.230 | 1.144 | 1.094 | 1.069 | 1.063 |
| 2/3 | 4 | 0 | 2 | 1.172 | 1.106 | 1.069 | 1.050 | 1.045 |
| 2/3 | 4 | 0 | 4 | 1.104 | 1.062 | 1.039 | 1.027 | 1.025 |
| 1/2 | 2 | 0 | 0 | 1.321 | 1.196 | 1.123 | 1.087 | 1.079 |
| 1/2 | 2 | 0 | 2 | 1.287 | 1.174 | 1.108 | 1.075 | 1.069 |
| 1/2 | 2 | 0 | 4 | 1.244 | 1.146 | 1.089 | 1.061 | 1.055 |
| 1/2 | 4 | 0 | 0 | 1.429 | 1.278 | 1.189 | 1.145 | 1.142 |
| 1/2 | 4 | 0 | 2 | 1.393 | 1.254 | 1.173 | 1.133 | 1.130 |
| 1/2 | 4 | 0 | 4 | 1.343 | 1.222 | 1.151 | 1.116 | 1.113 |
| 1 | 0 | 2 | 0 | 1.081 | 1.040 | 1.016 | 1.005 | 1.000 |
| 1 | 0 | 2 | 2 | — | 0.919 | 0.934 | 0.942 | 0.950 |
| 1 | 0 | 2 | 4 | — | 0.831 | 0.873 | 0.896 | 0.912 |
| 2/3 | 2 | 2 | 0 | 1.175 | 1.101 | 1.058 | 1.036 | 1.030 |
| 2/3 | 2 | 2 | 2 | 1.121 | 1.065 | 1.034 | 1.018 | 1.013 |
| 2/3 | 2 | 2 | 4 | 1.059 | 1.025 | 1.006 | 0.997 | 0.995 |
| 2/3 | 4 | 2 | 0 | 1.233 | 1.146 | 1.096 | 1.070 | 1.064 |
| 2/3 | 4 | 2 | 2 | 1.175 | 1.109 | 1.070 | 1.051 | 1.046 |
| 2/3 | 4 | 2 | 4 | 1.108 | 1.064 | 1.040 | 1.028 | 1.026 |
| 1/2 | 2 | 2 | 0 | 1.322 | 1.197 | 1.124 | 1.087 | 1.080 |
| 1/2 | 2 | 2 | 2 | 1.288 | 1.174 | 1.109 | 1.075 | 1.069 |
| 1/2 | 2 | 2 | 4 | 1.245 | 1.147 | 1.090 | 1.061 | 1.056 |
| 1/2 | 4 | 2 | 0 | 1.431 | 1.279 | 1.190 | 1.146 | 1.142 |
| 1/2 | 4 | 2 | 2 | 1.395 | 1.255 | 1.174 | 1.134 | 1.131 |
| 1/2 | 4 | 2 | 4 | 1.345 | 1.223 | 1.152 | 1.117 | 1.114 |

An appropriate choice for smoothing the corrective factors $\psi(a)$ appears to be a least-squares third-degree polynomial fit. The corrective coefficients $\xi$ are best approximated by fitting the normalized compliance $C(a)/B = \xi(a)a$ first. This can be done integrating the polynomial which fits $\psi$ and choosing the constant to match the central coefficient. In this way, approximation inaccuracies below 1% on both coefficients can be obtained. Nevertheless, such a choice may sometimes produce appreciable errors on the values of $\xi$, especially at small or large crack lengths. If this is the case, a second-order polynomial fit for the normalized compliance will produce more accurate results. Any extrapolation out of the range explored by the present analysis is not recommended.

The interpolating function for the compliance has to be used together with the measurement of the initial or final reference point $a_{i,f}$, $P_{i,f}$, to invert the evolution of the crack length $a(t)$ from the relaxation data $P(t)$, using Eq. (10).

Finally, the corrected values of $K_I$ and $v$ during the relaxation test are calculated, and the complete $v-K_I$ curve is obtained. Then, the data related to region III should be isolated, and the stress-corrosion index $n$ can be calculated by a least-squares linear fit.

## 5. Operational geometric constraints

The non-constancy of $K_I$ along the specimen was already pointed out in the literature [13,14], a problem which was practically tackled by assuming an operational range for the crack length in which the classical Evans' analysis could be used. The operational range

Table 4
The corrective factors $\xi$ for specimens of length $L = 25$ cm and width $W = 10$ cm

| $d_n/d$ | $g_w$ | $nl$ | $c$ | $a = 5.5$ cm | $a = 8.5$ cm | $a = 12.5$ cm | $a = 16.5$ cm | 20.5 cm |
|---|---|---|---|---|---|---|---|---|
| 1 | 0 | 0 | 0 | 1.054 | 1.018 | 1.002 | 0.996 | 1.010 |
| 1 | 0 | 0 | 2 | 0.765 | 0.815 | 0.861 | 0.889 | 0.922 |
| 1 | 0 | 0 | 4 | 0.626 | 0.717 | 0.791 | 0.835 | 0.875 |
| 2/3 | 2 | 0 | 0 | 1.168 | 1.093 | 1.054 | 1.036 | 1.055 |
| 2/3 | 2 | 0 | 2 | 1.067 | 1.025 | 1.007 | 1.000 | 1.022 |
| 2/3 | 2 | 0 | 4 | 0.987 | 0.971 | 0.970 | 0.972 | 0.996 |
| 2/3 | 4 | 0 | 0 | 1.225 | 1.134 | 1.086 | 1.065 | 1.087 |
| 2/3 | 4 | 0 | 2 | 1.120 | 1.064 | 1.038 | 1.028 | 1.054 |
| 2/3 | 4 | 0 | 4 | 1.036 | 1.007 | 0.998 | 0.998 | 1.025 |
| 1/2 | 2 | 0 | 0 | 1.362 | 1.221 | 1.142 | 1.107 | 1.135 |
| 1/2 | 2 | 0 | 2 | 1.300 | 1.179 | 1.113 | 1.085 | 1.114 |
| 1/2 | 2 | 0 | 4 | 1.242 | 1.140 | 1.087 | 1.065 | 1.093 |
| 1/2 | 4 | 0 | 0 | 1.479 | 1.304 | 1.205 | 1.165 | 1.206 |
| 1/2 | 4 | 0 | 2 | 1.414 | 1.260 | 1.175 | 1.142 | 1.184 |
| 1/2 | 4 | 0 | 4 | 1.350 | 1.217 | 1.146 | 1.119 | 1.158 |
| 1 | 0 | 2 | 0 | 1.063 | 1.020 | 1.004 | 0.997 | 1.010 |
| 1 | 0 | 2 | 2 | — | 0.818 | 0.863 | 0.890 | 0.923 |
| 1 | 0 | 2 | 4 | — | 0.722 | 0.793 | 0.837 | 0.876 |
| 2/3 | 2 | 2 | 0 | 1.173 | 1.094 | 1.054 | 1.036 | 1.055 |
| 2/3 | 2 | 2 | 2 | 1.072 | 1.026 | 1.007 | 1.001 | 1.022 |
| 2/3 | 2 | 2 | 4 | 0.993 | 0.972 | 0.970 | 0.972 | 0.996 |
| 2/3 | 4 | 2 | 0 | 1.230 | 1.136 | 1.087 | 1.065 | 1.088 |
| 2/3 | 4 | 2 | 2 | 1.127 | 1.066 | 1.038 | 1.028 | 1.054 |
| 2/3 | 4 | 2 | 4 | 1.044 | 1.009 | 0.999 | 0.998 | 1.026 |
| 1/2 | 2 | 2 | 0 | 1.365 | 1.221 | 1.142 | 1.108 | 1.135 |
| 1/2 | 2 | 2 | 2 | 1.303 | 1.179 | 1.113 | 1.085 | 1.114 |
| 1/2 | 2 | 2 | 4 | 1.246 | 1.141 | 1.087 | 1.065 | 1.093 |
| 1/2 | 4 | 2 | 0 | 1.483 | 1.304 | 1.206 | 1.165 | 1.206 |
| 1/2 | 4 | 2 | 2 | 1.418 | 1.261 | 1.176 | 1.142 | 1.184 |
| 1/2 | 4 | 2 | 4 | 1.354 | 1.218 | 1.146 | 1.119 | 1.158 |

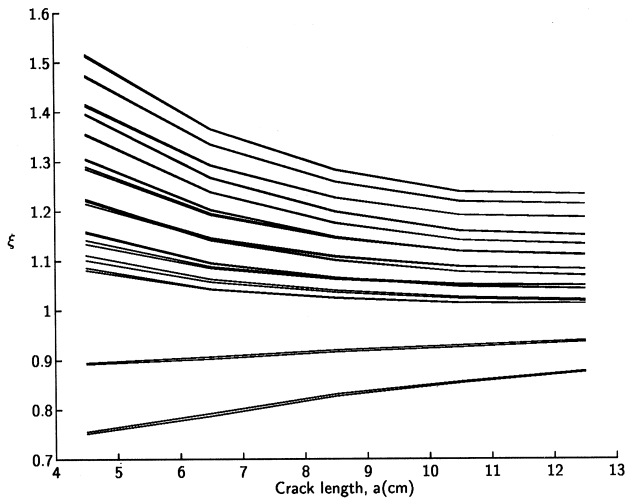


Fig. 3. The corrective coefficients of $\xi$ for specimens with length $L = 17$ cm and width $W = 6$ cm. The different curves represent all combinations of the other geometric parameters.

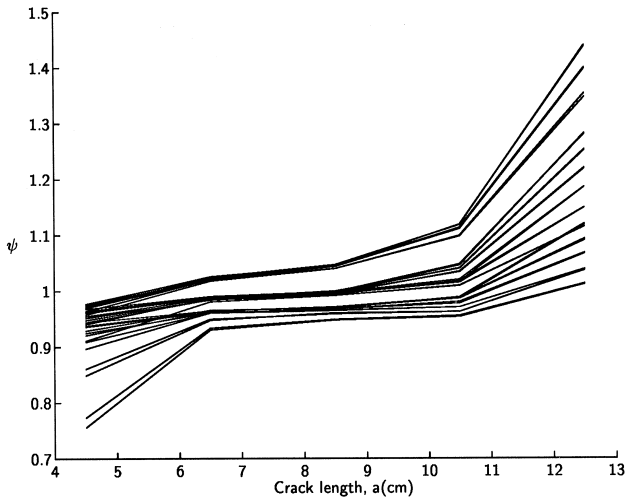


Fig. 4. The corrective coefficients of $\psi$ for specimens with length $L = 17$ cm and width $W = 6$ cm. The different curves represent all combinations of the other geometric parameters.

Table 5
The corrective coefficients $\xi$ and $\psi$ reported here were estimated to fill the gaps in Tables 1–4 in the present paper and in Tables 1–4 in [2], where the corrective coefficients $\psi$ are reported

| $L$ (cm) | 17 | 17 | 17 | 17 | 25 | 25 | 25 | 25 |
|---|---|---|---|---|---|---|---|---|
| $W$ (cm) | 6 | 6 | 10 | 10 | 6 | 6 | 10 | 10 |
| $c$ | 2 | 4 | 2 | 4 | 2 | 4 | 2 | 4 |
| $\xi$ | 0.895 | 0.756 | 0.772 | 0.624 | 0.896 | 0.765 | 0.769 | 0.631 |
| $\psi$ | 0.849 | 0.756 | 0.657 | 0.520 | 0.920 | 0.890 | 0.825 | 0.755 |

Table 6
The crack length operational range defined as the region in which the variations of $K_I$ with respect to the center of the specimen are within 5%. The symbols are the same as in Table 1. The specimen thickness is $d=7$ mm, and the crack front inclination is $c=4$ for all specimens

| $L$ | $W$ | $d_n/d$ | $g_w$ | $nl$ | $\frac{a_{min}}{W}$ | $\frac{(L-a_{max})}{W}$ |
|---|---|---|---|---|---|---|
| 17 | 6 | 1 | 0 | 0 | 0.89 | 0.66 |
| 17 | 6 | 2/3 | 2 | 0 | 0.57 | 0.76 |
| 17 | 6 | 2/3 | 4 | 0 | 0.58 | 0.80 |
| 17 | 6 | 1/2 | 2 | 0 | 0.59 | 0.95 |
| 17 | 6 | 1/2 | 4 | 0 | 0.69 | 1.01 |
| 17 | 6 | 1 | 0 | 2 | 0.91 | 0.66 |
| 17 | 6 | 2/3 | 2 | 2 | 0.69 | 0.75 |
| 17 | 6 | 2/3 | 4 | 2 | 0.71 | 0.80 |
| 17 | 6 | 1/2 | 2 | 2 | 0.62 | 0.95 |
| 17 | 6 | 1/2 | 4 | 2 | 0.70 | 1.01 |
| 17 | 10 | 1 | 0 | 0 | 0.61 | 0.54 |
| 17 | 10 | 2/3 | 2 | 0 | 0.47 | 0.64 |
| 17 | 10 | 2/3 | 4 | 0 | 0.48 | 0.66 |
| 17 | 10 | 1/2 | 2 | 0 | 0.49 | 0.69 |
| 17 | 10 | 1/2 | 4 | 0 | 0.54 | 0.72 |
| 17 | 10 | 1 | 0 | 2 | 0.62 | 0.53 |
| 17 | 10 | 2/3 | 2 | 2 | 0.52 | 0.64 |
| 17 | 10 | 2/3 | 4 | 2 | 0.54 | 0.66 |
| 17 | 10 | 1/2 | 2 | 2 | 0.54 | 0.69 |
| 17 | 10 | 1/2 | 4 | 2 | 0.59 | 0.72 |
| 25 | 6 | 1 | 0 | 0 | 0.77 | 0.59 |
| 25 | 6 | 2/3 | 2 | 0 | 0.33 | 0.77 |
| 25 | 6 | 2/3 | 4 | 0 | 0.39 | 0.90 |
| 25 | 6 | 1/2 | 2 | 0 | 0.45 | 1.12 |
| 25 | 6 | 1/2 | 4 | 0 | 0.52 | 1.23 |
| 25 | 6 | 1 | 0 | 2 | 0.77 | 0.58 |
| 25 | 6 | 2/3 | 2 | 2 | 0.39 | 0.78 |
| 25 | 6 | 2/3 | 4 | 2 | 0.45 | 0.88 |
| 25 | 6 | 1/2 | 2 | 2 | 0.48 | 1.11 |
| 25 | 6 | 1/2 | 4 | 2 | 0.53 | 1.23 |
| 25 | 10 | 1 | 0 | 0 | 0.60 | 0.63 |
| 25 | 10 | 2/3 | 2 | 0 | 0.44 | 0.76 |
| 25 | 10 | 2/3 | 4 | 0 | 0.45 | 0.79 |
| 25 | 10 | 1/2 | 2 | 0 | 0.43 | 0.86 |
| 25 | 10 | 1/2 | 4 | 0 | 0.44 | 0.91 |
| 25 | 10 | 1 | 0 | 2 | 0.64 | 0.63 |
| 25 | 10 | 2/3 | 2 | 2 | 0.48 | 0.76 |
| 25 | 10 | 2/3 | 4 | 2 | 0.49 | 0.78 |
| 25 | 10 | 1/2 | 2 | 2 | 0.47 | 0.85 |
| 25 | 10 | 1/2 | 4 | 2 | 0.48 | 0.90 |

was defined as the one in which $K_I$ remained constant within 5%.

According to the above constraint, the experimental study of Shetty and Virkar [13] determined as operational the following ranges of crack lengths:

$0.50W<a<L-1.00W$ for $d:W:L=1:31.25:75$,

$0.40W<a<L-0.80W$ for $d:W:L=1:50:75$.

The finite-element study of Trantina [14] determined the range:

$0.55W<a<L-0.65W$ for $d:W:L=1:10:20$.

The present numerical study allows a detailed and comprehensive analysis of the dependence of the operational range on the geometrical properties of the specimen (see Table 6). A general dependence on the $d:W:L$ ratio may be observed. At the same time, the depth and width of the groove are also important, while the presence of the initial notch has lesser effects. Only the ranges relative to the skewest crack fronts ($c=4$) have been reported because they are the only one close to the real shapes.

The range determined by Trantina was calculated for model specimens with a weak front inclination $c=1.7$ and should be compared with the ranges $0.50W<a<L-0.68W$ and $0.76W<a<L-0.70W$ obtained in the present study, respectively, for $c=0$ and 2 relative to specimens without notch and groove and with a $d:W:L$ ratio of $1:8.6:24.3$. The comparison can only be partial since the $d:W:L$ ratios are not coincident and the position of the loading points was presumably taken at the end of the specimen in Trantina's simulation. A detailed comparison with the ranges determined by Shetty and Virkar [13] is also impossible since their specimens are thinner than the ones considered here.

## 6. The "true" value of the stress-corrosion index

In order to investigate the effect of neglecting the use of the corrective coefficients, as it happened so far in all analyses, some relaxation experiments have been simulated numerically. A theoretical stress-corrosion $v-K_I$ curve was assumed with the form of a power law, as in Eq. (1), with the values of the parameters $n=40$ and $A=10^{-3}\,\mathrm{ms}^{-1}$ chosen as in typical igneous rocks [7].

Two specimens were simulated with geometries chosen in the explored set of parameters and the corresponding corrective curves were interpolated as described above. The first simulated specimen, 'Specimen 1', had geometrical parameters $L=17$ cm, $W=10$ cm, $d=7$ mm, $d_n/d=1/2$, groove width $g_w=2$ mm (see Fig. 1), notch length $nl=2$ cm, and crack front inclination $c=4$. The second simulated specimen, 'Specimen 2', had parameters $L=25$ cm,

$W = 10\,\text{cm}$, $d = 7\,\text{mm}$, $d_n/d = 1$, $g_w = 0\,\text{mm}$, $nl = 2\,\text{cm}$, and $c = 4$.

The third-order polynomials fitting the coefficients $\psi$ for the two specimens were, respectively,

$$\psi(a) = 4.504 \times 10^{-4}a^3 - 1.690 \times 10^{-2}a^2 + 2.094 \times 10^{-1}a + 3.990 \times 10^{-2} \quad (13)$$

and

$$\psi(a) = 3.219 \times 10^{-3}a^3 - 6.977 \times 10^{-2}a^2 + 5.274 \times 10^{-1}a - 3.988 \times 10^{-1}. \quad (14)$$

The interpolating functions for the $\xi$ coefficients were determined by interpolating the normalized compliance $C(a)/B = \xi(a)a$ with a second-order polynomial fit, and then dividing it by $a$. Respectively

$$\xi(a) = 5.991 \times 10^{-3}a + 8.100 \times 10^{-1} - 1.168\frac{1}{a}, \quad (15)$$

$$\xi(a) = 3.106 \times 10^{-2}a + 5.480 \times 10^{-1} + 2.881\frac{1}{a}. \quad (16)$$

The corrective functions of $K_I$ for the two specimen geometries are plotted in Figs. 5 and 6. The operational ranges are indicated in these figures, together with the ranges explored by our finite-element study.

Several relaxations were simulated, using an initial load $P = 100$ kg and different values of the initial crack length (reported in Table 7).

The scheme of the simulation was as follows:

(a) use Eq. (8) to derive $K_I$ from the initial load $P$, using the corrective coefficient $\psi$ calculated on the initial crack length;
(b) use the theoretical relation Eq. (1) to obtain the crack velocity $v$;

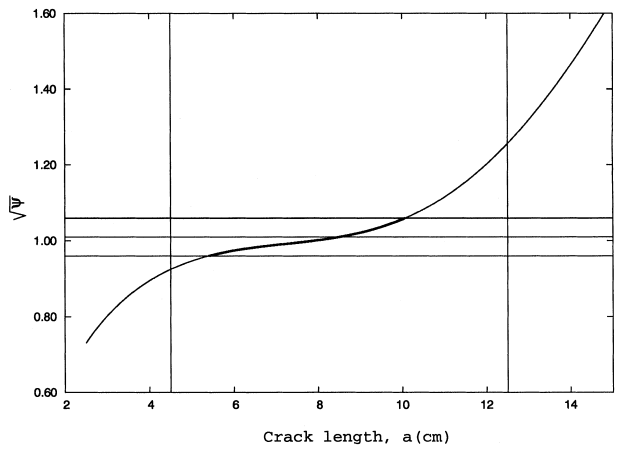


Fig. 5. The corrective function for $K_I$ for the geometry called 'Specimen 1' ($L = 17\,\text{cm}$, $W = 10\,\text{cm}$, $d = 7\,\text{mm}$, $d_n/d = 1/2$, $g_w = 2\,\text{mm}$, $nl = 2\,\text{cm}$, $c = 4$). The vertical lines delimit the range explored in the present analysis. The horizontal lines define the operational range in which $K_I$ is constant within 5% (thick line).

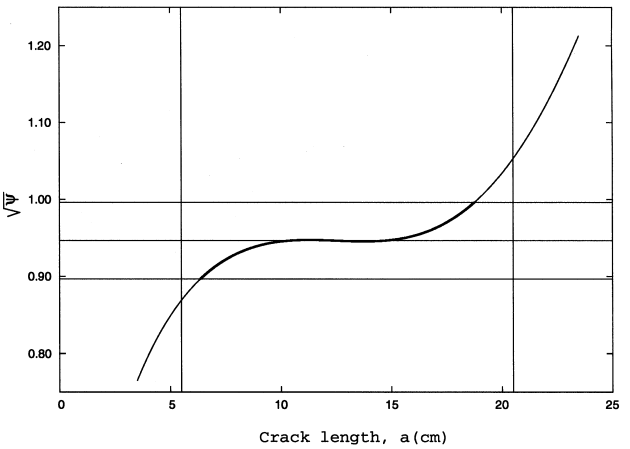


Fig. 6. The corrective function for $K_I$ for the geometry called 'Specimen 2' ($L = 25\,\text{cm}$, $W = 10\,\text{cm}$, $d = 7\,\text{mm}$, $d_n/d = 1$, $g_w = 0\,\text{mm}$, $nl = 2\,\text{cm}$, $c = 4$). The vertical lines delimit the range explored in the present analysis. The horizontal lines define the operational range where $K_I$ is constant within 5% (thick line).

Table 7
The power law parameters obtained by linear fit of the $v-K_I$ curves in Figs. 3 and 4. The geometrical parameters of Specimen 1 were $L = 17\,\text{cm}$, $W = 10\,\text{cm}$, $d = 7\,\text{mm}$, $d_n/d = 1/2$, $g_w = 2\,\text{mm}$, $nl = 2\,\text{cm}$, $c = 4$. Specimen 2 had $L = 25\,\text{cm}$, $W = 10\,\text{cm}$, $d = 7\,\text{mm}$, $d_n/d = 1$, $g_w = 0\,\text{mm}$, $nl = 2\,\text{cm}$, $c = 4$. The initial and final crack lengths for each test were reported and a symbol 'v' was marked in last column if the whole relaxation took place inside the range in which $K_I$ is constant within 5%

| Specimen 1 | $a_i$ (cm) | $a_f$ (cm) | $n$ | log $A$ | Match |
|---|---|---|---|---|---|
| Real parameters | | | 40.0 | −3 | |
| Operational range | 5.4 | 10.1 | | | |
| Explored range | 4.5 | 12.5 | | | |
| Estimated parameters | 4.5 | 5.1 | 25.8 | −4.5 | x |
| | 5.4 | 6.2 | 32.3 | −3.8 | v |
| | 6.0 | 7.0 | 34.5 | −3.6 | v |
| | 7.0 | 8.1 | 35.1 | −3.3 | v |
| | 8.0 | 9.4 | 31.3 | −3.1 | v |
| | 8.4 | 10.0 | 28.3 | −3.0 | v |
| | 9.0 | 11.3 | 20.9 | −2.8 | x |
| | 9.3 | 12.4 | 14.4 | −2.8 | x |
| Specimen 2 | | | | | |
| Real parameters | | | 40.0 | −3 | |
| Operational range | 6.4 | 18.8 | | | |
| Explored range | 5.5 | 20.5 | | | |
| Estimated parameters | 5.5 | 5.6 | 33.2 | −5.3 | x |
| | 6.0 | 6.2 | 33.8 | −5.0 | x |
| | 6.4 | 6.6 | 34.3 | −4.8 | v |
| | 7.0 | 7.3 | 35.1 | −4.5 | v |
| | 8.0 | 8.5 | 36.5 | −4.2 | v |
| | 9.0 | 9.6 | 37.9 | −4.0 | v |
| | 10.0 | 10.7 | 39.0 | −3.9 | v |
| | 11.0 | 11.7 | 39.9 | −3.9 | v |
| | 12.0 | 12.7 | 40.3 | −3.9 | v |
| | 13.0 | 13.8 | 40.1 | −3.9 | v |
| | 14.0 | 14.8 | 39.1 | −3.9 | v |
| | 15.0 | 15.9 | 37.1 | −3.9 | v |
| | 16.0 | 17.1 | 33.8 | −3.8 | v |
| | 17.1 | 18.6 | 28.5 | −3.6 | v |
| | 18.1 | 20.4 | 21.2 | −3.3 | x |

(c) increment of the crack length about $da = v\mathrm{d}t$ where $\mathrm{d}t$ is the time step of the simulation;
(d) calculate the new load corresponding to the new crack length using Eq. (10);
(e) repeat from (a) using the new values of load and crack length.

Each simulation was iterated for a total time of 100 s. The relaxation curves obtained were then analyzed with the classical Evans' method producing the $v-K_I$ curves reported in Figs. 7 and 8 together with the theoretical curve (thicker line). Substantial differences and a remarkable scatter are immediately apparent. Increasing the initial crack length, the location of the estimated curves moves progressively upwards in the bilogarithmic $v-K_I$ diagram. The shape of the curve gradually departs from linearity when the crack tip is near the borders of the explored range. In fact, in these regions the corrective coefficient $\psi$ is rapidly changing in a non-linear way as the crack length increases during the test. The slope of those curves is reduced proportionally to the local slope of the corrective curve $\psi(a)$. The values of the stress-corrosion index of such curves were calculated by a least-squares linear fit and the results are reported in Table 7. To test the stability of the results, the simulations were performed with two different time steps (0.5 and 0.1 s), and consistent results were obtained.

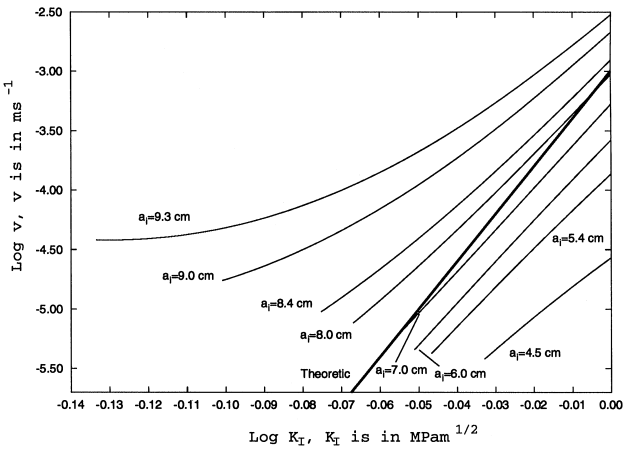


Fig. 7. The $v-K_I$ curves obtained by applying Evans' analysis to some relaxation experiments simulated with the aid of the corrective curves for the Specimen 1. The initial load is the same for all experiments, the different values of the initial crack length are indicated for each curve.

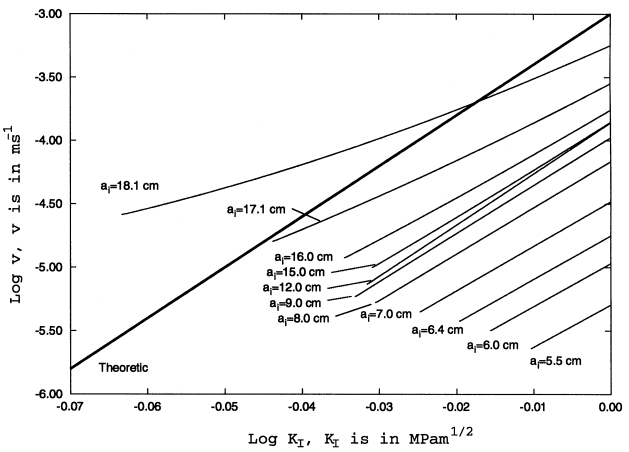


Fig. 8. The $v-K_I$ curves obtained by applying Evans' analysis to some relaxation experiments simulated with the aid of the corrective curves for the Specimen 2. The initial load is the same for all experiments, the different values of the initial crack length are indicated for each curve.

The simulations in which the initial and final crack lengths were both within the conservative operational range (in which $K_I$ is constant within 5%) are indicated with a symbol 'v' in Table 7. The first important result is that Evans' analysis underestimates the stress-corrosion index up to 30% even operating in this range. As a consequence, this definition of the operational range is insufficient for accurate estimates of the stress-corrosion index with the classical Evans' approach.

An attempt to salvage the classical Evans' approach could still be made by defining a new operational range in which the underestimate on $n$ itself is limited to 5%. Unfortunately, for Specimen 1, the smaller error obtained for $n$ is about 12%, making the definition of such a range impossible. As for Specimen 2, the errors on $n$ could be limited to 5% only if the whole relaxation were performed in a very narrow operational range of crack lengths (from 9 to 15 cm on a 25 cm long specimen, see Table 7). This constraint is a very strong one, since the attempts to produce an initial crack with a length in such a tight range would lead to discard most specimens. Moreover, the possibility of performing multiple relaxation tests on the same specimen would be considerably reduced.

On the contrary, by applying our corrective procedure there is no need to comply to such tight constraints, since the use of the corrective curves allows one to obtain accurate results working in a range that is much larger than the one required to obtain reliable estimates of $n$ by using the classical Evans' method. The range left unexplored by our finite-element analysis is just five centimeters from each end of the specimen, which, for example, implies operational crack lengths covering a comfortable 15 cm range on 25 cm-long specimens. Table 7 shows that in this interval the classical Evans' analysis would produce underestimates up to 65%.

## 7. Conclusions

The exhaustive finite-element analysis performed by Ciccotti [2] showed that Evans' analytical

approximation gives an unsatisfactory description of the double-torsion loading configuration, except in a very narrow region of crack propagation in very thin specimens. The relative corrective coefficients were calculated.

A full methodology has been presented here to apply these corrective coefficients to calculate the characteristic $v-K_I$ curve of subcritical crack growth. The most important effect of the corrective coefficients is that not only the location of the curves is changed, but also their shape, generally increasing the slope. In other words, substantial modifications are induced on the stress-corrosion index, which is the most interesting parameter of subcritical crack-growth under a physical modeling point of view.

According to two numerical experiments of load relaxation at constant displacement that we performed, the neglection of the corrective coefficients leads to underestimating the stress-corrosion index up to 30% even if the relaxation takes place in the classical "optimal" operational range of crack lengths, where the variations of $K_I$ do not exceed 5%. On the contrary, the use of the corrective coefficients allows one to obtain accurate estimates by using a wide range of specimen geometries and operational crack lengths. Furthermore, our corrective coefficients are based on a finite-element model which takes into account the influence of all the geometrical parameters of a real specimen, i.e., the presence of a side groove, its depth and width, the presence of an initial notch of given length, and the inclination of the curved crack front.

## References

[1] Evans AG. A method for evaluating the time-dependent failure characteristics of brittle materials — and its applications to polycrystalline alumina. J Mater Sci 1972;7:1137–46.
[2] Ciccotti M. A realistic finite-element model for the double torsion loading configuration. J Am Ceram Soc 2000, in press.
[3] Atkinson BK. Technical note. Int J Rock Mech Min Sci Geomech Abstr 1979;16:49–53.
[4] Williams DP, Evans AG. A simple method for studying slow crack growth. J Test Eval 1973;1:264–270.
[5] Timoshenko S, Goodier JN. Theory of elasticity, 2nd ed. New York: McGraw Hill, 1951. p. 277.
[6] Pollet JC, Burns SJ. Crack velocity correction factor for the crack-front shape in double-torsion specimens. J Am Ceram Soc 1979;62:426–7.
[7] Atkinson BK. Subcritical crack growth in geological materials. J Geophys Res 1984;89:4077–114.
[8] Swanson PL. Subcritical crack growth and other time- and environment-dependent behavior in crustal rocks. J Geophys Res 1984;89(B6):4137–52.
[9] Fuller Jr ER. An evaluation of double-torsion testing — analysis. In: Fracture mechanics applied to brittle materials, Vol. ASTM STP 678. American Society of Testing Materials, 1979. p. 3–18.
[10] Pletka BJ, Fuller Jr ER, Koepke BG. An evaluation of double-torsion testing — experimental. In: Fracture mechanics applied to brittle materials, Vol. ASTM STP 678. American Society of Testing Materials, 1979. p. 19–37.
[11] Virkar AV. Gordon RS. Crack front profiles in double-torsion specimens. J Am Ceram Soc 1975;58:536–7.
[12] Pabst RF, Weick J. Double torsion measurements with and without a guiding notch. J Mater Sci 1981;16:836–8.
[13] Shetty DK, Virkar AV. Determination of the useful range of crack length in double torsion specimens. J Am Ceram Soc 1978;61:93–4.
[14] Trantina GG. Stress analysis of the double torsion specimen. J Am Ceram Soc 1977;60:338–41.

## 2.2 Etude du processus de fracturation des roches sous l'action d'un taux de déformation très faible.

La propagation lente de fissures dans des matériaux fragiles et hétérogènes est accompagnée par un processus d'endommagement diffus dans une zone ('zone de process') entourant la pointe de fissure (Atkinson, 1987). Ce processus, constitué par la formation d'un nuage de micro-fissures en mode essentiellement ouvrant, suivi par l'avancement de la fissure principale à travers ce milieu endommagé, est responsable à la fois de la résistance élevée des roches à la fracture (en analogie à ce qui arrive dans les céramiques) et de la rugosité des surfaces de fracture.

Pour suivre le processus de rupture lente, j'ai mis au point un système de mesure des émissions ultrasoniques produites par les évènements de microfracture. Les émissions sont mesurées avec un système de 4 capteurs piézoélectriques (type Pinducer) et échantillonnés à une fréquence de 3 MHz. Un réseau neuronal a été développé par une étudiante en thèse (Silvia Castellaro, que j'ai co-encadré avec F. Mulargia) et ensuite entraîné pour reconnaître les vrais événements de microfracture.

La performance du système de reconnaissance et localisation est montré dans l'exemple de test montré en figure 2.2.1. Sur l'image de gauche on peut voir un échantillon de verre (longueur typique de 20 cm) sur lequel nous avons marqué quatre points cibles et deux parcours en couleur. Pour produire des émissions acoustiques localisées on a utilisé deux techniques : 1) nous avons brisé la pointe d'un crayon à mines sur les quatre points cibles ; 2) nous avons fait glisser un émetteur ultrasonique pulsé le long des parcours en couleur. Sur l'image de droite en figure 2.2.1 on peut voir les résultats du processus de localisation sur un rectangle représentant la forme de notre échantillon. La précision de la localisation est de l'ordre de 1 mm, ce qui est tout à fait satisfaisant.

a) 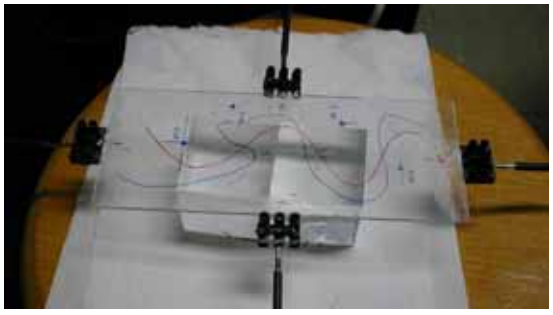 b) 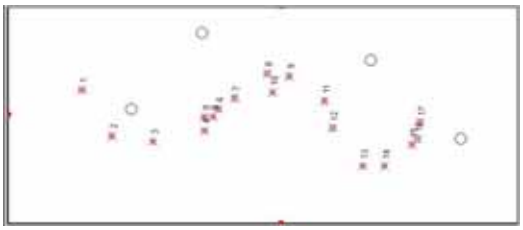

Figure 2.2.1 : a) Echantillon en verre utilisé pour tester le système de localisation des émissions acoustiques. Les points et le parcours cible pour la stimulation d'émissions acoustiques sont marqués en couleur. b) Résultats du processus de localisation des sources (en rond pour les quatre points cible, en croix pour le parcours rouge de la figure de gauche).

A toute autre échelle, un phénomène analogue est responsable des secousses sismiques qui précèdent souvent un gros tremblement de terre. L'étude des statistiques de distribution spatiale, temporelle et d'intensité des émissions acoustiques en laboratoire peut nous renseigner sur le processus sismique complexe, tout en restant dans des conditions bien définies et susceptibles d'être modélisées.

A présent, il reste une différence cruciale entre les expériences de rupture en laboratoire et le processus sismique dans la croûte terrestre. Celle-ci concerne le taux de

déformation en cause (de l'ordre de $10^{-15}$ $s^{-1}$ dans les zones sismiquement actives), qui au laboratoire dépasse encore de plusieurs ordres de grandeur. Pour pouvoir étudier l'influence de ce facteur, j'ai développé une nouvelle technique expérimentale qui permet de réduire le taux de déformation de deux ordres de grandeur par rapport aux techniques habituelles. La technique est basée sur la machine de Torsion Double décrite plus haut. La machine est équipée d'un moteur servo-contrôlé qui permet d'atteindre des taux de déformation de $10^{-8}$ $s^{-1}$. La nouvelle technique consiste en une première étape où l'échantillon est chargé avec le moteur près des conditions de travail. La seconde étape consiste à bloquer le moteur et à induire dans la cave thermostatée une diminution très lente de la température. Ceci a comme effet de produire une dilatation différentielle de la machine, construite avec deux différents alliages avec des coefficients de dilatation calibrés. De cette façon, nous sommes arrivés à obtenir un taux de déformation de l'ordre de $10^{-11}$ $s^{-1}$.

La fin des mon post-doc en Italie a coïncidé avec les premiers tests sur des échantillons de *Calcare Massiccio* (une des roches typiques de la zone focale pour la sismicité des Apennins en Italie) dans les conditions de chargement lent décrit ci-dessus. Ed figure 2.2.2 je reporte la distribution de l'énergie des évènements de microfracture (estimée à partir des signaux d'amplitude des émissions acoustiques en analogie à ce qu'on fait pour l'énergie des tremblements de terre). Les trois courbes représentent les estimations faites à partir de trois canaux d'acquisition différents et elles sont qualitativement en bon accord.

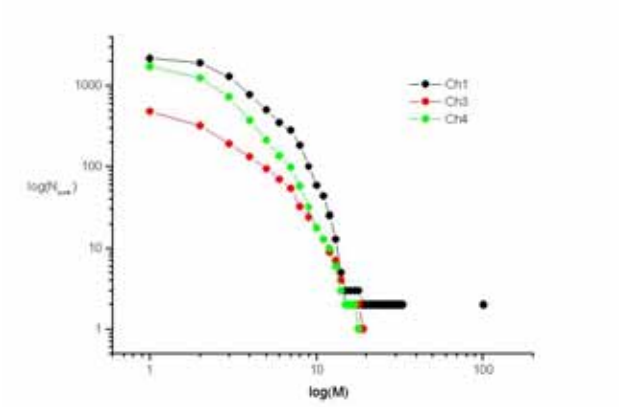


Figure 2.2.2 : Distribution de l'intensité d'énergie des émissions acoustiques dans un test de déformation lente d'un échantillon de *Calcare Massiccio.*

La précarité de ma situation dans la suite a rendu difficile d'obtenir un étudiant qui puisse démarrer une vraie campagne de mesures à l'Université de Bologne. Maintenant que mon activité à l'Université de Montpellier 2 est bien établie, je compte de pouvoir demander un étudiant de thèse en cotutelle avec mon directeur de thèse Francesco Mulargia. Dans les dernières années, d'autres travaux ont été effectues sur la distribution des émissions acoustiques lors de la rupture des matériaux hétérogènes (Dechanel, 2005 ; Dechanel *et al.*, 2006 ; Garcimartin *et al.*, 1997), mais je suis convaincu que ce montage accompli et originale mérite de vivre son épanouissement. En particulier, il sera porteur d'une compréhension sur les effets de la diminution progressive du taux de déformation et du changement de la taille de l'échantillon.

## 2.3 Etude de la différence entre les modules élastiques dynamiques et statiques des roches

Les modules élastiques des roches sont mesurés principalement par la méthode « statique » (basée sur la mesure des déformations induites par l'application d'une charge connue) ou « dynamique » (basée sur la mesure de la vitesse de propagation des ondes élastiques dans le matériau). En raison des phénomènes inélastiques et de l'hétérogénéité de ces matériaux, il n'est pas évident que ces deux valeurs soient les mêmes. Ceci est très important dans le cas des mesures des propriétés élastiques de la croûte terrestre, pour lesquelles souvent il n'existe que des mesures sismiques (dans le domaine de fréquence de 1 à 10 Hz).

Les roches étudiées sont des roches volcaniques provenant de l'Etna (Italie) pour leur importance dans la modélisation du volcan et le *Calcare Massiccio* dont on a parlé plus haut.

Les modules élastiques sont mesurés en fonction de la fréquence sur neuf ordres de grandeur, en utilisant trois différentes techniques standard : (a) le test de compression uniaxiale (dit 'statique', mais que l'on associera à une fréquence de 0.001 Hz à cause de sa durée de 20 minutes) ; (b) la mesure des oscillations forcées avec une machine Dual Cantilever (de 0.01 à 20 Hz) ; (c) la mesure de la vitesse des ondes ultrasoniques longitudinales et transversales (à 75 kHz et à 1 MHz). Les détails des techniques de mesure sont décrits in Ciccotti, Almagro *et al.*, 2004.

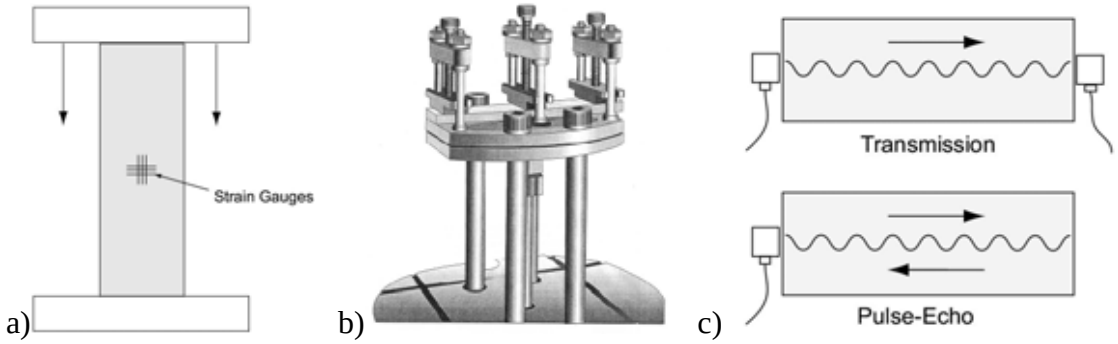


a) b) c)

Figure 2.3.1 Schéma de mesure des modules élastiques dans les domaines de fréquence a) faibles, b) intermédiaires et c) élevées.

Avant de discuter les résultas, il faut préciser que les trois techniques impliquent des déformations substantiellement différentes : de l'ordre respectivement de $10^{-3}$, $10^{-5}$ et $10^{-7}$. Tandis que les techniques dynamiques se sont montrées substantiellement indépendantes de l'amplitude de déformation, le test de compression uniaxiale peut révéler de fortes non-linéarités. Comme il est montré en figure 2.3.2, le *Calcare Massiccio* a montré un comportement assez linéaire et une rupture fragile soudaine. Au contraire, la roche volcanique provenant de l'Etna présente un comportement très dissipatif, et elle est capable d'accepter une déformation importante avant de se briser. Pour comparer le module élastique 'statique' avec les modules dynamiques il faut donc considérer la limite de faibles amplitudes, soit le 'module tangent' reporté en figure 2.3.3. Dans la même figure on reporte aussi la différence entre les modules statiques mesurés par la déformation moyenne (*average strain*) et par des jauges de contraintes disposées au milieu des faces (*strain gauges*). Cette différence, qui est souvent source d'ambiguïtés, est due à la non-uniformité

des contraintes en conséquence des conditions de non-glissement de l'échantillon contre les mors.

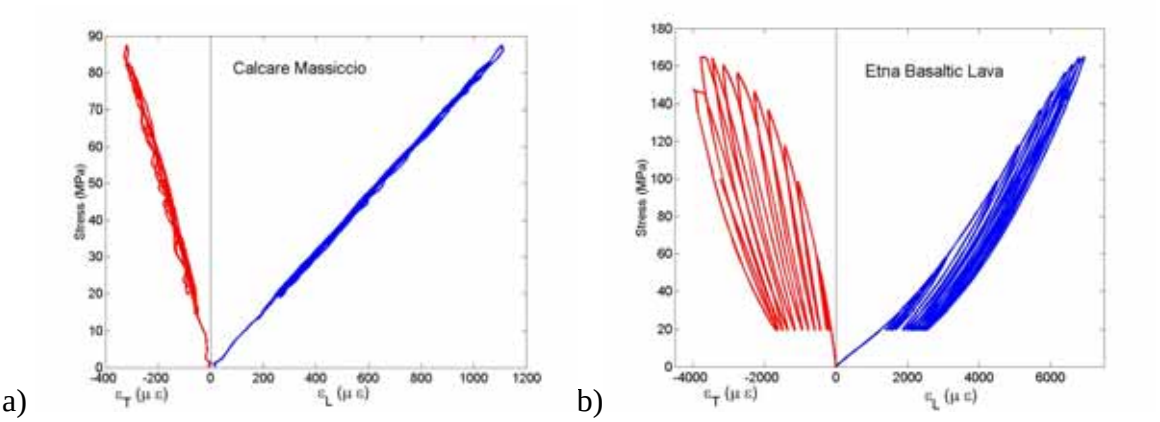


a) b)

Figure 2.3.2 Courbes de contrainte-déformation cycliques (longitudinale en bleu, transversale en rouge) pour a) le Calcare Massiccio et b) le basalte du Mont Etna.

Comme on peut voir en figure 2.3.3, la différence entre les modules statiques et dynamiques n'est pas significative pour le *Calcare Massiccio* (Ciccotti et Mulargia, 2004), mais elle est importante pour le basalte du Mont Etna, probablement à cause de la présence d'une plus forte porosité (8%) et de l'hétérogénéité de cette roche.

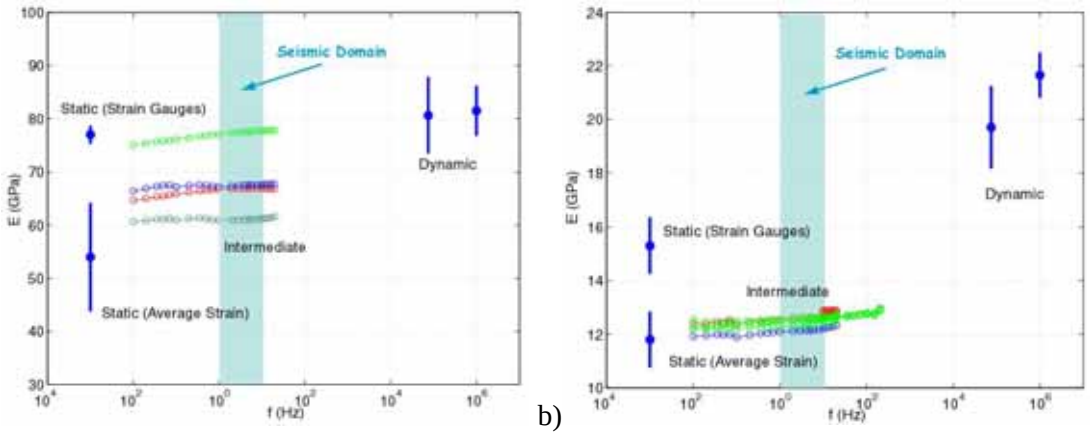


a) b)

Figure 2.3.3 Récapitulatif des résultats des mesures des modules élastiques en fonction de la fréquence de stimulation pour a) le *Calcare Massiccio* et b) le basalte du Mont Etna. La zone en bleu représente le domaine exploré par les ondes sismiques.

En tous cas, pour les deux roches on n'observe pas de dépendances significatives de la fréquence en dessous du domaine sismique, ce qui valide l'utilisation des modules sismiques pour la modélisation des déformations statiques de la croûte terrestre en l'absence d'endommagement des roches. Pour les modélisations sismiques et volcaniques qui comportent en générale des fortes déformations, il est recommandé de prendre en considération la mécaniques de l'endommagement pour rendre compte des variations de modules avec l'historique de la contrainte appliquée. En outre, nos mesures étant faites en absence de pression de confinement, elles sont plutôt adaptées pour des applications proches de la surface terrestre, telles que les modélisations en contexte volcanique.

## 2.4 Invariance d’échelle et biais dans l'analyse fractale des images naturelles

L’un des aspects intrigants des mécanismes naturels tels que la formation de failles dans la croûte terrestre est l’apparente absence d’une échelle caractéristique. Deux photos côte à côte d’un systèmes de failles dans la croûte terrestre et d’un réseau de fractures dans des roches sont difficilement discernables l’une de l’autre en l’absence d’un objet servant de référence de taille (qui est en conséquence toujours présent dans les photos des géologues). Cette invariance d’échelle, qui se manifeste dans la présence de lois de puissance (dites ‘fractales’ à cause des exposants fractionnaires qu’elles comportent) est ce qui justifie de pourvoir comprendre les mécanismes sismiques par des études en laboratoire.

Depuis la formalisation de la géométrie fractale par Mandelbrot dans les années 70, des évidences de fractales ont paru par centaines dans tous les domaines de la science, invoquant des lois d’invariance d’échelle pour tout expliquer. En opposition aux études théoriques basées sur la présence de limites asymptotiques, et aux études numériques qui peuvent simuler des fractales sur une gamme d’échelles très importante, les analyses des donnés empiriques (notamment des images naturelles), se sont toujours limitées à une gamme d’échelles restreinte, constituée la plupart du temps par une seule décade, voire deux. Dans ces conditions, l’analyse fractale est gravement affectée par plusieurs causes de biais qui sont souvent négligées (Gonzato *et al.*, 2000). Pour s’affranchir de certaines d’entre elles, on a développé le logiciel d’analyse VSBC2 (*ibid.*) disponible en ligne sur le serveur ftp://ibogeo.df.unibo.it/pub/vsbc.

Des études plus avancées m’ont ensuite amené à montrer que pour des types d'images tout à fait générales et pour plusieurs méthodes d'analyse, l’omniprésence de cutoffs physiques produit l'apparence de fausses fractales, si l'on se limite à vérifier la loi d’échelle sur un ou deux ordres de grandeur (Ciccotti et Mulargia, 2002, qui suit dans le texte). Ainsi la plupart des attributions de fractalité peuvent être remises en cause, avec les exceptions notables de quelques travaux qui ont en commun l’utilisation combinée de plusieurs techniques pour obtenir une résolution et une statistique suffisantes sur une gamme d’échelles significative. Parmi ces exemples les plus fondés concernent des grandeurs liées à la géophysiques, telles que la rugosité des surfaces de fracture (Bouchaud, 1997), la distribution des tailles de particules des sols (Wu *et al.*, 1993) et la distributions de l’intensité des tremblements de terre (Bak *et al.*, 2002). Ceci est un signe encourageant afin de continuer de comprendre la physique des tremblements de terres par des études en laboratoire.

# Pernicious effect of physical cutoffs in fractal analysis

M. Ciccotti* and F. Mulargia
*Settore di Geofisica, Dipartimento di Fisica, Università di Bologna, Viale Berti Pichat, 8 Bologna, Italy*
(Received 28 March 2001; revised manuscript received 6 September 2001; published 12 February 2002)

Fractal scaling appears ubiquitous, but the typical extension of the scaling range observed is just one to two decades. A recent study has shown that an apparent fractal scaling spanning a similar range can emerge from the randomness in dilute sets. We show that this occurs also in most kinds of nonfractal sets irrespective of defining the fractal dimension by box counting, minimal covering, the Minkowski sausage, Walker's ruler, or the correlation dimension. We trace this to the presence of physical cutoffs, which induce smooth changes in the scaling, and a bias over a couple of decades around some characteristic length. The latter affects also the practical measure of fractality of truly fractal objects. A defensive strategy against artifacts and bias consists in carefully identifying the cutoffs and a quick-and-dirty thumb rule requires to observe fractal scaling over at least three decades.

DOI: 10.1103/PhysRevE.65.037201 PACS number(s): 05.45.Df

## I. INTRODUCTION

The original definition of ''fractal'' is strictly related to the evaluation of the Hausdorff-Besicovitch dimension of a geometric set provided that this is not an integer. Since this definition is of difficult applicability, several alternative operational definitions are preferred, such as box counting, its mathematical twin the Minkowski sausage, and Walker's ruler.

The concept of ''fractals'' was then extended to include sets in which the number $N$ of objects of diameter up to $L$ scales as a power law with fractional exponent $D$. This definition disregards the location of the elements in the set and is not simply amenable to a geometric dimension. One more class of sets that has been included in the definition is the one in which the distribution of some more general property $P$ (such as the earthquake magnitude) scales as a power law with the fractional exponent, which disposes of any link with the geometry.

Considering the distribution of higher-order moments, the generalized fractal dimension $D_q$ is defined with $D_0$ the classical fractal dimension (capacity), $D_1$ being the information dimension and $D_2$ the correlation dimension. If these dimensions have different values, the set is called a ''multifractal.'' The evaluation of the correlation dimension $D_2$ is the scope of the Grassberger and Procaccia algorithm, which is commonly used to study the time or space distribution of point events and the ''strangeness'' of the attractors of chaotic orbits.

Although fractality ideally implies a power-law relation over an infinite range of scales, it is measured only over a very limited interval in most practical cases. Fractal analysis must face not only the two obvious cutoffs related to the limited resolution and extension of the images or data sets, but also other physical cutoffs linked to the measurement procedure or to the presence of characteristic lengths. All these cutoffs will be shown to have a critical importance in defining the fractal nature of the system.

*Email address: matteo@ibogeo.df.unibo.it

## II. PHYSICAL CUTOFFS AND THE DIMENSION OF EMPIRICAL SETS

The scope of this paper is limited to fractal analysis in relation to the geometric dimension, which considers sets of two main categories. The first one regards small unconnected objects, such as points, rods, spots, etc. Their fractal dimension (between 0 and the dimension of the embedding space) indicates clustering in their spatial distribution. Typical examples are earthquake epicentral maps, lake or mining resources maps, spatial distribution of pores or impurities, and time series. The second category regards connected sets and typical examples are topographic contours, piecewise linear patterns (such as geologic fault patterns), contour surfaces, or surface patterns in three-dimensional (3D) images, etc. The fractal dimensions of these categories are, respectively, greater than 1 and 2 and characterize the roughness and the branching complexity of the shapes.

The scaling behavior can be different over different ranges of scales. For example, a series of equispaced points on a line will scale with dimension zero at scales much smaller than the interpoint distance $\Delta$, and with dimension 1 (linelike) for scales much larger than this. If the points are substituted with rods of length $d$, three different scaling laws appear, since the set has again dimension 1 for scales much smaller than $d$. However, for the dimension zero to be well defined in the intermediate region, the distance between the two cutoffs must be sufficiently large. A set of balls of radius $R$ in a $N$-dimensional embedding space will always scale as $N$ dimensional for scales much smaller than $R$; information about the spatial distribution of balls would only emerge at somewhat larger scales. Similarly, in a set of small fractals of extension $R$ distributed in space following a different fractal distribution than their internal one, the fractal dimension of the objects will prevail for scales much smaller than $R$, while the fractal dimension of their spatial distribution will prevail for much larger ones. In general, stopping the generating process of a fractal set at some finite step in which the smallest details are segments of length $d$, dimension 1 would prevail. Contour lines and line networks always scale as one dimensional below the length of the smallest traced segment.

 

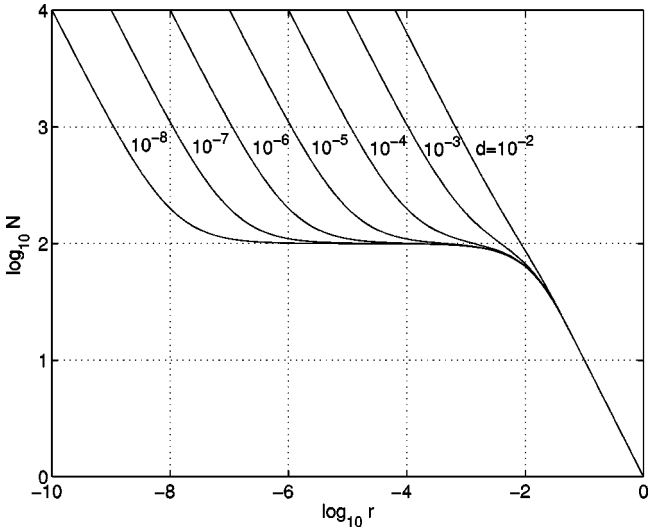


FIG. 1. Box counting $N(r)$ curves for random sets of $M=100$ rods for several values of the radius $d$. All lengths are normalized to the unit side of the analyzed sets.

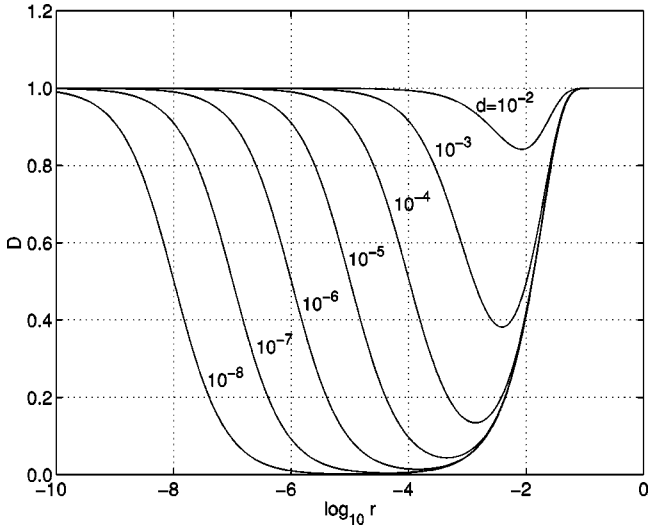


FIG. 2. Local box counting dimension $D(r)$ for the same sets as in Fig. 1.

At the same time, extending the analysis below the width of the traced lines, dimension 2 will prevail, while measuring the scaling much beyond the extension of the object will give dimension zero since this will appear isolated.

## III. FRACTAL ANALYSIS

### A. Several capacity dimensions

Since the original *capacity* or *minimal covering* fractal dimension is cumbersome and time consuming in more than one dimension [1], alternative definitions, more computationally efficient, were proposed. One of the most popular of these definitions is the *box counting* (BC). The covering is obtained by considering a uniform partition (generally dyadic) made of nonoverlapping boxes of radius $r$, and then counting the number of boxes $N(r)$ that have a nonempty intersection with the set. Automatization of BC requires the digitization of the sets, and the fractal dimension $D_{BC}$ is generally estimated through a least squares linear fit. Several traps are hidden in this apparently simple process, often leading to wrong dimension estimates [2,3].

A very similar method, called *Minkowski sausage* (MS), consists of taking a ball of radius $r$ around each point of the set and evaluating the volume $V(r)$ of the union of all balls. A fractal dimension $D_{MS}$ prevails at some range if the quantity $N(r)=V(r)/V_B(r)$ obeys a power law in that range ($V_B$ is the volume of each ball).

Hamburger *et al.* [4] derived an analytical calculation of the expected scaling curves $N(r)$ for a set of randomly distributed balls analyzed by BC and MS methods. Typical BC curves of $N(r)$ and local fractal dimension for 1D balls are reported in Figs. 1 and 2 for several values of the diameter $d$ of the balls. Examining these in terms of cutoffs, one sees that two of these are apparent, respectively, related to the diameter $d$ and to the average free distance $\Delta$. Dimension 1 prevails at scales external to these cutoffs, while dimension zero may only be established in the intermediate region if the distance between the cutoffs is larger than 3 decades. Otherwise, an apparent fractal dimension extending over a range up to 2 decades appears, with an apparent $d$ value changing progressively from zero to 1 as the density increases.

We analyzed several sets of points with normally distributed distances of fixed mean value $\Delta$ and different values of the standard deviation $\sigma$, ranging from zero (equispaced points) to $\Delta$ (see Figs. 3 and 4). The width of the corner region clearly increases with the dispersion of the interpoint distances, converging to the shape of the Poisson random distribution when $\sigma=\Delta$. We conclude that a width of 2 decades around the average distance cutoff is typical for objects distributed with a strong random component.

The shape of the transition around the lower cutoff is due to the redundancy of the box counting covering. As one can

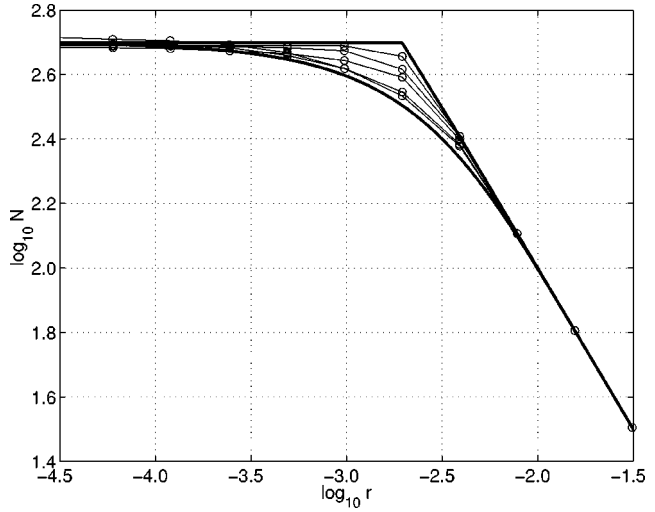


FIG. 3. Box counting $N(r)$ function for a set of 500 points with Gaussian interpoint distribution. Circled points correspond to a progressively increasing standard deviation $\sigma/\Delta=0.2,0.4,0.6,0.8,1$. The two thick curves correspond to equispaced and random placed points (Poisson).

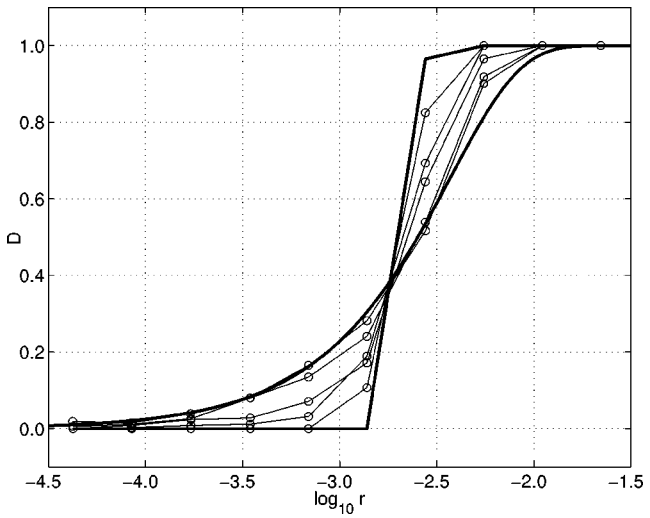


FIG. 4. Local box counting dimension $D(r)$ for the same sets as in Fig. 3.

observe in Fig. 5 the cutoff has substantially the same shape for a random set of 100 boxes of diameter $d=10^{-4}$ and for the same boxes distributed in an equispaced set. Analysis of the random set with the Bouligand minimal covering algorithm leads to a sharp cutoff (see Fig. 5). The redundancy of the BC covering depends on the random match between the uniform partition and the set points, but it is easy to show this to be statistically identical to that of the MS covering, which is simple to evaluate. The MS covered length for $N_r$ separated rods of diameter $d$ is

$$L(r)=N_r(d+r). \tag{3.1}$$

Dividing this expression by the diameter $r$ of the MS balls, one obtains the equivalent number of boxes to be compared with the BC curves in Fig. 5. It is immediate to see that the concavity of the cutoff has, again, a typical width of a couple of decades, which is simply due to the presence of an additive constant to the power law due to the change of scaling.

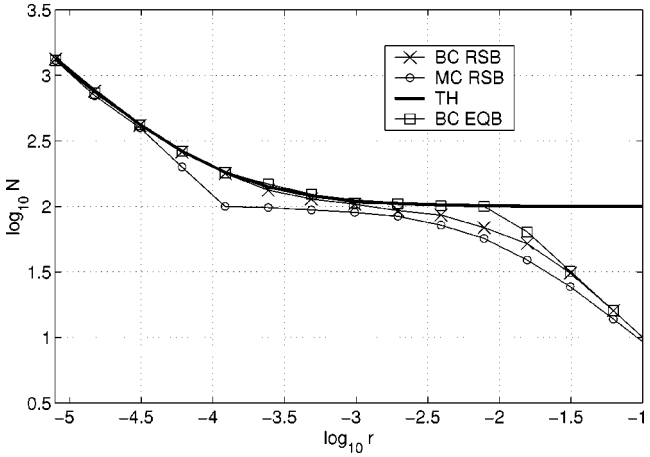


FIG. 5. Box counting (BC) and minimal covering (MC) $N(r)$ functions for 100 random (RSB) or equispaced (EQB) rods of length $\delta=10^{-4}$. The solid line represents the theoretical prediction of average redundancy.

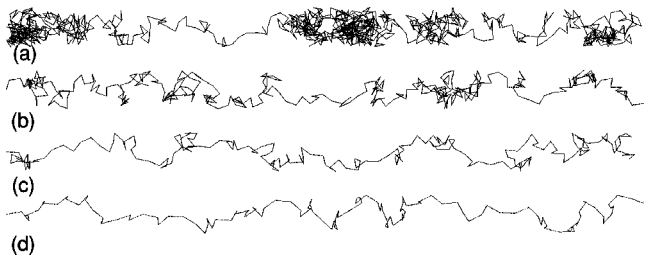


FIG. 6. Random walk drifted on a $2048\times128$ pixel stripe with velocities (a) $v=2$ pix/step, (b) $v=6$ pix/step, (c) $v=10$ pix/step, (d) $v=20$ pix/step.

### B. Walker's ruler dimension

Apparent fractality can also be shown to emerge as an artifact of cutoffs with the Walker's ruler (WR) dimension by analyzing a drifted random walk of given step $d$. The particle is forced to move in a narrow strip of width $w$ and drifted along the strip with a constant velocity $v$. Images of the resulting trace for several values of $v$ are shown in Fig. 6 and their WR analysis is shown in Fig. 7. The set behaves as a line for rulers either shorter than the step $d$ or longer than the width $w$ of the strip. The slope in the intermediate region takes the typical random walk value of 2 for slow drift velocity, but it takes apparent fractal values progressively decreasing from 2 to 1 as the drift velocity is increased with consequent disentanglement. This nonuniversal apparent fractal scaling spans again approximately one or two decades. BC analysis of the same pictures yields very similar results and provides an apparent counterproof to the artifact.

### C. The correlation dimension

The *correlation dimension* $D_2$ is estimated [5] as the slope of the log-log plot of $C(r)$,

$$C(r)=\lim_{N\to\infty}\frac{1}{N^2}\{\text{number of pairs } (i,j) \text{ with } |X_i-X_j|<r\}$$

$$\sim r^{D_2}. \tag{3.2}$$

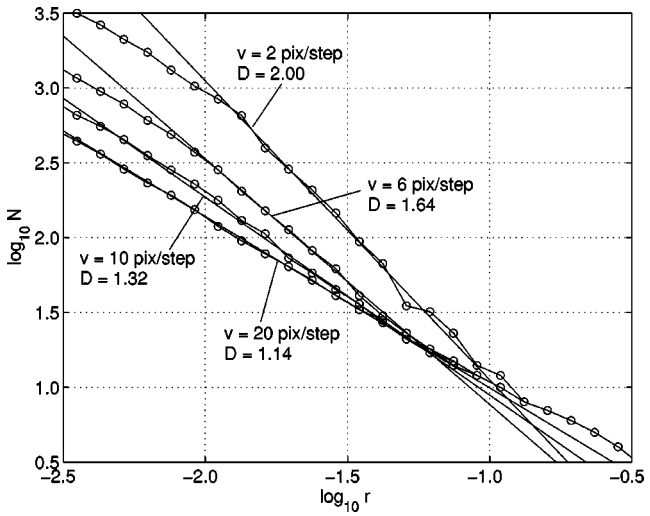


FIG. 7. Walker's ruler analysis of the curves of Fig. 6, along with the least squares fit of the linear regions.

Again, the presence of physical cutoffs in the data gives rise to smooth changes of scaling with the eventual emergence of apparent fractality. Kitoh *et al.* [6] showed that the cutoffs induce a concavity in their neighborhood due to the appearance of the additive constants to the power laws. This effect is identical to the one described in the BC section.

Several alternative estimators for the correlation dimensions were derived by Takens [7] and by Smith [8], mainly based on maximum likelihood. These statistical estimators are gathered by estimators of their variance, but they may prove to be inconsistent if physical cutoffs affect the scaling. Pisarenko *et al.* [9] proposed a method to estimate the presence of an upper cutoff in the power law, but the problem becomes very tricky if two cutoffs are present.

## IV. A STRATEGY OF DEFENSE AGAINST THE PERNICIOUS EFFECT OF PHYSICAL CUTOFFS

Since a modest difference between the values of cutoffs is typical, the emergence of an apparent fractal scaling extending over up to a couple of decades is expected to be a very common feature, which is independent of an effective fractal nature of the sets. This is valid for both connected and unconnected images and is irrespective of the definition of fractal dimension. As a consequence, serious doubts emerge on all empirical fractal claims—the vast majority in practice [10]—which do not span more than two decades.

The presence and the nature of the physical cutoffs is not generally known *a priori* for a given empirical image, but experience may provide great help. In an image constituted of spots, one should estimate the average diameter of the spots and the average distance among them. For line-based images, such as river patterns and fracture network, the minimal length free of intersections or sharp corners represents a lower cutoff, and one should observe whether there is some scale at which the set appears to uniformly cover the embedding space. If one identifies the nature and the value of the cutoffs, one can guess what the scaling curve will look like, and, if the difference between these cutoffs is insufficient, one can conclude that it is useless to estimate the fractal dimension since it would be both inaccurate and meaningless.

While this may require great care in future issues, as well as reassessment of published ones, a quick-and-dirty thumb rule caution against the effect of physical cutoffs is to ensure that each fractal estimate spans over at least three decades.

[1] K. Falconer, *Fractal Geometry* (Wiley, New York, 1990), Chap. 1.
[2] G. Gonzato, F. Mulargia, and W. Marzocchi, Geophys. J. Int. **132**, 275 (1998).
[3] G. Gonzato, F. Mulargia, and M. Ciccotti, Geophys. J. Int. **142**, 108 (2000).
[4] D. Hamburger, O. Biham, and D. Avnir, Phys. Rev. E **53**, 3342 (1996).
[5] P. Grassberger and I. Procaccia, Phys. Rev. Lett. **50**, 346 (1983).
[6] S. Kitoh, M. Kimura, K. Mori, K. Takezawa and S. Endo, Physica D **141**, 171 (2000).
[7] F. Takens, Lect. Notes Math. **1125**, 99 (1984).
[8] R.L. Smith, *Nonlinear Modeling and Forecasting. SFI Studies in the Sciences of Complexity*, edited by M. Casdagli and S. Eubank (Addison-Wesley, Reading, MA, 1992), Proc. Vol. XII.
[9] D.V. Pisarenko and V.F. Pisarenko, Phys. Lett. A **197**, 31 (1995).
[10] O. Malcai, D.A. Lidar, O. Biham and D. Avnir, Phys. Rev. E **56**, 2817 (1997).

## 2.5 Collaboration en tant qu'éditeur associé à l'écriture d'un livre résumant l'état d'avancement des connaissances dans la physique des tremblements de terre

Durant l'année 2000 j'ai participé avec mon directeur de thèse F. Mulargia à l'organisation d'un Advanced Research Workshop financé par l'OTAN (ARW2000: State of scientific knowledge regarding earthquake occurrence and implications for public policy. Le Dune, Piscinas - Arbus, Sardinia, Italy, October 15th - 19th, 2000) visant à établir l'état des connaissances sur la physique des tremblements de terre dans tous ses aspects et à fournir les indications sur les priorités dans la recherche à suivre au niveau mondial.

La suite de cette réflexion nous a conduit à la rédaction d'un livre scientifique :

Earthquake Science and Seismic Risk Reduction. NATO SCIENCE SERIES: IV: Earth and Environmental Sciences Volume 32. Edité par F. Mulargia et R. Geller. Kluwer. 2003.

qui comprend des contributions de premier niveau dans tous les aspects liés à la physique des tremblements de terre et à son impact sur la vie humaine. Nous n'avons pas fait une simple collection d'articles, mais un effort considérable afin de lui donner la structure d'un vrai livre qui puisse servir de référence actuelle dans le domaine. En particulier, je me suis chargé d'écrire plusieurs sections couvrant des sujets de caractère général non traités au cours du Workshop (voir CV).

## 2.6 Développement d'un nouveau modèle pour expliquer la physique des tremblements de terre

L'activité de rédaction du livre sus-mentionnée nous a amené à une profonde connaissance de la phénoménologie liée aux tremblements de terre et des problèmes ouverts, qui a crée les conditions propices à la phase finale de mon projet : tenter la formulation d'un modèle pour expliquer la physique des tremblements de terre.

Nous étions particulièrement étonnés qu'il n'y ait pas encore d'équation qui décrive l'énergie d'un tremblement de terre de façon satisfaisante, ce qui est normalement le premier pas dans le développement d'un modèle physique. Pour les tremblements de terre ceci est particulièrement difficile à cause de l'impossibilité d'un accès direct au phénomène et de la complexité de ses manifestations. Il existe des modèles satisfaisants pour ce qui concerne la radiation élastique en champ éloigné, mais qui n'arrivent pas à décrire les récurrences des évènements. La prévision des évènements individuels reste donc un but inaccessible. En outre, même le phénomène de base, soit le stick-slip de deux blocs de roches de la croûte terrestre, apparaît incompatible avec les mesures de flux de chaleur sur des systèmes de failles actifs, qui sont bien inférieures aux valeurs prévues (Ben-Zion, 2001).

On a développé un modèle qui propose une fonction approximée pour l'énergie d'un tremblement de terre, ne s'appuyant que sur l'analyse dimensionnelle et sur la constatation des différentes échelles de temps concernées (Mulargia *et al.*, 2004). Le modèle suppose l'autosimilarité du phénomène sur une gamme d'échelles comparable avec les observations et en conséquence il considère comme cellule de base un couple de blocs de 10 m d'arête.

Le modèle divise le processus sismique en trois phases. Dans la première phase un bloc élémentaire commence à glisser lentement avec un coefficient de frottement élevé typique, ce qui produit une augmentation rapide de la température sur la surface de faille. Dans la

deuxième phase, l'onde thermique produite se propage sur l'épaisseur de la zone de cisaillement dans un temps caractéristique de 100 s. En raison de la faiblesse de la perméabilité devant la conductibilité thermique, une augmentation de la pression de pore est induite, jusqu'à rejoindre la pression lithostatique. Ceci démarre la troisième phase, dans laquelle la faille glisse à une vitesse très élevée avec un coefficient de frottement presque nul, en convertissant la presque totalité de l'énergie en radiation élastique.

Comme le slip nécessaire pour démarrer la deuxième phase est très petit par rapport au slip de la troisième phase, le modèle explique le paradoxe du flux de chaleur. La taille globale du tremblement de terre est donnée par le nombre de cellules qui rentrent dans la phase 2 en même temps. Le modèle reconduit à la distribution de Gutenberg-Richter par des calculs statistiques. La petite valeur de la contrainte de déclenchement du modèle peut aussi expliquer l'évidence que des tremblements de terre soient stimulés par les petites variations de contraintes suite à d'autres évènements sismiques (Mulargia *et al.*, 2006). Le modèle est décrit en détail dans l'article qui suit.

*Geophys. J. Int.* (2004) **158,** 98–108 doi: 10.1111/j.1365-246X.2004.02262.x

# Earthquakes as three stage processes

F. Mulargia, S. Castellaro and M. Ciccotti

*Dipartimento di Fisica, Settore di Geofisica, University of Bologna, Italy. E-mail: mulargia@ibogfs.df.unibo.it*

Accepted 2004 February 6. Received 2004 February 6; in original form 2003 January 20

**SUMMARY**

Relying on basic physics, laboratory and field evidence, and accounting for the different timescales involved, we derive an approximate energy function for earthquakes. The fracture term is disregarded because virtually all earthquakes occur on pre-existing faults and because fault gouge has a very low fracture energy. Disregarding also the gravitational term, the importance of which depends on the type of seismic focal mechanism, yields that the energy function has only thermal and radiative terms. The self-similarity ranges in the bulk rocks and gouge suggest taking the basic element as two cubes of 10 m side, with in common one face, over which slip occurs. An earthquake is a cascade of such slip processes on a series of neighbouring elements and the volume involved can be self-similarly defined as the two megacubes embedding the set of elements participating in the slip. Dimensional analysis suggests that the slip process is composed of three stages. The first stage consists of a stick-slip episode with an average velocity $v \sim 10^{-1}$ m s$^{-1}$ over a time $t \sim 10^{-2}$ s. In this first stage, stage I, virtually all energy is converted into heat, with a temperature increase of the order of $10^2$ K on the sliding surface. The second stage, stage II, in which the occurrence of further slip episodes is hardly relevant, consists of the propagation of the thermal wave generated in stage I to the whole shear zone, with a characteristic time of the order of $10^2$ s. In light of the comparatively low permeability of fault gouge with respect to heat diffusivity, this temperature increase induces a pore fluid pressure increase. When the transition from hydrostatic to lithostatic pressure is completed over the whole shear zone, a third stage, stage III, is entered, in which, provided that the pressurization is maintained, virtually frictionless high-velocity slip occurs, converting all the available energy into elastic radiation. The duration of this purely radiative stage, the amount of slip and the size of the earthquake depend on the number of elements cooperatively participating in the cascade slip, which is ruled, just as in the usual single-stage cellular automata models, by the correlation length over which the strain level is near the rupture threshold. At odds with the classical single-stage cellular automata, the model does not require the introduction of strong jumps in stress to be ignited and appears thus also capable of explaining the Coulomb failure stress quandary of very small triggering stresses, with the ignition of large events requiring excess stresses of just $10^{-2}$ to $10^{-3}$ MPa. The global seismic efficiency, under the assumption that granular effects and viscous resistance are disregarded, is $\sim 1$. Assuming then statistical self-similarity on the fault plane for the patches that slip cooperatively and approximating their pattern as a Sierpinski carpet, yields partial and approximately constant stress drop values independent of event size. These emerge from the fractal nature of the slip surface interpreted according to the seismological assumption of constant homogeneous slip on the Euclidean rectangular plane fault, which embeds the slipping patches.

**Key words:** Coulomb failure stress, earthquake source mechanism, earthquake triggering, fluid pressure, ignition slip, self-similarity.



## 1 INTRODUCTION

In physics, the common approach to describe a phenomenon is to write its energy equation. Writing this equation for an earthquake is difficult for both its direct inaccessibility and its complex phenomenology. Earthquake models do exist that are satisfactory for what regards the far-field elastic radiation (Ben-Menahem 1995), but these are incapable of describing event recurrence, so that the

 

prediction of single earthquakes is an untenable goal (Geller *et al.* 1997a,b). In addition to this, even the basic physical phenomenon, which is the stick-slip of two crustal rock blocks, appears to be incompatible with the heat flow measurements on active fault systems. In fact, according to current earthquake models, very large amounts of frictional heat should be generated by seismic fault slip, but the heat flow measurements along the San Andreas and other faults have consistently reported only modest heat values (Brune *et al.* 1969; Lachenbruch & Sass 1980), leading to what is termed the fault strength paradox (*cf.* Ben-Zion 2001).

Here, relying on simple dimensional analysis and accounting for the very different timescales involved, we attempt first of all to write an approximate earthquake energy function. Secondly, based on this energy function, we cast a three-stage self-similar earthquake model able to accommodate the above as well as the other basic phenomenology.

## 2 EARTHQUAKE BASIC PHENOMENOLOGY

Earthquake phenomenology is complex. Its basic features are:

(i) Earthquakes are rare events.

(ii) Earthquakes are clustered in both space and time (Kagan & Jackson 1991).

(iii) Earthquakes are rupture and slip events, which occur mostly on pre-existing faults.

(iv) Earthquakes have an approximately constant stress drop, which is considerably smaller than ambient stress (Abercrombie & Leary 1993).

(v) The external forcing function, that is tectonic strain, is small and constant, inducing extremely low strain rates.

(vi) Faults are rough surfaces, with power-law scaling suggestive of fractal geometry, albeit with fractal dimension close to 2 (the Euclidean plane) in the range $10^2$ to $10^4$ m (Okubo & Aki 1987).

(vii) The spatial distribution of earthquake hypocentres and laboratory acoustic emission locations are power law in both space and time (Kagan & Knopoff 1980; Hirata *et al.* 1987).

(viii) Earthquakes are power-law distributed in size in terms of a variable $10^m$, where $m$ is magnitude (Gutenberg–Richter law).

(ix) Earthquakes have aftershock sequences that decay as a power law in time (Omori law).

The latter features share a generalized power-law behaviour, which in statistical mechanical terms is equivalent to the intrinsic self-similarity of the process (*cf.* Bak & Tang 1989; for a comprehensive view see Mulargia & Geller 2003).

## 3 THE SELF-SIMILAR SOURCE

Let us consider a portion of crust containing a fault patch that is large enough to disregard grain size. Because virtually all earthquakes occur on pre-existing faults, the grain size will be that of the fabric of fault gouge, which is the crushed and reworked incoherent material that surrounds the faults. This fabric has a power-law distribution with no apparent upper cut-off for lengths up to the order of a few $10^{-3}$ m (Sammis *et al.* 1986). Consistent with this, we take the thickness of the shear zone of the order of a few $10^{-2}$ m. We aim at a self-similar description over a finite range with the upper cut-off given by crustal thickness, which means that our self-similar description will include all but the largest earthquakes. As a lower cut-off we take a geometrical entity of linear dimension of $\sim$ 10 m,

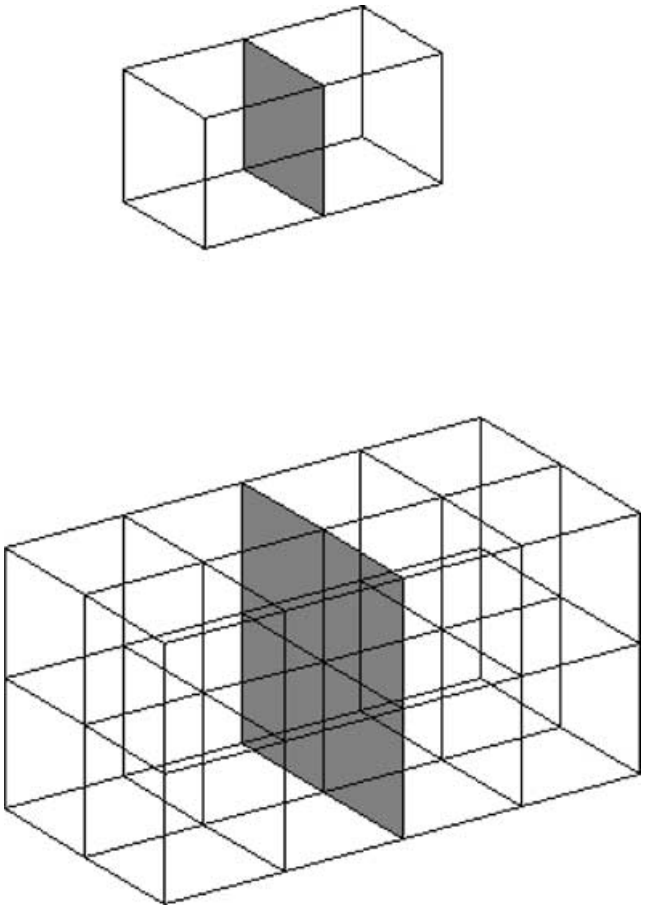

**Figure 1.** The self-similarity relation, with slip occurring at the contact face. Strain remains constant. The linear dimension of each cell is $\sim$ 10 m.

above which the scale invariance of crustal rocks appears reasonably well satisfied (*cf.* Ouillon *et al.* 1996). We will therefore define our basic element as two cubes of 10 m side, with the face in common representing the fault patch over which slip occurs (see Fig. 1). Self-similarity will be accommodated by letting this geometry repeat identically up to a 10 km side, with the obvious constraints imposed by the fact that self-similarity occurs on a finite range of approximately 3.5 decades, the details of which are discussed later in the paper. In the following, we first describe the process relative to the basic element.

## 4 EARTHQUAKE ENERGY FUNCTION

Disregarding the gravitational term, the importance of which varies depending on individual fault mechanism and geometry, four terms can be considered in the earthquake energy function $\Psi$:

$$\Psi = E_E + E_F + E_R + E_T, \tag{1}$$

where $E_E$ is the available elastic energy, $E_F$ is the fracture energy, $E_R$ is the radiated energy and $E_T$ is the thermal energy.

### 4.1 The elastic energy

Earthquakes are produced by shear deviatoric stresses. The most simple case restricts the discourse to a single shear strain component $\epsilon$ and from the theory of elasticity, the elastic energy stored in the

volume $V$ is

$$E_E = \int_V \frac{1}{2}\mu\epsilon^2\, dV, \tag{2}$$

where $\mu$ is modulus of rigidity. The largest coseismic crustal strains are of the order of $10^{-3}$, so that, because in the Earth's crust $\mu \sim 10^{10}$ Pa, the maximum available deviatoric elastic energy per unit volume is approximately $10^4$ J m$^{-3}$.

In order to proceed, we need to introduce a seismic source model. The standard seismic source model is a plane dislocation (Brune 1968) of linear dimension $r$ and area $A$ proportional to $r^2$. We approximate the crust as a 3-D lattice composed of our basic elements of side $r$ and apply the standard seismic model to the sliding patch of a basic element, which is subject on the sliding plane to a shear stress $\sigma$, assumed constant. Let us also assume that the friction stress is a material constant equal to $\sigma_f$.

Consider a slip $s$ on the patch, where $s$ is a small fraction $\eta \ll 1$ of $r$, $\eta \sim 10^{-3}$. Consistent with the assumed value for $r$ (10 m)

$$s = \eta r \simeq 10^{-2}\,\text{m}. \tag{3}$$

According to Volterra's theorem, the work done by this slip is (Landau & Lifshitz 1970; Ben-Menahem & Singh 1981)

$$\Delta W = \langle\sigma\rangle s A = E_E, \tag{4}$$

where $\langle\sigma\rangle$ is the average stress during the slip. This slip involves contributions in the radiated, fracture and thermal energies. Let us analyse how the work is partitioned among them by estimating the different contributions produced by a slip $s$.

### 4.2 The radiated energy

The radiated energy $E_R$ can be directly estimated from the recorded seismic waves by considering that the ground displacement $x$ at a given point reached at the time $t$ by a seismic wave of amplitude $a$ and period $T$ is (Gutenberg & Richter 1956)

$$x = a\cos\left(\frac{2\pi t}{T}\right). \tag{5}$$

The average kinetic energy $E_{\text{kin}}$ imposed by the passing wave in a medium of density $\rho$ per unit volume is then (*cf.* Kasahara 1981)

$$\begin{aligned} E_{\text{kin}} &= \frac{\rho}{2}\dot{x}^2 = \frac{\rho}{2T}\int_0^T \dot{x}^2 dt \\ &= \frac{\rho}{2T}\left(\frac{2\pi a}{T}\right)^2 \int_0^T \sin^2\left(\frac{2\pi t}{T}\right) dt = \rho\pi^2\left(\frac{a}{T}\right)^2 \end{aligned} \tag{6}$$

and the total energy is twice as much because it includes an identical amount of potential energy (ibid.). Integration over the boundary surface of a volume containing the source then gives the measure of the total energy of the radiated waves. In practice, it is convenient to rely on more readily measured quantities. Considering the slip of the patch as whole, the basic quantity is the scalar seismic moment $M$,

$$M = \mu s A, \tag{7}$$

in terms of which the total radiated energy can be written as

$$E_R = \Delta W_R = (\langle\sigma\rangle - \sigma_f)\frac{M}{\mu}, \tag{8}$$

where $\sigma_f$ is the average friction stress. Disregarding the difference between static and dynamic stress, considering the stress values before and after the slip, $\sigma_{\text{init}}$ and $\sigma_{\text{end}}$, respectively, the above formula can also be written as

$$E_R = (\langle\sigma\rangle - \sigma_{\text{end}})\frac{M}{\mu} = \frac{\Delta\sigma M}{2\mu}, \tag{9}$$

where $\Delta\sigma$ is the stress drop.

### 4.3 The fracture energy

The estimates of the fracture energy traditionally rely on energy conservation (Griffith 1920). If a new crack is formed or an existing crack propagates, free surfaces are created by the breaking of bonds. It would appear tempting to generalize the Griffith approach, which works reasonably well on homogeneous and isotropic laboratory brittle specimens of simple geometry and with a single crack, to include real systems, which regard a generic material with a population of cracks. Unfortunately, in the general case the simple Griffith picture does not work as a result of the presence of dissipative terms and (at propagation velocities comparable to those of the elastic waves) kinetic effects, which are often more important than the elastic terms themselves (*cf.* Herrmann & Roux 1990). In addition to this, seismic faults occur in fault gouge, which has mechanical features very different than those of bulk rock (*cf.* Mora *et al.* 2000).

As a consequence, the estimates of fracture energy $E_F$ made using the approximation of a single propagating mode III crack in an elastic brittle continuum (Kostrov 1966; Eshelby 1969; Dahlen 1977; Freund 1998), which are popular in the seismological approach to earthquake physics, must be regarded as restrictive. Physically, it appears more appropriate to rely directly on experimental fracture energy data relative to sliding experiments with realistic fault gouge. The latter indicate a fracture energy 3 to 4 orders of magnitude smaller than the total energy (Yoshioka 1986), so that, because we are not considering the case of fresh faulting, fracture energy can be comfortably disregarded.

### 4.4 The thermal energy

For energy balance we have

$$\Delta W_T = \sigma_f s A = E_T, \tag{10}$$

where the average friction stress $\sigma_f$ is equal to

$$\sigma_f = \sigma_n\phi, \tag{11}$$

with $\sigma_n$ indicating the stress normal to the fault surface and $\phi$ the coefficient of friction, which, under static and kinetic configuration for a variety of rocks at seismogenic depth conditions, falls in the range $\sim$ 0.6–0.9 according to both laboratory (Byerlee 1978) and borehole *in situ* stress measurements (McGarr & Gay 1978; Brudy *et al.* 1997). The values of $\sigma_n$ in the crust can be taken to be of the order of $10^8$ Pa (ibid.).

The rate of heat $q$ generated per unit area by fault slip can be roughly calculated by using the equation for a plane surface in an infinite medium

$$q = \sigma_n\phi v, \tag{12}$$

where $v$ is the slip velocity and $\sigma_n$ is the stress normal to the fault plane. If pore fluids are present, as it is the general case of water in fault gouge (Morrow *et al.* 1984), eq. (12) reads as

$$q = (\sigma_n - P_p)\phi v, \tag{13}$$

where $P_p$ is the fluid pore pressure, which is hydrostatic at equilibrium.

Assuming that heat generation starts at time $t = 0$ as a step function with a constant heat flux $q$, the temperature rise $\Delta T$ at a distance $x$ from the emitting plane surface after a time $t$ is, calling $C$ the specific heat and $K$ the thermal diffusivity (Carslaw & Jaeger 1986),

$$\Delta T = \frac{q}{\rho C}\left(\sqrt{\frac{t}{\pi K}}\right) e^{-\frac{x^2}{4Kt}} - \left[\left(\frac{q}{\rho C}\right)\left(\frac{|x|}{2K}\right)\mathrm{erfc}\left(\frac{|x|}{2\sqrt{Kt}}\right)\right], \tag{14}$$

which, close to the fault surface, i.e. when $|x| < \sqrt{Kt}$, can be approximated as (Sibson 1975)

$$\Delta T = \frac{q}{k}\sqrt{\frac{Ks}{\pi v}}, \tag{15}$$

where $k$ is the thermal conductivity and $s = vt$ is the displacement at time $t$. Combining the last equation with eq. (13)

$$\Delta T = \frac{\phi(\sigma_n - P_p)}{k}\sqrt{\frac{Ksv}{\pi}}. \tag{16}$$

Based on laboratory evidence, reasonable values of the parameters involved are $K = 10^{-6}$ m$^2$ s$^{-1}$, $k = 2$ J/(m s$^\circ C$) (Clark 1966). This yields that temperatures should raise locally above $10^3$ K for velocities and displacements typical of seismic events because, as indicated by the size of the shear zone, sliding seems to be concentrated in a zone of a few $10^{-2}$ m. However, the presence of melting products like pseudotachylites appears to be rare (Sibson 1975) and therefore some mechanism capable of substantially reducing friction and frictional heating must exist. Note that melting itself might in principle reduce friction (Kanamori & Heaton 2000), but there are basic difficulties for this (see discussion in Section 5.4).

## 5 EARTHQUAKES AS A THREE-STAGE PROCESS

Let us relax the assumption shared by all the proposed mechanisms of friction reduction that slip occurs at a single timescale (*cf*. Ben-Zion 2001) and consider a first stage of high friction stick-slip similar to that encountered in the laboratory.

### 5.1 Stage I

The process starts when strain build-up induces on the fault patch a stress $\sigma$ such that

$$\sigma > \sigma_f. \tag{17}$$

Sliding occurs, doing work

$$\Delta W = \Delta W_R + \Delta W_T, \tag{18}$$

because, as we have seen, the fracture energy can be disregarded.

This work is also equal to

$$\Delta W = \int_\Sigma \sigma\, Ads, \tag{19}$$

where $\Sigma$ is the propagation domain in which

$$\sigma > \sigma_f, \tag{20}$$

because slip stops when the elastic force is less than the friction force.

According to eqs (10)–(13) the thermal work is

$$\Delta W_T = \int_\Sigma (\sigma_n - P_p)\phi\, Ads, \tag{21}$$

which can be approximated as

$$(\sigma_n - P_p)\phi s A. \tag{22}$$

In agreement with laboratory phenomenology, slip occurs in stick-slip episodes, with $\phi \simeq 0.6$–$0.9$, average velocity values of the order of $10^{-2}$ m s$^{-1}$, peak velocity values of the order of $10^{-1}$ m s$^{-1}$ and a radiated elastic energy that is a fraction of order $10^{-2}$ of the thermal energy (e.g. Lockner & Okubo 1983), so that

$$\Delta W \simeq \Delta W_T. \tag{23}$$

In other words, virtually all the work done according to eq. (21) is transformed into heat

$$\Delta W_T = \Delta Q = CAw\rho\Delta T \sim Cr^2 w\rho\Delta T, \tag{24}$$

where $w$ the width of the thermal zone, the latter being the volume surrounding the fault plane in which temperature increases. Rewriting eq. (16), slip is accompanied by a temperature $\Delta T$ increase of the matter surrounding the slip plane equal to

$$\Delta T \simeq (\sigma_n - P_p)\frac{\phi}{k}\sqrt{\frac{Kv^2 t}{\pi}}, \tag{25}$$

where $t$ is time, which yields that temperatures of the order of $10^2$ K are attained by a stick-slip episode with an average $v^2\, t \sim 10^{-4}$ m$^2$ s$^{-1}$. Considering laboratory experiments, such an episode is likely to be constituted by a cluster of stick-slip events, with an average velocity $v \sim 10^{-1}$ m s$^{-1}$ over a time of $10^{-2}$ s, implying a total slip of the order of $10^{-3}$ m. On the unit patch this corresponds to a strain release of the order of $10^{-4}$ and, because the maximum accumulated strain is of the order of $10^{-3}$, stage I consumes a strain energy $\sim \Delta W_T$, which leaves the total strain energy almost intact (*cf.* eq. 2). The released strain decreases the stress from $\sigma > \sigma_f$ to $\sigma < \sigma_f$, thus stopping the slip.

### 5.2 Stage II

Stage I has raised the temperature on the friction surfaces within the shear zone to a value of the order of $10^2$ K with a slip episode of a duration of $10^{-2}$ s. The width $w$ over which heat is carried by thermal diffusion is

$$w(t) = 2\sqrt{Kt}, \tag{26}$$

which means that the heat wave will propagate to the whole shear zone, which has a width $w$ of the order of a few $10^{-2}$ m, in a time of the order of $10^2$ s after the slip event. Experimental values for permeability in fault gouge after a sliding of the order of $10^{-3}$ m are around $10^{-9}$ Darcy (or $<10^{-21}$ m$^2$) (Morrow *et al.* 1981, 1984; Zhang & Tullis 1998) and the resulting Darcy diffusivity $K_D$, of the order of $10^{-8}$ m$^2$ s$^{-1}$, is smaller than thermal diffusivity $K$ (of the order of $10^{-6}$ m$^2$ s$^{-1}$). Therefore, the temperature increase resulting from frictional sliding diffuses faster than the thermally expanded pore fluid and, when it extends to the whole shear zone, it raises the fluid pressure from hydrostatic to lithostatic, decreasing the effective normal stress, and thus (static) friction, towards zero. Because in frictional sliding the largest asperities dominate the process (Scholz 1990), only when the whole shear zone has been pressurized a transition to friction values near zero occurs. Further stick-slip episodes may take place during this stage, but they can reduce the time required to heat the whole shear zone only if their position is such that they generate thermal waves that travel ahead of the original one.

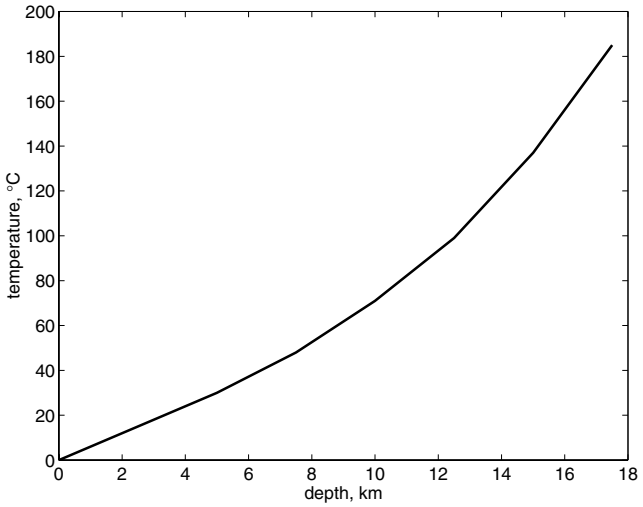


**Figure 2.** The temperature rise required to increase water pressure from hydrostatic to lithostatic (data are from Burnham *et al.* 1969).

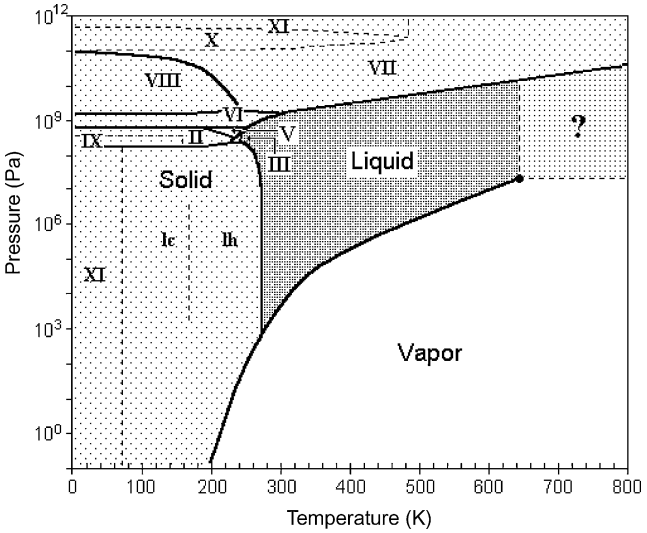


**Figure 3.** The phase diagram of water. The roman numbers indicate the different structures of ice. (Redrawn from IAPWS Release on the values of temperature, pressure and density of ordinary water substance, 1976 and 1994; http://www.iapws.org/release.htm).

While propagating, the temperature of the heat wave decreases, but this is hardly a problem because thermal energy is abundant compared with the heat necessary to bring water pressure, which is the main pore fluid constituent, from hydrostatic to the lithostatic transition by differential thermal expansion (see Fig. 2; *cf.* also Sibson 1977; Lachenbruch 1980; Mase & Smith 1987). For example, considering a depth of 10 km, a temperature rise of approximately 70 °C produces a pressure increase $\sim 0.2$ GPa, which is sufficient to decrease friction towards zero in the approximation that dynamic effects can be disregarded. These are essentially granular and viscous resistance effects. The first ones can be traced to transgranular friction induced by dilatancy and are likely to be overcome by a slight fluid overpressure. The second ones are small because sliding velocities should be at most of the order of 1 m s$^{-1}$.

### 5.3 Stage III

The stick-slip episode of stage I has generated a frictional heat wave, which in stage II propagates to the whole shear zone inducing a transition of pore pressure from hydrostatic to lithostatic. Once the shear zone has been pressurized, slipping can occur in a completely different way and the process enters stage III. Note that because the grains in the gouge follow a power-law distribution (*cf.* Section 3), slipping will be a threshold process ruled by the largest grains, which have a size comparable to that of the shear zone. In other words, no slip will occur until the whole shear zone is pressurized.

Propagation was stopped at the end of stage I by reaching the boundary of the set $\Sigma$ on which

$$\sigma = \sigma_f = (\sigma_n - P_p)\phi, \tag{27}$$

with $\phi \simeq 0.6$–$0.9$. However, the thermalization of the shear zone, which occurred in stage II, has brought the coefficient of friction $\phi$ to $\sim 0$, so that $\sigma$ is largely unbalanced and slip starts again.

The energy function is now

$$\Psi = E_E - \Delta W_T > 0 \tag{28}$$

and, disregarding granular effects and viscous resistance, slip will occur with

$$E_E \simeq E_R \tag{29}$$

virtually radiating all the residual deviatoric elastic energy in seismic waves. In light of this, seismic efficiency is $\sim 1$. The total accumulated strain, which is of the order of $10^{-3}$, is released. On a single patch, the latter corresponds to a slip of $10^{-2}$ m, which occurs at velocities that seismology allows to estimate as of the order of 1 m s$^{-1}$ (*cf.* Ben-Menahem & Singh 1981), yielding a characteristic time $\sim 10^{-2}$ s.

Note how the assumption upon which stage III is based is that no reduction in the pressure of the shear zone occurs before the radiative slip is completed. This assumption is unfortunately very difficult to verify for experimental reasons: the current knowledge of frictional sliding in fault gouge material at velocities larger than $10^{-2}$ m s$^{-1}$ is extremely limited even at room pressure (Tsutsumi & Shimamoto 1997; Hammerberg *et al.* 1998; Roder *et al.* 1998, 2000) and at the 10 MPa pressures of the seismic focal regions, when slip velocity increases, high-friction–high-velocity slip possibly occurs at some spots. On the latter, high temperatures are locally attained, which possibly induce a water-vapor transition producing a local abatement in friction, as well as a decrease in temperature as a result of the latent heat of evaporation, preventing the formation of melting products. Data are lacking also in this respect, because the phase diagram of water is virtually unknown in the region above 600 K and 10 MPa (see Fig. 3), in which water is probably in a supercritical phase, with liquid-like hydrogen-bonded clusters dispersed within a gas-like phase. The physical properties of the latter, such as gas- or liquid-like behaviour, are likely to vary abruptly in response to changing density (Hasegawa *et al.* 2003). Another possibility is that a gel is formed (Iler 1979).

### 5.4 Parallel with the classical single-stage case

All the current earthquake models, including the cellular automata of the complex physics approach (Main 1996; Rundle *et al.* 2000; Mulargia & Geller 2003), assume a single stage. This is similar to our stage I, but has the fast slip of our stage III. To start such a single-stage process on a patch, the value of $\sigma$ should suddenly jump to a value

$$\sigma \gg \sigma_f \tag{30}$$

to produce a slip large enough to emit significant elastic radiation, because this is proportional to the slip $s$ (*cf.* eq. 9), while our model requires much smaller stress jumps to be ignited. Stress variations in the Earth's crust are related to several factors. The largest changes are caused by tectonic loading, which acts at constant and very low strain rates lower than $\sim 10^{-15}$ s$^{-1}$. Tidal stresses are periodic with strain rates of $10^{-13}$ s$^{-1}$ and similar values are attained also by atmospheric loads, albeit with no periodicity (e.g. Ohtake & Narakahara 1999). In addition to these, there is the stress transfer induced by the occurrence of other earthquakes [e.g. the Coulomb failure stress; *cf.* Harris (1998); *cf.* also Section 6.2], which may reach similar strain values, but with shorter insertion times and thus higher rates. Disregarding tectonic load for its constant low rate, stress jumps are thus induced by the superposition of mostly non-periodic functions. The probability of a stress jump $\Delta\sigma$ of energy $E_{\Delta\sigma}$ can therefore be assumed as random and taken to follow a Boltzmann statistic

$$p(E) \propto e^{-(E_{\Delta\sigma}/k_B T)}, \tag{31}$$

or (*cf.* eq. 2)

$$p(\Delta\sigma) \propto e^{-(C^{-1}\Delta\sigma)^2/k_B T}, \tag{32}$$

where $C$ and $k_B$ are respectively the elastic and Boltzmann constants. The last equation suggests that the large jumps required by single-stage models are (square-)exponentially less likely than those required by the three-stage model.

Another possibility is that no large jump occurs, but there exist alternative single-stage processes capable of abating friction. There seem to be two candidates. The first one is a roller bearing effect resulting from generalized rolling processes in the fault gouge grains (*cf.* Mora *et al.* 2000). However, this effect appears at best capable of reducing the friction coefficient $\phi$ to 0.3 (ibid.), which according to eq. (13) merely implies a factor of $\sim 2$ reduction in the heat produced, insufficient to accommodate the heat flow paradox.

The other candidate is that local melting, produced by initial sliding, acts as a lubricant for further slip (*cf.* Kanamori & Heaton 2000). There are basic difficulties in applying such a mechanism. First, at the timescale involved by a single-stage process (eq. 26) all thermal processes regard only a thin zone of $<10^{-3}$ m around the sliding plane. Melting can therefore possibly act as a lubricant only on sliding surfaces flat with $<10^{-3}$ m accuracy. While the latter is easily attained on 10 m machined blocks with good industrial equipment, such an accuracy is unthinkable in natural materials, particularly in fault gouge, where the power-law distribution of grain size makes the larger grains, with size $\sim 10^{-2}$ m, control the slipping. Secondly, the presence of melting products (i.e. pseudotachylites) is so scarce in exhumed faults (Magloughlin & Spray 1992; Sibson 1992) that frictional melting appears to be a secondary effect, occurring only locally in a highly fractured and crushed environment, (*cf.* McKenzie & Brune 1972; Sibson 1973; Spray 1987). Some further discussion on this point is given in Section 6.3 below.

This concludes our elementary description relative to a single patch. However, earthquakes are cooperative phenomena and a number of patches will always be involved. We will now therefore discuss the process for a set of patches.

## 6 EARTHQUAKES AS COOPERATIVE PHENOMENA

Let us first of all analyse the number of patches that cooperatively take part in the slip. If we were to apply strict self-similarity to our basic element (Fig. 1), we would have an earthquake represented by the simultaneous slip of all the patches within the two megacubes of side $R$ with 10 m $\leq R \leq 10^4$ m, where $R^2$ gives a direct measure of event size. We will rather assume self-similarity as a statistical property so that not all the patches on the domain $R \times R$ slip, but $R \times R$ defines the characteristic size of the slipping domain. Recall also that our assumption of self-similarity, just as any real self-similarity, regards a finite range (*cf.* Section 3). In our case this is limited below by the characteristic length of fault gouge and above from the vertical dimension of the seismogenic crust.

### 6.1 Earthquake size

Assuming self-similarity as a statistical property, the size of the earthquake is given by the number of patches that undergo together a stage III slip, which are primarily (but not only, see strain transfer in Section 6.3 below) the geometrically connected patches that have simultaneously entered stage I. This means that the size of the event will be determined $\sim 10^2$ s before the start of stage III in which the radiation of elastic waves occurs. The patches simultaneously entering stage I are those for which at the instant $t = t_0$ there is a transition with a stress level just above the friction stress $\sigma_f$

$$\sigma_{t<t_0} < \sigma_f \quad \rightarrow \quad \sigma_{t=t_0} > \sigma_f. \tag{33}$$

The occurrence of such a transition over a set of patches as a result of random fluctuations (generally superimposed to a deterministic evolution function) is described in statistical mechanics by the correlation length $\ell$, which represents the length over which cooperative effects occur. This length depends on the laws defining the model and its evolution, which are generally based on local threshold processes (as it happens for our single patches) and this leads to strongly non-linear dynamics.

The most simple description of such systems is provided by percolation theory (e.g. Stauffer & Aharony 1994), while more detailed pictures are given by cellular automata (e.g. Burridge & Knopoff 1967; Bak & Tang 1989; Carlson & Langer 1989), which are computer algorithms simulating a lattice of cells ruled by laws describing their interaction and the external forcing. The general result of all such models is that the correlation length is distributed according to an inverse power (e.g. Stauffer & Aharony 1994; Castellaro & Mulargia 2002), so that the probability of an event of given size follows a power law, reproducing the observed distribution for earthquake size, which is known as Gutenberg–Richter law. This behaviour, which is one of the main phenomenological features of earthquakes, can possibly be derived by using simple mean-field arguments (*cf.* Anton 1999). All these approaches concur in that the probability of an event of given size is tied to the probability of having the corresponding correlation length, which follows a negative power law. This happens in all single-stage cellular automata models and also in the three-stage model we propose, with some minor differences related to strain transfer discussed below.

### 6.2 Global radiative and ignition slips

The second effect produced by the cooperative nature of the process is on global slip.

Relying on statistical self-similarity, we assume that the region involved in the process is defined by the double cubic domain embedding the set of patches that slip (see Fig. 4). The side $l$ of each cube is $\Omega$ times the unit patch and is equal to the correlation length $\ell$. Consistently with our original self-similarity assumption, we take the maximum strain on such volume as constant and equal to

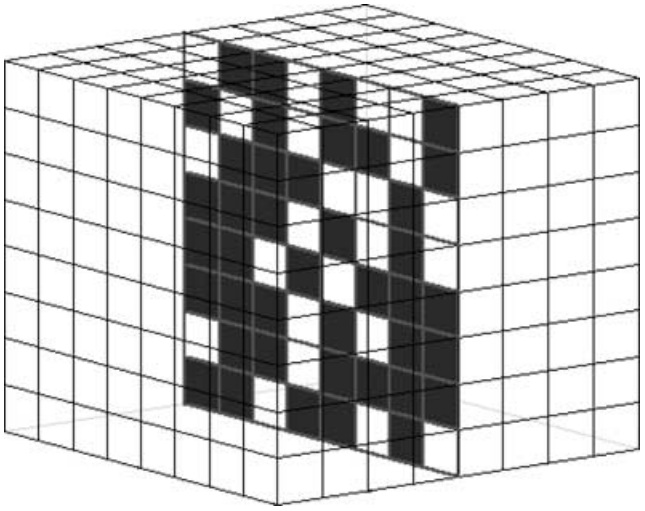

**Figure 4.** The 3-D square lattice that we assume for a portion of crust containing the seismic fault, which is shown as a 2-D slice. The cells that have slipped in a given event are shown in black. The linear dimension of each cell is $\sim 10$ m.

$\epsilon \sim 10^{-3}$ so that the global volume involved in the release of elastic energy (see Fig. 1) is $\propto \Omega^3$. According to eq. (3), the global fault slip $s$ that releases this strain is $\propto \Omega$ and the slip surface is $\propto \Omega^2$. The way in which self-similar strain release on the megacubes leads to the addition of local slip contributions in each patch to give the global (average) slip of eq. (3) is pictorially shown in Fig. 5. This yields a global slip of the order of 1 m for $\Omega \sim 10^2$, i.e. for correlation lengths $\sim 10^3$ m. Note how this would imply slip durations of the order of 1 s, during which the pressurization of the shear zone would have to stay at (or above) the lithostatic value.

Which portion of this slip is used for thermalization (from now on we call this the ignition slip) and which for radiation (from now on we call this the radiative slip)? Starting from stage I, we consider that, because the ignition slip is fixed at $\sim 10^{-3}$ m irrespective of correlation length, the strain release required to complete stage I and the following stage II (the ignition strain), is $10^{-4}\Omega^{-1}$. This means that each single patch contributes to the ignition strain proportionally to $\Omega^{-1}$, i.e. spending for ignition a smaller proportion of the accumulated strain, the larger is the domain entering stage I.

This argument makes large events energetically favoured by a factor $\propto \Omega$. However, such events require also on the strain level a correlation length $\propto \Omega$, which has probability

$$p \propto \Omega^{-\beta} \tag{34}$$

with $\beta$ (*cf.* Stauffer & Aharony 1994) depending on the specific model (for example, for a Bethe lattice $\beta = \frac{5}{2}$). This yields that large events are unfavoured by a factor $\propto \Omega^{1-\beta}$ (for a Bethe lattice $\Omega^{-1.5}$ which incidentally matches the Gutenberg–Richter law, because taking event size $10^m \propto \Omega^2$ requires that $m$ is distributed as $\log\ N = a - bm$, with $b \simeq 1$).

Because the strain release in stage III is $\sim 10^{-3}$, while the strain required for thermalization is $\sim 10^{-4}\Omega^{-1}$, we can define the ratio of ignition strain to the radiative strain as

$$\gamma \simeq 10^{-1}\Omega^{-1}, \tag{35}$$

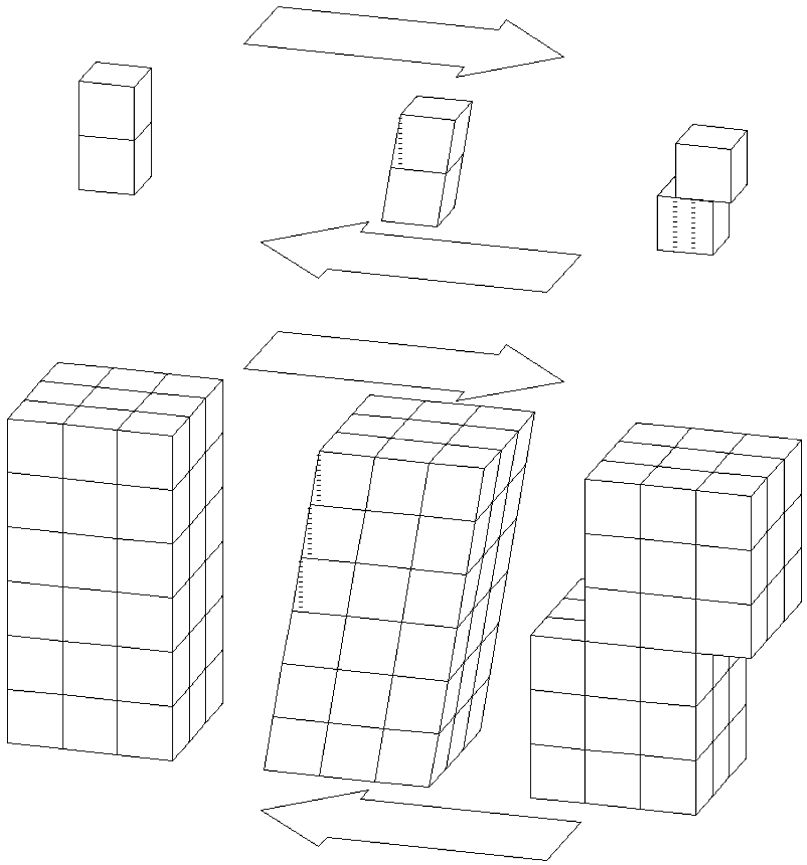

**Figure 5.** The self-similar way in which a constant and unitary shear strain release at each patch combines to produce global constant slip equal to $\Omega$ times that on a single patch, under the assumption that boundary effects are disregarded.

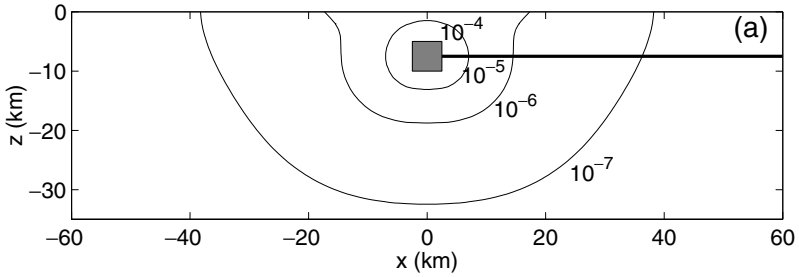


**Figure 6.** Strain contours on the fault plane for a vertical strike-slip square fault with 5 km side, 5 km depth of the upper rim and slip equal to $\frac{5}{3}$ m according to the formulation of Okada (1992). The line (a) is related to Fig. 7.

so that for any sizable earthquake (i.e. with source size $\geq 10^3$ m) the energy required to start the process is some orders of magnitude smaller than the later elastically radiated energy. The expression $\eta \simeq 1 - \gamma$ is the seismic efficiency of the process, which increases with earthquake size, and is in any case very close to 1, at odds with classical models, where it is of the order of a few $10^{-2}$ (e.g. Shearer 1999).

Finally, note that the ignition stress of an event with $\Omega \sim 100$–1000, i.e. with a source slip surface of $1 \times 1$ to $10 \times 10$ km is $\sim 3 \times 10^{-2}$ to $3 \times 10^{-3}$ MPa. Therefore, the model provides an explanation for the fact that small values of stress transfer may trigger seismic events, an issue that has been long questioned on physical grounds (*cf.* Harris & Simpson 1992; Du & Aydin 1993; Bennett *et al.* 1995; Dodge *et al.* 1995; Astiz *et al.* 2000). The last two results appear capable to reconcile Coulomb failure stress theory with experimental evidence.

### 6.3 Strain transfer

The third effect produced by the cooperative nature of the process is the strain transfer that an element that slips induces on the neighbouring elements. Let us consider a neighboring patch $\Lambda$ on which this strain transfer has increased the stress level of $\Delta\sigma$ from the value $\sigma_0$ to the value $\sigma_{\text{transf}} = \sigma_0 + \Delta\sigma$. There are three possible cases, considering that the radiated energy is proportional to the slip $s$ (*cf.* eq. 9):

(i) Case A:

$$\sigma_{\text{transf}} < \sigma_f; \tag{36}$$

nothing happens.

(ii) Case B:

$$\sigma_{\text{transf}} \geq \sigma_f; \tag{37}$$

the element $\Lambda$ exhibits a small slip sufficient to make it enter stage I and after $\sim 10^2$ s it undergoes a stage II–III transition.

(iii) Case C:

$$\sigma_{\text{transf}} \gg \sigma_f; \tag{38}$$

the element $\Lambda$ exhibits a slip sufficient to make it enter stage I and to continue slipping. If $\Delta\sigma$ is large it may induce a slip $s$ sufficient to emit significant elastic radiation, albeit with high friction, low efficiency and a strong production of heat that should show up in melting products. After $\sim 10^2$ s it undergoes a stage II–III transition releasing the residual strain.

Disregarding the directional effects, cases A, B and C can be expected to correspond approximately to $\Delta\epsilon$ values respectively $10^{-7} \leq \epsilon \leq 10^{-5}$ and $10^{-4} \leq \epsilon$. To estimate the importance of this effect let us analyse a practical example.

Following our self-similar geometry, let us take the slip surface as a dislocation on a square domain and estimate the local change in strain from the (static) elastic solution of Okada (1992). The detail of the spatial distribution of $\Delta\varepsilon$ depends on the specific fault parameters, but the general behaviour is a strong decrease with distance $r$ from the fault (see Fig. 6), which is well approximated by a power law $r^{-\alpha}$ with $\alpha$ between 2 and 3 (*cf.* Cotton 1995). For example, taking a vertical strike-slip square fault with 5 km side, 5 km depth of the upper rim and slip equal to $\frac{5}{3}$ m (the reason for the latter choice will be apparent in next section) and limiting the analysis to the fault plane, yields a value of $\alpha = 2.2$ (see Fig. 7). This stands for a fairly short-range behaviour, with strain transfer perturbations extending over comparatively small areas.

Note how the cascades in all the classical single-stage cellular models are ruled by case C alone. This means that a large event involving the slip of $\Omega^2$ patches requires a correlation length $\propto \Omega$ both in the classic single-stage model and three-stage model we propose. The only difference is that in the model we propose small perturbations are required to induce a case B behaviour, while in the classic case (much less likely) large stress jumps are required to induce a case C behaviour.

### 6.4 Self-similarity on the fault plane and stress drop

The fourth effect produced by the cooperative nature of the process regards the geometry of the slip on the fault and the stress drop. In the present section, let us for simplicity disregard border effects, so that patches on the fault that are neighbour to non-slipping patches experience no slip reduction.

Geometrically, a fault is a fractal, albeit not too far from a plane (Okubo & Aki 1987), so that it can be roughly approximated as a plane. Let us use this approximation and assume statistical self-similarity for the slipping patches over the fault plane. In statistical mechanical terms this is equivalent to the proximity to a critical state (*cf.* Mulargia & Geller 2003). This also suggests a fractal geometry with fractal dimension close to that of percolation, which is equal to 1.896. To set the discussion in the most simple possible terms, we note that the latter is very similar to the fractal dimension of a square Sierpinski carpet (see Fig. 8), which is equal to 1.893, and we take this geometry as representative of the global slip on the fault surface, disregarding any specific lacunarity problem. Obviously, the fractal geometry has to be intended on a finite scaling range, as is customary for all applications to the real world (e.g. Feder 1988). In other words, geometrical self-similarity occurs over a finite domain, which in our case is limited to approximately 3.5 decades, consistent with the

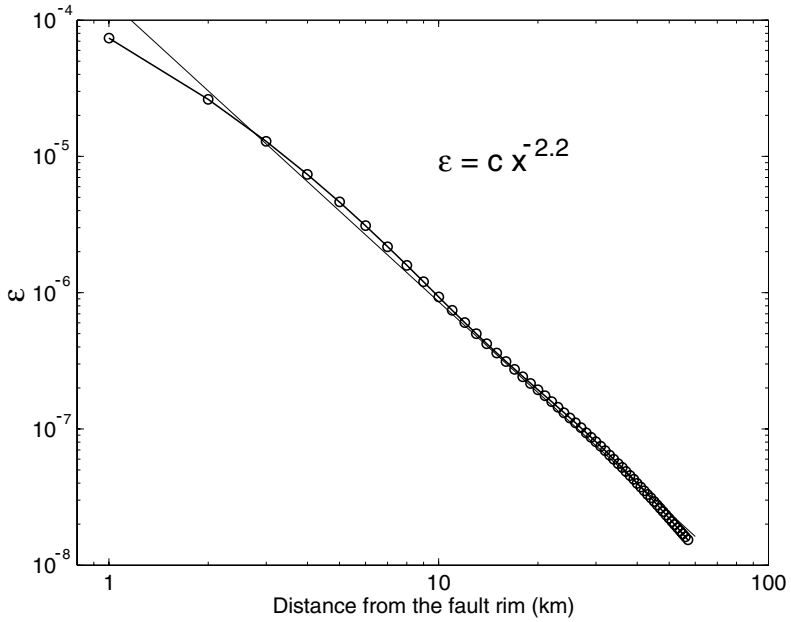


**Figure 7.** The decay of shear strain with distance from the fault front rim along the line (a) for the fault of Fig. 6. The data are well fitted by a power law with exponent −2.2.

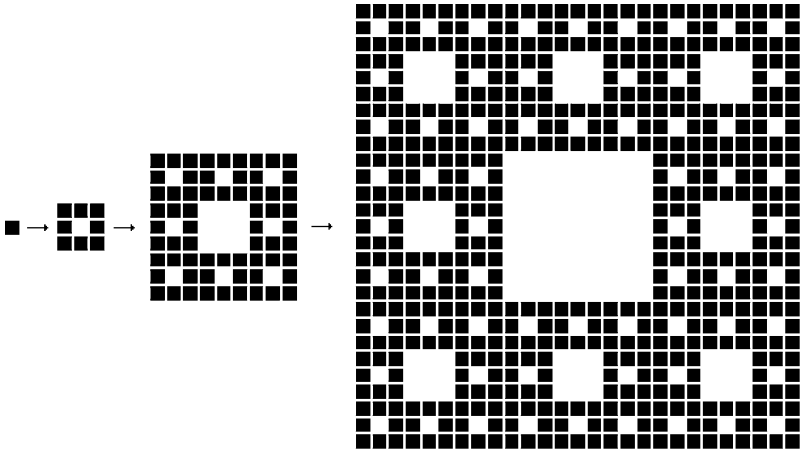

**Figure 8.** A Sierpinski carpet, which has a fractal dimension very close to that of percolation and can thus be taken as roughly representative of criticality (see text). The slipped patches are in black. Note that at zero order the whole patch seems to slip, as in the seismological model.

definition of our patch (*cf.* eq. 3) as well as with the constraint for a correct fractal attribution (*cf.* Ciccotti & Mulargia 2002).

Assuming that slip occurs on the latter finite range fractal domain (see Fig. 4) rather than on the entire fault surface implies first of all that the total area of the slipped patches is approximately $\frac{2}{5}$ that of the embedding square. As a consequence, the stress drop calculated according to the standard average over the embedding square fault gives a value that is $\sim \frac{2}{5}$ of what really occurs on each patch, making it appear as a partial strain release. Border effects around each slipping patch, which have been disregarded here, are likely to further reduce this fraction. This apparent partial release is an artefact of considering the slip averaged on the square embedding the fractal set of the patches. The fraction of the apparent partial release depends on the self-similarity range and fractal dimension, but not on the embedding fault size. It is therefore independent of event size, in agreement with the apparent stress drop approximate constancy, which seems a well established phenomenological and unexplained empirical result (Abercrombie & Leary 1993). In addition to this, one has to recall that the embedding fault area cannot be accurately constrained by seismological and geodetic measurements and is likely to be overestimated (*cf.* Hardebeck *et al.* 1998), so that the usual average interpretation is likely to imply a further, and possibly large, reduction of the apparent average stress drop.

Following the same reasoning also, the average slip will be apparently reduced by the same factor. In fact, taking an event of seismic moment $M = \mu\, sA$, its value can be reconciled with the usual average over the embedding fault by either reducing the apparent stress drop, as we just did, or the slip $s$, or by reducing both by the appropriate fraction. Note also how a set of patches of linear dimension $10^2$ (with a global length of $10^3$ m) following Euclidean geometry would have a total slip of the order 1 m, but following the above reasoning would have an apparent average slip of a few tenths of a metre, in agreement with field data (Purcaru & Berckhemer 1982; Jackson *et al.* 1982). For this reason we choose $s = \frac{5}{3}$ m in our example, Fig. 6.

In summary, the assumption of slip over a finite range that is a fractal rather than Euclidean domain implies that only a fraction of the patches on the fault plane slip and only a fraction of the available stress is released. This fraction depends on the geometry ruling the process alone and not on the event size.

## 7 VALIDATION

The model we propose is rooted in basic physics, but relies on a number of assumptions. At odds with current seismic source models it agrees with the available phenomenology. However, as any physical model, it is not credible without a strict validation. The latter appears difficult, because it requires casting a stringent null hypothesis on a system that is not directly accessible.

Such a null hypothesis can be hopefully formulated in terms of observing two new effects, which are predicted by the model. The first of them is that stage III should induce slip in the non-slipping patches neighbouring the slipping ones within the main-shock fault (Fig. 4) according to case C above. In the example fault we have worked out, which disregards the fractal nature of the faulting and therefore overestimates the strain field, the induced shear strain on the fault plane is $10^{-4}$ only immediately outside the fault. The induction of high-friction slip is therefore expected close to the border of the slipping patches, where a stronger concentration of pseudotachylites should be observed.

The second effect is that, because the induced strain is $\sim 10^{-6}$–$10^{-7}$ at distances equal to $\sim$ 3–6 fault lengths, a surge of aftershocks should be observed in a quite large area with a delay of $\sim 10^2$ s from the main shock.

Neither of these effects appears easy to observe. The first one because later-stage deformation and weathering tend to inhibit the detection of pseudotachylytes. The second one because the coda of the main event blurs the seismic records for an interval that has a duration $t_e$ (*cf.* Lee *et al.* 1972; Gasperini 2002)

$$\log t_e \simeq mC_1 + C_2, \tag{39}$$

where $m$ is magnitude and the constants $C_1 \sim \frac{2}{5}$, and $C_2 \sim \frac{4}{5}$, which gives coda durations larger than $10^2$ s for events with $m \geq 3$.

## 8 CONCLUSIONS

Based on the physical arguments of self-similarity, energy balance and scale analysis, we developed an earthquake source model in which energy release occurs in three stages rather than in a single stage and slip occurs over a fractal rather than Euclidean domain, as it happens in all current models. Our model, which has a global radiative efficiency close to unity, seems capable of reconciling the available and apparently contradictory laboratory and *in situ* evidence, including high- and near-zero friction values, lack of heat flow anomaly, aftershock triggering according to Coulomb formulation, self-similar strain release, partial and constant stress drop. On the other hand, it relies on the assumption that the pressurization of the shear zone can be sustained during the radiative slip process, an issue that is experimentally very poorly constrained as a result of the almost total lack of data on high-velocity slip and phase diagram of water above 600 K and 10 MPa. The model lacks in any case a strict validation, which may come from the observation of two additional effects it predicts: a higher concentration of pseudotachylites near the border of slipping patches and a surge of aftershocks in a wide area surrounding the main-shock fault with a $\sim 10^2$ s delay.

## ACKNOWLEDGMENT

The authors wish to thank Ian Main and Stefan Hergarten for their constructive reviews.

## REFERENCES

Abercrombie, R. & Leary, P., 1993. Source parameters of small earthquakes recorded at 2.5 km depth, *Geophys. Res. Lett.,* **20,** 1511–1514.

Anton L., 1999. Simple equation for earthquake distribution, *Phys. Rev.*, E., **59,** 7213–7215.

Astiz, L., Shearer, P.M. & Agnew, D.C., 2000. Precise relocations and stress change calculations for the upland earthquake sequence in southern California, *J. geophys. Res.,* **105,** 2937–2953.

Bak, P. & Tang, C., 1989. Earthquakes as a self-organized critical phenomenon, *J. geophys. Res.,* **94,** 635–637.

Ben-Menahem, A., 1995. A concise history of mainstream seismology – origins, legacy, and perspectives, *Bull. seism. Soc. Am.,* **85,** 1202–1225.

Ben-Menahem, A. & Singh, S.J.S., 1981. *Seismic waves and sources*, Springer-Verlag, New York.

Bennett, R.A., Reilinger, R.E., Rodi W. & Li, Y., 1995. Coseismic fault slip associated with the 1992 m(W)-6.1 Joshua-Tree, California, earthquake - implications for the Joshua-Tree Landers earthquake sequence, *J. geophys. Res.,* **100,** 6443–6461.

Ben-Zion, Y., 2001. Dynamic ruptures in recent models of earthquake faults, *J. Mech. Phys. Solids,* **49,** 2209–2244.

Brudy, M., Zoback, M.D., Fuchs, K., Rummel, F. & Baumgartner, J., 1997. Estimation of the complete stress tensor to 8 km depth in the KTB scientific drill holes: implications for crustal strength, *J. geophys. Res.,* **102,** 18 453–18 475.

Brune, J.N., 1968. Seismic moment, seismicity, and rate of slip along major fault zones, *J. geophys. Res.,* **73,** 777–784.

Brune, J.N., Henyey, T.L. & Roy, R.F., 1969. Heat flow, stress and rate of slip along the San Andreas Fault, California, *J. geophys. Res.,* **74,** 3821–3827.

Burnham, C.W., Holloway, J.R. & Davis, N.F., 1969. Thermodynamic properties of water to 1000 C and 10,000 bars, *Geol. Soc. Am. Spec. Paper*, Paper 132.

Burridge, R. & Knopoff, L., 1967. Model and theoretical seismicity, *Bull. seism. Soc. Am.,* **57,** 341–371.

Byerlee, J.D., 1978. Friction of rocks, *Pure appl. Geophys.,* **116,** 615–629.

Carlson, J. M. & Langer, J. S., 1989. Properties of earthquakes generated by fault dynamics, *Phys. Rev. Lett.,* **22,** 2632–2635.

Carslaw, H.S. & Jaeger, J.C., 1986. *Conduction of heat in solids*, 2nd edn. Oxford University Press, Oxford.

Castellaro, S. & Mulargia, F., 2002. What criticality in cellular automata models of earthquakes?, *Geophys. J. Int.,* **150,** 483–493.

Ciccotti, M. & Mulargia, F., 2002. Pernicious effect of physical cutoffs in fractal analysis, *Phys. Rev.*, E., **65,** 37 201–37 204.

Clark, S.P., 1966. *Handbook of physical constants*, Geol. Soc. Am. Mem., New York.

Cotton, F., 1995. Imagerie de la source seismique par inversion des mouvements forts et étude des variations de contraintes associés aux seismes, *PhD Thesis,* Joseph Fourier University, Grenoble.

Dahlen, F.A., 1977. The balance of energy in earthquake faulting, *Geophys. J. R. astr. Soc.,* **48,** 239–261.

Dodge, D.A., Beroza, G.C. & Ellsworth, W.L., 1995. Foreshock sequence of the 1992 Landers, California, earthquake and its implications for earthquake nucleation, *J. geophys. Res.,* **100,** 9865–9880.

Du, Y.J. & Aydin, A., 1993. Stress transfer during 3 sequential moderate earthquakes along the central Calaveras fault, California, *J. geophys. Res.,* **98,** 9947–9962.

Eshelby, J.B., 1969. The elastic field of a crack extending nonuniformly under general anti-plane loading, *J. Mech. Phys. Solids,* **17,** 177–199.

Feder, J., 1988. *Fractals*, Plenum Press, New York.

Freund, L.B., 1998. *Dynamic fracture mechanics*, Cambridge University Press, Cambridge.

Gasperini, P., 2002. Local magnitude revaluation for recent Italian earthquakes (1981–1996), *J. Seismol.,* **6,** 503–524.

Geller, R.J., Jackson, D.D., Kagan, Y.Y. & Mulargia, F., 1997a. Earthquakes cannot be predicted, *Science,* **275,** 1616–1617.

Geller, R.J., Jackson, D.D., Kagan, Y.Y. & Mulargia, F., 1997b. Cannot earthquakes be predicted?, *Science,* **278,** 488–490.

Griffith, A.A., 1920. The phenomena of rupture and flow in solids, *Phil. Trans. R. Soc. Lond.*, A., **A221,** 163–198.

Gutenberg, B. & Richter, C.F., 1956. Earthquake magnitude, intensity, energy and acceleration, *Bull. seism. Soc. Am,* **46,** 105–145.

Hammerberg J.E., Holian B.L., Roder J., Bishop A.R. & Zhou S.J., 1998. Non-linear dynamics and the problem of slip at material interfaces, *Phys.*, D., **123,** 330–340.

Hardebeck, J.L., Nazareth, J.J. & Hauksson, E., 1998. The static stress change triggering model: Constraints from two southern California aftershock sequences, *J. geophys. Res.,* **103,** 24 427–24 437.

Harris, R.A., 1998. Introduction to special section: stress triggers, stress shadows and implications for seismic hazard, *J. geophys. Res.,* **103,** 24 347–24 358.

Harris, R.A. & Simpson, R.W., 1992. Changes in static stress on southern California faults after the 1992 Landers earthquake, *Nature,* **360,** 251–254.

Hasegawa, H.H, Li, C.B. & Ohtaki, Y., 2003. Fractional power scaling of excess heat production, *Phys. Lett.*, A., **307,** 222–228.

Herrmann, H.J. & Roux, S., eds, 1990. *Statistical models for the fracture of disordered media*, North-Holland, Amsterdam.

Hirata, T., Satoh, T. & Ito, K., 1987. Fractal structure of spatial distribution of microfracturing in rock, *Geophys. J. R. astr. Soc.,* **90,** 369–374.

Iler, R.K., 1979. *The chemistry of silica*, 866 pp., John Wiley & Sons, New York.

Jackson, J.A., Gagnepain, J., Houseman, G., King, G.C.P., Papadimitriu, P., Soufleris, C. & Virieux, J., 1982. Seismicity, normal faulting and the geomorphological development of the Gulf of Corinth: the Corinth earthquakes of February and March 1981, *Earth planet. Sci. Lett.,* **57,** 377–397.

Kagan, Y.Y. & Jackson, D.D, 1991. Long-term earthquake clustering, *Geophys. J. Int.,* **104,** 117–133.

Kagan, Y.Y. & Knopoff, L., 1980. Spatial distribution of earthquakes: The two-point correlation function, *Geophys. J. R. astr. Soc.,* **62,** 303–320.

Kanamori, H. & Heaton, T.H., 2000. Microscopic and macroscopic physics of earthquakes, in, *Geocomplexity and the Physics of Earthquakes*, pp. 147–164, eds, Rundle, J.B., Turcotte, D.L. & Klein W., AGU Publ., Washington.

Kasahara K., 1981. *Earthquake Mechanics*, Cambridge University Press, Cambridge, pp. 248.

Kostrov, B.V., 1966. Unsteady propagation of longitudinal shear cracks, *J. appl. Math. Mech.,* **30,** 1241–1248.

Lachenbruch, A.H., 1980. Frictional heating, fluid pressure, and the resistance to fault motion, *J. geophys. Res.,* **85,** 6097–6112.

Lachenbruch, A.H. & Sass, J.H., 1980. Heat flow and energetics of the San Andreas fault zone: Magnitude of deviatoric stresses in the Earth's crust and uppermost mantle, *J. geophys. Res.,* **85,** 6185–6222.

Landau, L.D. & Lifshitz, E.M., 1970. *Theory of elasticity*, 2nd edn. Pergamon Press, Oxford.

Lee, W. H. K., Bennet, R.E. & Meagher, K.L., 1972. A method of estimating magnitude of local earthquakes from signal duration, *U.S. Geol. Surv. Open-File Rep. 28*.

Lockner, D.A. & Okubo, P.G., 1983. Measurements of frictional heating in granite, *J. geophys. Res.,* **88,** 4313–4320.

Magloughlin, J.F. & Spray, J.G., 1992. Frictional melting processes and products in geological materials: introduction and discussion, *Tectonophysics,* **204,** 197–206.

Main, I., 1996. Statistical Physics, Seismogenesis and seismic hazard, *Rev. Geophys. Space Phys.,* **34,** 433–462.

Mase, C.W. & Smith, L., 1987. Effect of frictional heating on the thermal, hydrologic and mechanical response of a fault, *J. geophys. Res.,* **92,** 6249–6272.

McGarr, A. & Gay, N.C., 1978. State of stress in the earth's crust, *Ann. Rev. Earth planet. Sci.,* **6,** 405–436.

McKenzie, D. & Brune, J.N., 1972. Melting on Fault Planes During Large Earthquakes, *Geophys. J. R. astr. Soc.,* **29,** 65–78.

Mora, P., Place, D., Abe, S. & Jaumé, S., 2000. Lattice solid simulation of the Physics of fault zones and earthquakes: the model, results, and directions, in, *Geocomplexity and the Physics of Earthquakes*, pp. 105–126, eds, Rundle, J.B., Turcotte, D.L. & Klein W., AGU Publ., Washington.

Morrow, C.A., Shi, L.Q. & Byerlee, J.D., 1981. Permeability and strength of San Andreas fault gouge under high pressure, *Geophys. Res. Lett.,* **8,** 325–328.

Morrow, C.A., Shi, L.Q. & Byerlee, J.D., 1984. Permeability and strength of San Andreas fault gouge under confining pressure and shear stress, *J. geophys. Res.,* **89,** 3193–3200.

Mulargia, F. & Geller, R.J., 2003. *Earthquake Science and Seismic Risk Reduction*, Kluwer Academic Publishers, Dordrecht, pp. 334.

Ohtake, M. & Narakahara, H., 1999. Seasonality of great earthquake occurrence at the northwestern margin of the Philippine Sea plate, *Pure appl. Geophys.,* **155,** 689–700.

Okada, Y., 1992. Internal deformation due to shear and tensile faults in a half-space, *Bull. seism. Soc. Am.,* **82,** 1018–1040.

Okubo, P.G. & Aki, K., 1987. Fractal geometry in the San Andreas fault system, *J. geophys. Res.,* **92,** 345–355.

Ouillon, G., Castaing, C. & Sornette, D., 1996. Hierarchical geometry of faulting, *J. geophys. Res.,* **101,** 5477–5487.

Purcaru, G. & Berckhemer, H., 1982. Quantitative relations of seismic source parameters and a classification of earthquakes, *Tectonophysics,* **84,** 57–73.

Roder, J., Hammerberg J.E., Holian B.L. & Bishop A.R., 1998. Multichain Frenkel-Kontorova model for interfacial slip, *Phys. Rev.*, B., **57,** 2759–2766.

Roder, J., Bishop A.R., Holian B.L., Hammerberg J.E. & Mikulla R.P., 2000. Dry friction: modeling and energy flow, *Phys.*, D., **142,** 306–316.

Rundle, J.B., Turcotte, D.L. & Klein, W., 2000. *Geocomplexity and the Physics of Earthquakes*, AGU Publ., Washington DC.

Sammis, C.G., Osborne, R. Anerson J., Banerdt, M. & White, P., 1986. Self-similar cataclasis in the formation of fault gouge, *Pure appl. Geophys.,* **124,** 53–78.

Scholz C.H., 1990. *The mechanism of earthquakes and faulting*, Cambridge University Press, Cambridge.

Shearer, P., 1999. *Introduction to Seismology*, Cambriudge University Press, Cambridge.

Sibson, R.H., 1973. Interactions between temperature and pore fluid pressure during earthquake faulting—a mechanism for partial or total stress relief, *Nature, Phys. Sci.,* **243,** 66–68

Sibson, R.H., 1975. Generation of pseuodtachylyte by ancient seismic faulting, *Geophys. J. R. astr. Soc.,* **43,** 775–794.

Sibson, R.H., 1977. Kinetic shear resistance, fluid pressures and radiation efficiency, *Pure appl. Geophys.,* **115,** 387–400.

Sibson, R.H., 1992. Power dissipation and stress levels during seismic faulting, *J. geophys. Res.,* **85,** 6239–6247.

Spray, J.G., 1987. Artificial generation of pseudotachylyte using friction welding apparatus: simulation of melting on a fault plane, *J. Struct. Geol.,* **9,** 49–60.

Stauffer, D. & Aharony, A., 1994. *Introduction to percolation theory*, 2nd edn. Taylor & Francis, Philadelphia.

Tsutsumi, A. & Shimamoto, T., 1997. High-velocity frictional properties of gabbro, *Geophys. Res. Lett.,* **24,** 699–702.

Yoshioka, N., 1986. Fracture energy and the variation of gouge and surface roughness during frictional sliding of rocks, *J. Phys. Earth,* **34,** 335–355.

Zhang, S.Q. & Tullis, T.E., 1998. The effect of fault slip on permeability and permeability anisotropy in quartz gouge, *Tectonophysics,* **295,** 41–52.

# Chapitre 3

# Etude par AFM des mécanismes de propagation des fissures dans les matériaux vitreux

## 3.1 Introduction

En 2003 j'ai décidé de faire une autre expérience de recherche en France, notamment dans le Laboratoire de Physique de l'ENS-Lyon grâce à l'invitation de Sergio Ciliberto, qui était l'un de mes rapporteurs de thèse. L'idée initiale était de participer à ces expériences sur l'étude des émissions acoustiques dans la fracture de matériaux composites à hétérogénéité contrôlée. Une fois sur place, Sergio m'a proposé un acte courageux, c'est à dire de changer profondément de thématique pendant un an, pour m'ouvrir aux problèmes émergents liés au vieillissement des verres colloïdaux. Ce défi, que j'ai relevé après une brève hésitation, s'est révélé très stimulant et il a ouvert de nouvelles perspectives à mon parcours de recherche.

Non seulement il m'a conduit à maîtriser de nouvelles techniques telles que la diffusion dynamique de la lumière (DLS), la mesure fine des fluctuations thermiques des grandeurs physiques et la préparation d'échantillons en conditions très pures, mais il m'a surtout introduit aux problématiques insidieuses et fascinantes des matériaux amorphes. Cet état encore mal compris de la matière condensée se situe entre l'état figé et ordonné des solides et l'état désordonné et très mobile des liquides : il en résulte un état presque figé dans une condition amorphe qui tend à échapper à toute modélisation traditionnelle. Il est en fait un état hors équilibre qui évolue de façon de plus en plus lente vers un équilibre qu'il ne rejoindra jamais, d'où les mots de 'vieillissement' et de système 'frustré' !

Cet état vitreux peut être obtenu dans plein de matériaux différents, tel que les mélanges d'oxydes (verres classiques), les polymères, les métaux, ou bien les liquides moléculaires, si l'on essaye de forcer leur passage de liquide à solide par une trempe thermique très rapide. On a alors ce que l'on appelle la 'transition vitreuse', encore objet de nombreuses études, qui comporte le fort ralentissement de la dynamique au sein de ces matériaux ainsi qu'une forte augmentation de leur viscosité.

Pendant mon stage postdoctorale à l'ENS-Lyon (auquel je dédierai une première section séparée du reste du chapitre) j'ai eu l'occasion d'avoir des contacts avec Luca Cipelletti de l'actuel LCVN à propos des ses techniques avancées de DLS appliquées au vieillissement des systèmes colloïdaux et, dans le même laboratoire, avec Christian Marlière, qui était en train d'obtenir des résultats enthousiasmants sur les mécanismes de propagation de fissures dans les verres d'oxydes étudiés à l'échelle nanométrique par microscopie à force atomique.

La rencontre intéressante avec le premier m'a stimulé à approfondir mes analyses sur les fluctuations dans les systèmes vitreux, mais le '*virus*' de la fracture était prés de me rattraper et c'est comme ça que je me suis retrouvé l'année suivant dans l'équipe 'Nanomécanique' de Christian Marlière pour commencer les études sur la fracture des verres d'oxyde que je relaterai dans la suite de ce chapitre et qui sont au centre de mes projets actuels.

## 3.2 Etude du vieillissement dans les verres colloïdaux

Comme annoncé, cette section ne parle pas de fractures, mais d'une phase de mes études dédiée à l'étude des fluctuations dynamiques qui accompagnent le vieillissement des matériaux amorphes.

Plus spécifiquement, l'objet d'étude est une suspension colloïdale de particules chargées de taille nanométrique (Laponite). La particularité de ce système est que pour des concentrations très faibles (de l'ordre de 3%) il présente une transition d'un état plutôt fluide à un état plutôt solide, que l'on peut appeler un 'verre colloïdal' en raison de sa structure amorphe. Cette transition se passe à température ambiante et elle n'est pas liée à une transition vitreuse traditionnelle, mais plutôt à un phénomène d'encombrement. Ceci est tout à fait analogue à ce qui arrive dans les systèmes de sphères dures à forte concentration, avec la différence que le volume effectif occupé par les particules de Laponite est plutôt déterminé par la répulsion électrostatique entre les particules et donc par l'activité ionique de la solution hôte.

En analogie aux verres traditionnels, après figeage, les propriétés physiques de ce système (telles que la viscosité et la résistivité électrique) continuent à évoluer ('vieillir') de plus en plus lentement avec de lois typiquement logarithmiques. Le ralentissement de la dynamique interne peut aussi être bien mis en évidence par la mesure de la fonction de corrélation par DLS.

De nombreux modèles sont proposés pour modéliser ce ralentissement de la dynamique (références in Bouchaud *et al.*, 1998), mais surtout pour donner un fondement thermodynamique à ce système hors équilibre. Curgliandolo et Kurchan (1993), notamment, proposent de définir une température effective de ces systèmes à partir de la mesure de leurs fluctuations thermiques, en analogie au théorème fluctuation dissipation valable pour les systèmes à l'équilibre :

$$S(\omega) = \frac{2k_B T}{\pi \omega} \mathrm{Im}[\chi_{Vq}(\omega)]$$

Ceci relie la densité spectrale S(ω) des fluctuations thermiques d'une observable du système à la fonction de réponse correspondante χ(ω). On obtient ainsi une température effective $T_{eff}(\omega)$ (voir figure 3.2.1) qui est consistante avec la température ambiante pour les degrés de liberté rapides du système, mais qui peut en dévier de façon significative pour les degrés lents à thermaliser (Bellon *et al.*, 2001).

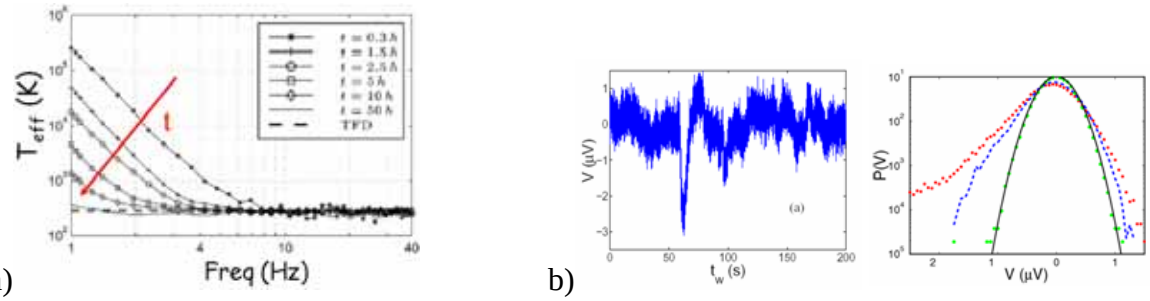


Figure 3.2.1 a) Evolution de la température effective au cours du temps dans une suspension de Laponite à partir de mesures spectrales diélectriques. b) intermittences dans les fluctuations temporelles du signal diélectrique et asymétrie de leur distribution.

Ma participation dans ce projet a porté sur la dynamique des fluctuations dans le domaine temporel (voir figure 3.2.1 b). Sans vouloir rentrer ici dans les détails (pour lesquels je renvoie aux articles Buisson, Ciccotti *et al*., 2004 et Bellon *et al.*, 2004), j'ai centré mon étude sur les fluctuations du bruit diélectrique aux bords d'une cellule remplie de Laponite et du bruit qui affecte la fonction de corrélation dans la diffusion dynamique de la lumière dans la même substance, afin de mieux comprendre l'origine des phénomènes d'intermittence liés au processus de vieillissement.

L'expérience a pour but de mettre en relation les intermittences dans la fonction de corrélation de la lumière diffusée avec les intermittences dans les mesures du bruit diélectrique pour comprendre si elles sont liées au même processus et si l'on peut identifier une dynamique hétérogène au sein du milieu.

Les premiers résultats concernant les mesures diélectriques montrent que les intermittences sont plus intenses lorsqu'on augmente la concentration de Laponite dans l'eau, en analogie à ce que l'on obtient en augmentant la vitesse de trempe thermique dans un verre de polymère (Buisson, Ciccotti *et al*., 2004 ; Bellon *et al.*, 2004). En mettant en œuvre des mesures du bruit diélectrique en DC, j'ai mis en évidence la présence de marches dans le signal et des alternances de zones de calme et d'activité intermittente, présentes sur toute la gamme d'échelles temporelles mesurées.

Pour ce qui concerne les mesures de diffusion dynamique de lumière, j'ai mis au point un dispositif qui permet à la fois de bien observer le vieillissement des fonctions de corrélation de la Laponite et d'utiliser la technique de « Time Resolved Correlation » développé par Luca Cipelletti (Cipelletti *et al.*, 2003) pour mettre en évidence la présence d'intermittences dans la fonction de corrélation. Suite à mon transfert au LCVN, je suis à même de continuer cette investigation à travers le co-encadrement avec Luca d'étudiants de master de l'UM2. Les résultats sont encourageants, mais encore en cours de validation.

J'arrêterais ici cette parenthèse sur les systèmes colloïdaux pour revenir au sujet principal : la fracture.

## 3.3 La fracture des verres et l'équipe 'Nanomécanique'

Dans mon passé d'études sur les roches, le verre représentait un matériau de test idéal et fiable : transparent, homogène, bien élastique dans ses déformations avant rupture. J'étais loin d'imaginer la complexité intrinsèque à ce matériau amorphe, hors équilibre et d'une chimie souvent complexe. Tous ces aspects se révèlent de façon dramatique quand on essaye d'étudier ce qui se passe à l'échelle nanomètrique aux alentours le la pointe de fissure.

Le verre est le prototype du matériau 'fragile', caractérisé par la rupture soudaine lorsque l'intensité des contraintes autour de l'un de ses défauts dépasse une valeur critique. L'avancement des fissures dans les matériaux fragiles est schématisé comme la rupture consécutive des liaisons atomiques présentes en pointe de fissure, en l'absence d'une déformation plastique dans la zone circonstante. En présence d'humidité dans l'atmosphère, les fissures sont en mesure de se propager même pour des contraintes plus faibles que les valeurs critiques. C'est ce que l'on appelle la 'propagation sous-critique' (déjà discutée pour les roches) ou 'corrosion sous contraintes' pour emphatiser la coopération entre la concentration de contraintes à la pointe de fissure et l'action corrosive des molécules d'eau (Wiederhorn, 1967). Dans ces conditions la propagation peut devenir très lente (voir figure 3.3.1 b), mais elle est censée rester un processus qui sépare les atomes de façon individuelle selon le paradigme de la fragilité (Lawn, 1993).

Quand en 2004 je suis arrivé dans l'équipe Nanomécanique de l'ex Laboratoire des Verres, Christian Marlière venait d'atteindre d'importants résultats concernant la mise en évidence d'un phénomène de ductilité à l'échelle nanométrique qui modifiait profondément la vision classique de la propagation de fissures dans les verres (Célarié *et al.*, 2003), ceci à l'aide de son thésard Fabrice Célarié et d'une collaboration avec Elisabeth Bouchaud et Daniel Bonamy du CEA Saclay.

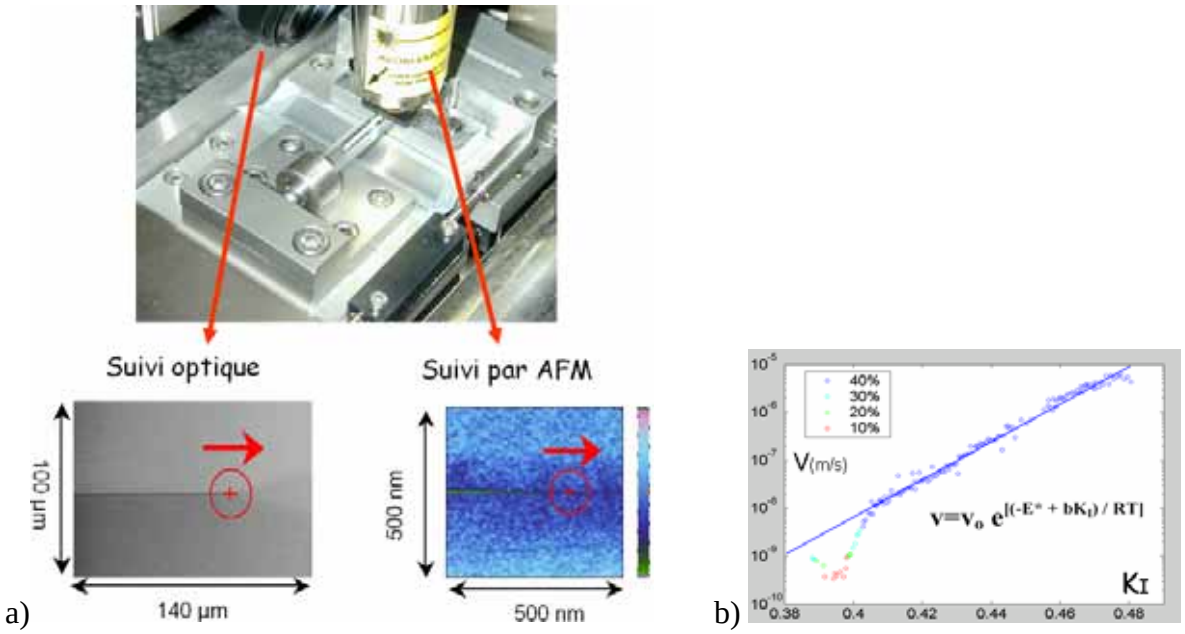


Figure 3.3.1 a) Aperçu de la platine d'application des contraintes et images typiques de la pointe de fissure par microscopie optique et AFM. b) Exemple de mesure d'une courbe K-v pour un échantillon de verre de silice pure (la déviation en couleur représente l'effet d'une variation d'humidité relative).

Ces études ont eu lieu sur un banc expérimental récemment mis en place au LCVN (voir figure 3.3.1 a), centré sur un équipement de dernière génération de microscopie à champ proche, combiné à une table d'application des contraintes mécaniques, l'ensemble travaillant en atmosphère soigneusement contrôlée. En combinant ainsi microscopie optique et Microscopie à Force Atomique (AFM), ils ont été en mesure de suivre en temps réel l'avancée de la tête de fissure pour des vitesses comprises entre $10^{-3}$ m/s et $10^{-12}$ m/s. Pour les détails de ce montage et de l'échantillon DCDC utilisé je renvoie à la thèse de Fabrice Célarié (2004).

Après de nombreux efforts de l'équipe technique du laboratoire, la réduction des bruits environnementaux est devenue suffisamment efficace pour permettre des observations de la fissure pendant son avancement (in-situ) sur des zones de 100 nm, ce qui rendait possible l'accès en temps réel aux mécanismes de propagation à l'échelle typique des hétérogénéités des verres, où on pouvait s'attendre à des déviations par rapport au mécanisme idéal de fracturation fragile.

Lors de mon arrivée deux résultats notables avaient déjà été obtenus :

1) Le premier a été l'observation que l'avancement lent d'une fissure dans un verre d'aluminosilicate de lithium se produit à température ambiante (T<<Tg) par un mécanisme de nucléation, croissance et coalescence de cavités de taille nanométrique comme montré en figure 3.3.2.

a) 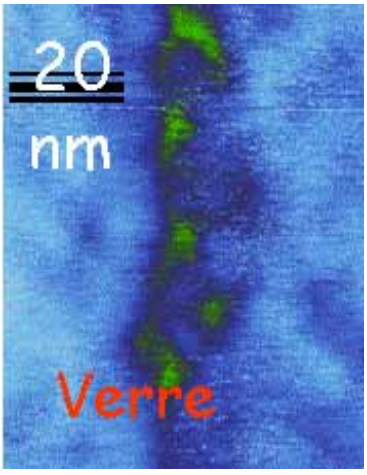

b) 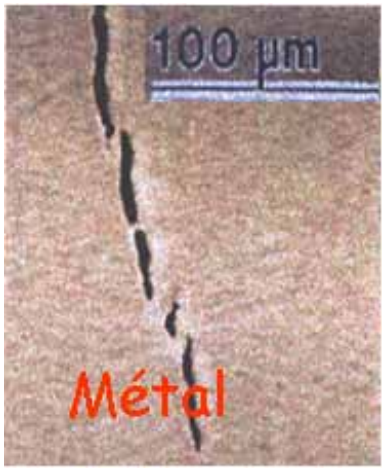


Figure 3.3.2 Mécanisme de nucléation, croissance et coalescence de cavités a) à l'échelle nanométrique dans un verre et b) à l'échelle micrométrique dans un alliage métallique.

Cette observation fait un lien entre les mécanismes de fissuration des matériaux ductiles (métaux) et des matériaux fragiles (verres). La différence s'opère au niveau des échelles de longueur des cavités respectivement micrométriques et nanométriques, mais aussi au niveau de l'échelle temporelle : pour observer cette ductilité dans les verres il faut que la fissure se propage à une vitesse inférieure à $10^{-10}$ m/s (Célarié *et al.*, 2003) afin de laisser le temps aux mécanismes de relaxation lente du verre.

2) Une autre observation très intéressante concerne l'apparition d'un nuage de plots avec une forme parabolique aux alentours de la pointe de fissure dans des verres sodo-silicatés (figure 3.3.3). L'origine physique de ce phénomène est vraisemblablement liée à une diffusion locale des atomes de sodium, induite par le fort gradient des contraintes autour de la pointe de fissure, et qui peut être mise en évidence grâce aux longues échelles de temps associées à la très faible vitesse de fissuration qui peut être atteinte.

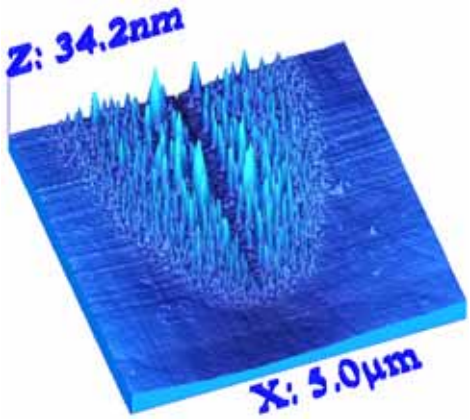


Figure 3.3.3. Image AFM de la topologie de surface autour de la tête de fissure dans un verre sodo-silicaté.

Ces deux observations ont profondément attiré mon attention et je me suis plongé dans des études pour connaître tous les détails de la technique de mesure et les subtilités de la physico-chimie des verres d'oxydes pour pouvoir réussir une interprétation bien fondée de ces phénomènes.

## 3.4 Le rôle de l'eau dans la propagation des fissures dans les verres

Une interrogation importante est la constatation que la teneur en humidité relative a aussi des effets importants sur la formation des plots de sodium et sur l'altération des propriétés de la couche superficielle des verres.

J'ai donc décidé, en parallèle aux efforts d'interprétation des observations précédentes, de démarrer une nouvelle étude originale concernant un approfondissement sur le rôle de l'eau dans la propagation des fissures dans les verres. Il est bien connu que l'humidité relative a un effet direct sur la vitesse d'avancement des fissures dans le domaine de corrosion sous contraintes (Wiederhorn, 1967), ce qui est expliqué par la contribution dans l'énergie de fracture de l'énergie de chimisorption des molécules d'eau à travers la réaction d'hydrolyse :

$$\equiv Si—O—Si\equiv + H_2O \Rightarrow 2 \equiv SiOH$$

Mais l'eau peut jouer un rôle plus subtil en fonction des différents parcours d'accès au réseau formateur du verre constitué principalement de tétraèdres de silice :

(1) formation d'une couche de condensation à la surface extérieure du verre,
(2) formation d'un ménisque de condensation à l'intérieur de la cavité de fissure,
(3) perméation de molécules d'eau dans le volume de la silice,
(4) préexistante d'un taux de molécules d'eau dans la structure du verre,
(5) interdiffusion des ions $H^+$ (ou $H_3O^+$) avec les cations alcalins plus mobiles présents dans le verre.

### 3.4.1 Etude de la formation d'un condensat capillaire à la pointe de fissure

Pour pourvoir mieux comprendre le rôle de l'eau, nous avons décidé d'étudier un verre modèle de composition bien définie, soit un verre de silice très pure (Suprasil 311) pour lequel il serait aussi possible de réaliser des simulations de dynamique moléculaire. L'expérience réalisée est analogue aux expériences précédentes de suivi de fissure, mais avec la particularité d'induire des cycles très lents de variation de l'humidité relative (en atmosphère d'azote) avec des extrêmes de l'ordre de 1% et 80%.

Les premières observations topographiques ont permis de séparer la pointe de fissure en trois zones (voir figure 3.4.1 a) : dans la zone A la fissure est bien ouverte ; dans la zone C le matériaux est déformé par les contraintes liées à la pointe de fissure (c'est aussi le lieu de nucléation des cavités), dans la zone B on observe un léger relief qui, comme nous le montrerons, est associé à la présence d'un ménisque liquide à l'intérieur de la fissure (Wondraczek, Ciccotti *et al.*, 2006).

La signature caractéristique de la présence du ménisque d'eau est la présence d'un contraste marqué sur le signal de phase AFM en mode 'tapping', soit le déphasage entre la stimulation et l'oscillation du levier (figure 3.4.1 b). Un effort expérimental très poussé a été consacré à l'analyse correcte de ce signal. Il sera détaillé dans la section 3.5.

En conditions d'asservissement à amplitude d'oscillation constante, ce signal est lié à l'énergie dissipée dans le contact entre la pointe de l'AFM et la surface de l'échantillon (Cleveland *et al.*, 1998 ; Aigouy *et al.*, 2006). Il faut compter qu'en conditions très pures, la surface du verre est toujours recouverte d'une fine couche d'eau condensée d'épaisseur nanométrique (Nony *et al.*, 2002). Le contact entre la pointe AFM (en silicium, mais

oxydée à la surface) et l'échantillon comporte donc la formation d'un pont capillaire qui induit une force attractive supplémentaire. L'hystérésis entre les valeurs de cette force à l'approche et au retrait de la pointe est responsable d'une dissipation nette d'énergie dans l'oscillation du levier (Zitzler *et al.*, 2002). Quand la pointe AFM passe de la surface mouillée du verre au ménisque d'eau, l'hystérésis dans la force capillaire va se retrouver augmentée à cause du fait que le ménisque est alimenté par une source d'eau qui lui permet une plus longue élongation avant d'être brisé par l'éloignement de la pointe. Ceci est la cause du fort contraste du signal de phase qui indique les contours du ménisque liquide.

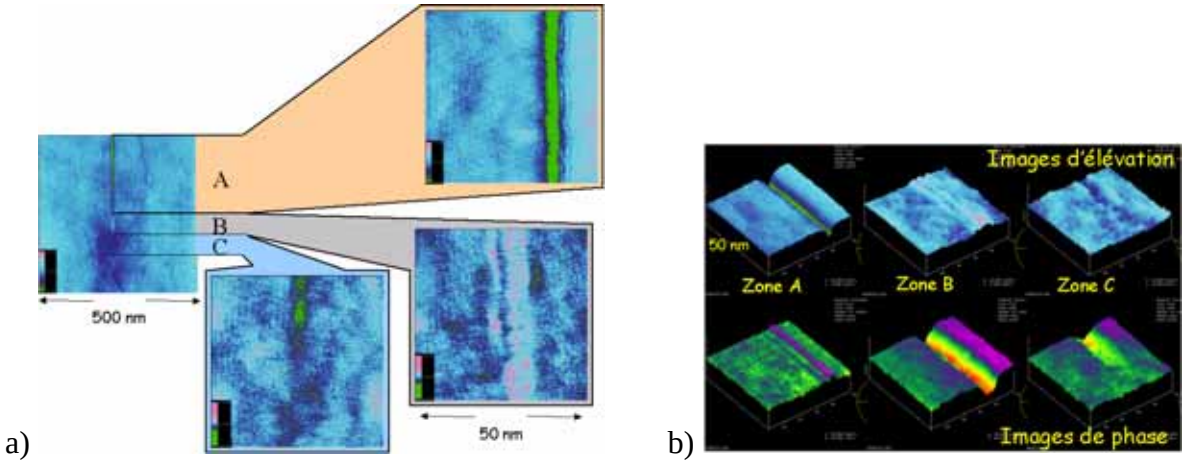


Figure 3.4.1 a) Observation par AFM de la topographie de la surface d'un verre de silice aux alentours de la pointe de fissure. La couleur verte représente des creux, la couleur rose des reliefs. b) Comparaison du signal topographique avec le signal de phase pour les trois zones de la pointe de fissure.

En réalité la situation est plus complexe que ça à cause de la non-linéarité de l'interaction pointe-surface, qui comporte la présence d'une multi-stabilité dans l'oscillation du levier. Je laisse ces explications à l'article qui suit (George, Ciccotti *et al.*, 2006), dans lequel nous discutons aussi les conditions de formation et d'évolution du ménisque liquide en fonction des changements de l'humidité relative.

La présence de ce ménisque en pointe de fissure, que l'on peut expliquer par un phénomène de condensation capillaire, a des conséquences très importantes sur la physico-chimie de la pointe de fissure lors d'une propagation très lente. D'un coté la présence d'eau liquide nous éloigne d'expliquer la cinétique d'avancement de la fissure en relation à la cinétique de diffusion des molécules d'eau vers les sites d'hydrolyse à la pointe. De l'autre coté la taille très réduite de ce ménisque (qui s'étend sur une longueur de l'ordre de la centaine de nanomètres, tout en restant confiné entre deux parois distantes de quelques nanomètres) constitue une condition très différente par rapport à la fracture dans l'eau. En premier lieu parce-que les échanges ioniques et de corrosion avec le verre peuvent altérer la composition (et notamment le pH) de ce liquide, qui est déterminant pour la chimie de la corrosion à la pointe. En deuxième lieu, la présence d'une interface air/eau avec un rayon de courbure nanométrique comporte une forte dépression à l'intérieur de ce ménisque avec des conséquences directes sur la chimie de la réaction, mais aussi sur les contraintes qui agissent localement sur la pointe de fissure.

# FORMATION AND EVOLUTION OF A CONFINED LIQUID CONDENSATE AT THE CRACK TIP IN GLASSES

M. George, M. Ciccotti,
Laboratoire des Colloïdes, Verres et Nanomatériaux, UMR CNRS 5587,
University of Montpellier 2, France

L. Wondraczek,
Corning European Technology Center,
Corning SAS, Avon, France

A. Dittmar, C. Oelgardt, F. Célarié,
Institute of Non-Metallic Materials,
Clausthal University of Technology, Germany

C. Marlière
Laboratoire de Tectonophysique, UMR CNRS 5568
University of Montpellier 2, France

## ABSTRACT

Crack propagation in oxide glasses at low crack velocities is controlled by stress corrosion. Proper knowledge of the crack tip chemical environment is thus crucial to understand the slow fracture process of these materials. The formation of a liquid condensate in the confined area of the crack tip is theoretically expected and is classically mentioned to explain specific behavior during the crack propagation. Since this condensate is of the nanometer scale and cannot be traced post mortem, it had yet never been observed. This paper reports the experimental evidences of the presence of a liquid condensate at the tip of a crack propagating by stress corrosion in silica glass. The observation has been performed in real time under carefully controlled atmosphere through in situ phase imaging by atomic force microscopy (AFM). The evolution of the condensate has been followed as a function of the relative humidity. The impact of those evidences of the liquid condensate, added with information on its size or evolution kinetic will be discussed.

## INTRODUCTION

The study of crack propagation at slow velocity in oxide glasses is of great interest on both practical and fundamental bases. Long-term behavior of vitreous material is particularly important considering the large proportion of these materials used in architectural structures and their role in the encapsulation of nuclear wastes. On the fundamental aspect, slow advancing crack can be an accurate probe of the molecular structure of glasses.

Stress corrosion is known to control slow propagation of crack in oxide glasses. The preferential corrosive role of water molecules at the crack tip sustaining tensile stresses is generally acknowledged[1,2,3,4]. Wiederhorn et al have shown that in the stress corrosion regime, for low applied stresses, crack velocity was highly dependent on relative humidity[2,3]. The physical and chemical environment in which stress corrosion takes place, as well as the mechanisms of transport of the water molecules towards the crack tip are less well-established[5].

Several experimentally observed anomalous behaviors[5,6,7] do not perfectly fit in the global model for crack velocity proposed by Wiederhorn et al.

Under usual conditions of temperature and pressure, capillary condensation theory predicts the presence of a liquid condensate between the newly created surfaces of the crack which at the vicinity of the crack tip are only distant from a few nanometers[8]. Such a liquid condensate is classically acknowledged to account for the anomalous behavior that can be observed. Its presence will indeed influence largely the chemistry of the corrosion since direct contact between liquid water and glass will replace interactions between isolated gas water molecules and glass made uneasy inside the confined area created at the crack tip in a fragile material.

To our knowledge, observations of the condensate have not yet been reported by other teams. In situ observations that are necessary to reveal such a phenomenon are indeed difficult to perform with the required resolution. In this paper, we will present evidences of the liquid condensate at a crack tip slowly propagating in a silica glass under variable relative humidity. These evidences have been obtained by Atomic Force Microscopy (AFM) in situ observations of the crack propagation.

## 1. EXPERIMENTAL

An experimental technique has been developed in the Laboratoire des Colloides, Verres et Nanomateriaux (LCVN) from the University of Montpellier to observe in situ by AFM the propagation of crack in glass at slow velocity under controlled environmental conditions, as described in a previous paper[9].

Samples of type III silica glass (Suprasil 311, Heraeus, Germany) with a bulk $OH^-$ - content of 200 ppm have been studied using this technique. They were cut into 4x4x40 $mm^3$ rods with a drilled hole of 1 mm diameter in the centre to fit with doubled cleavage drilled compression (DCDC) geometry. The surface was mechanically and chemically polished with $CeO_2$ to a RMS roughness of 0.25 nm for an area of 10x10$\mu m^2$.

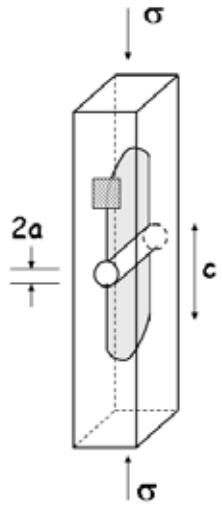


*Figure 1 - Geometry of the sample. The hatched zone corresponds to the zone observed by AFM. The two cracks propagating on both sides of the hole (in grey) are in opening mode (mode I).*

DCDC technique allows to create mode I tensile cracks with highly controllable speeds in oxide glasses. For an applied stress $\sigma$, the stress intensity factor $K_I$ in our DCDC experiment is given by $K_I = \sigma a^{1/2}/(0.375c/a+2)$, where $a$ is the radius of the hole in the DCDC specimen and $c$ is the length of the crack[10]. The load cell has been interfaced with an AFM (D3100, Veeco) used in tapping mode to observe the intersection between the moving crack plane and the polished

surface of the sample, as indicated in figure 1. The neighborhood of the crack tip can thus be imaged for velocities from $10^{-9}$ m.s$^{-1}$ to ~$10^{-12}$ m.s$^{-1}$. Optical microscopy can be used to record higher crack velocities.

Generation and propagation of the crack were performed at 22.0±0.5 °C in a carefully controlled atmosphere of pure nitrogen and pure water vapor, which allows to vary relative humidity (RH) between ~ 1 % and 80 % (± 2 %).

## 2. RESULTS AND DISCUSSION

### 2.1 Phase contrast related to liquid layers

To explain how AFM can be used to track the presence of water on a surface, we will firstly review briefly the principle of tapping mode. Tapping mode is currently used to image the topography of surfaces, with lower wearing of both the sample and the tip, but can also be used to obtain information on the local mechanical properties of the surface[11]. The vibrating tip-cantilever system can be modeled as a harmonic oscillator sustaining non-linear interactions with the surface of the sample. In tapping mode (also called amplitude modulation mode), this oscillator is driven at a chosen frequency $\omega$, close to the resonance frequency $\omega_0$. The displacement z of the oscillator as a function of time can then be written as:

$$z(\omega,t) = A(\omega) \cos(\omega t+\phi(\omega)) \quad (1)$$

where A is the amplitude of the oscillations and $\phi$ the phase delay between the measured oscillation and the stimulation of the cantilever.

For a cantilever without interaction with a surface, the phase decrease from 0 to -180° when the frequency goes from 0 to infinity and is equal to -90° at the resonance when $\omega=\omega_0$. The amplitude of the oscillation during imaging (amplitude set point) is determined either automatically or by the operator. The feedback loop of the microscope is then used to maintain constant this amplitude by acting on the vertical position of the cantilever holder. Different signals can be recorded, among which:

- The amplitude variation $\Delta A$ (error signal) which should be as low as possible if the parameters of the feedback loop are well defined.
- The vertical displacement of the cantilever, which gives essentially topographical information.
- The phase $\phi$ of the oscillator, which can be related to dissipative interactions between the tip and the substrate and thus yields useful information on the local mechanical properties of the surface, such as viscosity or adhesion.

The non-linear behavior of the oscillator is difficult to analyze in a quantitative way and focuses the efforts of many researchers[12,13]. One of the main difficulties lays in the existence of multi-stable solutions for the response of the oscillator. These multi-stabilities have been frequently documented to explain the hysteresis commonly observed in amplitude- and phase-distance curves[12-14]. Typically, two stable modes of oscillation can be observed which corresponds to different interactions between the tip and the surface. One of these modes corresponds to an interaction which is mainly attractive, that means that during the oscillation the tip is not brought closely enough to the surface to feel the repulsive forces. This mode is also called “non-contact” mode. In the second mode, called “intermittent contact” mode, the tip comes closer to the surface and feels both the attractive forces and the repulsive forces. Figure 2 represents two theoretical typical amplitude- and phase- distance curves[12-15] for a driven

frequency chosen below the resonant frequency ($\omega<\omega_0$). Solid line curve corresponds to a pure "non contact" mode and dashed line curve to the transition between a "non-contact" and an "intermittent contact" mode. The two modes are easily distinguishable on the phase-distance curves. The "non-contact" mode, respectively the "intermittent contact" mode, corresponds to a phase which is below, respectively above, -90°. In both modes, the amplitude and the frequency of oscillations being constant, the power dissipated by the interactions between the tip and the surface is proportional[16] to $\sin(\phi)$. An increase of dissipative interaction between the tip and the surface will thus corresponds in both modes to a phase closer to -90° (which means an increase of the phase in "non-contact" mode and a decrease of the phase in "intermittent contact mode).

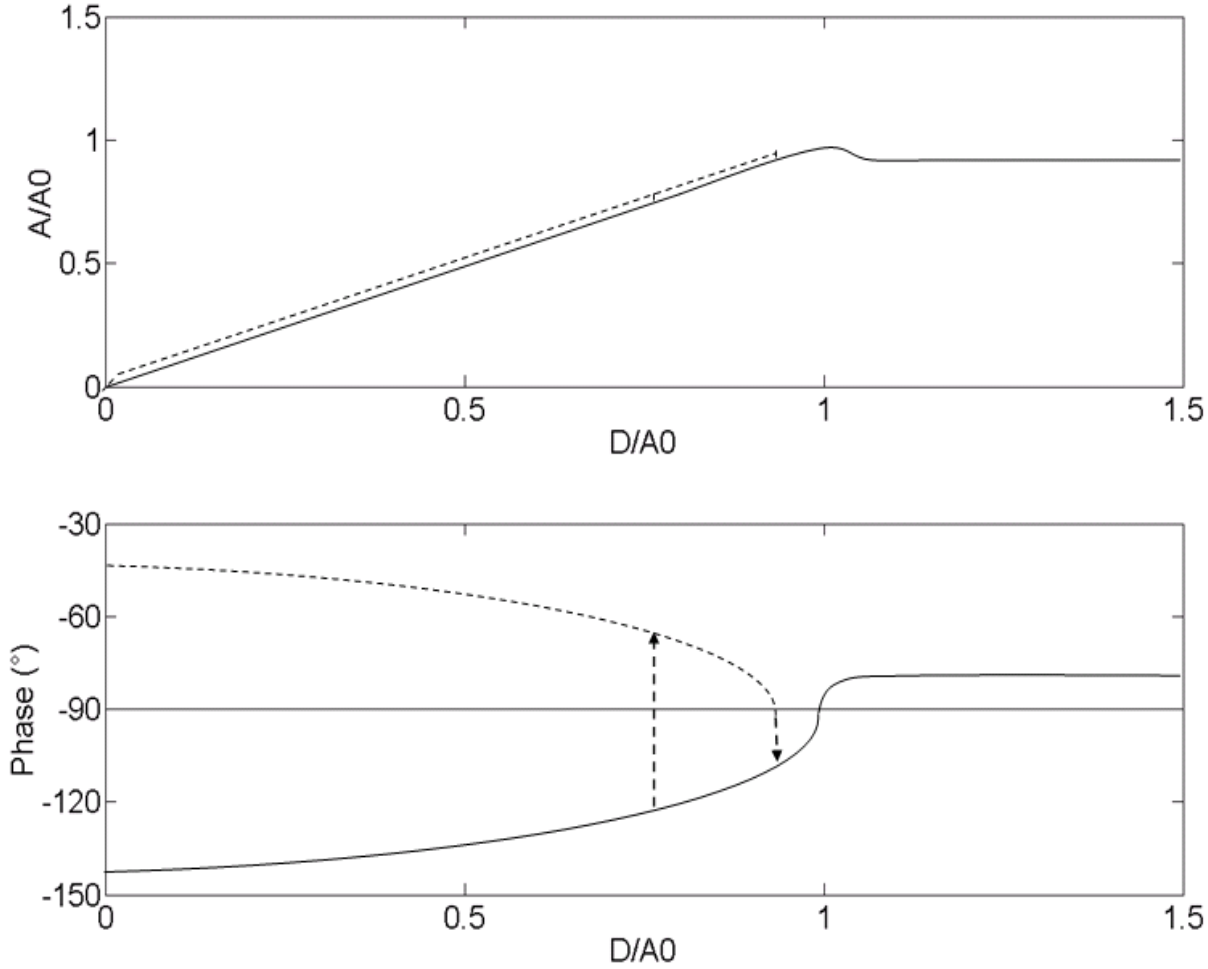


*Figure 2 - Scheme of usual amplitude- and phase- distance curves for $\omega<\omega_0$. $A_0$ is the free amplitude at the resonance and D the distance between the equilibrium position of the cantilever and the surface. Solid line represents the "non contact" branch. Dashed line is the "intermittent contact" branch.*

The interactions leading to the predominance of one or the others of these modes are not yet well-established, but the influence of relative humidity has been shown by several experiments[14,17]. Under normal conditions of temperature and pressure, even at very low relative humidity (below 1%), silica glass and silicon tips are covered by a few layers of water molecules[18,19] (layer thickness around 0.5 nm). An increase of the relative humidity leads to the formation of a thicker liquid film[8,18,19] (towards layer thickness of the order of the nanometer).

When intermittent contact occurs, the minimal contact distance between the tip and the interface glass sample/water layer is $d_c$ = 0.165 nm[18]. For non-contact mode, in our experiments, the minimal distance between the tip and the surface has been found to be around $d_c$+0.8 nm (around 1 nm). From these values, one can assume that in both modes, in our glass box, the water layers on tip and on glass will connect during the oscillation leading to formation of capillary neck and thus the existence of capillary forces. The strength of the capillary neck is dependent on the volume of water available[8] and so will be the dissipation induced by the formation and destruction of this neck. Another effect of the growth of water layer is that it makes purely attractive "non contact" mode become more and more predominant[14].

2.2 Observations of the condensate at the crack tip and analysis

Tapping mode AFM observations of the crack tip have been performed during an overall cycle of variation of the relative humidity. The relative humidity as a function of time is shown in figure 3a. The velocity of the crack varied as a function of humidity and applied stress between 0.05 and 1 nm.s$^{-1}$.

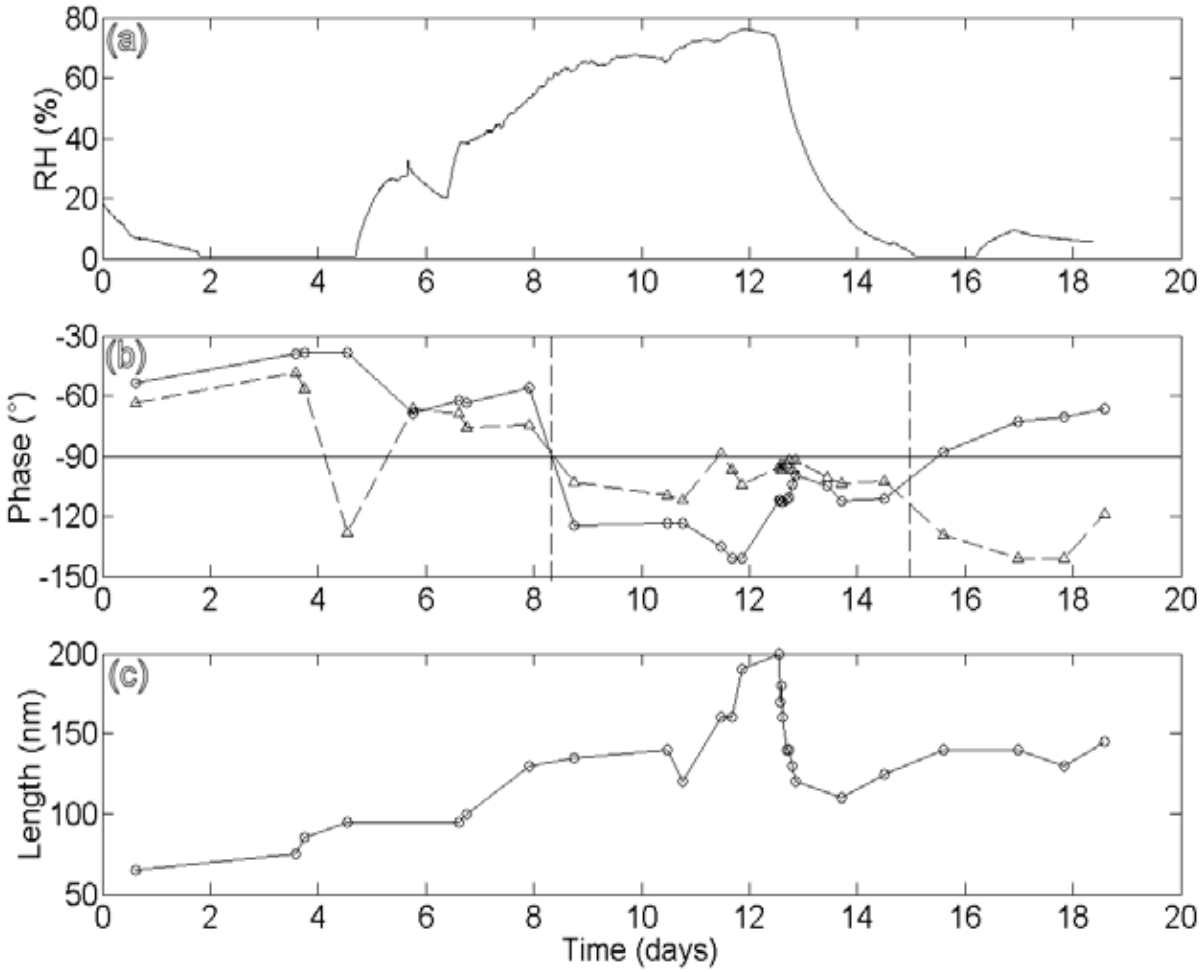


*Figure 3 - Curves of relative humidity (a), phase (b) and condensate length (c) vs time. In graph (b), the circles (solid line) correspond to the average phase on the silica glass the triangles (dashed line) correspond to the phase on the condensate.*

Figure 4 represents two phase images of the neighborhood of the crack tip at two levels of relative humidity of respectively 1% and 70%. On both images, the crack is vertical, propagating from top to bottom of the picture. The crack tip is characterized by a distinct area showing an important contrast of phase. On the left image, at low humidity, the contrast is negative, whereas on the right image, at high humidity, the contrast is positive. We will show that in both cases this contrast can be associated with an increase of the dissipation, revealing the presence of a liquid condensate at the crack tip.

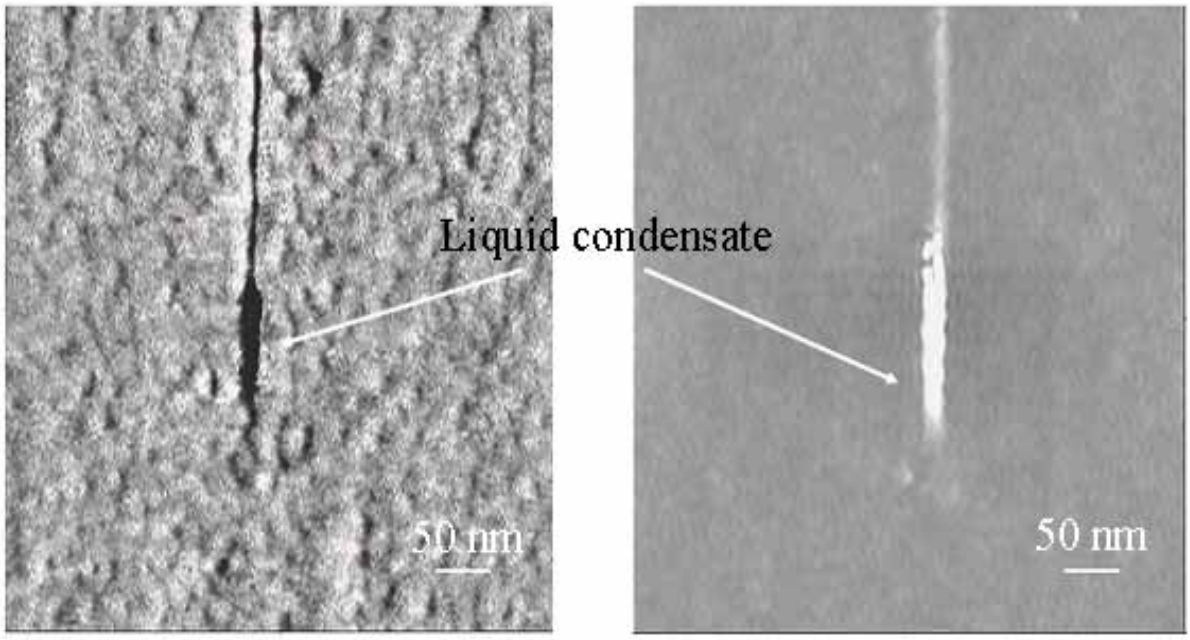


*Figure 4 - AFM phase images of the crack tip. (left) RH = 1% (right) RH = 70%. The phase is coded in grey level and increases from black to white.*

In figure 3b, the average phase on the silica surface (circles) has been reported as a function of time, in comparison with the maxima phase measured in the area of the crack tip (triangle). During the several weeks of the experiments, the amplitude set point, frequency and amplitude stimulation of the oscillation have varied, but in a range small enough for the variation of the phase to be analyzed qualitatively. The curve presents three areas:

- From day 0 to day 8, both the average phase on the silica surface and the maxima phase at the crack tip are higher than -90° (one point excepted for which the behavior is similar to the points in third area). The AFM works in “intermittent contact” mode. The phase in the area around the crack tip is closer to -90°: this area is more dissipative than the rest of the silicate surface.
- From day 8 to day 15, both the average phase on the silica surface and the maxima phase at the crack tip are lower than -90°. The AFM works in “non contact” mode. The phase in the area around the crack tip is still closer to -90°: this area is still more dissipative than the rest of the silicate surface.
- From day 15 to day 18, the AFM remains in “non contact” mode in the area around the crack tip but works in “intermittent contact” mode on the rest of the silicate surface.

From the explanation given in section 2.1, the variation of phase observed during the cycle of relative humidity variation can be well explained by condensation of water at the crack tip. For low relative humidity, at the beginning of the observations, the amount of water on the surface of the glass is quite low, for the set point amplitude which has been chosen, the AFM operates in “intermittent contact” mode. At the crack tip, the existence of a liquid condensate that has not been dried out by the preliminary drying of the set-up, entails an increase of the capillary dissipative interaction in this area. With the increase of relative humidity, the thickness of water layer on all the surfaces increase. When this thickness is large enough, the AFM switches to “non contact” mode. The area around the crack tip still holds a larger tank of water for capillary forces and we can observe that the dissipation is still larger in this area. The switch between the two modes of operation of the AFM explains the inverted contrast noticed in figure 4. When the atmosphere is dried again, we can see that, after a certain delay, the AFM starts to operate in “intermittent contact” mode again on the silicate glass surface. Yet, it still works in “non contact” mode on the condensate. This leads us to think that the condensate has not been totally dried out.

The persistence of the condensate is confirmed by figure 3c, in which the length of the condensate along the longitudinal direction of the crack has been plotted as a function of time. The length of the condensate as deduced from raw AFM data has been corrected, taking into account propagation speed of the crack and drift of the AFM. Due especially to the difference of contrast between one mode and the other, the length is difficult to evaluate precisely and the error on the measurement have been evaluated to be of 20 nm. During the experiments, we can yet see that the condensate grows regularly with the increase of the relative humidity from 70 nm to 200 nm. When decreasing the relative humidity, the length begins to decrease but then stop at a size of around 140 nm even when the RH is below 1%. The size of the condensate has not been observed to start reducing more during the experiment presented in this paper. In a preliminary experiment performed on the same experimental device by Wondraczek et al[20] what seemed the beginning of the dry out of the condensate has been observed after 5 days in dry atmosphere.

Condensation of water is expected at equilibrium, between surfaces as close as the lips of the cracks near the crack tip. The curvature of a condensate meniscus $r_K$ is related to the relative humidity radius by the Kelvin equation[21]:

$$r_k = \frac{\gamma.V}{RTlog(P/P0)} \tag{2}$$

with $\gamma$, the surface energy of water; V, the molar volume of liquid water; T, the temperature and $P/P_0$, the relative humidity.

With our experimental conditions, the Kelvin radius is plotted versus the relative humidity in figure 5. Since the velocity of crack propagation in this study is low, the use of equilibrium of the meniscus is relevant. The condensate will grow with relative humidity until a distance from the crack tip where the separation between the lips of the crack is around twice the Kelvin radius. The crack in the fragile materials is very sharp: the average angle formed by the lips of the crack can be estimated to be 2.5° from measurements of the width of the crack as a function of the distance from the crack tip. From figure 3, the length of the crack is then expected to vary from 50 nm for RH equal to 20% to 180 nm for RH equal to 70%. This good agreement between theoretical length of the condensate and the size of the phase contrast area corroborates that this is indeed the condensate which is observed. It is useful to remark that the roughness of the crack

new surfaces (of the order of the nanometer) will however play an important role in the size and in the dynamic of evolution of the condensate. Bocquet et al have shown long time dependencies and meta-stabilities of capillary condensate in wetted granular due to confinement of the system[22]. In a similar way, close-by rough fracture surfaces could certainly account for the difficulty to dry out the condensate.

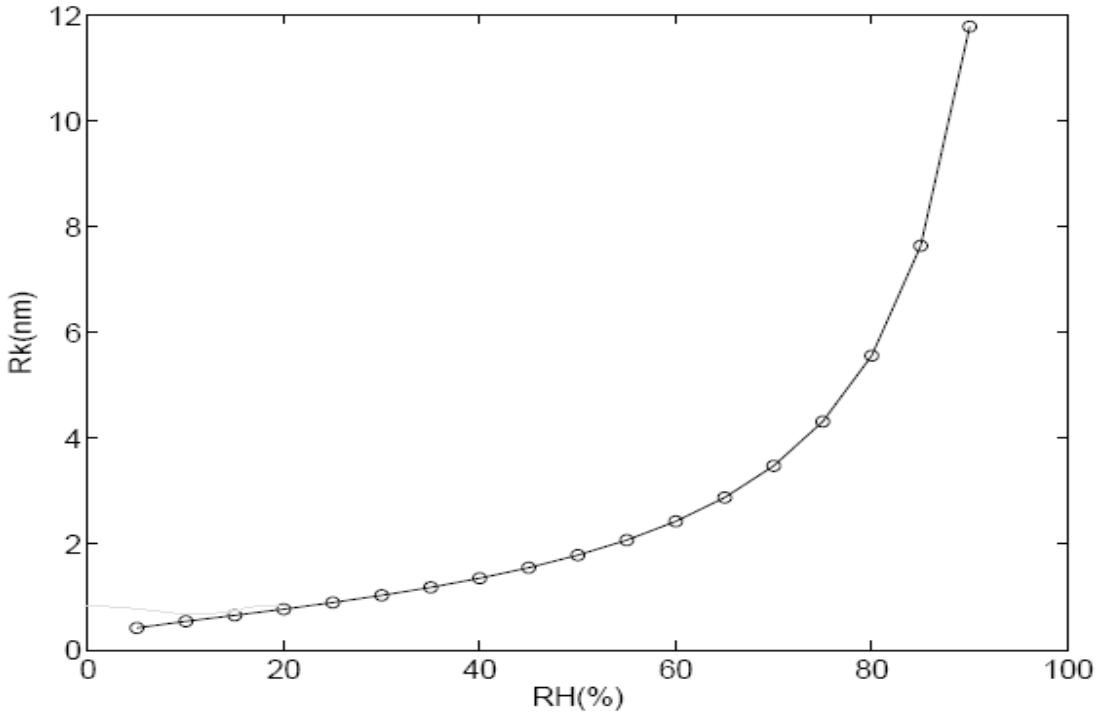


*Figure 5. Theoretical curve of the Kelvin radius vs the relative humidity, at 293K*

CONCLUSION

All the results obtained by in situ phase imaging tends to confirm a mechanism of water condensation inside the crack tip, leading to the formation of a confined liquid condensate whose extent evolves with the ambient humidity around the crack. Such a condensation is classically assumed for low velocity crack propagation but had never been experimentally clearly evidenced. The experimental device developed at the LCVN has demonstrated its ability to follow the evolution of this liquid condensate under variable environmental and loading conditions.

This is particularly promising since the existence of a condensate would have a crucial impact on stress corrosion mechanisms. On the purely mechanical point of view, liquid condensation implies the existence of a significant depression inside the condensate. The resulting forces on the crack lips across the whole width of the sample might lead to a non negligible effect of crack closure, directly dependent on the size of the condensate. More importantly, the presence of a confined condensate changes totally the chemistry at the crack tip. Velocity measurement as a function of the applied load have shown different behavior in humid air and in water[2,5]. In low humidity, the presence of a plateau (region where the velocity does not increase with the applied load any more, usually called region II) is related to corrosive agent (water) transport limitation. Condensation of liquid water at the crack tip in the area where gas molecule mobility is usually limited by the narrowness of the crack might explain the gradual disappearance of the plateau when humidity increases. Different effects are expected according to

the nature of the cracked glass, since the ion concentrations inside the confined condensate will clearly evolve through ion transfer and lead for instance to pH and surface energy of "water" changes or time-dependent behaviors. It would thus be interesting to study phosphate glasses for instance, where anomalous crack velocity measurements have been reported[6,7]. Since the crack tip is the site of enhanced diffusion processes, as shown in sodo-silicate glasses by Marliere et al[22], we can also wonder what will be the role of the condensate in these processes.

Further experiments will be devoted to understand more precisely the kinetic of the condensate formation under various conditions of humidity and crack velocities. It is believed that experimental data on the liquid condensation at the crack tip will be of important help to further analyze the mechanisms of stress corrosion of oxide materials.

ACKNOWLEDGEMENT

The authors thank Dr Christian Fretigny, Dr Lyderic Bocquet and Dr Michel Ramonda for fruitful discussions.

REFERENCES

[1]R. J. Charles, W. B. Hillig, in *Symposium on mechanical strength on glass and ways of improving it.* Union Scientifique Continentale du verre, Charleroi, Belgium p. 511 (1962)

[2]S. M. Wiederhorn, "Influence of water vapor on crack propagation in soda-lime Glass" *J. Am. Ceram. Soc.* 50, 407-414 (1967)

[3]S. M. Wiederhorn, L. H. Bolz, "Stress corrosion and static fatigue of glass" *J. Am. Ceram. Soc.* **53**, 543-548 (1970)

[4]K. M. Davis, M. Tomozawa, "Water diffusion into silica glass: structural changes in silica glass and their effect on water solubility and diffusivity" *J. Non-Cryst. Solids* **185**, 203-220 (1995)

[5]B. Lawn "Fracture of Brittle Solids",2nd edition, Cambridge University Press, Cambridge (1993)

[6]T.I. Suratwala, R.A. Steele, G.D. Wilke, J.H. Campbell, K. Takeuchi, "Effects of OH content, water vapor pressure, and temperature on sub-critical crack growth in phosphate glass" *J. Non-Cryst Solids* 263&264, 213-227 (2000)

[7]TY.-K Lee, M. Tomozawa "Effect of water content in phosphate glasses on slow crack growth rate" *J. Non-Cryst Solids* 248, 203-210 (1999)

[8]J. N. Israechvili, "Intermolecular and Surface Forces, 2nd edition, Academic Press, New York,1992

[9]F. Célarié, S. Prades, D. Bonamy, A. Dickelé, E. Bouchaud, C. Guillot, C. Marlière, "Surface fracture of glassy materials as detected by real-time atomic force microscopy (AFM) experiments," *Appl. Surf. Sci.* **212-213**, 92-96 (2003)

[10]M. Y. He, M. R. Turner, A. G. Evans, "Analysis of the double cleavage drilled compression specimen for interface fracture energy measurements over a wide range of mode mixities," *Acta Mater.* **43**, 3453-3458 (1995)

[11]S. N. Magonov, V. Elings, M.-H. Whangbo, "Phase imaging and stiffness in tapping-mode atomic force microscopy," *Surf. Sci.* **375**, L385-L391 (1997)

[12]L. Nony, R. Boisgard, J.-P. Aimé, "Nonlinear dynamical properties of an oscillating tip-cantilever system", *J. Chem. Phys.* 111,4, 1615-1627 (1999)

[13]R. Garcia, R. Perez, "Dynamic atomic force microscopy methods", *Surf. Sci. Reports*, 47, 197-301 (2002)

[14]L. Zitzler, S. Herminghaus, F. Mugele, "Capillary forces in tapping mode atomic force microscopy", *Phys. Rev. B*, 66, 155436 (2002)

[15]M. Ciccotti, M. George et al, to be published
[16]J. P. Cleveland, B. Anczykowski, A. E. Schmid, V. B. Elings, "Energy dissipation in tapping-mode atomic force microscopy", *App. Phys. Letters*, 72, 20,2613-2615 (1998)
[17]L. Nony, T. Cohen-Bouhacina, J.-P. Aimé, "Dissipation induced by attractive interaction in dynamic force microscopy: contribution of adsorbed water layers," *Surf. Sci.* 499, 152-160 (2002)
[18]T. Bouhacina, B. Desbat, J.-P. Aimé, "FTIR spectroscopy and nanotribological comparative studies: influence of the adsorbed water layers on the tribological behaviour," *Tribol. Lett.* 9, 111-117 (2000)
[19]D. Beaglehole, H.K. Christenson, "Vapor adsorption on mica and silicon: entropy effects, layering, and surface forces" *J. Phys. Chem.* 96, 3395-3403 (1992)
[20]L. Wondraczek, A. Dittmar, C. Oelagrdt, F. Celarie, M. Ciccotti, C. Marliere, "Real-time observation of a non-equilibrium liquid condensate confined at tensile crack tips in oxide glasses" *Journal Of The American Ceramic Society*, 89, 746-749 (2006)
[21]A. W. Adamson, Physical Chemistry of surfaces, 3rd edition, Wiley, New York and London (1976)
[22]F. Restagno, L. Bocquet, T. Biben, "Metastability and Nucleation in Capillary Condensation" *Phys. Rev. Lett.* 84, 2433-2436 (2000)

### 3.4.2 Interprétation du phénomène de diffusion ionique

Les nouvelles connaissances sur la mesure de l'eau à la surface du verre et à l'intérieur de la fissure, nous ont permis de revisiter dans le détail les mesures sur la diffusion du sodium dans les verres sodo-silicatés (voir section 3.3). L'analyse des images de phase AFM, en particulier, nous a permis de constater la présence du ménisque liquide à l'intérieur de la fissure et de constater les altérations de la couche liquide superficielle qui précédent la formation des plots montrés en figure 3.3.3 et qui accompagnent leur croissance et évolution pendant l'avancement de la pointe de fissure.

Nous en avons conclu que la migration du sodium vers la fissure se manifeste à la surface par une altération des propriétés d'hydrophilie locales. Les plots se forment en conséquence d'un processus de démouillage d'une couche liquide enrichie en composés à base de sodium (comme confirmé par des analyses SIMS). Cette substance est suffisamment fluide pour présenter un phénomène de croissance par coalescence des nodules en analogie à ce qui arrive pour la formation de la buée quand on respire sur une vitre ; mais elle est aussi assez visqueuse pour permettre à l'AFM de mesurer sa topographie.

Il est intéressant de remarquer qu'encore une fois ce phénomène se présente quand la vitesse de propagation de la fissure dévient suffisamment faible (de l'ordre de $10^{-9}$ m/s) pour permettre au lent processus de diffusion d'avoir lieu. En diminuant ultérieurement la vitesse de propagation, la parabole d'influence de ce phénomène s'ouvre progressivement jusqu'à prendre une forme plutôt circulaire quand la vitesse d'avancement de la fissure devient faible par rapport à la diffusion. Cette condition pourrait expliquer la présence d'un seuil de propagation dans ce type de verre : la diffusion induite par un gradient de contraintes est aussi un mécanisme de réduction locale de l'énergie de déformation, ce qui comporte un écrantage de la pointe de fissure vis à vis du champ de déformation présent à l'extérieur de la zone de diffusion. Quand la vitesse de fissure dévient suffisamment faible pour permettre le développement de cet écrantage sur un volume suffisant, la chute des contraintes à la pointe comporte un arrêt de la fissure.

Ce sujet est décrit extensivement dans l'article Célarié, Ciccotti and Marlière, 2006 à paraître sur JNCS, mais je reporterai ici un autre article à paraître les actes de la conférence Fractography of Glasses and Ceramics V (Rochester, USA, juillet 2006) qui contient des mises à jour et qui est confortablement plus court.

# EFFECT OF STRESS GRADIENT AT THE VICINITY OF A CRACK TIP ON IONIC DIFFUSION IN SILICATE GLASSES: AN AFM STUDY.

F. Célarié
Institute of Non-Metallic Materials, Clausthal University of Technology, Clausthal-Zellerfeld, Germany
M. Ciccotti, M. George
Laboratoire des Colloïdes, Verres et Nanomatériaux (L.C.V.N.), University Montpellier 2, CNRS, France.
C. Marlière*
Géosciences Montpellier (G.M.), University Montpellier 2, CNRS, 34095 Montpellier Cedex 05, France.
** Corresponding author. Email address : christian.marliere@univ-montp2.fr*

## ABSTRACT

The slow advance of a crack in sodo-silicate glasses was studied at nanometer scale by in-situ atomic force microscopy (AFM) in a well-controlled atmosphere ($N_2$ and $H_2O$). An enhanced diffusion of sodium ions in the stress-gradient field at the sub-micrometric vicinity of the crack tip was revealed through several effects: growth of nodules in height images, changes in the AFM tip–sample energy dissipation as detected in phase images. Ex-situ chemical micro-analyses completed the AFM measurements. The nodules patterns revealed a dewetting phenomenon evidenced by "breath figures", i.e. analog to the fogging that occurs when a vapour condenses onto a 'cold' surface [D. Beysens et al., Phys. Rev. Let. **57,** 1433 (1986)].

These experimental results were explained by a two-step process: i) a fast migration of sodium ions towards the fracture surfaces as proposed by Langford et al. [J. Mat. Res. **6**, 1358 (1991)], ii) a slow backwards diffusion of the cations as evidenced in these AFM experiments (typical time: few minutes). Measurements of the diffusion coefficient of that relaxing process were done at room temperature. Our results strengthen the theoretical concept of a near-surface structural relaxation due to the stress-gradient at the vicinity of the crack tip. Raman and SIMS studies revealed that *nodules* – for samples studied after exposition to common air - are preferentially covered by an organic overlayer of a carboxylate salt with a long aliphatic chain. The catalytic role of sodium ions in that chemical process is suspected.

## KEYWORDS

Ionic Diffusion; Soda−lime−silica Glass; Crack Growth; Atomic Force Microscopy

## PACS INDEXING CODES

| | |
|---|---|
| 62.20.Mk | Fatigue, brittleness, fracture, and cracks |
| 66.30.-h | Diffusion in solids |
| 68.03.Cd | Surface tension and related phenomena |
| 68.37.Ps | Atomic force microscopy (AFM) |

## I. INTRODUCTION

The study of mechanisms of rupture in so-called brittle materials is still of great importance both for knowledge of basic mechanisms of bond(s) breaking and for practical reasons such as understanding and possibly correcting the degradation of nuclear waste containers or optical glass fibers or predicting rupture in the upper Earth's crust as well. However, and despite of recent tremendous research work, discussions about the real processes and their characteristic length scales are still intense. In order to try and clarify the debate we aim to study the sub-micrometric vicinity of the tip of a crack running in silicate glass with mobile ions (as sodium cations) and check for possible chemical mass transfer at nanometer range. Soda-lime glasses, despite of their chemical complexity, were good candidates as i) samples with a high homogeneity of composition (a mandatory condition for the double cleavage drilled compression –DCDC- samples we used) can be easily obtained and ii) such local ionic migration was already suspected in complex conditions [1-2]. This paper is based on a study on *in-situ* AFM and *ex-situ* complementary experiments in the low crack speed regime. We evidence a slow diffusion process of sodium thanks to the observation of the growth of nodules in the vicinity of the crack tip. The source of the diffusion species are shown to be located at the nanometer vicinity of the crack surfaces. The diffusion zone is evidenced by an increased energy dissipation by AFM tip –sample interaction compared to corresponding "bulk" glass. Measurements of diffusion coefficient were done at room temperature by the study of the advance of diffusion front by AFM. The latter was visible in height images thanks to a dewetting-like process and in phase images thanks to an increased energy dissipation in the interaction between AFM tip and substrate. The process of nucleation and growth of these nodules was locally investigated and explained by a phenomenon of local condensation of an aqueous phase the viscosity of which is increased due to an ionic ($Na^+$) enrichment. It will be pointed out that these observations of the sodium migration in the stress gradient field were possible thanks to an adequation between characteristics times related to both diffusion process and crack propagation.

## II. EXPERIMENTAL SETUP

Commercial soda-lime glasses[1] were used for this work. The composition of the glass by molar fraction (%) is as follows: $SiO_2$ : 70.9; $Na_2O$ : 13.2 ; CaO : 10; MgO : 5.4 ; $Al_2O_3$ : 0.4; $K_2O$ : 0.1. The samples were cut from the same piece of that soda-lime silicate glass. A thermal treatment (530°C) was done before fracture experiment in order to remove residual stresses. Fracture is performed on DCDC (double cleavage drilled compression) [3], parallepipedic (4mmx4mmx40mm) samples designed with a cylindrical hole (radius: 0.5 mm) drilled at the center of two parallel 4mmx40mm surfaces and perpendicularly to them. The hole axis defines the Z-direction. We worked with both the "genuine" surfaces (in contact with air or with tin bath during cooling of glass melt) without any further polishing or with bulk samples in which the 4×40 $mm^2$ surfaces were polished. In all cases the measured RMS roughness was lower than 0.25 nm for a 10×10 $\mu m^2$ scan-size. No change in the presented results was detected versus the nature of the studied surface. These fracture experiments are performed at a constant temperature of 21.0 ± 1°C in a leak-proof chamber under an atmosphere composed of pure nitrogen and water vapour (preceding by a careful out-gassing). The macroscopic relative humidity (RH) can be controlled from 5% to 75% with an accuracy of about 1%. AFM experiments were done in intermittent contact (tapping) mode. After the AFM experiments, samples were removed from the glove-box and studied by Secondary Ions Mass Spectroscopy (SIMS) analyses or Raman spectroscopy experiments.

[1] From Saint-Gobain company.

## III. RESULTS

### III.A. AFM experiments: evidence of a diffusion process.

It must be noted that the phenomena described below were not detectable when relative humidity rate was lower than 30%. A typical topographical (height) AFM frame in the neighborhood of the crack tip, for $K_I$ = 0.41 MPa.m$^{1/2}$, v = 1.5 nm.s$^{-1}$ and RH = 45 %, is presented in figure 1.

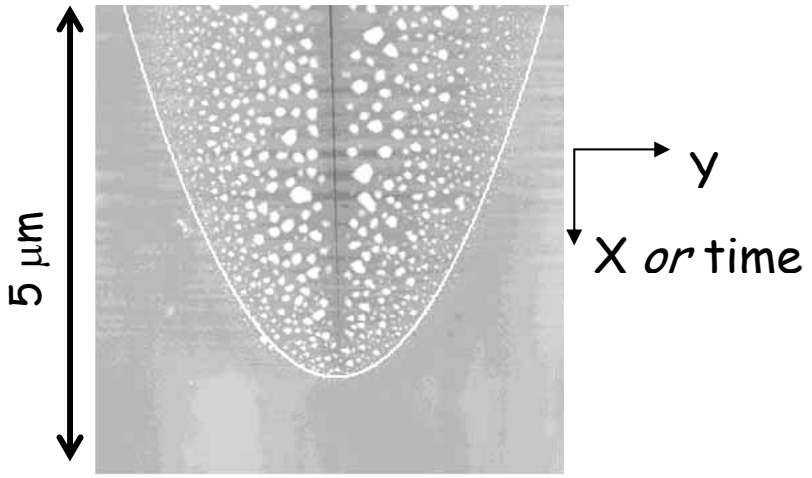


*Figure 1: AFM height image in tapping mode for a soda-lime glass at 45% RH. The white line corresponds to the best quadratic fit for delimiting contour between zones with and without nodules. Crack speed: $v_c$ = 1.5 nm.s$^{-1}$. The height signal is coded in grey levels corresponding to a vertical range of 10nm (between black and white levels).*

It clearly reveals many nodules typically 200 nm in diameter for the largest (respectively 10nm for the smallest) and 20 nm in height for the highest (resp. 2 nm). It must be emphasized that, in the same conditions of humidity and mean crack speed, this phenomenon was not observed with silica samples [4] and neither with lithium alumino-silicate glasses[1] [5].The X axis (along direction propagation of crack) can be rescaled as a time axis: With chosen values of AFM scan rates the crack speed can indeed be considered as constant during a set of AFM data. The contour delimiting the zones with or without nodules (what will be called "diffusion front") has a parabolic profile characterized by equation $(x - x_0) = B \,.\, (y - y_0)^2 = v_c \,.\, (t - t_0)$ where $v_c$ is the mean crack speed. This quadratic relation can be interpreted as due to a diffusion process in which the source of diffusing species is located on crack surfaces ($y = 0$ represents the crack lips in the 2D representation provided by AFM techniques). Classical theories of diffusion [6] predict indeed that the local concentration of the diffusion species is a function of variable $u$ with $u = (y - y_0)/(2 \,.\, \sqrt{D_{eff}.(t - t_0)})$ where $D_{eff}$ is an effective diffusion coefficient.

It must be emphasized that the shape of the parabola of delineation does change with crack speed. However the deduced values of $D_{eff}$ are constant, within experimental error bars, for a given humidity rate whatever the crack speed. More details will be given in [7].

Careful experiments as detailed in [7] allowed us to estimate the value of the diffusion coefficient at different humidity rates. $D_{eff}$ is equal to 1.0 $10^3$ nm$^2$/s for RH=45% and slightly increases with humidity : $D_{eff}$ = 18 $10^3$ nm$^2$/s for RH=58%. The comparison with values from literature is delicate as many studies were done by the leaching action of *liquid* water on glass substrates. For instance Lanford et al. [8] measured diffusion coefficient of $Na^+$ and $H_3O^+/H^+$ for the hydration of a soda-lime glass the composition of which is similar to that of the glass studied in the present paper.

[1] $SiO_2$ mol 70% ; $Al_2O_3$ mol 20%; $Li_2O$ mol 6%; $TiO_2$ mol 4%

Then the sodium content was profiled in depth by a resonant nuclear reaction method the spatial resolution of which is at least few micrometers. Typical values for diffusion coefficients were: $D_{Na^+}$ = 10 nm$^2$/s at 90°C. Gehrke's work gave [9]: $D_{Na^+}$ = 0,29 nm$^2$/s for soda-lime glass rods of similar composition corroded in distilled water at 23°C. In these studies there was no feedback on pH but its value was supposed constant. More recently leaching behaviour of sodium from small particles of soda–lime glass in acid solution was studied [10]. Two types of fine glass spheres were investigated: "small", respectively "large", ones with an averaged diameter of 50 (resp. 20) microns. The sodium diffusion coefficients at a temperature of 25°C are $D_{Na}^{large}$ = 0.06 nm$^2$/s and $D_{Na}^{small}$ = 0.6 nm$^2$/s. These values are very near of those obtained in former studies as in [9]. It must be noted too that the water content of silicate glasses has an influence on sodium diffusion coefficient. For instance, Tomozawa et al. [11] showed that, for $Na_2O$-3$SiO_2$ glasses, with increasing water content sodium diffusion coefficient decreases initially to a minimum at 3-4wt % water and then increases. Nevertheless it should be concluded from literature that sodium diffusion inside silicate glasses with no or low content of sodium and without any applied mechanical stress is far below (around three orders of magnitude) values measured in this paper. Please note that these former studies were done by physical or chemical investigations at length scales much higher than those studied in the present paper.

AFM phase images reveal too the presence of similar diffusion front. An example of the profile of the phase signal corresponding to height signal (figure 1) along a line parallel to Y axis is shown in figure 2.

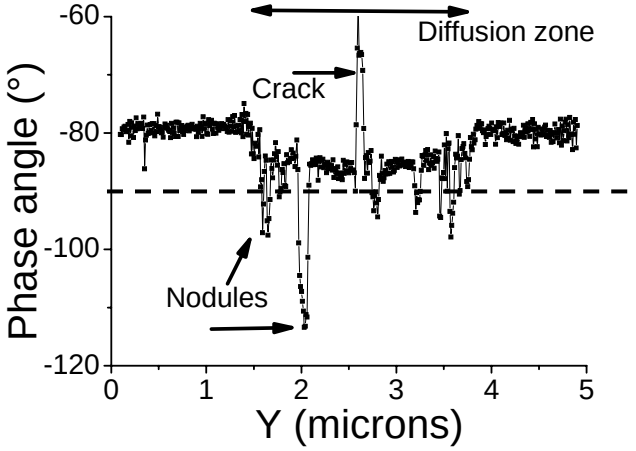


*Figure 2: Profiles along the Y direction from the phase image corresponding to height data in Fig.1. The dashed line corresponds to a phase angle, $\phi$, equal to -90°: when $\phi > -90°$ AFM works in intermittent contact mode; in the opposite case in non-contact mode.*

As well known [12], the phase signal in AFM tapping mode is a function of changes in the tip–sample energy dissipation. In figure 2 we observe that the phase signal is lower in diffusion zone (inside the parabolic envelop line as mentioned above) than in the not-disturbed zone and corresponds, when phase angle is higher than -90°), to an *increase* in dissipation the physical origin of which will be explained later. Nodules are related to zones with a phase angle lower than -90°: the interaction between the AFM tip and the nodules is therefore purely attractive as due to capillary interactions. At the position of crack line: the value of the phase signal is the one expected for a cantilever "flying" over the crack filled with the standard surrounding gaseous atmosphere.

In order to get more accurate information about the origin and nature of the diffusion species we studied the growth of the nodules by AFM at higher magnification. For that purpose we used a much higher spatial resolution that allows us to work with relatively small times of acquisition (84s between two consecutive images). We observed that in a first step the nucleation of nodules of very small size occurs all over the AFM scanned surface inside the diffusion zone. Then the nodules grow in height and lateral radius before coalescing.. Two nodules (see arrows in

figure 3) are first growing independently before coalescing to form one unique bigger nodule the height of which further increases. This behavior can be interpreted by the phenomenon of nucleation and coalescence of droplets (nodules) as in the case of the so-called "breath figures" [13, 14]. To better understand the origin of these condensation-like patterns we measured by AFM the evolution of the contact angle of nodules on the glassy surface versus time (figure 4).The contact angle is increasing from ~ zero (complete wetting) to 18 ± 3°. This study proves then that nodules grow by a process similar to that involved in breath figures when liquid droplets are condensing on a cold surface. As water plays a major role in local chemistry at crack tip that condensation phenomenon evidenced by the observation of nucleation and growth of nodules is likely due to two conjugate effects: i) a local dewetting of the native thin layer continuous water (as evidenced by variation of contact angle) and ii) a condensation from the gaseous atmosphere. This aqueous liquid phase in nodules is likely enriched with sodium ions and consequently has a higher viscosity.

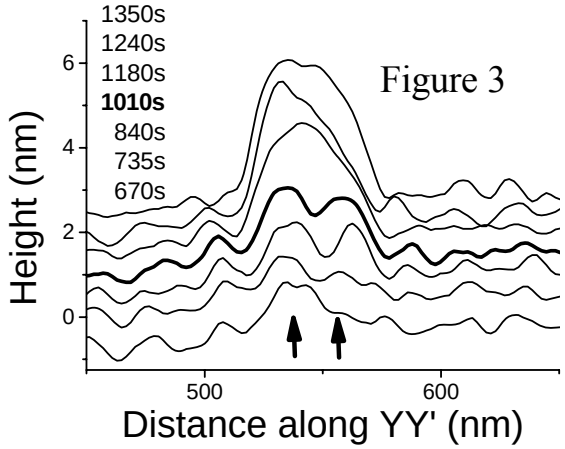


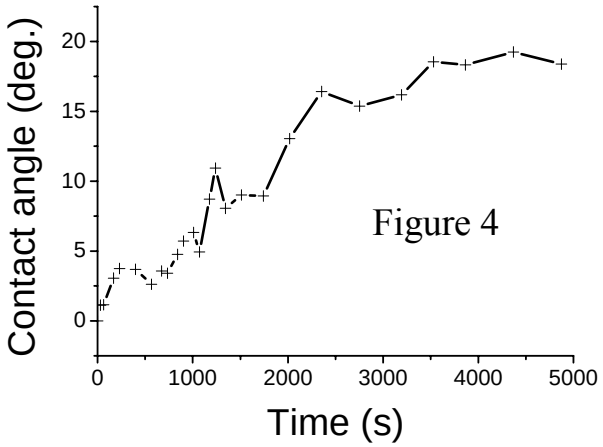


*Figure 3: Time evolution of a height profile. The arrows are a guide for the eye to follow on the process of growth and coalescence (bold line) of two nodules. RH=48%, $v_c$ = 0.21nm/s.*
*Figure 4: Variation of contact angle of nodules versus time. RH=48%, $v_c$ = 0.21nm/s.*

### III.B. Ex-situ chemical micro-analysis: SIMS studies.

In order to get deeper insight in the chemical nature of nodules we worked as presented now. Mean crack speed was chosen low enough (0.1 nm/s) and humidity high enough (48%) in order to allow an increase of the mean size of nodules with time. These experiments were done at room temperature and in the pure ($N_2$ +$H_2O$) atmosphere. Nodules of microscopic size laterally and in thickness were obtained. The sample was then withdrawn from the glove box, removed from the mechanical stage and stayed in standard atmosphere during a maximum of one hour before being put in high vacuum conditions. The (X,Y) surface of the sample was then studied in the vicinity of the crack tip. Firstly SIMS revealed much higher carbon content at the *near-surface* of nodules as compared with the surface of glass outside of diffusion zone. Then few tens of nanometers in thickness were removed by ionic sputtering in order to probe the *inside* of nodules. We observed then a much stronger signal of sodium at nodules in contrast to the bulk glass. On the opposite, Si signal was weaker while Ca, Mg and Al ones roughly constant within the accuracy of the experiments.

### III.C. Ex-situ chemical micro-analysis: RAMAN studies.

These measurements were done in standard air. The Raman spectra for both bulk glass and nodules for wave numbers between 250$cm^{-1}$ and 3500$cm^{-1}$ are shown in figure 5. They both reveal typical bumps related to the amorphous silicate glass as the diameter of the laser spot is larger that the typical size of nodules and bulk glass is thus slightly lightened. However narrow peaks are

present on spectrum of nodules. We subtracted the signal related to the glassy part of the spectrum (as deduced from the lower graph in figure 5) from the raw data of nodules). The resulting spectrum is shown in figure 6 (upper curve). In this lower frequency region ($\sigma$<1400 $cm^{-1}$) we observe a strong analogy between the measured spectrum and that of carboxylic salts, such as Na-stearate [15] (or more generally a carboxylate with variable values of aliphatic length, *n,* in (-$CH_2$-)n ) - see figure 6 lower graph. The corresponding peaks in spectrum of nodules are marked by full squares in figure 6. As expected, bands at around 1400 $cm^{-1}$ (star in figure 6), typical of $CH_2$ scissors and $CH_3$ asymmetrical deformations, are detected. It must be noted too that the peak at 1610$cm^{-1}$ (triangle in figure 6) can be explained by the absorption of two equivalent C=O bonds in carboxylic salt. We also observed bands at wave numbers around 3000$cm^{-1}$ (see insert figure 5) *only* present when nodules are lightened by the laser spot.

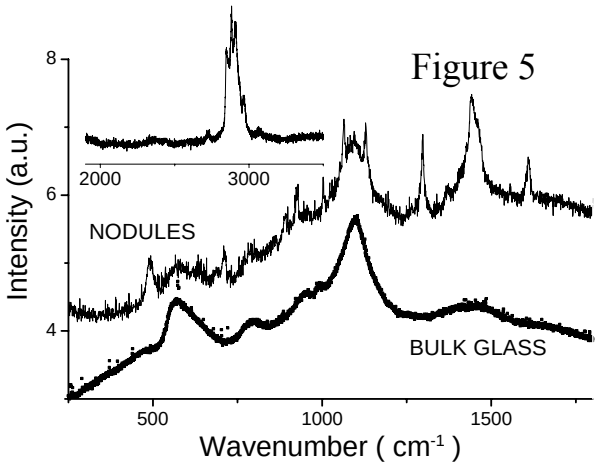


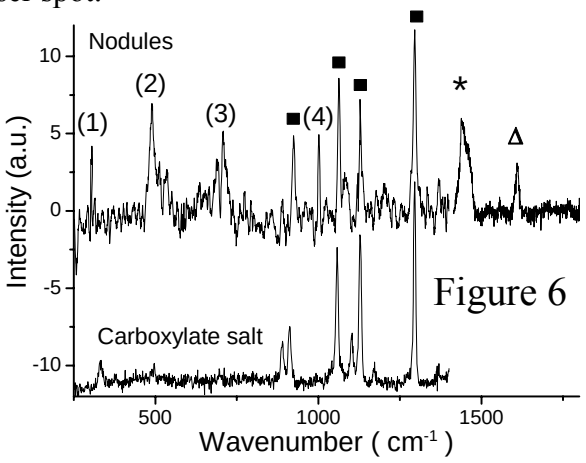


*Figure 5: Raman spectra for bulk glass and nodules. The insert corresponds to high wave number spectrum for nodules (no signal was detected for bulk glass).*
*Figure 6: Raman spectrum for nodules (bulk glass contribution was removed). See text for symbols. Lower graph: spectrum for carboxylate salt [15].*

These bands are typical of aliphatic C-H stretching vibrations as in –$CH_3$ and –$CH_2$ groups [16]. Thus Raman data reveal the presence of a carboxylic salt *only* on nodules. From SIMS studies it can be concluded that this compound is located at the near-surface region of the nodules and not in the bulk. The remaining peaks in Raman spectrum (numbered in figure 6) might be related to the presence of a crystallized inorganic compound in nodules. A screening of the Raman data bases related to inorganic compounds showed us that the best similarity was obtained with the spectrum of oligoclase (sodium calcium aluminum silicate) [17]. It must be emphasized that the usual data bases are pretty poor in mineral compounds based on Na, Si elements. Presence of crystals of cristobalite, devitrite, diopside or tridymite, as usually evidenced in high temperatures experiments on crystallization of soda-lime like glasses [18] is not completely ruled out but fits are of lower quality.

## IV DISCUSSION

The nucleation, growth and coalescence of nodules and the propagation of the diffusion front delimiting the zones with or without nodules were observed at nanometer scale in the vicinity of the crack tip by AFM measurements in tapping mode. Experiments were done in a carefully controlled surrounding atmosphere. Following features were observed:

- These experiments revealed that the diffusion front is related to the process of nucleation of the nodules. These data can be well interpreted by a diffusion process. The source of diffusing species is locating on (in the vicinity) of crack lips (in our 2D AFM study; crack surfaces in case of

general 3D conditions). Values of diffusion coefficient were measured at room temperature for different rates of relative humidity.
- By further chemical microanalyses we revealed that nodules are characterized by a higher concentration of sodium element than in bulk glass. We then deduced that Na ions were migrating during the diffusion process.
- The measured values of sodium diffusion coefficient in the vicinity of the crack tip are around three orders of magnitude larger than those deduced from former studies on similar bulk composition of glasses. As stress field is drastically enhanced in the vicinity of crack tip, the role of stress gradient in the origin of this enhanced diffusion process was suspected.
- AFM phase images showed that important changes in the tip–sample energy dissipation occurred. Water was proved to play an important role in that phenomenon. Complementary AFM studies revealed a nanometric process of growth and coalescence of the nodules connected to an increase of the contact angle.
- Raman study showed that an organic compound (constituted by carboxylic salt with a long aliphatic chain) is preferentially formed at the surface of nodule. As Raman studies were done in a standard atmosphere these compounds are likely synthesized or adsorbed on nodules when sample is removed from the glove-box. The presence of an inorganic crystallized compound the growth of which occurs at an undetermined step is suspected too.

The presence of local variation (in the nanometer range) of concentration of sodium ions near by the crack tip is the cause of local variations of surface tension and thus can explain the appearance of local aqueous droplets as it will be shown now. We indeed proved that the advance of diffusion front was related to a local and slight increase of wetting angle. On the opposite, far away from the crack tip, we did not observe any variation of the roughness of the glass surface: it is covered by a continuous thin layer of adsorbed water (the wetting angle, $\theta$, is equal to zero) the thickness of which is in the nanometer range: from 0.5nm to 1.5nm depending on humidity rate [19-20]. As it is well known the wetting angle is related to interfacial tensions by the Young–Laplace equation $\cos\theta = ( \gamma_{SG} - \gamma_{SL} ) / \gamma_{GL}$, where $\gamma_{XY}$ is the interfacial tension between phases X and Y. Subscript L is for liquid, G for gas and S for solid phase. At first it should be mentioned that because of the exchange in sodium and hydronium ions between bulk glass and water overlayer the concentration of $H_3O^+$ in the liquid phase decreases and then the solution becomes more basic. It is directly connected to the fact that sodium-containing glasses are regarded to be more basic than pure silica glasses [21]. It has been known for a long time that interfacial tension between liquid water and air, $\gamma_{GL}$, depends on the nature of the inorganic aqueous salt solution: $\gamma_{GL}$ increases when the pH of the liquid medium increases [22]. More recently molecular dynamics (MD) calculation [23] showed with more details that alkali cations are repelled from the liquid/gas interface in case of basic pH and, consequently, cause an *increase* of interfacial tension, $\gamma_{GL}$. As a consequence the concentration in alkali cations near the solid/liquid interface should likely increase or remain constant. Thus $\gamma_{SL}$ should remain constant or slightly decrease. Experiments [24] and MD calculations [25] showed that there is small predominance of sodium ions at the interface of $Na_2O$-$3SiO_2$ glass and air, causing a little increase or no change in interface tension, $\gamma_{SG}$. Thus from the Young–Laplace equation it can be predicted that the contact angle should increase at the places where chemical heterogeneities (higher concentration of sodium cations) are present. The stability of the continuous wetting film as observed far away from the diffusion zone is due to long-range van der Waals repulsive force [21] can be modified by external disturbances as the incoming of sodium cations causing local hydrophobic spots acting as nucleation centers for dewetting. As already shown [26] that circular droplets pattern –especially in the case of the thinnest (aqueous) film – may develop by nucleation on more hydrophobic centers, ripen and merge. The nodule pattern is thus predicted to propagate with the diffusion front of sodium ions as it is observed in our experiments.

Diffusion process is very clearly revealed too by phase images in AFM intermittent-contact mode. In figure 2 we observed that the phase signal is lower in diffusion zone (inside the parabolic envelop line as mentioned above) than in the not-disturbed zone It was shown [12] that if the amplitude of the cantilever is held constant, the sine of the phase angle, $\phi$, of the driven vibration is then related to changes in the tip–sample energy dissipation (the origin of phase is chosen to be equal to -90° at resonance when the cantilever is far away from the sample). Calculation of dissipated energy are under progress [27] and will not detailed in this paper. We observe that $\phi$ is higher than (-90°) almost everywhere on substrate (except on nodules). The AFM is thus working in intermittent contact mode (*i.e.* the AFM tip undergoes repulsive forces during its vibrating movement at least partially) and a decrease in $\phi$ corresponds to an increase of dissipated energy during the tip-sample interaction. On the opposite, the nodules are imaged in a non-contact mode (as $\phi$ <-90°) meaning that the interaction force is attractive all along the movement of the AFM tip as in the case of pure capillary forces. As mentioned in [28, 29] the principal source of energy dissipation during the tip-sample interaction is mainly the adhesion energy hysteresis. The adhesion forces can be in the present experiments from two different origin [30]: capillary forces and acid/basic interactions [21]. In the first case the energy dissipation is related to the formation and rupture of a capillary neck between the tip and sample[31]. It is known that the capillary force is proportional to the liquid-vapor interfacial energy, $\gamma_{GL}$ [32]. As earlier mentioned, $\gamma_{GL}$ is expected to increase due to an enrichment of the liquid-like phase in cations, we can thus easily explain the decrease in phase angle when the AFM tip is in intermittent contact in diffusion zone. On the other hand, the higher acid/basic interactions due to the already mentioned difference in acid-basic properties of both the silica AFM tip and sodium enriched zone on the substrate near the crack tip may also contribute to an increase of the dissipation in the diffusion zone. As mentioned by Fowkes et al. [21], work of adhesion between two silicate glasses (AFM tip and sample) is equal to the sum of two contributions: a van der Waals contribution and an acid-base contribution related to the ability to hydrogen-bonding. That last one is very likely increased due to more acid character of silica surface (AFM tip) and the more basic surface in Na-enriched glassy region. Because of the AFM regime of non-contact over the nodules it can be concluded too that nodules are covered by a thicker or/and more viscous liquid-like film than over the rest of diffusion zone.
These comments reinforced our experimental observation of an enhanced migration of sodium ions in the vicinity of crack tip. The high value of $D_{eff}$ we measured is compatible with the idea of a local enrichment of glassy material in sodium around the crack tip. Indeed a study by Gehrke et al. [9] revealed the influence of the composition of silicate glass with sodium content on the effective diffusion coefficient of sodium. Soda-lime like (17 mol% in $Na_2O$) and binary glasses ($Na_2O$ and $SiO_2$) with values of sodium content (12 mol% in $Na_2O$) near that of the glass studied in the present paper were characterized by $D_{eff} \pm 0.3$ nm$^2$/s. However it was revealed an important increase of $D_{eff}$ with sodium content for instance glasses made from 36% $Na_2O$ and 64% $SiO_2$ are characterized by $D_{eff} = 1.3\ 10^3$ nm$^2$/s. That value is of the same order of magnitude as the one deduced from our experiments ($D_{eff}$ = 1 to 18 x $10^3$ nm$^2$/s for RH between 45% and 58%). The measured value of $D_{eff}$ by our local AFM measurements is thus fully compatible with the hypothesis of a zone, located in the surroundings of the crack tip, made of a silicate glass with an enhanced concentration of sodium.

Two plausible scenarios for the migration path may be regarded. The first one corresponds to a *surface* migration of the diffusing species from the crack surfaces or from medium between them). The second scenario is related to a migration through the volume of material from crack surfaces to the outside of material: in this case transition between plane strain and plane stress regions makes the observation of that phenomenon possible in these AFM experiments. The first scenario is very unlikely. It must be noted indeed that for usual values of relative humidity in our experiments (RH~45%) the glass surfaces are covered by an aqueous film the equilibrium thickness of which is in the range of few tenths of nanometers, depending on the electrolyte

concentration in the water film [19,20]. Thus it could be possible that the migration of alkali species occurs in an aqueous liquid phase. In these conditions mobility of sodium cations in a bulk aqueous liquid phase is well known : $b_{Na} = 3.2\ 10^{11} mN^{-1}/s$ [33]. Thanks to Stokes-Einstein relation we can calculate at 25°C the diffusion coefficient of $Na^+$ ions in water, $D_{Na}^{water} = b_{Na}.k_B.T = 1.33\ 10^9 nm^2/s$, six orders of magnitude higher than the value we measured. As a consequence the interpretation of our experiments by a surface migration of sodium in the surface aqueous film can be very likely ruled out. On the opposite, we note that the typical value of $D_{eff}$ we measured by our AFM experiments is very near from those obtained in case of diffusion of sodium through a bulk glass with an enriched content in sodium. We thus think that the migration of alkali ions we evidenced around the crack tip occurs through the bulk structure of glass. This effect is likely detected on the free surface of our sample -via a dewetting process- through the transition between plane strain conditions in the bulk to plane stress ones on the investigated surface.

As the observed enhanced migration is localized in the vicinity of the propagating crack the enhanced value of stress around the crack tip is of major importance for the diffusion process. It is indeed known that mechanical stress has a great influence on diffusion processes. McAfee [34] studied the effect of stress upon the diffusion constant of gases (He, $H_2$ and other gases) in a borosilicate glass at room temperature. It was shown that an enhanced diffusion of helium (and hydrogen but with lower magnitude) is obtained in glass under high tensile stresses. The diffusion of water in silica glass was studied as a function of applied uniaxial stress [21, 35, 36]: the diffusion coefficient increases when a tensile stress is applied in the case of temperature lower than 250°C. As ionic volume for $Na^+$ is ranged between those of $H^+$ and $H_3O^+$ ions the occurrence of a similar diffusion process for $Na^+$ ions in a soda-lime like glass can be predicted. A migration of sodium ions in the applied stress gradient was indeed deduced from electrical measurements [37] on bent soda-lime silicate glass plates studied at temperatures between 75°C and 120°C. More recently, Na peak emissions were detected [38] in vacuum by quadrupole mass spectrometry and surface ionization techniques when soda lime and sodium trisilicate glasses were dynamically fractured. These experiments revealed a fast diffusion (typical time in the range of milliseconds) of $Na^+$ when sodo-silicate glasses were fractured under high stress gradient in vacuum. These observations are coherent with theoretical results from thermodynamics applied to chemo-elastic solid [39, 40] which allows the calculation of the diffusion coefficient versus the applied stress gradient. The sodium ions are thus predicted to concentrate in the region of maximum tensile stress, i.e. in the nanometer surroundings ahead of the crack tip. As the main contribution to value of stress is mostly due to the $r^{1/2}$ factor ( $r$ is the distance from crack tip to the relevant point) the stress gradient should have values of same order of magnitude in both regimes of slow and fast fracture. Therefore a fast migration of alkali ions from compressive zone to tensile one (at crack lips and near crack tip) should likely occur in our AFM experiments. Thus that fast migration likely causes the presence of a reservoir of sodium ions in the nanometric vicinity of the crack lips which relaxes -in a second step- in a diffusion process with much higher time constants (few minutes) as evidenced in the AFM experiments detailed in this paper.

The observation of an increasing diffusion coefficient with humidity reinforced the conclusions of Agarwal et al. [41] of a faster relaxation in the presence of water vapour. It is also compatible with recent observations of Tian et al. [42] on silica glass. These authors showed indeed that the uptake of water in the structure of the studied silica glass causes a structural relaxation occurring in the near-surface region leading to an initial rapid decrease in the sodium diffusivity followed by a slow increase with the water content. Our results strengthen the theoretical concept of a near-surface structural relaxation [43]. We believe that the stress-gradient present at the vicinity of the crack tip is of major importance to enable the glass network to undergo a structural relaxation causing long-range structural changes, leading to modifications of bonding angles and distances and consequently enhancing mobility of alkali cations. These structural changes may cause a relaxation of stresses at crack tip probably coupled to compressive

stress due to replacements of $Na^+$ by $H_3O^+$ ions [44] leading to the existence of the fatigue threshold.

Raman spectroscopy and SIMS studies revealed that *nodules* – for samples studied after exposition to common air - are preferentially covered by an organic overlayer of a carboxylate salt with a long aliphatic chain. The presence of a crystallized inorganic compound inside the nodules was evidenced too. The presence of the organic overlayer could result from the preferential adsorption of volatile organic compounds present in the standard air atmosphere on the nodules the higher content in sodium ions could play the role of nucleation center. Another explanation could come from a local conversion of carbon dioxide, present in the surrounding standard atmosphere[1], to methane or to a longer aliphatic chain : It was indeed shown [45] by using mass spectroscopy that the $CO_2$ peak disappeared during fracture of a soda-lime and boro-silicate glasses while CH4 peak increased. Reaction $CO_2 + H_2 \rightarrow 2H_2O + CH_4$ was proposed. We thus suspect that the sodium present in nodules could have a catalytic role in that chemical process. Such a behavior could provide a hypothetic complementary explanation to fatigue limit in glasses: thanks to this chemical reaction a chemical compound with an hydrophobic part could be deposit on the fracture surface of sample. Water molecules might thus not reach the bulk glass and consequently the stress corrosion process at the crack tip might be stopped. In order to check that hypothesis further experiments are needed. The experimental evidence of crystallized mineral compounds in nodules by Raman spectroscopy could provide an alternative explanation to surface crystallization of oxide glasses [18] or observation of nm-scale structures on air-exposed fractured surfaces of soda-lime silica [46].

## V. CONCLUSION

AFM experiments were done in a gaseous atmosphere composed of a mixture of pure nitrogen/water gases with soda lime silicate glasses. An enhanced diffusion of sodium ions in the stress-gradient field at the sub-micrometric vicinity of the crack tip was evidenced for relative humidity rate higher than 30%. The study of height and phase images (in AFM tapping mode) clearly evidenced a slow diffusion process thanks to the observation of the growth of nodules in the vicinity of the crack tip and/or variation in phase signal. The source of the diffusion species was shown to be located at the nanometer vicinity of the crack surfaces. That phenomenon related to sodium and hydronium interdiffusion process was detected by AFM through the observation of several effects: a dewetting-like phenomenon evidenced by “breath figures”-like patterns, changes in the tip–sample energy dissipation as observed in phase imaging mode and growth of nodules in height images for lower crack speeds. Ex-situ experiments confirm that sodium ions are the diffusing species. These experimental results have been explained by a two-step process: i) a fast migration of sodium ions towards the fracture surfaces as proposed by Langford et al. [38] (typical time for a dynamic fracture in vacuum: few tens of milliseconds), ii) a slow backwards diffusion of the cations as evidenced in these AFM experiments (typical time: few minutes). Diffusion coefficients of that relaxing process have been measured at room temperature for different relative humidity rate. The corresponding values were found to be much higher than those reported in literature with glasses of the same composition in similar conditions but were found to be compatible with those obtained for silicate glasses with a higher sodium content.

Raman spectroscopy and SIMS studies revealed that *nodules* – for samples studied after exposition to common air - are preferentially covered by an organic overlayer of a carboxylate salt with a long aliphatic chain. Such a result could provide an hypothetic explanation to fatigue limit in glasses as this aliphatic chain is hydrophobic and could contribute stopping the stress corrosion process at the crack tip. Furthermore these studies reveal that surface crystallization of oxide

[1] The occurrence of that chemical process inside the glove-box due to the presence of a residual content in $CO_2$ may not be ruled out even if very unlikely. Hypothetic migration of residual traces of $CO_2$ dissolved in bulk glass towards the crack tip could be an alternate explanation too.

glasses [18] or observation of nm-scale structures on air-exposed fractured surfaces of soda-lime silica [46] stems very likely from the ionic migration due to residual stress gradient and the related process of interdiffusion with $H^+/H_3O^+$ ions.

Our results strengthen the theoretical concept of a near-surface structural relaxation [43]. We believe that the stress-gradient present at the vicinity of the crack tip is of major importance to enable the glass network to undergo a structural relaxation causing long-range structural changes, leading to modifications of bonding angles and distances and consequently enhancing mobility of alkali cations. Such sodium migration likely causes a relaxation of stresses in the vicinity of crack tip and a decrease of the local value of $K_I$ factor: this effect could explain, at least partially, the presence of the fatigue limit.

However much more work is needed in order to better understand the role of the chemical composition of glasses and their physical structure on these stress gradient enhanced migration of alkali cations. Another important point would be to better understand the role of that sodium migration towards fracture surface on local chemical and physical properties as wetting, chemical reaction in the vicinity of the crack tip with standard air.

## VI. REFERENCES


1 B. Nghiem, thesis, University Paris-VI, 1998
2 R. Gy, J. Non-Cryst. Solids **316**, 1 (2003)
3 C. Janssen, in: Proceedings of the 10th International Congress on Glass, 1974, p. 10.23.
4 S. Prades et al., Int. J. Sol. Struct. **42,** 637 (2005)
5 F. Célarié et al., Phys. Rev. Lett. **90**, 075504 (2003)
6 J. Crank 1975 The Mathematics of Diffusion. Clarendon Press, Oxford/London
7 F. Célarié, M. Ciccotti and C. Marliere, to be published (2006)
8 W. Lanford et al., J. Non-Cryst. Sol. **33**, 249 (1979)
9 E. Gehrke, C. Ullner and M. Hähnert, J. Mater. Sci. **26** 5445 (1991).
10 T. Akai et al., J. Am. Ceram. Soc., **88**, 2962 (2005)
11 M. Tomozawa et al., J. Am. Ceram. Soc. **65,** 182 (1982)
12 J. P. Cleveland et al., Appl. Phys. Let., **72** (1998) 2613.
13 D. Beysens and C. Knobler, Phys. Rev. Let. **57,** 1433 (1986)
14 J. Viovy, D. Beysens and C. Knobler, Phys. Rev. A **37**, 4965 (1988)
15 Raman Spectra Database of Minerals and Inorganic Materials - the National Institute of Advanced Industrial Science and Technology, Japan
16 Clthup N., Daly L., Wiberley S., Introduction to Infrared and Raman Spectroscopy- 3rd edition, 1990, Academic Press.
17 Mineral Spectroscopy Server - California Institute of Technology - Pasadena, California, USA, http://minerals.caltech.edu/FILES/raman
18 R. Müller, E.D. Zanotto and V.M. Fokin, J. Non-Cryst. Sol. **274**, 208 (2000)
19 T. Bouhacina, B. Desbat and J.P. Aimé, Tribology Letters **9,** 111 (2000)
20 D. Beaglehole, H.K. Christenson, J. Phys. Chem. **96**, 3395 (1992)
21 F. Fowkes, D. Dwight, D. Cole and T. Huang, J. Non-Cryst. Solids **120**, 47 (1990)
22 J. Randles,. Phys. Chem. Liq., **7**, 107 (1977)
E. Washburn, Ed. International Critical Tables; McGraw-Hill: New York, 1928; Vol. IV.
23 M. Mucha et al. , J. Phys. Chem. B, **109**, 7617 (2005)
24 C. Pantano, J. Kelso and M. Suscavage in Advances in Materials Characterization - Vol. 15, D. R. Rossington, R. A. Condrate, and R. L. Snyder, Eds., Plenum Press, New York, (1983).
25 S. Garofalini and S. Levine, J. Am. Ceram. Soc. **68**, 376 (1985)
26 A. Sharma and R. Khanna, J. Chem. Phys., **110**, 4929 (1999)
27 M. Ciccotti *et al.* to be published

28 R. Garcia, R. Pérez, Surf. Sci. Reports, **47**, 197 (2002)
29 H. Bodiguel, H. Montes, C. Fretigny, Rev. Sci. Inst. **75**, 2529 (2004)
30 B. Cappella and G. Dietler, Surf. Sci. Reports, **34**, 1 (1999)
31 L. Zitzler, S. Herminghaus, and F. Mugele, Phys. Rev. B **66**, 155436 (2002)
32 J. N. Israelachvili, *Intermolecular and Surface Forces*, 2nd ed. Academic, London, 1991
33 S. Pride, Phys. Rev. B **50**, 15678 (1994)
T. Vora, B. Corry, S.-H. Chung, Biochimica et Biophysica Acta **1668** (2005) 106
34 K. McAfee, J. Chem. Phys. **28**, 218 (1958)
35 M. Nogami and M. Tomozawa, J. Am. Ceram. Soc. **67**, 151 (1984)
36 A. Agarwal, M. Tomozawa and W. Lanford, J. Non-Cryst. Solids **167,** 139 (1994)
37 N. Weber and M. Goldstein, J. Chem. Phys. **41**, 2898 (1964)
38 S. Langford, L. Jensen, J. Dickinson and L. Pederson, J. Mat. Res. **6**, 1358 (1991)
39 F. Larché and J. Cahn, Acta Metall. **26,** 1579 (1978)
40 F. Larché and P. Voorhees in Defect and Diffusion Forums. **129-130**, 31 (1996), Scitec Publications, Switzerland.
41 A. Agarwal and M. Tomozawa, J. Non-Cryst. Solids **209,** 264 (1997).
42 L. Tian, R. Dieckmann, J. Non-Cryst. Solids **352** (2006) 679
43 M. Tomozawa and M. Hepburn, J. Non-Cryst. Solids. **345-346,** 449 (2004)
44 J.P. Guin and S. Wiederhorn, J. Am. Ceram. Soc. **88**, 652 (2005)
45 R. Baptist and F. Levy, Vacuum **43**, 213 (1992).
46 Y. Watanabe et al., J. Non-Cryst. Solids **177,** 9 (1994)

## 3.5 Développements instrumentaux

Quand en octobre 2005 je suis devenu permanent au LCVN, j'ai dû prendre le relais de Christian Marlière dans la direction de l'équipe 'Nanomécanique'. Christian a eu sa mutation vers la géophysique et les problématiques qu'il aborde a présent (le comportement des fluides confinés dans les fractures des les roches) nous lient ultérieurement dans des nouvelles collaborations, ainsi que dans la continuation du projet 'Nanomécanique'. Ma petite équipe s'est enrichie en même temps par l'heureuse embauche de Matthieu George, qui avait aussi travaillé à la fois dans la fracture et dans la microscopie à force atomique.

C'était le moment de s'approprier plus profondément toutes les subtilités du montage instrumental pour maîtriser son potentiel et démarrer de nouveaux projets ambitieux. La meilleure façon était de se lancer dans une campagne de développements instrumentaux sur chacun des composants, pour pouvoir travailler directement avec les techniciens du laboratoire qui les avaient construits (P. Solignac, R. Vialla, J.-M. Fromental, G. Prevot, E. Alibert, S. Clément) et impliquer des étudiants de stage dans des petits projets bien définis. Le passage entre les premières observations du contraste de phase à une compréhension plus quantitative et complète de la relation avec l'énergie dissipée a bénéficié profondément de la maîtrise conséquente à ces travaux. Je reporterai ici les étapes fondamentales du parcours suivi et, dans la section suivante, j'évoquerai les projets à venir.

### 3.5.1 Mesure de la phase AFM par détection synchrone

Le microscope AFM installé sur le montage, un *Dimension 3100* équipé d'un contrôleur *Nanoscope 3a* (Veeco), tout en restant un excellent AFM, ne fournit pas une mesure directe du signal de phase (en mode 'tapping'). Après discussion avec les techniciens de Veeco et d'autres utilisateurs experts que je remercie de tout cœur, nous avons conclu que l'instrument fournit plutôt un signal proportionnel au cosinus du déphasage, qui est étalé linéairement sur la gamme +/-90° (ce que les utilisateurs appellent 'degrés Bocek'). J'ai donc décidé d'entreprendre à la fois une campagne de calibration de l'instrument (pour pouvoir réinterpréter au mieux les données du passé) et d'installer sur le montage une détection synchrone externe de qualité (Perkin Elmers 7280). Une nouvelle campagne de mesure nous a permis de valider la procédure de réinterprétation de nombreuses données acquises et de fournir de nouvelles données de fiabilité certaine.

En parallèle, avec Matthieu George (et sous les stimulants conseils de Christian Frétigny) nous avons effectué une étude sur les courbes approche-retrait (soit les variations d'amplitude et phase obtenues en rapprochant le levier de l'échantillon de façon cyclique) qui nous a permis d'établir un contrôle sur la mesure de l'énergie dissipée au contact entre pointe et échantillon en présence de la couche d'eau.

C'est à ce moment que, comme par magie, le puzzle des données de phase s'est recomposé et que nous avons pu acquérir de fortes certitudes sur le bien fondé de nos interprétations.

### 3.5.2 Estimations des effets de l'humidité relative sur l'équipement de mesure

Une particularité de notre montage est que la plupart des systèmes de mesure se trouvent à l'intérieur de la boîte à gants pour permettre les mouvements mécaniques nécessaires à l'application des contraintes et au suivi de la fissure en temps réel. Même si le

système est visiblement très performant, l'ambition de réaliser des mesure de nanomécanique quantitatives impose de vérifier que toutes les composantes de la chaîne de mesure répondent de façon stable en conditions d'humidité élevée (de l'ordre de 80%). Ce que l'on a accompli avec succès dans une campagne de mesure visant à tester chaque élément de façon séparée ou combinée (oscillation du levier AFM, stimulation électromécanique du levier, mesure de la déflection du levier par réflexion d'un faisceau laser et diode quatre-cadrans, mouvement du tube piézoélectrique qui supporte la tête AFM, transmission des signaux et performance des cartes d'électronique). Comme résultat on a pu valider le processus entier, après avoir identifié son maillon faible : le couplage entre le levier AFM et son support de stimulation se révèle particulièrement sensible aux changements d'humidité, mais ceci peut être facilement soigné par un suivi attentif des paramètres de stimulation en cours d'expérience.

### 3.5.3 Modélisation des dérives de l'interféromètre

Le suivi in-situ de la propagation de fissures, ainsi que la réalisation des mesures *post-mortem* (décrites ensuite), nécessitent un système de mesure de la position de la platine AFM avec précision nanométrique. Ceci n'est par atteignable par les moteurs pas-pas qui déplacent la platine avec précision micrométrique. Notre montage expérimental était donc équipé initialement d'un interféromètre hétérodyne (Zygo) capable de mesurer la position X et Y de la platine avec une précision de 10 nm. Ce montage a bien servi dans la phase de mesure sous des conditions environnementales constantes, mais il s'est révélé non adapté aux mesures en conditions variables.

Pour résoudre ce problème, nous avons installé une série de capteurs de température, pression et humidité relative et nous avons enregistré les dérives de l'interféromètre en conséquence des différents types de variations environnementales. A travers une modélisation du fonctionnement de l'interféromètre hétérodyne ainsi que des changements d'indice de réfraction de l'air en fonction des variations environnementales, nous avons pu réduire les dérives de quelques micromètres à une centaine de nanomètres, ce qui rend possible l'utilisation de l'instrument dans nos conditions de travail les plus difficiles.

## 3.6 Projets et perspectives

Pour continuer notre démarche vers la compréhension du rôle complexe de l'eau dans la propagation de fissures dans les verres, nous devrons clarifier le processus de perméation de l'eau dans le volume du verre. Selon Tomozawa (1996) and Oehler (2004) la diffusion de l'eau augmente exponentiellement avec la tension appliquée sur le verre ; ceci devrait être un phénomène plutôt intense en proximité de la pointe de fissure à cause de très hautes valeurs des contraintes. Ce phénomène mérite que l'on s'y intéresse car, comme annoncé par Tomozawa (2004), la diffusion d'eau dans le volume comporte une profonde modification de la structure de la silice à cause de la forte réactivité de l'eau. Ces altérations peuvent être décrites par une augmentation de la température fictive locale, qui est une mesure du degré de désordre dans le verre, ce qui comporterait une réduction de la viscosité et des modules élastiques locaux.

Il est immédiatement clair qu'on ne peut pas négliger cet effet dans la compréhension des mécanismes d'avancement des fissures à très faible vitesse. Par exemple, la réduction de la viscosité locale peut être révélatrice dans l'explication du mécanisme de nucléation et croissance des cavités. La taille de 20 nm observée expérimentalement (voir section 3.3) est en fait trop grande par rapport à ce qu'on attendrait d'une modélisation théorique fondée sur les propriétés du verre non-altéré.

Pour comprendre les modifications induites dans le verre lors la pénétration de l'eau, nous envisageons de mesurer les propriétés d'une série de verres qui présentent un taux d'eau préexistante différent. Pour exclure la diffusion d'eau ultérieure par les surfaces externes du verre, nous pourrons effectuer des traitements de hydrophobisation des surfaces, ou bien de densification superficielle.

Une deuxième direction de recherche, consiste à vérifier que le phénomène de nucléation, croissance et coalescence des cavités, observé en temps réel en surface de l'échantillon (voir section 3.3), soit aussi le phénomène qui contrôle l'avancement de la fissure à l'intérieur du volume du verre.

Cette observation est très difficile à cause de la petite taille des cavités qui exclue l'utilisation de techniques globales, telles que les rayons X ou la diffusion de neutrons. Nous envisageons donc de chercher la signature de ces procès dans la morphologie des surfaces de fracture opposées, après que la fracturation lente (en conditions contrôlées) soit complétée.

La difficulté principale de ces mesures (que l'on appelle tests *post-mortem*) est de faire correspondre les deux surfaces opposées avec précision nanométrique. Un atout important nous viendra de l'utilisation de l'interféromètre décrit en section 3.5.3. L'application de la technique FRASTA (FRActure Surface Topography Analysis, voir Célarié et al., 2003) nous permettra ensuite d'estimer la distribution tridimensionnelle de l'endommagement dans le verre et de déterminer sa variation avec la distance de la surface extérieure, ainsi qu'avec les conditions de chargement, les conditions environnementales et la composition du verre. Cette étude sera menée en collaboration avec le CEA de Saclay.

Pour permettre à ces recherches de viser plus loin, il faut accroître le potentiel du montage expérimental pour permettre une caractérisation plus complète des propriétés physico-chimiques aux alentours nanométriques de la pointe de fissure.

Le développement récent de techniques de nanomécanique permet de transformer l'AFM d'un instrument de mesure topographique vers un outil beaucoup plus versatile et capable de mesurer de nombreuses propriétés physiques avec une résolution latérale de

l'ordre de la dizaine de nanomètres. On a vu dans la section 3.4.1 comment on a pu obtenir des renseignements sur l'adhésion capillaire induite par la couche d'eau superficielle ou bien par le condensat liquide dans la fissure. Mais les potentialités sont beaucoup plus larges et passent de la mesure de la variation locale des modules élastiques ou viscoélastiques, des propriétés d'adhésion et de frottement (Arribart et Abriou, 2000 ; Garcia and Pérez, 2002) vers des mesures de caractère plus chimique, telles que le caractère d'acido-basicité des surfaces, les propriétés de mouillage, et la détection de groupements chimiques spécifiques (Aigouy *et al.*, 2006 ; Aimé *et al.*, 2002).

Ces potentialités dérivent d'une modélisation de plus en plus fine des interactions au niveau moléculaire entre les derniers atomes de la pointe AFM et les molécules à la surface de l'échantillon, par l'intermédiaire d'une atmosphère donnée ou d'une couche liquide (Israelachvili, 1985). Mais le développement au niveau plus quantitatif de ces techniques ne peut avancer que par le progrès des connaissances de la physique à l'échelle nanométrique : comment les lois fondamentales qui regardent les propriétés sus-mentionnées se modifient elles à l'échelle nanométrique ?

Le mode 'tapping' revêt un intérêt particulier parmi ces techniques, parce que l'interaction entre la pointe et l'échantillon devient plus intense même si elle se produit pendant un temps très bref. Le caractère fortement non-linéaire des interactions est responsable d'une réponse mécanique du levier AFM très complexe, mais qui peut devenir très riche en renseignements. Pour en profiter il faut abandonner les traitements de signaux opérés par les instruments commerciaux et réaliser nous-mêmes toutes les étapes de pilotage et d'analyse.

En section 3.5.1 j'ai décrit la première phase de cette démarche, consistant à effectuer la mesure de la phase AFM avec une détection synchrone. Dans un futur proche, nous avons l'intention de réaliser une chaîne d'acquisition directe des signaux haute-fréquence relatifs à l'oscillation du levier. L'accès direct à la forme du signal va nous permettre en premier lieu une étude des harmoniques supérieures de l'oscillation, qui contiennent beaucoup de renseignements sur la partie non-linéaire de l'interaction ; en deuxième lieu on pourra effectuer une étude du bruit thermique du levier non stimulé, qui fournit aussi des renseignements très sensibles sur les propriétés du levier, de l'atmosphère et, espérons-le, de l'interaction avec l'échantillon.

Une fois que nous aurons maîtrisé ces techniques, nous pourrons jouer sur les différentes fonctionnalisations des pointes AFM ou bien des surfaces du verre pour rendre la mesure plus ou moins sensible à l'une ou l'autre propriété physique. Nous pourrons par exemple altérer la susceptibilité de la pointe au mouillage - qui conduit à la formation du pont capillaire - et observer les effets sur l'énergie dissipée lors du contact, en fonction de la composition de l'eau de la couche superficielle. Nous pourrons en outre avoir plus de renseignements sur la nature des nodules qui accompagnent la diffusion ionique dans les verres sodo-silicatés.

# Bibliographie


Aigouy L., Dewilde Y., Frétigny C., 2006. Dynamic force microscopy methods (Belin, Collection Echelles, Paris), sous presse.

Aimé J.P., Boisgard R., Couturier G., 2002. Microscopie de Force Dynamique. Cours présenté au Forum de Microscopies à Sonde Locale 2002 tenu à La Grande Motte.

Arribart, H. and Abriou D., 2000. Ten years of atomic force microscopy in glass research. *Ceramiks – Silikàty*. **44**, pp. 121-128.

Atkinson B.K., 1984. Subcritical crack growth in geological materials. *J. Geophys. Res.*, **89**, pp. 4077-4114.

Atkinson B.K. Fracture mechanics of rock (Academic Press, 1987).

Bak P., Christensen K. Danon L., Scanlon T., 2002. Unifies scaling laws for earthquakes. *Phys. Rev. Lett.* **88**, pp. 178501-178504.

Barquins M., Ciccotti M., 1997. On the kinetics of peeling of an adhesive tape under a constant imposed load. *Int. J. Adhes. Adhes.* **17**, pp. 65-68.

Bellon L., Buisson L., Ciccotti M., Ciliberto S. et Douarche F., Thermal noise properties of two ageing materials. Proceedings of the XIX Sitges (June 2004) Conference on "Jamming, Yielding, and Irreversible Deformation in Condensed Matter", M.-C. Miguel and M. Rubí eds., Springer Verlag, Berlin.

Bellon L., Ciliberto S. and La Roche C., 2001. Violation of the fluctuation-dissipation relation during the formation of a colloidal glass. *Europhys. Lett.*, **53 (4)**, pp. 511–517.

Ben-Zion Y., 2001. Dynamic ruptures in recent models of earthquake faults, *J. Mech. Phys. Solids*, **49**, pp. 2209–2244.

Bouchaud E., 1997. Scaling properties of cracks. *J. Phys: Condens. Matter*. 9, pp. 4319-4344.

Bouchaud J.P., Cugliandolo L.F., Kurchan J. and Mézard M., Out of equilibrium dynamics in Spin Glasses and other glassy systems, in Spin Glasses and Random Fields, edited by A. P. Young (World Scientific, Singapore, 1998).

Buisson L., Ciccotti M., Bellon L. and Ciliberto S.. Electrical noise properties in aging materials. In: “Fluctuations and Noise in Materials”, edité par D. Popovic, M.B. Weissman et Z.A. Racz. Proceedings of SPIE Vol. 5469 (SPIE, Bellingham, WA, 2004). Invited paper. pp. 150-163.

Célarié F., 2004. Dynamique de fissuration à basse vitesse des matériaux vitreux. Thèse à l’Université Montpellier II.

Célarié F., Prades S., Bonamy D., Ferrero L., Bouchaud E., Guillot C. and Marlière C., 2003. Glass breaks like metals, but at the nanometer scale. *Phys. Rev. Lett.* **90**, p. 075504.

Célarié F., Ciccotti M., George M. and Marlière C, 2006. Effect of stress gradient at the vicinity of a crack tip on ionic diffusion in silicate glasses: an AFM study. . Proceedings of the conference Fractography of Glasses and Ceramics V. 9-12 July 2006. Rochester, NY (USA). A paraître.

Célarié F., Ciccotti M. and Marlière C., 2006. Stress-enhanced ion diffusion at the vicinity of a crack tip as evidenced by atomic force microscopy in silicate glasses. *J. Non-Crist. Solids.* A paraître.

Ciccotti M., 2000. A realistic finite element study of the Double Torsion loading configuration. *J. Am. Cer. Soc.* **83 [11]**, pp. 2737-44.

Ciccotti M., Giorgini B., Barquins M., 1998. Stick-slip in the peeling of an adhesive tape : evolution of theoretical model. *Int. J. Adhes. Adhes.* **18**, pp. 35-40.

Ciccotti M. and Giorgini B. The emergence of complexity in a common scotch roller. Dans: « Symétries, brisures de symétries et complexité ». Edité par L. Boi (Peter Lang, Bern, 2006) pp. 187-216.

Ciccotti M., Giorgini B., Vallet D. and Barquins M., 2004. Complex dynamics in the peeling of an adhesive tape. *Int. J. Adhes. Adhes.* **24/2**, pp. 143-151.Célarié F., Ciccotti M., George M. and Marlière C. Effect of stress gradient at the vicinity of a crack tip on ionic diffusion in silicate glasses: an AFM study. Proceedings of the conference Fractography of Glasses and Ceramics V. 9-12 July 2006. Rochester, NY (USA). Soumis en juillet 2006.

Ciccotti M. and Mulargia F., 2002. Pernicious effect of physical cutoffs in fractal analysis. *Phys. Rev. E*. **65**, pp. 37201-04.

Ciccotti M., Negri N., Sassi L., Gonzato G. and Mulargia F., 2000. Elastic and fracture parameters of Etna, Stromboli and Vulcano lava rocks. *J. Volc. Geoth. Res.* **98/1-4**, pp. 209-217.

Ciccotti M., Gonzato G., and Mulargia F., 2000. The double torsion loading configuration for fracture propagation: an improved methodology for the load-relaxation at constant displacement. *Int. J. of Rock Mech. and Mining Sciences.* **37/7**, pp. 1103-1113.

Ciccotti M., Negri N., Gonzato G., Mulargia F., 2001. Practical application of an improved methodology for the Double Torsion load relaxation method. *Int. J. of Rocks Mech. and Mining Sciences*, **38**, pp. 569-576.

Ciccotti M., Almagro R. and Mulargia F., 2004. Static and dynamic moduli of the seismogenic layer in Italy. *Rock Mech. and Rock Eng.* **37[3]**, pp. 229-238.

Ciccotti M., Mulargia F., 2004. Differences between static and dynamic measurements of the elastic moduli in a typical seismogenic rock. *Geophys. J. Int.* **157[1]**, pp. 474-477.

Cipelletti L., Bissig H., Trappe V., Ballesta P. and Mazoyer S., 2003. Time-resolved correlation: a new tool for studying temporally heterogeneous dynamics. *J. Phys.: Condens. Matter*, **15,** pp. S257–S262.

Cleveland J.P., Anczykowski B., Schmid A.E., Elings V.B., 1998. Energy dissipation in tapping-mode atomic force microscopy, *App. Phys. Lett.*, **72**, pp. 2613-2615.

Cugliandolo L., and Kurchan J., 1993. Analytical Solution of the Off Equilibrium Dynamics of a Long Range Spin Glass Model, *Phys. Rev. Lett.* **71**, p. 173.

Cortet P.-P., Ciccotti M. and Vanel L. Imaging the stick-slip peeling of an adhesive tape. *Int. J. Adhes. Adhes.* En preparation.

Deschanel, S. 2005. Dynamique des précurseurs de la rupture des matériaux hétérogènes: application aux mousses polymères vitreuses. Thèse INSA de Lyon.

Deschanel, S., Vanel, L., Vigier, G., Godin, N., & Ciliberto, S. 2006. Statistical properties of microcracking in polyurethane foams under tensile test, influence of temperature and density. *Int. J. Fracture*, à paraître.

Evans A.G., 1972. A method for evaluating the time-dependent failure characteristics of brittle materials - and its applications to polycrystalline alumina. *J. Mater. Sci.* **7[10]** pp. 1137-1146.

Garcia R. and Pérez R., 2002. Dynamic force microscopy methods. *Surf. Sci. Rep.* **47**, pp. 197-301.

George M., Ciccotti M., Wondraczek L., Dittmar A., Oelgardt C., Célarié F. and Marlière C., 2006. Formation and evolution of a confined liquid condensate at the crack tip in glasses. Proceedings of the conference Fractography of Glasses and Ceramics V. 9-12 July 2006. Rochester, NY (USA). A paraitre.

Gonzato G., Mulargia F., Ciccotti M., 2000. Measuring the fractal dimension of ideal and actual objects: implications for application in geology and geophysics. *Geophys. J. Int.* **142**, pp. 108-116.

Garcimartin, A., Guarino, A., Bellon, L., and Ciliberto, S., 1997. Statistical properties of fracture precursors. *Phys. Rev. Lett.*, **79**, 3202.

Kumar J., De R., Ciccotti M. and Ananthakrishna G. Unfolding the hidden order in acourstic emission data in the peeling of an adhesive tape. Proceedings of the conference : Multiscale Material Modeling, September 18-22, 2006. Freiburg, Germany.

Israelachvili J. N., Intermolecular and Surface Forces (Academic, London, 1985).

Lawn B. Fracture of Brittle Solids, 2nd edition (Cambridge University Press, Cambridge, 1993)

Maugis D. and Barquins M. Dans: 'Adhesion 12', Ed : K.W. Allen (Elsevier Applied Science, London, 1988), pp. 205-222.

Mulargia F. and Ciccotti M. Ingredients for sound (multi)fractal attribution. Soumis à *Phys. A.*

Mulargia F. and Geller R. Earthquake Science and Seismic Risk Reduction. NATO SCIENCE SERIES: IV: Earth and Environmental Sciences Volume 32. Edité par F. Mulargia et R. Geller. Kluwer. 2003.

Mulargia F., Castellaro S. and Ciccotti M.. Earthquakes as three stage processes. *Geophys. J. Int.* **158[1]**, pp. 98-108.

Mulargia F., Castellaro S. and Ciccotti M.. Ignition threshold and self-similarity allow earthquakes to be triggered by tiny stresses. Soumis à *Geophys. Res. Lett.*

Nony L., Cohen-Bouhacina T. and Aimé, J-P, 2002. Dissipation induced by attractive interaction in dynamic force microscopy: contribution of adsorbed water layers. *Surf. Sci.* **499**, pp. 152-160.

Oehler A. and Tomozawa M., 2004. Water diffusion into silica glass at a low temperature under high water vapor pressure, *J. Non-Cryst. Solids*, **347**, p. 211.

Swanson P.L., 1984. Subcritical Crack Growth and Other Time - and Environment - Dependent Behavior in Crustal Rocks. *J. Geophys. Res.* **89 B6**, pp. 4137-4152.

Tomozawa M., 1996. Fracture of Glasses. *Annu. Rev. Mater. Sci.* **26**, p. 43.

Tomozawa M. and Hepburn R.W., 2004. Surface structural relaxation of silica glass: a possible mechanism of mechanical fatigue, *J. Non-Cryst. Solids,* **345**, p. 449.

Wiederhorn S.M., 1967. Influence of water vapor on crack propagation in soda-lime Glass. *J. Am. Ceram. Soc.* **50**, pp. 407-414.

Wondraczek L., Ciccotti M., Dittmar A., Oelgardt C., Célarié F. and Marlière C., 2006. Real-time observation of non-equilibrium liquid condensate confined at tensile crack tips in oxide glasses. *J. Am. Cer. Soc.* **89[2]**, pp. 746-749.

Wu Q., Borkovec M. and Sticher H., 1993. On particle size distribution in soils. *Soil Sci. Soc. Am.* **57**, pp. 883-890.

Zitzler L., Herminghaus S., Mugele F., 2002. Capillary forces in tapping mode atomic force microscopy, *Phys. Rev. B,* **66**, p. 155436.